

University of
Strathclyde
Glasgow

**Nanoscale 3D Transfer Printing for Hybrid
Photonic Device Fabrication**

PhD Thesis

Miles Toon

Institute of Photonics
Department of Physics
University of Strathclyde, Glasgow

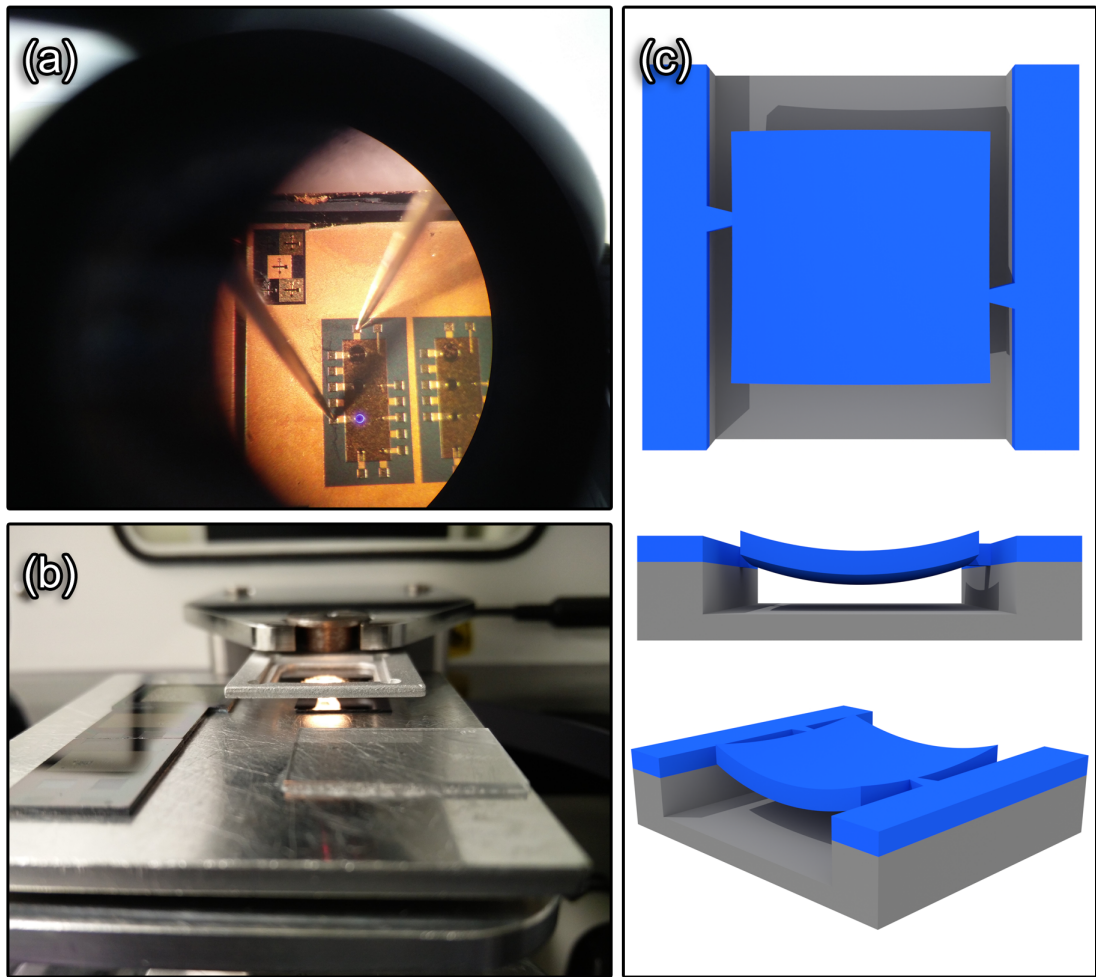
May 2025

This thesis is the result of the author's original research. It has been composed by the author and has not been previously submitted for examination which has led to the award of a degree.

The copyright of this thesis belongs to the author under the terms of the United Kingdom Copyright Acts as qualified by University of Strathclyde Regulation 3.50. Due acknowledgement must always be made of the use of any material contained in, or derived from, this thesis.

Signed : Miles Toon

Date : May 2025



(a) Probing bespoke GaN LED wafer test sample emitting 450 nm wavelength light to test the IV characteristics. (b) Transfer printing suspended GaN LED material membranes to a silica test receiver to test printability. (c) 3D render of a typical individual suspended square membrane illustrating the bowed morphology caused by internal strain once the supporting material is removed.

Abstract

This thesis presents the development of gallium nitride (GaN) and other III-V nitride semiconductor material fabrication protocols to create transfer printable device coupons, such as light emitting diodes (LEDS) and distributed Bragg reflectors (DBRs), for use in the construction of vertically stacked hybrid devices. The epilayer material is refined using systematic processing and metrology of a series of epitaxially grown wafers to determine optimal ammonia dosage in growth to create flatter devices with the goal to minimise the air-gaps introduced from stacking. A thicker strain managed buffer structure succeeds in reducing the bow by a factor of three compared to devices from commercially available material. The novel structures had a radius of curvature of 2.98 mm and 3.13 mm compared to the commercial material's 0.88 mm. The geometry of the tethers suspending the devices was assessed with a systematic study; two tethers with a width of 3 μm and a straight shape being determined optimal for this particular material platform by the success rate of transfer printing the resultant suspended devices. A two stage lithography process was developed to successfully fabricate DBR coupons for transfer printing and use in hybrid devices; overcoming the difficulties of device release and wet-etch damage presented by using a novel porous GaN material. Using finite difference time domain (FDTD) simulation software the optimal LED layer structure for a 450 nm resonant cavity LED (RCLED) was determined for combining with the aforementioned DBRs. The design was to be used by transfer printing the LED onto a DBR or metal bottom mirror and then stacking an exit DBR mirror on top, although has yet to be realised.

Acknowledgements

To my late mother, *Louise*, who never got to see me flourish. I will never be praised by you, but I would give anything to remember your voice. I have tried my best to be a good person and strive to improve, knowing that my beginnings were not ideal. I have been told that you would be very proud, which in itself brings a lump to my throat.

To my grandparents, *Malcolm* and *Mary*, who took me in, raised me, and supported my studies. They may have had a generational divide that limited their understanding, but they always wished for my happiness. For that, I love you. And sadly now, grandma, I miss you. I am also thankful to my aunt, *Rachel*, for her love and compassion throughout.

I met my partner, *Megan Clapperton*, during the second year of this PhD, while we were all isolating due to the COVID-19 outbreak. I was very much isolated—alone in my flat, with my grandparents over 300 miles away, I had no one to see or talk to. Thankfully, Megan thought I was worth bringing into her bubble, and I was free to recoup my sanity at a socially distanced 2 m. She started her own PhD at the University of Strathclyde, and I greatly enjoyed pointing out the pitfalls and successes she was yet to experience! We have supported each other through our various personal troubles, making a great team. While writing this thesis, I was accompanied by our cat, Pudge (pictured), for the majority of the time. She alleviated much of my mental strain and loneliness, and in exchange, she received just as much love—and occasionally, a wee piece of cheese. She is worth my state of perpetual rhinitis and tears—I am quite allergic to my darling girl.



Pudge

From my undergraduate studies, *Alex Coates* and *Chris Oliver* have kept a special place in my heart. Alex began his PhD at Heriot-Watt University when I started mine, so we occasionally referred to ourselves as the “Scot-Squad”, as we were the only two from our university friends’ group to cross the border. Alex and I took turns visiting each other’s respective cities, embracing the local culture with familiar company. Chris also began his PhD at the same time but at the University of Birmingham. His sense of humour closely reflects my own, so we have always got along well. He and I have talked for hours about life, with a dash of inane topics that have kept us both mentally sound. Without these two, I would have struggled to make it.

Thank you to *Emma Butt* and the rest of the friends I made at the Institute of Photonics (where I completed my PhD). It was nice to have a group of people to be social with and share Friday afternoon tea breaks! The activities we arranged together helped bring me out of my self-imposed introverted barriers. It was such a shame that many of these gatherings were cut short due to the lockdown and everyone progressed with their lives.

Thanks to my supervisors, *Prof. Michael Strain* and *Prof. Martin Dawson*, for their guidance during my PhD, and to *Dr. Benoît Guilhabert* and *Dr. Ian Watson* for taking the time to share their valuable knowledge and training. I worked closely with Benoît in the cleanroom, adapting many of his processes to be my own. He also dedicated

time to fabricating devices to assist with my projects, for which I am very grateful. I would also like to thank the administrative staff, *Sharon* and *Lorraine*, for organizing the important bits and arranging enjoyable events! A big thanks to *Leanore Ferrans* from IT support, who ensured my office PC functioned properly and provided kindness and compassion, which I greatly appreciated.

Finally, I would like to thank my collaborators at the University of Cambridge for providing materials and assisting in the various studies detailed in this thesis. *Prof. Rachel A. Oliver* and her group were invaluable in providing insight when designing the GaN LED structures, as well as helping me understand a significant portion of the III-V material growth background.

SARs COVID-19 Impact

Statement

The original duration of my PhD funding was set from October 2018 to April 2021. The COVID-19 pandemic began to significantly disrupt my studies in March 2020 and continued to do so for over a year, with its effects still being felt beyond that period. In early March 2020, I was instructed to gather as much data as possible to work from home, with the expectation of returning after an estimated three-month lockdown. Unfortunately, it ultimately took a full year—until March 2021—before I was granted access to the cleanroom where I worked. Even then, social distancing restrictions imposed occupancy limits that prevented any functional fabrication from taking place.

Tooling had to be booked two weeks in advance, which was incompatible with the inherently uncertain nature of novel fabrication. Additionally, the equipment frequently suffered downtime, a problem exacerbated by the departure of the maintenance technician at the time. Training on the equipment I needed was also delayed due to limited access and social distancing requirements. I was scheduled to complete my training on the transfer print tool for independent research, but a lack of available qualified personnel prevented this from happening.

Laboratory access was cut off midway through my second year, just as I was beginning to ramp up the production of transfer-printable devices. Fortunately, I had already fabricated and measured a few systematically produced sets of devices corresponding to

the growth of their respective wafers. The results of this work are presented in Chapter 3. The morphological measurements were processed at home and contributed to my first publication [1]. During this period, in correspondence with collaborating groups, I redirected my research toward simulating a hybrid photonic device to determine the optimal design for bespoke LED wafers to process upon my return to the cleanroom. This simulation work is detailed in Chapter 6.

When I was finally able to return, access remained highly restricted due to occupancy limits designed to curb viral spread. The functionality of the tooling was inconsistent, and combined with material lead times and delayed training, I ultimately ran out of time to achieve what I had originally intended. Given the resources and skills available, I focused on optimizing the fabrication of the individual components of the compound device, as detailed in Chapters 4 and 5. The bespoke material I designed arrived only as my time was running out and, unfortunately, was never processed as intended.

Research Output

Publications

B. F. Spiridon, M. Toon, A. Hinz, S. Ghosh, S. M. Fairclough, B. J. E. Guilhabert, M. J. Strain, I. M. Watson, M. D. Dawson, D. J. Wallis, R. A. Oliver, “Method for inferring the mechanical strain of GaN-on-Si epitaxial layers using optical profilometry and finite element analysis,” *Optical Materials Express*, Vol. 11, no. 6, pp. 1643—1655, 2021. DOI: 10.1364/OME.418728.

N. Kolja Wessling, S. Ghosh, B. J. E. Guilhabert, M. Kappers, A. M. Hinz, M. Toon, R. A. Oliver, M. D. Dawson, M. J. Strain, “Fabrication and transfer printing based integration of free-standing GaN membrane micro-lenses onto semiconductor chips,” *Optical Materials Express*, Vol. 12, no.12, pp. 4606—4618, 2022. DOI: 10.1364/OME.472999.

B. J. E. Guilhabert, M. Toon, S. Ghosh, J. F. Carreira, R. A. Oliver, M. D. Dawson, M. J. Strain, “Heterogeneous Integration of GaN-Based Devices by Transfer Printing,” Manuscript in preparation.

Posters

M. Toon, B. J. E. Guilhabert, A. Hinz, B. F. Spiridon, S. M. Fairclough, I. M. Watson, R. A. Oliver, M. D. Dawson, M. J. Strain, “Strain Managed GaN LED Structures for 3D Transfer Printing,” Poster, Institute of Physics, Photon 2020. 2020.

Contents

Abstract	i
Acknowledgements	ii
SARs COVID-19 Impact Statement	v
Research Output	vii
List of Abbreviations	xviii
1 Introduction	1
1.1 Motivation	2
1.1.1 Gallium Nitride	3
1.1.2 Light Emitting Diode Devices and Their Alternatives for Visible Light Communication	5
1.2 Transfer Printing Technology	9
1.3 Our Approach to Nitride RCLEDs	10
1.4 Thesis Outline	12
2 Cleanroom Microfabrication Processes	14
2.1 Overview	14
2.2 Solvent Cleaning	15
2.3 Oxygen Plasma Ashing	17
2.4 PECVD - SiO ₂ Deposition	18

2.4.1	Function of the PECVD Tool	19
2.4.2	Operation of the PECVD Tool	20
2.5	Photolithography	21
2.5.1	Photoresist Spinning	22
2.5.2	Exposure Methods	27
2.5.3	Development	29
2.6	RIE - Dry Etching Using the Soft-Mask	29
2.6.1	Function of the RIE Tool	30
2.6.2	Operation of the RIE Tool	31
2.7	ICP-RIE - Dry Etching Using a Hard-Mask	32
2.7.1	Function of the ICP Tool	32
2.8	RIE - Dry Etching Silicon Trenches	35
2.9	PECVD - Applying Sidewall Protection	36
2.10	Wet Etching Using KOH	36
2.11	Metal Deposition - Electron Beam	39
2.11.1	Function of the E-Beam Deposition Tool	40
2.12	RTA - Rapid Thermal Annealer	41
2.13	Metal Deposition - CVC Sputter	42
2.14	Transfer Print Tool	43
2.14.1	Elastomeric Transfer Print Stamps	44
2.14.2	Sample Preparation	47
2.14.3	Calibration of the Printing	48
2.14.4	Making a Print	49
2.15	Metrology Equipment	49
2.15.1	Optical Microscopy	49
2.15.2	White Light Reflectometry	50
2.15.3	Stylus Profilometry	51
2.15.4	Optical Profilometry of Suspended Membranes	52
2.15.5	Function of the Optical Profilometry Tool	53
2.15.6	AFM - Atomic Force Microscopy	54

2.15.7	Probe Station	55
3	Effect of Ammonia Pre-Dose on Wafer-Level and Device-Level	
	Flatness	57
3.1	Overview	57
3.2	HEMT Systematic Bowing Study	60
3.2.1	Fabrication	62
3.2.2	Membrane Bow Measurements	65
3.2.3	Optical Profilometry	66
3.2.4	Optical Profilometry Data Processing	67
3.2.5	AFM of Membrane Backsides	72
3.3	LED Systematic Bowing Study	74
3.3.1	Fabrication	75
3.3.2	Transfer Printing of the LED Devices	77
3.3.3	Topography Measurements	79
3.4	Summary and Discussion	81
4	Membrane Tether Design and PDMS Stamp Release Process	83
4.1	Overview	83
4.2	Custom GDS File Creation Using Python	84
4.2.1	Membrane Fabrication Using the Heidelberg DWL66 Tool	87
4.3	PDMS Stamp Ratio Adhesion Measurement	87
4.4	Transfer Print Measurement	88
4.5	New ‘Bow Tie’ Tether Development and LED Fabrication Python Scripting	91
4.6	Summary and Discussion	92
5	DBR Membrane Fabrication for Transfer Printing	94
5.1	Overview	94
5.2	The Mesoporous GaN DBR Material	95
5.2.1	Structure of the DBR Material	96
5.3	Optimising Microfabrication for Porous GaN DBR Material	97

5.3.1	Single Stage Photolithography Suspended Membrane Fabrication Using Mask Aligner	98
5.3.2	White Light Reflectometry Measurements	106
5.3.3	Transfer Printing Full Thickness DBR Membranes	109
5.4	Selectively Reducing the Thickness of the DBR Material	110
5.4.1	Laser Lithography on Existing Membranes	111
5.4.2	Two Stage Laser Lithography to Thin Tethers	113
5.4.3	Two Stage Photolithography Suspended Membrane Fabrication Using the Mask Aligner	114
5.4.4	Transfer Printing Thinned DBR Membranes	116
5.5	Summary and Discussion	117
6	Designing the GaN Resonant Cavity LED	120
6.1	Overview	120
6.2	Creating Refractive Index Sets for Material Simulations	121
6.2.1	III/V Nitride Alloy Ratios	121
6.3	Finding the Number of DBR Layers Required for ~ 0.6 and ~ 1 Reflectivities Using Porous GaN	125
6.4	DBR Design Using FDTD Simulations	128
6.5	RCLED Design Using FDTD Simulations	132
6.5.1	RCLED Design Using Full Thickness LED Coupon	133
6.5.2	RCLED Design Using Shortened LED Coupon	135
6.6	Post-Simulation Adjustments to Finalise the LED Designs	137
6.7	Summary and Discussion	139
7	Conclusions and Future Work	140
7.1	Conclusions	140
7.2	Next Steps and Future Work	144
A	Python Code	158
B	Research Output	176

List of Figures

1.1	III-nitride band gap energy as a function of lattice constant.	4
1.2	Everyday uses of LEDs.	5
1.3	GaInP/AlGaInP/GaAs MQW RCLED structure.	8
1.4	Alternative RCLED fabrication method process flow.	11
2.1	Process flow for membrane fabrication.	16
2.2	The ultrasonic cleaner and solvent bench.	17
2.3	The Matrix plasma asher.	17
2.4	The PECVD tool.	18
2.5	Simplified systematic diagram of PECVD chamber.	19
2.6	Silica deposition step.	21
2.7	Schematic diagram differentiating positive and negative resists.	22
2.8	Asymmetry issue with photoresist spinning diagram.	23
2.9	The photoresist spinner lined with cleanroom wipes ready to spin a sample.	24
2.10	Diagram of HMDS bubbling to priming samples for photoresist.	24
2.11	Diagram of common photoresist spinning issues.	26
2.12	The Karl SUSS mask aligner tool.	28
2.13	The photoresist development step.	30
2.14	The RIE tool and schematic diagram.	31
2.15	SiO ₂ hard mask formation with RIE step.	32
2.16	The ICP tool and schematic diagram.	33
2.17	ICP etching aspect ratio diagram.	34
2.18	The primary ICP etching of epilayers step.	35

2.19	The SiO ₂ sidewall protection layer deposition step.	36
2.20	Silicon (111) etch direction geometry.	37
2.21	The KOH under-etch process.	38
2.22	The final SiO ₂ removal step.	39
2.23	The E-beam evaporator used for thin metal film deposition.	40
2.24	The rapid thermal annealing tool.	41
2.25	Wafers being loaded into the CVC sputter tool.	42
2.26	The converted Nanoink NLP2000 tool used for transfer printing.	43
2.27	Illustration of PDMS stamps used for transfer printing.	44
2.28	Stamp mould fabrication process diagram.	45
2.29	Diagram of a stamp adhered to its holder.	46
2.30	Two close up shots of the stamp and holder installed into the transfer print tool.	47
2.31	A closer view of the stage and working area of the transfer print tool.	48
2.32	The Leica DMR microscope.	50
2.33	The Filmetrics F20 thin film measurement device.	51
2.34	The Dektak 3 stylus profilometer.	52
2.35	The Wyko NT1100 optical profiling system.	53
2.36	Schematic diagram of optical profilometer.	54
2.37	The Park Systems AFM.	55
2.38	The probe station tool.	56
2.39	Output plot of a Python script processing probe station IV data.	56
3.1	Graphic representation of bowed membrane on a flat surface.	58
3.2	Epilayer structure of HEMT material for ammonia dosage study.	61
3.3	Graph of ammonia dosage for the series of HEMT wafers.	62
3.4	The photolithography mask design for making suspended HEMT material membranes.	63
3.5	Microscope images of the minimum and maximum ammonia dosage samples after ICP etch showing defects.	64
3.6	Microscope images of completed suspended HEMT material membranes.	66

3.7	Raw image from optical profiler of suspended HEMT material membrane to be processed using Gwyddion software.	67
3.8	Three point levelling tool in Gwyddion software.	68
3.9	Setting the z-range colourbar in Gwyddion software.	69
3.10	The profile drawn across the membrane and the resultant cross-sectional plot.	71
3.11	Output of Python code which approximates the suspended membrane curvature to a circle.	72
3.12	AFM measurements of the backside of the suspended HEMT material membranes.	73
3.13	Epilayer structure of the LED material used in the dislocation blocking layer study.	75
3.14	The fully fabricated LED suspended membranes.	76
3.15	Diagram showing the effect of tether geometry causing incomplete KOH under-etch.	77
3.16	The transfer printing of the LED membranes.	78
3.17	Microscope image of transfer printed LED membranes.	79
3.18	Side by side comparison of suspended membranes from all three sample types using optical profilometry with a false colour scale representing height in (μm).	80
3.19	Comparison optical profilometer images of transfer printed LED membranes.	80
4.1	GDS Helpers tutorial Python script output.	85
4.2	Schematic diagram of GDSII file hierarchy.	86
4.3	Illustration of tether geometry categorisation for systematic tether study.	86
4.4	Microscope images of all the final suspended membranes with varied tether geometries giving a representation of the fabrication quality.	90
4.5	The newly developed bow tie tether design.	91
4.6	GDSII output of Python script containing all geometries required to create a suspended LED device.	92

5.1	Mesoporous GaN DBR wafers.	96
5.2	Layer structure design for the DBR material before the porosification of the n^+ layers, with primary reflectance band centred on 460 nm. Material grown and provided by the University of Cambridge.	97
5.3	Schematic diagram showing the dicing of the DBR half-wafers.	99
5.4	Microscope images of the DBR photolithography to assess quality.	100
5.5	Schematic diagram of ICP etch depth calculation.	102
5.6	Microscope images of DBR membranes after KOH under-etch.	104
5.7	Microscope images of DBR membranes after sidewall protection removed.	105
5.8	SEM image of damage to DBR layers from KOH etch.	106
5.9	White light reflectometry spectra of DBR samples.	108
5.10	Microscope images of transfer printing DBR membranes.	110
5.11	Schematic diagram of selective material thinning ICP etch.	111
5.12	Microscope image of the 5 layer DBR sample after the development of the ma-N 1410 photoresist pattern used to isolate the suspended membranes.	112
5.13	Example images of photoresist burnt from RIE etching.	113
5.14	Microscope images of selectively etched DBR mesas to thin device tethers.	115
5.15	Vacuum baked photoresist to pattern the tether geometries on the DBR membranes.	116
5.16	The finalised DBR membranes with selectively thinned tethers.	117
5.17	Microscope images of transfer printing DBR membranes.	118
6.1	Refractive index against wavelength for mesoporous GaN.	122
6.2	Calculated refractive indices against wavelength for GaN and InGaN.	124
6.3	Interpolation parameters against mole fraction for calculating AlGaIn refractive indices.	126
6.4	Calculated refractive indices for AlGaIn against wavelength for the full range of mole fractions.	127
6.5	Calculated reflectivity of DBR for various number of repeated pairs.	128
6.6	Lumerical FDTD setup for reflection and transmission simulation.	129

6.7	Reflection and transmission plot comparison of simulated DBRs using Lumerical.	130
6.8	Reflection and transmission plot of simulated Pd mirror using Lumerical.	131
6.9	Reflectivity of common metals versus wavelength at normal incidence. .	132
6.10	Illustration of the two designs of RCLED.	133
6.11	Plot of electric field against length for full LED structure.	134
6.12	Labelled setup of the Lumerical FDTD optical cavity simulations. . . .	136
6.13	Visualisations of the electric field against refractive index to find optimal quantum well overlap in an RCLED structure.	137

List of Tables

2.1	Process configuration for annealing Ni/Au bilayer on the RTA.	42
3.1	Wafer bow measurements compared to suspended HEMT membrane bow.	72
3.2	RMS roughness of the HEMT membranes backsides.	73
3.3	Mean values of radius of curvature of LED membranes measured using optical profilometry.	81
4.1	Success rates of transfer printing membranes with various tether geometries.	89
5.1	Measured ridge height on DBR test pieces after being ICP etched for 8 min.	101
5.2	Measured ridge height on DBR samples after being ICP etched for 8 min including the height of silica hard mask.	101
5.3	Parameters used for the DWL66 laser lithography tool to expose ma-N 1410 photoresist on a GaN DBR substrate.	112
6.1	Finalised designs for LEDs to be grown by the University of Cambridge.	138
6.2	Details of LED growth data for the first series produced using the design from FDTD simulations.	138

List of Abbreviations

AFM	Atomic Force Microscope	GaInP	Gallium Indium Phosphide
Ag	Silver	GaN	Gallium Nitride
AlAs	Aluminium Arsenide	GDSII	Graphic Data Stream II
AlGaAs	Aluminium Gallium Arsenide	GDS	Graphic Data Stream
AlGaInP	Aluminium Gallium Indium Phosphide	HEMT	High Electron Mobility Transistor
AlGaN	Aluminium Gallium Nitride	HF	Hydrogen Fluoride
AlN	Aluminium Nitride	HIR	Heterogeneous Integration Roadmap
Au	Gold	HMDS	Hexamethyldisilazane
BOE	Buffered Oxide Etch	ICP	Inductively Coupled Plasma
CCD	Charge Coupled Device	IEEE EPS	Institute of Electrical and Electronics Engineers Electronics Packaging Society
CHF₃	Fluoroform	InGaN	Indium Gallium Nitride
CVC	Cascade Vacuum Consulting	IPA	Isopropyl Alcohol
DBR	Distributed Bragg Reflector	IRDS	International Roadmap for Devices and Systems
DI	Deionised Water	ITRS	International Technology Roadmap for Semiconductors
DWL66	Direct Write Laser 66	IV	Current Voltage
EPSRC	Engineering and Physical Sciences Research Council		
FDTD	Finite Difference Time Domain		
GaAs	Gallium Arsenide		

KOH	Potassium Hydroxide	RIE	Reactive Ion Etching
LASER	Light Amplification by Spontaneous Emission of Radiation	RMS	Root Mean Square
LED	Light Emitting Diode	ROC	Radius of Curvature
LiFi	Light Fidelity	RPM	Rotations Per Minute
MQW	Multiple Quantum Wells	RTA	Rapid Thermal Annealing
NH₃	Ammonia	sccm	Standard Cubic Centimetre per Minute
N₂O	Nitrous Oxide	SEM	Scanning Electron Microscope
Pd	Palladium	Si	Silicon
PDMS	Polydimethylsiloxane	SiH₄	Silane
PECVD	Plasma Enhanced Chemical Vapour Deposition	SiN_x	Silicon Nitride
PGMEA	Propylene Glycol Methyl Ether Acetate	SiO₂	Silicon Dioxide
PIC	Photonic Integrated Circuit	TEM	Transmission Electron Microscope
POF	Plastic Optical Fibre	TiO₂	Titanium Dioxide
PR	Photoresist	TP	Transfer Printing
PTFE	Polytetrafluoroethylene	UV	Ultraviolet
RCLED	Resonant Cavity Light Emitting Diode	VCSEL	Vertical Cavity Surface Emitting Laser
RF	Radio Frequency	VLC	Visible Light Communication
		VSI	Vertical Scanning Interferometry

Chapter 1

Introduction

The content of this thesis focusses on the optimisation of microfabrication techniques used to create devices suitable for a method known as transfer printing (TP) [2], a technique which allows for one to pick up and place flat objects on the micron to sub-micron scale. These devices could potentially become part of photonic applications such as photonic integrated circuits (PICs) [3], visible light communications (VLC) with high data rates, or displays that push the fidelity of digital screens to new heights [4]. The goal of this work was to advance closer to these applications through an iterative process of design, microfabrication, and using the transfer printing technique. The assembly of devices in the vertical axis is the main focus of this study and so creating flat, stackable devices was a major objective to facilitate the assembly. For this work the target device was a resonant cavity light emitting diode (RCLED) consisting of an optical cavity created by sandwiching an LED between two distributed Bragg reflectors (DBRs) [5], and with the novelty of being based on the direct-bandgap material gallium nitride (GaN). By releasing individual devices from their growth substrate and transferring them to a new hybrid configurations, transfer printing is able to take advantage of properties such as better reflectivities in the case of DBRs or heat dissipation on diamond.

In 2015, the IEEE Electronics Packaging Society outlined the Heterogeneous Integration Roadmap (HIR) [6] to guide research towards creating devices using

combinations of semiconductor material to improve on the capabilities of the current state of the art. This is a subset of the overarching International Roadmap for Devices and Systems (IRDS) [7] which took over from the International Technology Roadmap for Semiconductors (ITRS) which is more general in its goals to advance device technology. Workshops and conferences were arranged to aid discussion of new heterogeneous integration technologies and innovations, which allowed members to review the direction of upcoming technology in the next 15 years. The HIR creates clear objectives for research such as that included in the thesis and details the logical routes to achieve them. This work is part funded through the EPSRC ‘Hetero-Print’ programme grant [8, 9]. This grant involved multiple institutions focussing on different aspects of the hybrid integration of photonic devices such as the the chemistry of the adhesive stamps, a switchable adhesion for these stamps, large scale parallel printing of devices, and device material development. The most important Hetero-Print partner for the work covered in this thesis was the University of Cambridge. Said work pertains to the development of the transfer printing method, the fabrication of printable devices, and the materials involved in the device printing.

1.1 Motivation

The reasoning for using transfer printing instead of the current standard of in situ growth is that it allows for new combinations of materials to be used as some are limited by the substrate on which they are grown. A limitation of material growth is that the crystallographic lattice constants of the materials in epitaxial growth need to be the same or very close for bonds to form between the existing crystal and a new epitaxial layer on top—in other words, for pseudomorphic growth. The main material used in this project was gallium nitride (GaN) which is grown on substrates of silicon carbide, sapphire (0001) and silicon (111) which have respective lattice mismatches of: 3.5%, 16% and 17% [10–12]. The ideal substrate would be bulk GaN but the cost of these remains prohibitive. The mismatch is managed in practice by using intermediary layers of other materials such as aluminium nitride (AlN) and aluminium gallium nitride (AlGaN) as buffer layers which gradually transition from one lattice

constant to the next. AlGaAs based RCLEDs which are an established technology use AlAs/AlGaAs DBRs which require 20 to 30 repeated quarter wave pairs to have satisfactory reflectivity to create the optical cavity [5]. For a GaN RCLED targeting the 450 nm wavelength it is difficult to use epitaxially grown DBRs because of lattice mismatch and low refractive index contrast issues. Transfer printing solves this problem by allowing one to transfer separately produced DBR materials on to GaN LEDs to combine the optimal performances of both materials.

There are many requirements which need addressing to succeed with transfer printing materials. With the intent to vertically stack thin film devices to create a hybrid optoelectronic device the layers must all lay flat to provide good adhesion and optical functionality. The cumulative mismatch between the epilayer structures causes growth defects called dislocations and internal stresses which can affect the band gap of the material itself. In the growth of the device wafers, the substrate and subsequent layers will have a variance in thermal expansion coefficients. As the growth temperature can exceed 1000 °C, once the wafer is cooled the layers contract by varying amounts to form a bowed deformation of the wafer. This deformation is present in the individual devices once under-etched as the strain is released from the Si substrate of the GaN epilayer which will cause the stacking to fail.

1.1.1 Gallium Nitride

Silicon based electronics have been the industry standard for most semiconductor devices like transistors due to the evolution of the technology past the vacuum tube era, and the relative low cost and abundance of the source material. The development of the silicon industry massively revolutionised the technology and computing power that we have available, and created a drive to discover other semiconductor materials. One such promising material is gallium nitride (GaN) which belongs to the III-V semiconductor category, and is the primary focus of this work.

The material itself has some intrinsic qualities which give it a performance advantage over other semiconductors for applications such as energy efficient lighting and high

voltage and high-frequency electronics. The high electron mobility and saturation velocity allows for high switching speeds. In the context of the light emitting diodes in this work this relates to wavelength coverage and to the speed at which they can be turned on and off to send data signals (modulation).

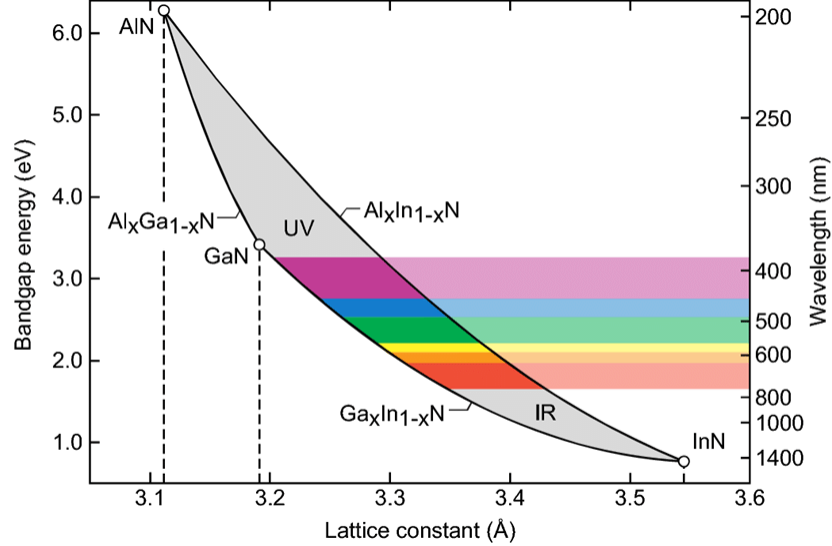


Figure 1.1: Band gap energy as a function of lattice constant for III-nitrides at room temperature. Taken from [13].

In an LED structure, the active region commonly consists of a set of layers called quantum wells. A narrower bandgap (the well) is sandwiched between layers of wider bandgap material to confine the charge carriers [5]. The well's thickness is on the order of the wavelength of light and can be tuned to target specific wavelengths for the LED to output. The quantum wells also determine the wavelength of light by the material's band gap energy. In the $\text{Al}_x\text{In}_y\text{Ga}_{1-x-y}\text{N}$ regime, the composition of the various nitrides alters the band gap and the lattice constant of the material as shown in Figure 1.1. In the epitaxial growth, one can effectively target desired wavelengths for LED devices for varied applications from the ultraviolet to infrared range making this material platform flexible.

The GaN material that comprises the multiple device wafers in this thesis are all grown on the silicon substrate platform as this is what the transfer print method in practice was developed for with it being the lower cost material. The lower cost of the substrate

is factored in by the abundance of the Si wafers from the vast Si industry previously mentioned as well as the relatively low cost of fabrication into suspended coupons for transfer. A drawback of using Si is that the lattice constant differs significantly from GaN meaning that multiple layers of other nitride materials need to be stacked before the GaN to gradually change the lattice constant and minimised the formation of dislocations—discontinuities in the crystal lattice which may affect the optoelectronic performance of devices.

1.1.2 Light Emitting Diode Devices and Their Alternatives for Visible Light Communication

Light emitting diodes (LEDs) are found everywhere in everyday life from the screens in our phones, to the lights illuminating the rooms we live in, to transmitting data through data communications, see Figure 1.2. This broad applicability is reflected in the value of the industry—the global LED lighting market being valued at USD 81.48 billion in 2023 alone [14]. Hence there is great economic incentive to innovate this technology to create better performing and cost effective products.

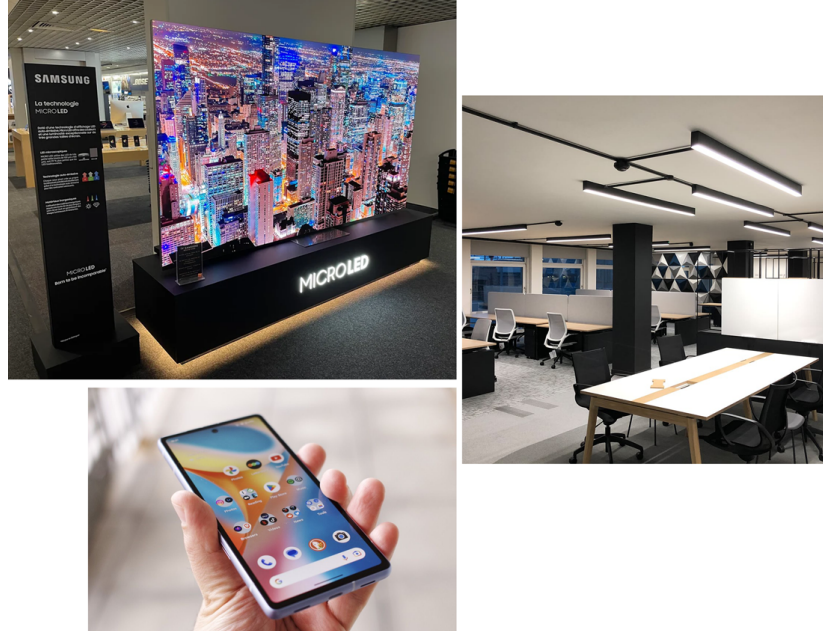


Figure 1.2: Images of the various uses of LEDs in modern technology including a Samsung micro-LED screen, a smartphone, and office lighting.

The LED device utilises what is referred to as a p-n junction to generate light of a certain wavelength. The spectrum of light produced generally follows a Gaussian distribution where the maximum is the central wavelength. The p-type semiconductor material has elements with fewer electrons (the dopant) substituted into the crystal structure (the act of doping) to create areas relatively lacking in negative charge called “holes” which carry the charge through the material. The n-type semiconductor material has elements with more electrons substituted in to the crystal structure to create areas with relatively high negative charge. These extra electrons are the “charge carriers”. When these two materials are placed together, as illustrated in the figure 1.3, and a voltage is applied across them then the charge carriers migrate to the interface and recombine to generate energy in the form of a photon which is then released from the material as light [5].

The devices to be worked on in this thesis are related to visible light communication (VLC), in which data is transmitted using light in the visible spectrum with wavelengths 400 nm to 700 nm. In this communication system a light source is modulated to transmit data through a particular medium. A current standard is data communications using plastic optical fibres (POF) which have a low attenuation coefficient in the visible spectrum, thus high data rates with minimal loss can be achieved [15, 16]. Suitable light sources for VLC include LEDs, laser diodes, or other visible light emitters. These can be modulated by either sending pulses of light, altering the frequency or amplitude. Another form of VLC is free-space optical communications such as “LiFi” in which data is transferred through free space without a waveguide [17]. A beam of light sent through a channel from a transmitter and received by a detector, this may be directional such as with a laser or even integrated into the lighting of a room. An industrial leader in the LiFi market is PureLiFi which already produce products for portable LiFi capability [18].

Vertical cavity surface emitting lasers (VCSELs) are a particular variant of laser diode which achieve high data rates and have more concentrated optical power compared to standard LEDs [19]. In these devices light is emitted perpendicular to the plane of

the epitaxial structure through sandwiching a short ($\sim \mu\text{m}$) cavity active gain region between two highly reflecting mirrors (usually in the form of DBRs). LEDs provided the original 10 Mbit/s to 100 Mbit/s broadband capability in the early 2000s but were surpassed by a cheap form of VCSEL that could exceed the ~ 622 Mbit/s limit of the LEDs at that time [20].

An intermediary technology between LEDs and VCSELs is the resonant cavity light emitting diode (RCLED) which is VCSEL-like and fundamentally consists of an LED between two reflectors, one fully reflective and the other partially reflective [5]. The advantages of an RCLED over an ordinary LED is that they achieve a higher efficiency through the Purcell cavity enhancement [5] in which the spontaneous emission is enhanced by a factor of 2 to 10 for the same input electrical power thus increasing the internal quantum efficiency. These can also generally produce a narrower linewidth output at a much greater power in this central wavelength, improving the modulation capabilities. RCLEDs are already well integrated into industry with use in optical links that control trains, wind turbines, solar farms, and power distribution to our cities [21]. A single RCLED has been shown to produce up to 500 Mbit s^{-1} [22]. It should be noted in passing that conventional LED structures, when shrunk to the $1 \mu\text{m}$ to $100 \mu\text{m}$ diameter microscale, are also useful communication components. Such devices have reduced capacitance and high current density, which, via reduced RC time constants and carrier lifetimes, enables high modulation bandwidth. Individual micro-LEDs can reach data rates of $>800 \text{ Mbit s}^{-1}$ [22, 23] and even tens of Gbit s^{-1} when advanced data encoding techniques are applied. Arrays of micro-LEDs can be used to send patterns of light in which more data can be encoded. Including these technological advancements into the with the RCLED could achieve even greater data rates.

The majority of RCLEDs in current use are $\sim 650 \text{ nm}$ wavelength and are fabricated in a monolithic fashion with AlGaInP/AlGaAs material multiple quantum wells (MQW) and AlAs/AlGaAs DBR layers which are sufficiently lattice matched to be viable with the GaAs substrates. The structure of such a device is shown in Figure 1.3 and illustrates the functional layers of an RCLED. This is challenging for GaN as there

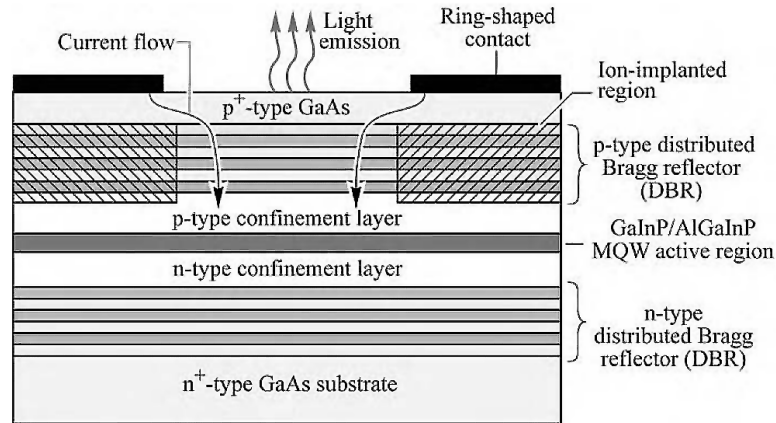


Figure 1.3: Structure of a GaInP/AlGaInP/GaAs MQW RCLED emitting at 650 nm used for plastic optical fibre applications. This structure illustrates the functional layers of an RCLED. Taken from [5].

are no high refractive index contrast materials that could be grown to form the DBRs. Transfer printing, which is introduced below, enables the construction of these GaN resonant cavity devices where the growth substrate is independent of the final device construction.

When characterising the electrical performance of LED devices, a probe station is used to supply a voltage with the current draw being measured (described later in Section 2.15.7). The diode exhibits a nonlinear relationship between the current as a function of voltage referred to as the IV characteristics. As the supply voltage increases the relationship will begin to tend to a linear relationship when the LED begins to emit light. The gradient of the linear region is known as the differential resistance and is the series resistance of the LED device. The turn-on voltage is the potential at which the LED emits light and is found by extrapolating the linear region to intercept the voltage axis. A high resistance would generate more heat and reduce efficiency so ideally a lower turn-on voltage is preferred.

1.2 Transfer Printing Technology

Transfer printing conceptually involves mechanically picking up an object, referred to as a “coupon”, from its native substrate and transferring it to a new one [2, 24]. The method by which this is done varies depending on what is being transferred. The transfer printing used in this thesis involves the use of an elastomeric stamp made of polydimethylsiloxane (PDMS) which is cast from a mould and attached to a translational platform with a microscope for alignment [25–30]. This method was adapted from the work of John Rogers’ group [2, 31] and utilises GaN grown on a Si (111) substrate to allow for anisotropic under-etching to release the upper layers as well as the Rogers PDMS stamp approach. The epistructure is then processed using the microfabrication techniques described in Chapter 2 to create arrays of individual devices with their own metallised electrical contacts (if they are required). Channels are etched around each individual device down to the substrate such that a potassium hydroxide (KOH) wet etch can remove the Si material underneath. The etch only proceeds along the [110] direction of the Si crystal due to the large disparity in etch rates of the crystal planes. Small tabs or “tethers” are purposefully left in the devices’ design to allow the devices to be suspended once under-etched. An elastomeric stamp is then used to make contact with the top surface of the device and pick it up with a quick motion. This method of transfer printing relies on the speed of pick up to determine the contact force between the stamp and device. These devices can then be slowly lowered onto a non-native substrate. Details of this technique are given in later chapters.

Other groups opt for other material platforms such as using patterned photoresist to create the tether structures instead of relying on the device material itself [24]. Yet others opt for encapsulating the devices prior to printing to improve the transfer success by eliminating surface roughness and improving adhesiveness [32].

This technology has predominantly been used to date in academic institutes to create proof of concept devices; however it has started to become commercialised with the company X-Celeprint, for example, creating custom transfer printing tools and services

[33]. Even before the beginning of this project in 2018 more companies have started to offer equipment to facilitate micro transfer printing [34, 35]. This thesis predominantly focusses on the fabrication processes to facilitate the transfer printing with GaN devices instead of the development of the technology itself; considerations are made for the inevitable development of the current standard process implemented.

An ideal technology would permit a reversible adhesion stamp in which the forces between stamp and device coupon could be selectively switched on or off. Work has been done by other members of the Hetero-Print programme grant involving a light-activated coating for the PDMS but has yet to be successfully implemented into transfer printing technology. This reversible adhesion would greatly increase the yield of the transfer printing technology presented in this thesis.

1.3 Our Approach to Nitride RCLEDs

In this thesis the foundation work is undertaken to produce suitable coupons (i.e. suspended membrane devices ready for transfer printing) to construct a GaN RCLED. The challenge of bowed wafers and suspended membranes is addressed by multiple systematic material studies in which several series of device wafers are fabricated into suspended devices and compared to assess the growth parameters of each. With this information the optimal buffer structure for the GaN-on-Si platform can be realised and implemented in the growth of future structures. Using this buffer structure as a foundation, the optimal LED structure is simulated to find the layer thicknesses which produce a suitable overlap between the electric field maxima and the quantum wells to enhance the cavity effect once the printed device is sandwiched between mirrors.

The fabrication techniques for suspended device coupons are developed for the thicker buffer structures to accommodate the elastomeric transfer printing to facilitate ease of release using the conventional pick up method. These techniques are further refined to work with a novel porous GaN material (developed at the University of Cambridge) to create suspended DBR coupons. These GaN DBRs are comprised of alternating layers of bulk GaN and porosified GaN achieved through electrolysis [36]. These offer a

higher refractive index contrast and lower internal strain compared to epitaxially grown GaN/AlGaN DBRs deposited directly to GaN LED wafers. This novel porous GaN material offers an interesting alternative to be explored in the integration via transfer printing.

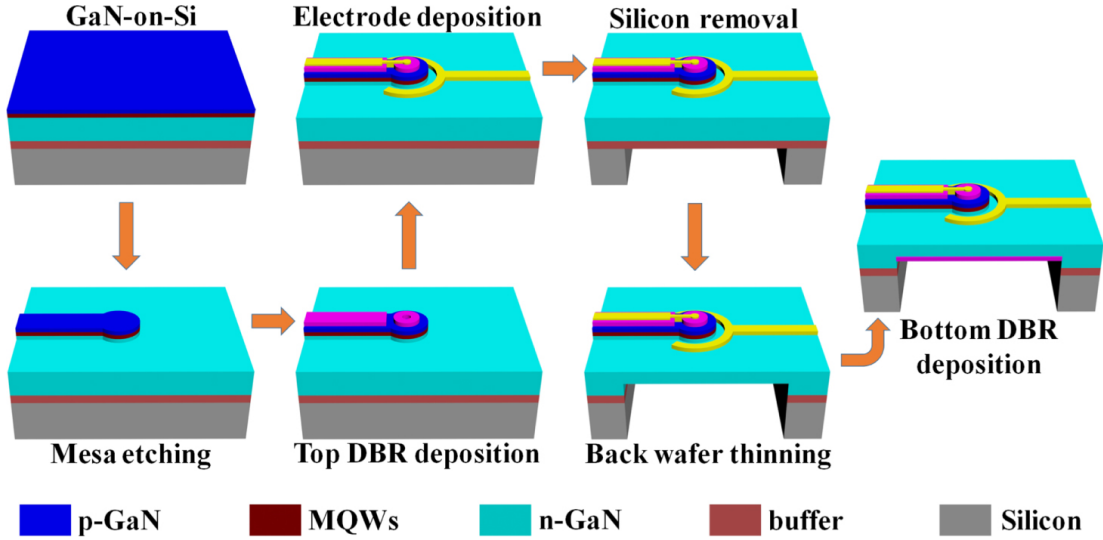


Figure 1.4: Alternative RCLED fabrication process flow using backside thinning and E-beam deposition of dielectric DBRs. Taken from [37].

An alternative route to achieve a hybrid RCLED could include attempting to deposit dielectric type mirrors on a polished device surface using epitaxial lateral overgrowth, but previous attempts have had difficulty controlling the cavity length such a device [38]. In this case an extremely complex growth process is required to be able to supply the device with power through the channel electrodes and encapsulating the n-side DBR. Another method includes the deposition of $\text{TiO}_2/\text{SiO}_2$ DBRs using electron beam evaporation and lift off techniques. Once again this method would require extensive complex patterning to achieve the back-side thinning to access the device region of the epistructures as shown in Figure 1.4 [37]. Each step of this complex fabrication process would add to eventual costs if it were to be commercialised, especially when scaled up to a large industrial batch production. The transfer printing method requires fewer processes with potentially limitless combinations with the pick-and-place of specifically tailored functional coupons such as DBRs, LEDs, lasers, resonators and waveguides.

1.4 Thesis Outline

Chapter 2 outlines the core processes and equipment used in the microfabrication of the particular devices mentioned. The majority of these processes are performed inside a cleanroom facility. Having an understanding of how the equipment functions on a basic level allows one to better understand the reasoning behind each step of processing; often a lot of the work is figuring out order of operations to make sure that material is manipulated in the intended way with no wastage.

Chapter 3 details a materials study in which the flatness of GaN-on-Si wafers was affected by the amount of exposure to ammonia during the growth process. A novel buffer structure was tailored to minimise this bowing. A systematic fabrication process was applied to a series of wafers to create basic suspended square membranes. These were measured to verify the flattest ones by using optical profilometry such that the best sample from the series could have its growth parameters used as a foundation for future growths. In the second half of this chapter two more wafers were assessed by the same method to verify the efficiency of the buffer structure to control this device-level flatness, this time with the inclusion of an extra dislocation blocking layer in one of the samples. When compared to a commercial wafer sample fabricated in parallel, the custom GaN-on-Si structures produced much flatter devices.

Chapter 4 addresses an emergent issue from Chapter 3, namely that the produced devices are too difficult to release using transfer printing due to the increased thickness of the buffer structures. The bespoke GaN-on-Si material was used to create a series of identical suspended membranes with varied tether designs to find the best design. Twenty printing attempts were done for each tether design. Using the optimum parameters a custom tether design method which also included a bow tie shape fracture point which could be used in future devices.

Chapter 5 details the fabrication of custom GaN DBR wafer into transfer printable coupons for use in hybrid photonic devices. Issues arise due to the material being created from porosified GaN which would deteriorate in the etching processes. The

buffer structure of this material also prevents the transfer printing of completed coupons due to its thickness, requiring a two stage selective thinning process to reduce the tether regions. This chapter solves many of the issues that were revealed from using this porous material as well as theorising improved iterations on the process for future device fabrication. A few DBR coupons were transfer printed with limited success proving that further research into the fabrication process needs to be done.

Chapter 6 brings together all aspects of the previous work in the design of the final hybrid device, a GaN resonant cavity LED. Using the LED and DBR structures worked with previously, a time dependent simulation was created using the LumericalTM finite difference time-domain (FDTD) software to model the electric field inside a cavity created by the LED sandwiched between two DBRs. The layers of the structure were adjusted to create an optimal overlap between the standing wave antinode and the quantum well region of the LED to maximise the efficiency of the device (Purcell cavity effect [5]). This design was modified in collaboration with growth experts to realise a series of LED wafers which could be fabricated into coupons to use in a hybrid device.

Chapter 2

Cleanroom Microfabrication Processes

2.1 Overview

The majority of the experimental work described in this thesis took place in a cleanroom facility as the fabrication of optical microstructures demands an extremely low particle count in the atmosphere to produce quality devices. The facility used is classed as an ISO 2 class cleanroom, which is an international standard defined as the ability to reduce the count of $0.5\ \mu\text{m}$ or larger sized airborne particles to under four per cubic metre with none larger than $1\ \mu\text{m}$ [39]. This is achieved through: an interlock system for each room in the laboratory which prevents external detritus entering, an air filtration system which removes any particles present, cleanroom suits to be worn by each user to prevent natural shedding of dust and dirt reaching the atmosphere and other procedures [39].

Within the cleanroom facility the majority of the work consists of microfabrication and metrology. In the following sections, each process and tool will be described to help the reader understand the work later in this thesis. The main focus will be on functions relevant to this work, not the complete functionality available. More in depth information can be found in the literature and related documentation, see [39–41]. As

the nature of this study was largely empirical, optimisation of processes was driven by the performance metrics detailed in the following chapters. This chapter only introduces the equipment and the processes used; the modified settings and parameters will be found in the sections corresponding to each line of study.

There will be reference to a “recipe” which is a term referring to the parameters of a process such as temperature, duration and specific tool settings. A full fabrication protocol will consist of multiple recipes which need constant amendments to accommodate the changing nature of the different materials used. The most common device fabricated is what is called a “suspended membrane” which can be seen as the most basic of all the suspended devices considered here and a foundation for all others. An example of the protocol followed to create such a device is outlined in Figure 2.1. Individual process steps are more or less standard for most devices with extra steps introduced for more complicated ones. The relevant steps are described in detail in sections that follow.

2.2 Solvent Cleaning

Cleanrooms involve a lot of cleaning to ensure that foreign matter does not interfere with the preparation or function of the devices. The material for fabricating the devices comes in the format of a wafer, with a typical diameter of 150 mm. These are then cleaved using a scoring method similar to cutting glass or diced with a dicing saw [42] into many “samples” of appropriate size for the photolithography mask used later, typically of the order 15 mm × 19 mm.

The wafers occasionally arrive with a thin layer of photoresist coating the device surface for protection. This is removed along with any other unwanted dirt by submerging each sample in an acetone filled beaker and agitating in an ultrasonic cleaner for a minimum of 3 min, which is shown in Figure 2.2. The beaker is then removed and methanol is flowed in slowly to rinse away the acetone into the solvent waste drain of the fume cupboard. This is done to prevent drying residue from the acetone. Once the beaker has been rinsed three times and the sample is covered with methanol, the beaker is

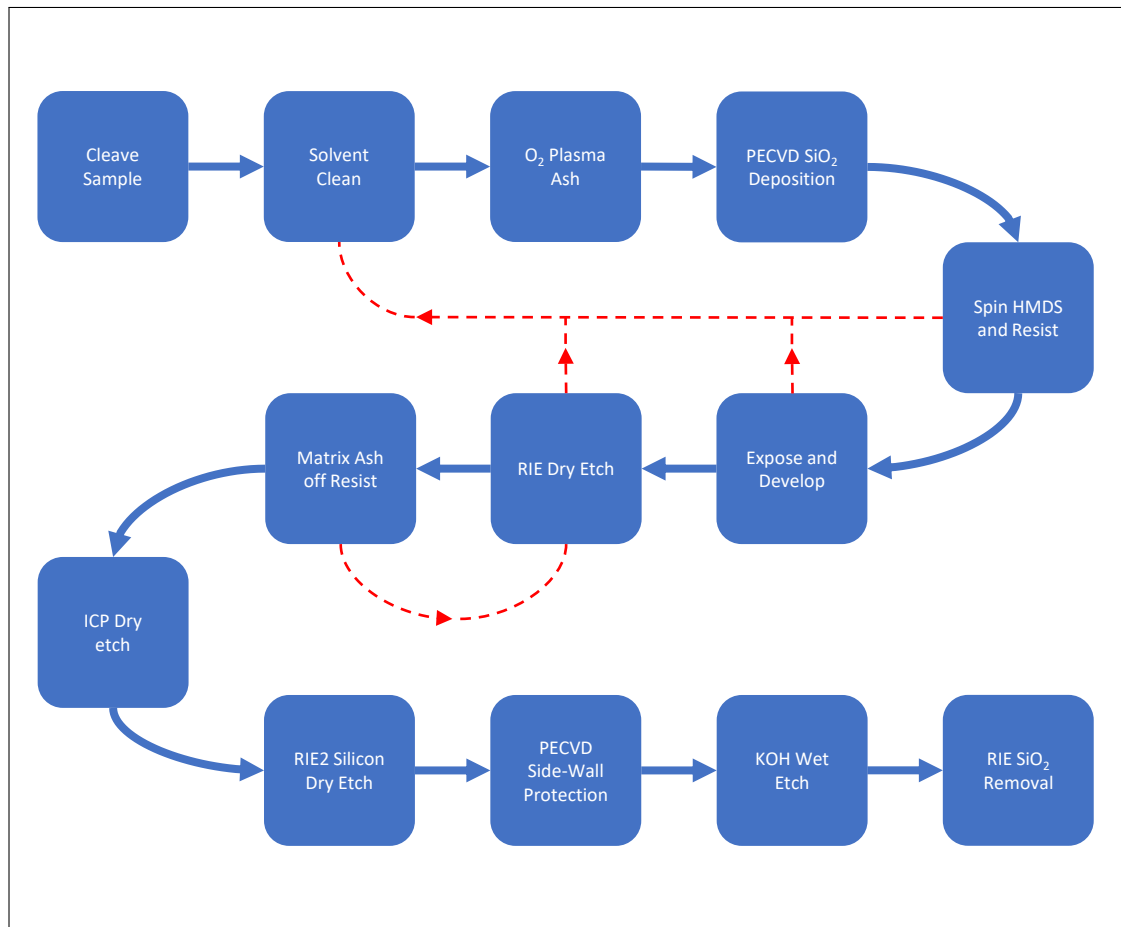


Figure 2.1: Process flow for membrane fabrication. The blue arrows represent the forward progression through each step and the red dashed arrows represent the route one must take if the previous operation was not satisfactory. After some steps the opportunity to redo processing is lost due to permanent alteration to the device material.

returned to the ultrasonic cleaner for a further 3 min. This is once again repeated with isopropanol (IPA). The samples are then rinsed using de-ionised water (DI) by filling the beaker and emptying at least three times. The samples are then laid out on a polycellulose cleanroom wipe and dried using compressed nitrogen.

This method is used between fabrication steps to remove photoresists and general contaminants should the sample be left for some time or made dirty. The methanol step may be skipped as the difference in cleaning is marginal with or without it and because it is considered the most harmful of the three solvents used.



Figure 2.2: The ultrasonic cleaner and solvent bench.

2.3 Oxygen Plasma Ashing



Figure 2.3: The Matrix plasma asher.

Often paired with a solvent clean is a oxygen plasma ashing Figure 2.3. The tool used is the Matrix plasma asher which creates a free radical ion discharge oxygen plasma

2. Cleanroom Microfabrication Processes

at a high RF (radio frequency) power and temperature [43]. This process can remove more stubborn organic compounds such as burnt-on photoresist while having minimal surface damage to the sample.

As the tool in our cleanroom is fairly dated, the recipes are stored on a magnetic strip card which limits the complexity of the process. These recipes are generally set to change the temperature of the chuck in which the samples are placed and the duration of the plasma. For a photoresist strip the 250 °C, a 10 minute recipe is used after a solvent clean. For the dehydration of sample surfaces, 150 °C for 5 minutes suffices.

2.4 PECVD - SiO₂ Deposition



Figure 2.4: The PECVD tool.

Plasma enhanced chemical vapour deposition (PECVD) shown in Figure 2.4 is primarily used for the deposition of silicon dioxide, often referred to as silica, fused quartz or chemically: SiO₂. For most cases, the SiO₂ is the primary material used for insulating layers and masking of photonic device fabrication. The etch chemistry of the material makes it ideal for use in both dry and wet etching with many commonly used semiconductor materials. The two main processes used in the work of this thesis

which require SiO_2 are the masking for the inductively coupled plasma (ICP) dry etch where the selectivity of the etch is approximately 10 to 1 for GaN to SiO_2 , and for creating a side-wall protection layer prior to a KOH wet etch. The selectivity means that for every 1 nm of SiO_2 etched down, 10 nm of GaN material is removed. This selectivity is what determines the minimum layer thickness of SiO_2 to be deposited such that the mask it forms does not fully deteriorate before transferring the desired pattern to the epilayer stack below it.

2.4.1 Function of the PECVD Tool

The tool consists of a heated chamber in which samples are placed and then sealed off from the atmosphere. With the chamber purged and pressure lowered, a flow of gases are introduced through a feature known as the “shower-head”, a nozzle consisting of evenly distributed holes to create an even flow. For the creation of SiO_2 films, silane (SiH_4) and nitrous oxide (N_2O) are used [40]. The gas flow rates to most cleanroom tools are measured in sccm (standard cubic centimetres per minute).

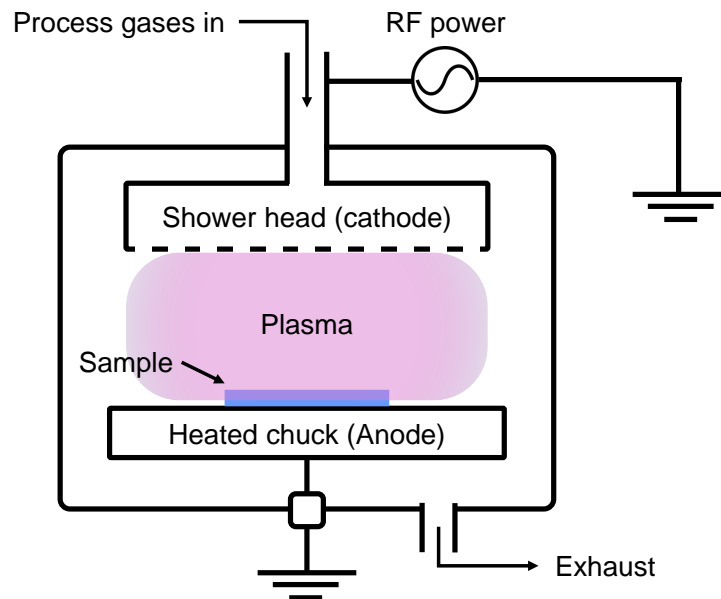
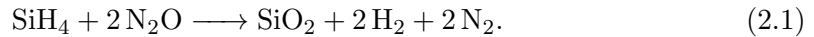


Figure 2.5: Simplified systematic diagram of PECVD chamber.

In the chamber, two electrodes ionise the gases with an RF power of 30 W with chamber

temperature of 300 °C to form the reactive plasma [40]. The source gases then diffuse down onto the receiving surface to form a thin film of SiO₂ following the reaction:



The standard recipe file stores the parameters required to complete this process automatically and was used unaltered throughout the various device fabrication runs. The gas flow rates were 170 sccm for the silane and 710 sccm for the nitrous oxide to result in a deposition rate of ~40 nm/min. The rate would change dependent on the state of the chamber and the usage since the last chamber clean.

2.4.2 Operation of the PECVD Tool

Before PECVD, the sample should be clean and free of debris, ideally by using a Matrix ash process. This ensures good film adhesion as well as avoiding any micro-masking transferring to the material below in the photolithography process. Using the control computer interface the standby process is stopped and the venting process is started and this brings the chamber to atmospheric pressure and allows the lid interlock to open. Once vented, the chamber is opened using the manual controls. Using heat-resistant tweezers, the samples are arranged on the chuck to optimize uniformity. With one sample, it is placed in the centre of the round heated chuck such that the shower head flows uniformly as shown in Figure 2.5. Multiple samples are arranged with radial symmetry in a ring shape such that the flow is the same for each.

The white light reflectometry test for deposition described later in Section 2.15.2 has a discrepancy of roughly ±15 nm, so the samples rarely show the sample value for deposition—at best we can estimate the thickness from the last recorded deposition rate. The chamber is then closed ensuring that the lid fully seats otherwise the process would fail. The time for the process is then set dependent on the deposition rate last logged and the process is started. The samples are retrieved and the chamber put into standby under vacuum once complete. An example of the finished process is shown in Figure 2.6.

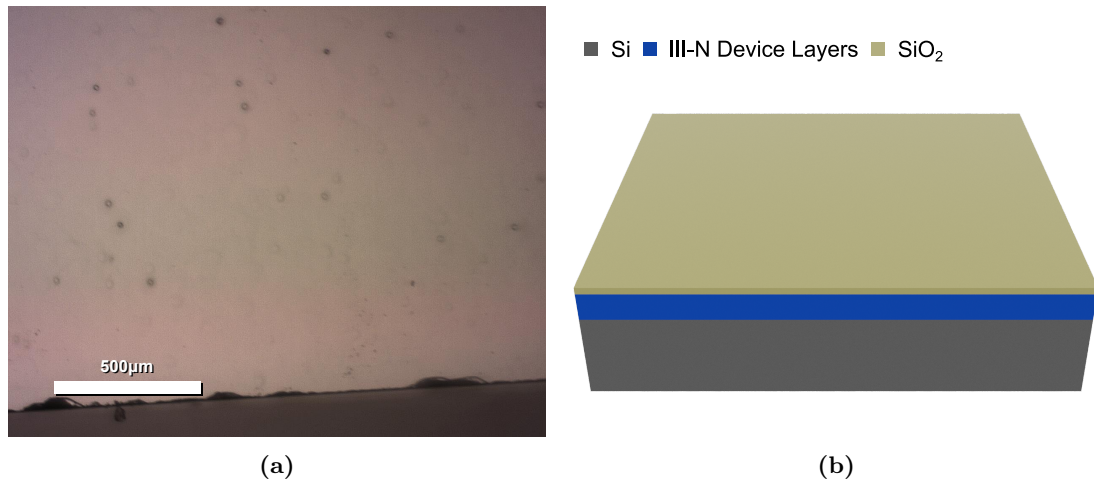


Figure 2.6: (a) Microscope image of part of a GaN LED sample after depositing a layer of SiO₂. (b) A computer generated 3D view of the material at this stage, later figures will develop from this. The dark grey represents the Si substrate, the blue the epistructure device layers, and the beige the SiO₂.

2.5 Photolithography

Photolithography is a technique used to transfer a pattern onto a surface by the use of light reactive reagents called photoresists. A photolithography mask is an object which has opaque regions to block the light in certain areas to form the desired pattern. Generally these are made of glass with a chrome coating to block ultraviolet (UV) light. Resists can be categorised into two types: positive and negative [44]. Positive photoresists become soluble to photoresist developer solvent when exposed to UV light, so when designing a mask the areas that one wishes to be etched must allow the light to pass through. This creates a positive one-to-one mask of photoresist on the surface of the material once developed. Negative photoresists are the opposite: when exposed to UV light the chemical structure cross-links forming a developer-resistant coating and so would produce a negative of any mask used with this resist. This is illustrated in Figure 2.7. Each type of resist has its benefits but usually the type chosen is dependent on process flow and device pattern dimensions.

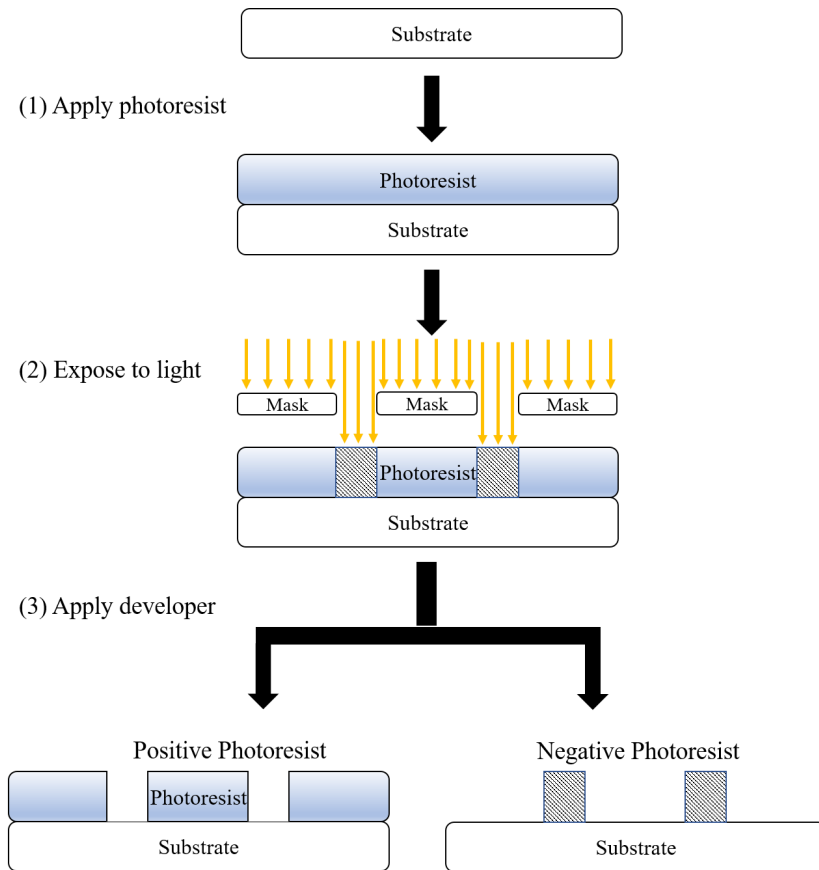


Figure 2.7: Schematic diagram showing the difference between positive and negative photoresists. Taken from [45].

2.5.1 Photoresist Spinning

The method for applying photoresists in the microfabrication discussed here is depositing a small amount of photoresist centrally on a sample and then spinning on a bench spinner at speeds up to and around 4000 rotations per minute (rpm) to distribute it. Each photoresist is unique with spinning protocols that generally relate to the viscosity of the chemical. Full wafers are spray coated for larger scale operations but here sections of a 150 mm diameter wafer were spin coated. The advantage of using a full wafer is that the circular shape allows the resist to flow radially equally meaning that the uniformity is much better. The rectangular shape of the 15 mm by 19 mm samples used would cause photoresist to build up at the trailing corner of the long-edge when using more viscous resists as shown in Figure 2.8. The solution to this

was to make the intended design only cover the more uniform central region.

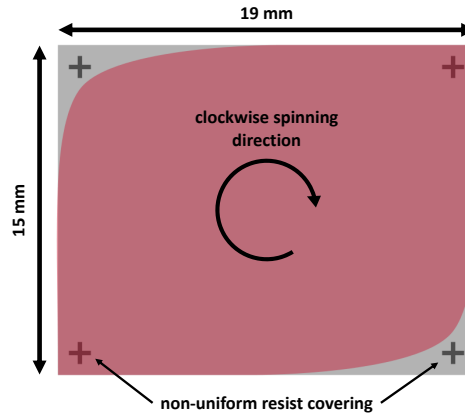


Figure 2.8: A schematic diagram of typical sample, of size used in this work covered in an asymmetrical coating of photoresist which often occurs with more viscous photoresists.

To begin, the samples were dehydrated if not fresh from the PECVD tool as the water vapour in the environment would have collected on the surface. This moisture can interfere with the photoresists and prevent them from adhering fully, resulting in the photoresist layers floating off in the development solution later on in the process. Moisture and oxides can be removed in the Matrix asher, but a hotplate can suffice but does not provide any cleaning. The photoresist spinner, shown in Figure 2.9, is cleaned if required, making sure the vacuum chuck is free of resist to allow the air to pass through freely. This tool works by pulling air through a central chuck which distributes the low pressure through channels in the mating top surface holding the sample in place. This chuck can then rotate and be driven by a speed controlled electric motor. This rotating assembly is surrounded by a splash guard and swing-top lid to catch any resist that would be flung outwards. With the sample in place on the chuck, the speed of rotation can be set using the user panel. Speeds calibrated for commonly used resists were saved for repeated use. The mass of the sample affects the speed of rotation, so it is good to check that the speed is set correctly by starting the spin dry. After cancelling the spin the speed is confirmed, a quick clean using the nitrogen gun is advised to ensure cleanliness.



Figure 2.9: The photoresist spinner lined with cleanroom wipes ready to spin a sample.

The primer hexamethyldisilazane (HMDS) is used for positive photoresists to help prepare the surface of the samples for better adherence of the photoresists. With exposure to the atmosphere including oxygen, many semiconductor wafers form an oxide layer which is hydrophilic and can prevent photoresist from properly coating the surface, similar to how oil may bead-up on a non-stick pan when cooking. The silicon atom in the primer chemically bonds to the oxygen in the oxide layer and releases ammonia molecules which leave methyl groups of the HMDS fragment, in turn making the surface hydrophobic and thus improving resist spreading and adhesion [46].

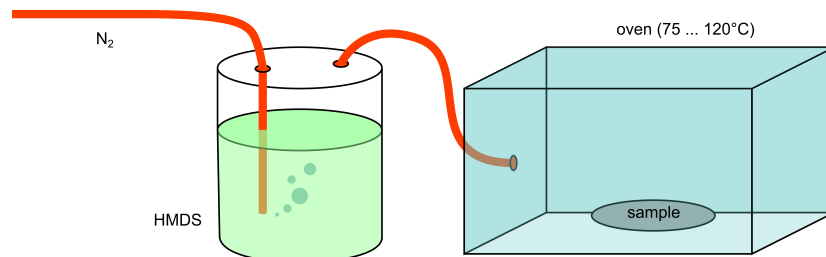


Figure 2.10: A schematic diagram for the correct method of ‘bubbling’ for the application of HMDS primer for photoresist spinning.

The preferred method for applying HMDS would be a bubbler system wherein nitrogen

gas is passed through the HMDS and into a heated oven (75 °C to 120 °C) containing the wafer, as shown in Figure 2.10. This produces an almost monomolecular layer of HMDS able to fully react with the oxide layer in a water-free environment. The compromise used in most of the fabrication in this thesis, is to apply the HMDS with the spinner and bake off the excess with a hotplate. This method was used due to the lack of bubbling apparatus available in the cleanroom.

The downside of spinning the HMDS is that the spin-coated layer is fairly thick, leaving excess HMDS on the surface after resist coating. This can release ammonia throughout the photolithography and diffuse into the photoresist causing unwanted cross-linking near the substrate [46]. This can have the effect of increasing development time, deteriorating the resist profile and lowering the resolution attainable. These effects were managed by slightly adjusting development times and carefully tuning the HMDS application. As previously mentioned, the substrates were thoroughly dehydrated prior to spinning to ensure proper resist wetting allowing the HMDS to chemically bond. The HMDS was spun at 4000 rpm for 60s which is at the upper end of the speed available from the spinners. This ensures the thinnest possible layer of HMDS on the substrate. The HMDS is then soft baked on a hotplate set at 115 °C to encourage the bonding and evaporate off excess ammonia.

Every photoresist will have a datasheet available which will include optimal application parameters to achieve the desired thickness of resist. Thinner layers of resist are generally achieved by less viscous resists at higher spin speeds. Thicker resists may also need a slow speed at the beginning to ensure adequate distribution across the sample before ramping up to full speed otherwise the blob of resist may simply be spun off the substrate. Thicker resists have the advantage of being able to last longer in dry etching processes but also come with a high risk of carbonisation and losing its shape under exposure to plasma from dry etch processes commonly referred to as “burning”. Burnt resist is chemically and mechanically resistant to standard removal methods which can ruin a fabrication run. Thinner resists can be used to create finer details and are less susceptible to burning. The resists commonly used in our cleanroom were

already characterised and only minor adjustments were needed to achieve the desired results. The positive photoresist MicropositTM S1805 [47] is the thinnest of the series and was commonly used for most devices. After the application of HMDS, a 0.05 mL drop of resist is placed in the centre of the sample using a syringe with a 0.2 μm filter attached. If the preparation was done correctly then the drop should immediately coat the entire sample forming a convex meniscus at the edges. The filter was used to remove any dried resist that may have found its way into the bottle during storage. The program is set for a 500 μm thick film of S1805 which is 3800 rpm for 60 s with a 100 rpm/s ramp up. After the spinning is complete, the sample is carefully removed with tweezers and the backside is wiped on an IPA wetted wipe to remove any resist. The sample is then placed on a hotplate at 115 $^{\circ}\text{C}$ for 60 s to soft bake. At this stage the resist is fairly stable and can be stored, however it is preferable to expose and develop the pattern immediately to avoid rehydration of the resist and debris landing on the surface over time.

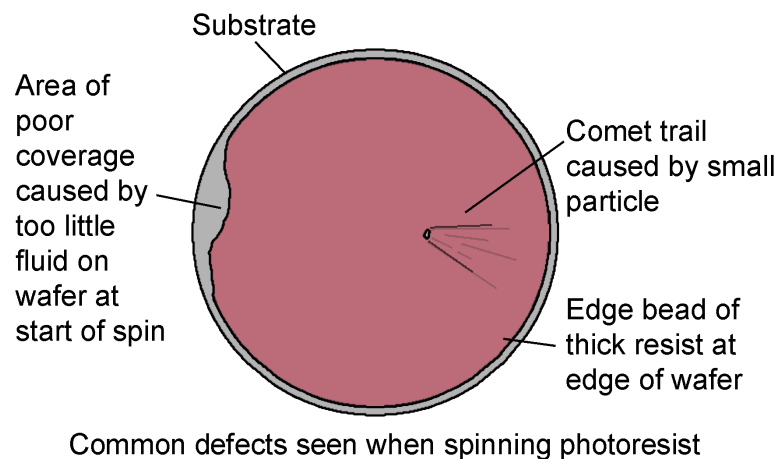


Figure 2.11: A Schematic diagram showing common issues when spinning photoresists. Adapted from [41].

Problems to identify before proceeding (Figure 2.11) are most likely due to inadequate preparation of the sample surface. The most common issue is if there was a speck of dirt on the surface before spinning which shows itself as a comet-like pattern on the surface where the resist has formed a wake behind the dirt when forced radially

outwards, as shown in Figure 2.11. This causes an issue because even if the dirt is small in relation to the pattern, the comet effect on the resist is much larger and affects the thickness uniformity which will later transfer into the material. Applying too little resist will cause the a non uniform spread of resist with areas of the sample missing coverage. When the resist is spun on it migrates to the edge of the sample because of the centrifugal forces acting on it. This will cause it to bead-up at the edges which can cause issues with exposure as the UV light dosage is calibrated for defined resist thicknesses. The solution for these problems is to clean off any traces of resist and dirt using the solvent clean in the ultrasonics and plasma ash once again. An alternative method for drying is to place the sample on a hotplate for 10 min above 100 °C after the solvent clean to drive off any water, but this does not provide any cleaning functionality.

2.5.2 Exposure Methods

The main method for exposing the samples in the cleanroom is to use the Karl SUSS MA-6 mask aligner shown in Figure 2.12 which takes samples on a vacuum chuck and exposes them to a dose of ultraviolet (UV) light through a mask held above the sample. The UV light is produced via a high-voltage high-pressure mercury xenon lamp. The lamp is ignited with a voltage of 30 kV and operates at 180 V, with currents of 5 A to 30 A.

The tool is set to the load position by default after switch on and after every exposure. The vacuum chuck for the mask is set upside-down on the left of the tool, ready to accept the mask. The masks used are glass with a chrome coating to define the pattern and this means that the exposed area is where there is no chrome. As described previously, one must know that when a positive photoresist is used, the area that is exposed to UV light will be removed with development. The opposite is the case for negative resists. The mask is placed in the vacuum chuck with the chrome side upwards so that it will be close to the sample when flipped into position. The vacuum is engaged and then the chuck is loaded into position and fastened with the thumb screws. The drawer below the mask holder slides out when pulled and contains a vacuum chuck to hold the sample in place. The samples are placed centrally, keeping in mind the orientation of the mask



Figure 2.12: The Karl SUSS mask aligner tool.

above so that the pattern is correct. This is very important for samples which involve an under-etch as they rely on the crystallographic plane directions to determine the direction of the anisotropic etch.

A recent addition to our cleanroom is the Heidelberg Direct Write Laser 66+ or DWL66 for short. This is a mask-less exposure system which uses a UV laser to write the desired pattern into the resist. The laser point is moved using fine adjustments of mirrors which can achieve highly precise features down to a size of roughly $0.3\ \mu\text{m}$.

The main advantage of this tool is the adaptability in design and function for prototyping fabrication processes. The lead time on designing and producing a physical glass mask for the mask aligner can be months, where as the DWL66 can have the new design input into the tool on the same day. The tool uses a GDSII file designed by the user in software such as LEdit or KLayout, or even from a Python script which will be described later in Chapter 4. The GDSII file is put into the connected computer and converted using the tool's software into a "job" file which is utilised in the main software controlling the tool. The full scope of the tool's functionality is beyond this thesis but the main benefit is that a small repeatable sample may be

exposed with varying parameters to empirically find the optimal settings. When using new materials with complex epilayer structures, the light from the laser will react very differently than what may be expected from a bulk medium. A key example of this to be discussed later will be the attempt at processing a mesoporous GaN distributed Bragg reflector (DBR) which required very different dosages to a standard GaN LED material.

2.5.3 Development

The development of the photoresist depends on which type of photoresist was used. The main photoresist series used was the positive MicropositTM S1800 which uses an aqueous alkaline solution called MicropositTM developer concentrate to develop. The concentrate is mixed in a 1:1 ratio with deionised (DI) water to achieve the correct concentration according to the data sheet [47]. The exposed samples were submerged for the appropriate time and then carefully removed from the mixture so as to not disturb the remaining resist. The samples were then immediately submerged into a beaker of pure DI water to rinse off any developer such that there is no over-development. A way to check the development of the sample is to look at it under a microscope and identify the features as shown in Figure 2.13. An underdeveloped sample will have the resist remaining where it is not wanted which can appear as a light pink haze. An overdeveloped sample may have broken pieces of photoresist floating where they should not be and straight features may become warped. The samples are then dried using a nitrogen gun and set back into protective cases.

2.6 RIE - Dry Etching Using the Soft-Mask

Different semiconductor materials require differing etching processes to effectively remove material. For structures primarily consisting of GaN and other group III-nitrides, reactive ions in a reactive ion etching (RIE) tool are used to both bombard and chemically react with atoms of the material being etched. The purpose of this step is to etch the mask pattern into the SiO₂ to form the layer into what

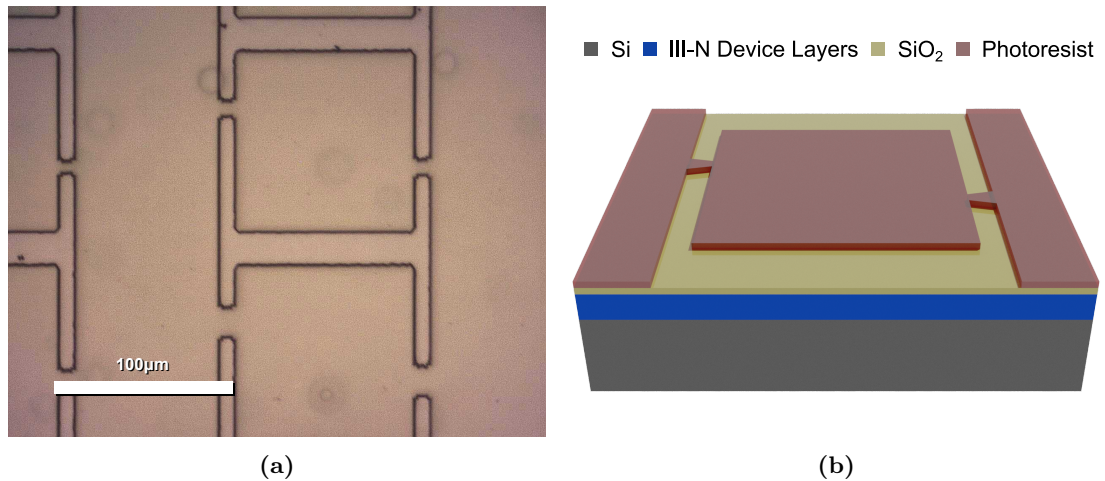


Figure 2.13: (a) Microscope image of a GaN LED sample after developing the resist mask. (b) A computer generated 3D view of an individual membrane at this stage, with the red section representing photoresist. Here the square elements represent the LED device and these each have two tethers for later suspension of the devices after under-etching.

is called a “hard mask”. The hard mask is necessary to resist the etching required to cut through the III-nitride materials that constitute the epilayer structures. The quality of the soft-mask transfers to the hard-mask with compounding errors so it is imperative to ensure that the photolithography steps are correct before any dry etching proceeds.

The same process would be used after the required processing steps are complete to remove any remaining silica, such as after the KOH wet etch. An alternate method for silica removal is to use a buffered hydrogen fluoride (HF) etch (also referred to as buffered oxide etch, BOE) [48]. This can be undesirable if one does not wish to wet the sample again or use an extremely dangerous substance.

2.6.1 Function of the RIE Tool

The particular etch used to cut through the silicon dioxide is an argon (Ar) and fluoroform (CHF₃) etch using an Oxford Plasmalab 80 Plus Reactive Ion Etcher (RIE) tool shown in Figure 2.14a. The flow rates of the fluoroform and argon gas are 5 sccm and 15 sccm respectively, with a platen power of 120 W and a pressure of 0.03 Torr [49]. In the chamber (see Figure 2.14b) the gases are excited at a low temperature and low

pressure using RF power (usually 13.56 MHz). The process gases gain kinetic energy from the RF field and collide with other molecules to form ions and free radicals. Both of these products etch the exposed sample surface: accelerated ions oblate the material, and free radicals react with the material to create volatile compounds [40].

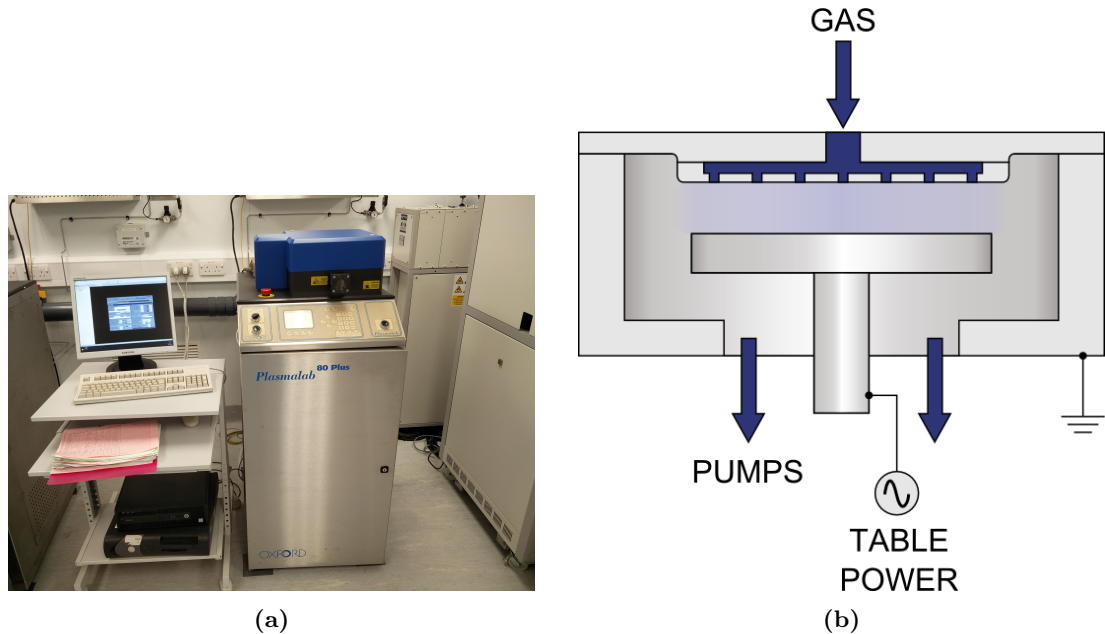


Figure 2.14: (a) Picture of the RIE tool and (b) a schematic diagram of its chamber. The latter taken from [50]. The blue arrows show the injection of the reactive ion gases at the top and the exhaust at the bottom.

2.6.2 Operation of the RIE Tool

Generally only the duration of the etch is altered to provide process conditions matching the thickness of the silicon dioxide on the sample. The recipes defined above have been created as standard calibrated mixes of gas ratios and platen power to give a known etch rate. The recipe used in this work etches silicon dioxide at 25 nm/min but will vary depending on how much has been cumulatively etched since the last chamber clean cycle. It is imperative to ensure that one does not exceed the recommended cumulative etch duration of the tool to ensure consistent results. The samples were placed evenly about the circular platen and the lid is closed. The recipe is selected through the computer interface and set to run which pressurises the chamber automatically when finished allowing one to open the tool to retrieve the samples. A microscope image of

an LED sample having just finished this process along with a 3D representation may be found in Figures 2.15a and 2.15b.

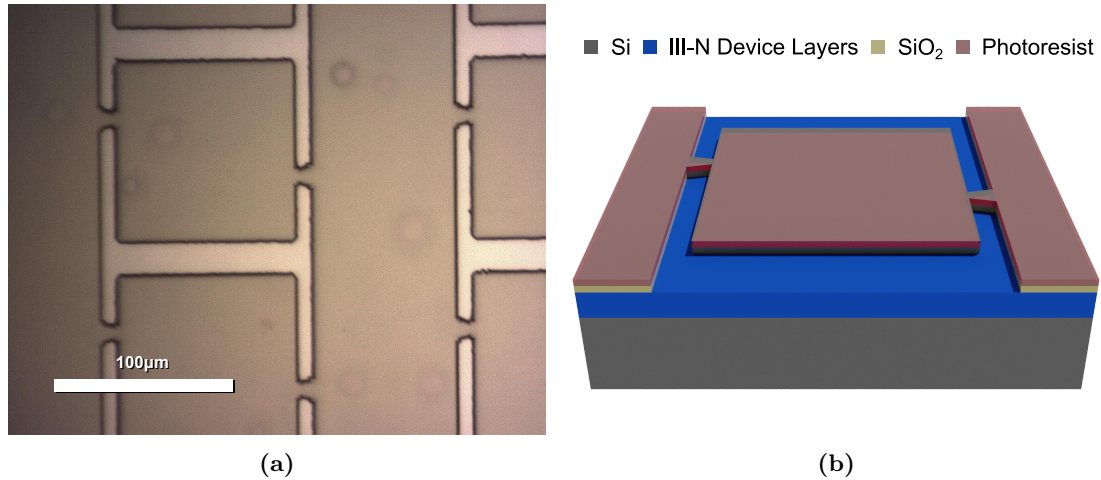


Figure 2.15: (a) Microscope image of a GaN LED sample after etching the hard mask using RIE. (b) A computer generated 3D view of an individual membrane at this stage. The SiO₂ (beige) has been removed where there was no resist mask (red) compared to Figure 2.13b.

2.7 ICP-RIE - Dry Etching Using a Hard-Mask

2.7.1 Function of the ICP Tool

The inductively coupled plasma RIE (ICP-RIE) tool shown in Figure 2.16a is the SPTS Multiplex ICP Etch System used to etch the GaN device layers of the samples. The advantage of an ICP tool is that the etching is directed vertically using an electromagnetic field generated by a coil (represented cross-sectionally by the orange circles in the figure) to direct the charged ions towards the surface as shown in Figure 2.16b [40, 52]. This creates an etch with very uniformly straight side-walls with minimal undercutting. The aspect ratio of the etch is defined as the ratio of etch depth to the opening available in the mask pattern, as shown in Figure 2.17. Small aspect ratios can focus the ions into a point and critically slow down the etch rate which can upset the process if a certain etch depth is desired [53]. ICP is used instead of normal RIE for the device layer etching because it is able to etch deeper.

For most device fabrication the maximum etch depth H is determined by the device

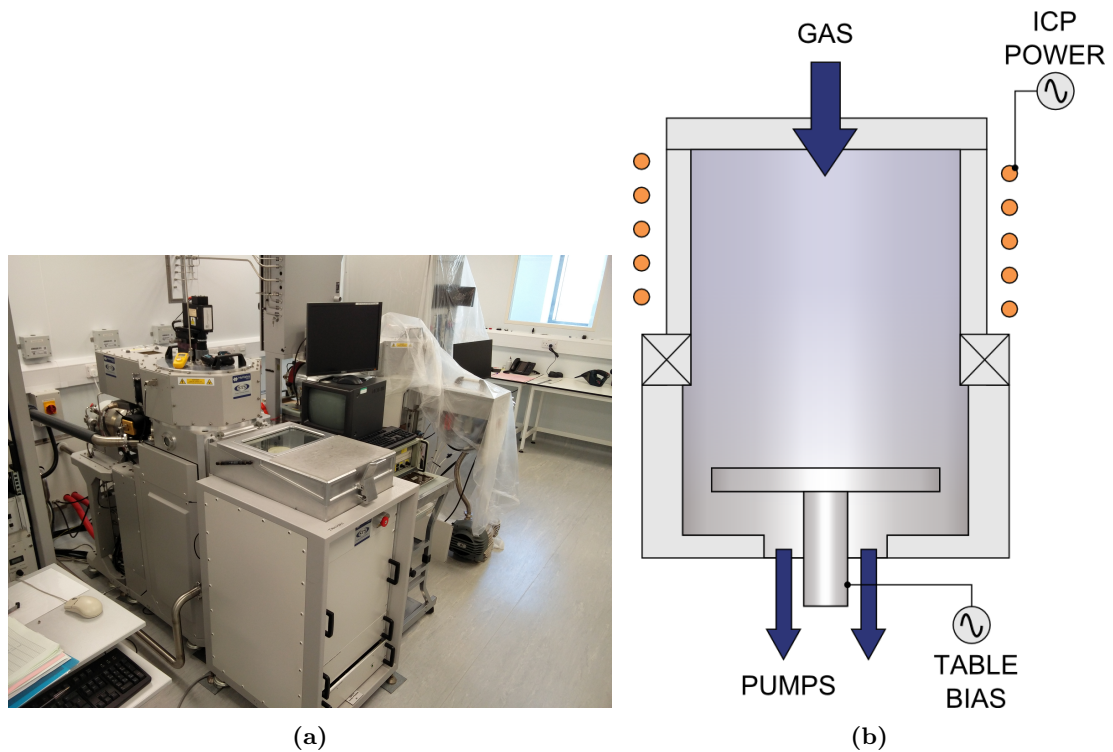


Figure 2.16: (a) Picture of the ICP tool and (b) a schematic diagram of its chamber. The latter taken from [51]. The blue arrows show the injection of the reactive ion gases at the top and the exhaust at the bottom.

layers in GaN epistructures. This would typically be $3.5\ \mu\text{m}$ with a $1\ \mu\text{m}$ SiO_2 hard mask. The minimum feature size of the mask would determine the opening W , and for the standard $100\ \mu\text{m} \times 100\ \mu\text{m}$ suspended membranes this is $10\ \mu\text{m}$. This gives the an aspect ratio of 0.45 which is low but would rise if the devices were to be made smaller.

These tools were designed to receive 6 inch imperial (or 150 mm metric) wafers and so our smaller samples have to be mounted on a carrier wafer. Pure silicon wafers are used for this purpose as they are relatively cheap and have a low etch rate in comparison to the nitrides intended to be etched. Before use, each wafer is cleaned in solvent and then a buffered HF oxide etch is applied to remove any unwanted contaminants. Samples may be mounted using a special ICP wax by heating the wafer on a hotplate and dabbing the wax carefully to create a small spot to place the sample down upon. Once cooled, the samples no longer shift about and can easily be removed by gently

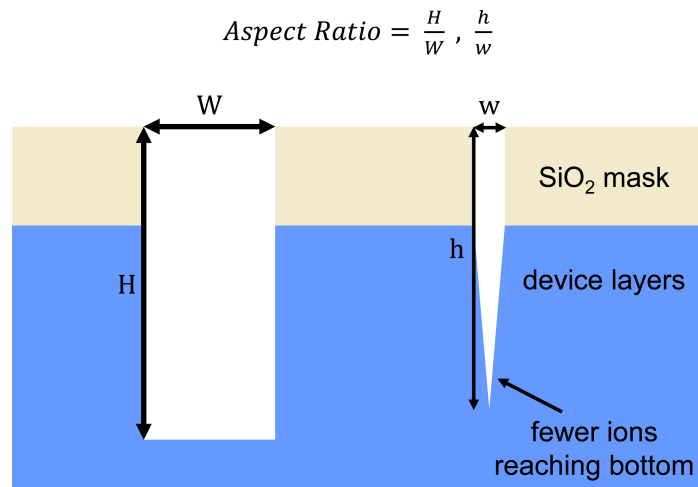


Figure 2.17: Schematic diagram of low (left) and high (right) aspect ratio features affecting ICP etching.

heating again. The bonding wax is formulated such that it would not contaminate the chamber of the ICP if it were to be etched, however care is still taken to ensure that no wax is exposed. These wafers must have their usage recorded as over time they will become thinned by the etching and need to be disposed of. A fractured carrier wafer could damage the chamber of the ICP and also lose the sample.

Unlike the RIE tools, the ICP works using an interlocked chamber system to transfer the sample from the atmosphere to the etching location. The lid to the transfer chamber is brought up and the carrier wafer is carefully placed into the ceramic prongs, paying attention to locate the major flat of the wafer in alignment with the tool's marker. This is so that the transfer happens cleanly without dropping the sample and that the prongs satisfactorily clamp the correct area. With the samples on the carrier wafer, the lid may now be lowered and the latch locked.

The software provides a sequencer that can be used to automate the process steps. It can run each individual step in order: depressurising chamber, transferring sample through the interlock system, starting the process, pressurising and releasing. There

is the option to do each step manually but is only advantageous to do so if a custom recipe demands it or if there is a fault. The recipe used, which is comprised of 10 sccm flow of Ar, 30 sccm flow of Cl_2 , platen power of 200 W, a coil power of 400 W, and a pressure of 20 mTorr, was used for all device iterations as it was tailored to etch GaN epistructures. The only setting that was changed in the recipe was the duration of the process which depended on the etch depth one wished to achieve. Once the sequencer has finished, the lid is lifted and the carrier wafer with samples is retrieved. What remains are deep trenches following the pattern of the silica mask as shown in Figure 2.18.

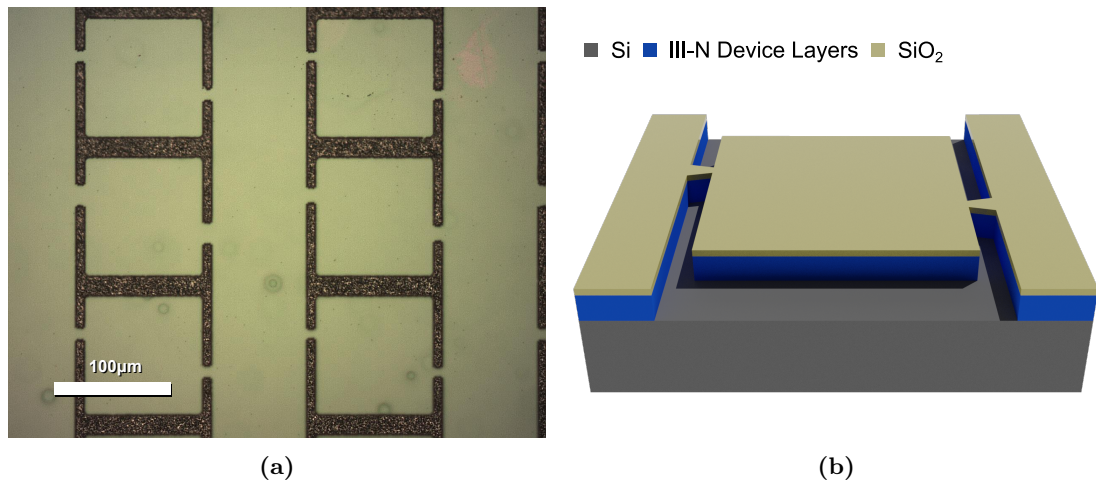


Figure 2.18: (a) Microscope image of a GaN LED sample after etching through device layers using ICP. (b) A computer generated 3D view of an individual membrane. At this stage the epitaxially grown GaN device layers (blue) have been removed where there was no hard mask (beige) compared to Figure 2.15b.

2.8 RIE - Dry Etching Silicon Trenches

A second Oxford Plasmalab 80 Plus Reactive Ion Etcher is kept to use solely on etching silicon and various metals to prevent contamination of chambers. Generally after the device layers comprising various nitrides have been fully etched to the silicon substrate a second dry etch is required to etch down into the silicon to provide access for the wet etch to come later.

The process consists of 10 sccm of Ar, 10 sccm of O_2 and 60 sccm of SF_6 at a

pressure of 0.05 Torr. The process is usually run for 2 min to give an ample depth of approximately $2\ \mu\text{m}$ whilst not fully breaking through the hard mask as the selectivity is quite low.

2.9 PECVD - Applying Sidewall Protection

Prior to the wet etch, the samples have another $1\ \mu\text{m}$ thick layer of silica deposited to protect the exposed sides of the device layer structure as shown in Figure 2.19. Otherwise the KOH would begin to etch the edges of the device which could have an impact on its performance. The aspect ratio discussed in Section 2.7 also applies to the PECVD such that the deposition tapers down towards the bottom of the trench meaning that KOH can penetrate into the silicon substrate.

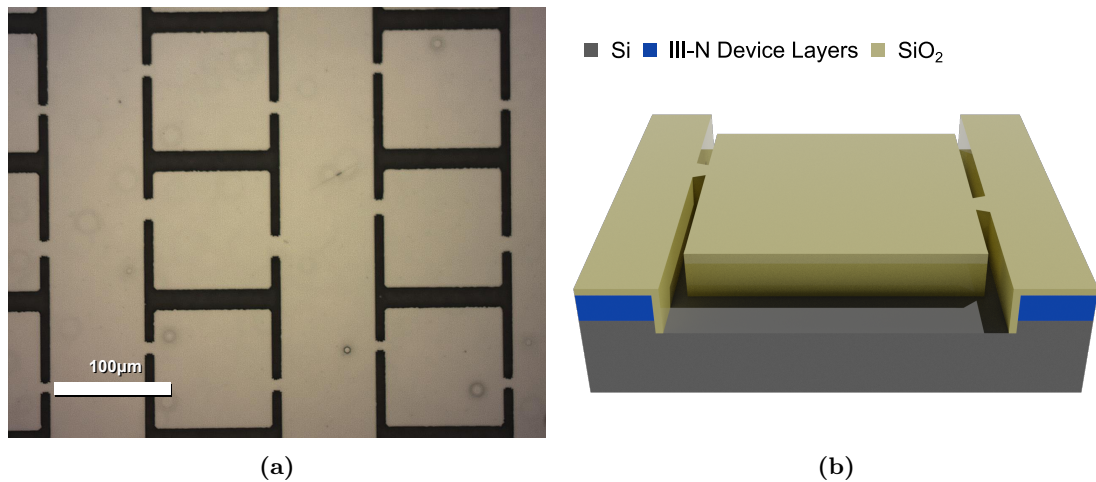


Figure 2.19: (a) Microscope image of a GaN LED sample after applying $1\ \mu\text{m}$ of SiO_2 for sidewall protection and (b) a computer generated 3D view of an individual membrane. At this stage all exposed surfaces shown in Figure 2.18b are now coated in SiO_2 (pale yellow), minimal deposition reaches the bottom surface of the trenches.

2.10 Wet Etching Using KOH

A reason why the devices fabricated were grown on a Si (111) wafer was that this exhibits the property of anisotropic etching when exposed to a heated potassium hydroxide (KOH) solution. Due to the selectivity in the etch rates between the crystallographic faces exposed in the etched sections of the prepared devices, only the

direction $\langle 110 \rangle$ [2, 54–56] will proceed in the time limit allowed as shown in Figure 2.20. The other directions will etch at a rate three orders of magnitude slower.

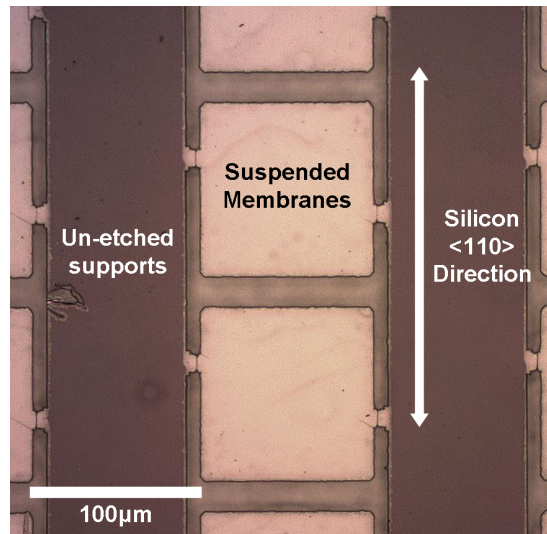


Figure 2.20: Microscope image of fully etched suspended GaN devices with labels showing the etch direction geometry.

In a fume cupboard a large glass container is filled with a continuous supply of water to dilute the waste products of the etch. A secondary water bath is set to 80°C and two beakers of deionised (DI) water are placed inside to heat to that temperature. Each beaker must be large enough to fit the etch resistant PTFE plastic device cradle used to hold the devices in the solution, and filled full enough to submerge them completely. The primary water bath is set up comprising a hotplate with a stirring option, a thermocouple, and a large round glass tank to act as the bath. This bath is used for the reaction to contain and heat the reaction vessel. The bath is filled with water to a level which reaches half way up the beaker containing the KOH solution. Other small empty glass beakers are added around the main PTFE beaker just to centralise it so that the stirrer may function; this is shown in Figure 2.21. The thermocouple is lowered into the the water bath and the target temperature is set to 80°C .

The samples to be etched are placed in the PTFE cradle edge-wise to allow the solution to flow freely over the faces of the devices. The cradle was designed with holes in the bottom to assist in the flow of the solution as well as with feet to raise the cradle off

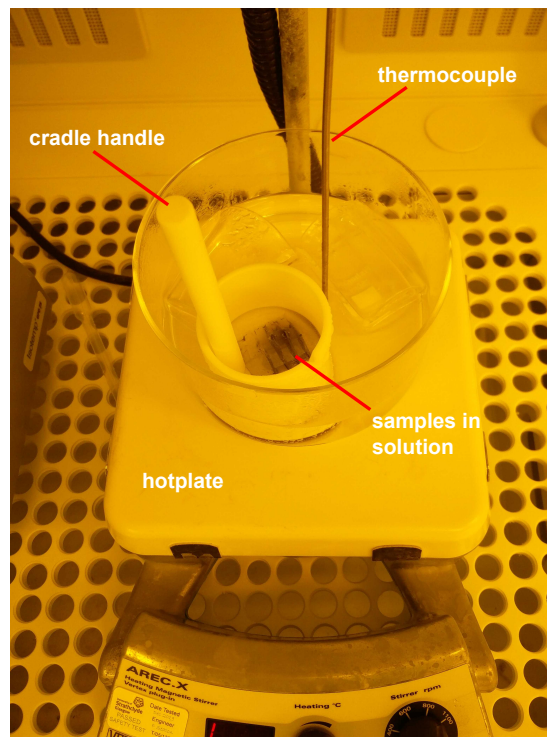


Figure 2.21: Labelled photograph of the KOH etch mid process with the cradle here containing 4 GaN-on-Si samples.

the bottom of the beaker to allow for the rotation of the magnetic stirrer.

The solution is created by precisely measuring out 26.6 g of solid KOH granules and 40 mL of DI water and adding one small magnetic stirrer. A PTFE lid is loosely fitted to the beaker to prevent the violent reaction from contaminating the surrounding workspace as well as to minimise water loss via evaporation. The beaker is then replaced into the centre of the primary water bath with the stirring action set to the lowest setting to fully mix the solution. When the target temperature is reached, the lid is removed and the cradle gently lowered into the solution to begin the etch. A timer is set for 50 min as an initial duration to check the state of etch progression. Variations in the previous fabrication steps can cause a major variation in the time required to etch. One's own judgement is needed to estimate the remaining required time but this should not exceed a cumulative time of 90 min, with 70 min being more reasonable for 100 μm wide membranes. The etch will self terminate in the faster direction when two $\{111\}$ planes meet, but the device layers may suffer with prolonged KOH exposure.

One of the beakers of DI water is removed from the second water bath and is used to rinse the whole cradle of devices by gently submersing. A stream of DI water is then directed into the beaker to slowly lower the temperature and dilute the KOH to trace levels. This step was devised and added to the standard protocol during this study to minimise the thermal shock to the suspended devices. The cradle is removed and set aside whilst each device is lowered into a small beaker of IPA to displace the water in the sample. As there is water underneath the individual devices, it is very difficult to dry the samples otherwise. The IPA is volatile and can be removed with a gentle stream of N_2 from an air-gun to dry. The device can then have the excess silica removed with either a RIE process or a BOE wet etch to produce the final suspended membranes as shown in Figure 2.22.

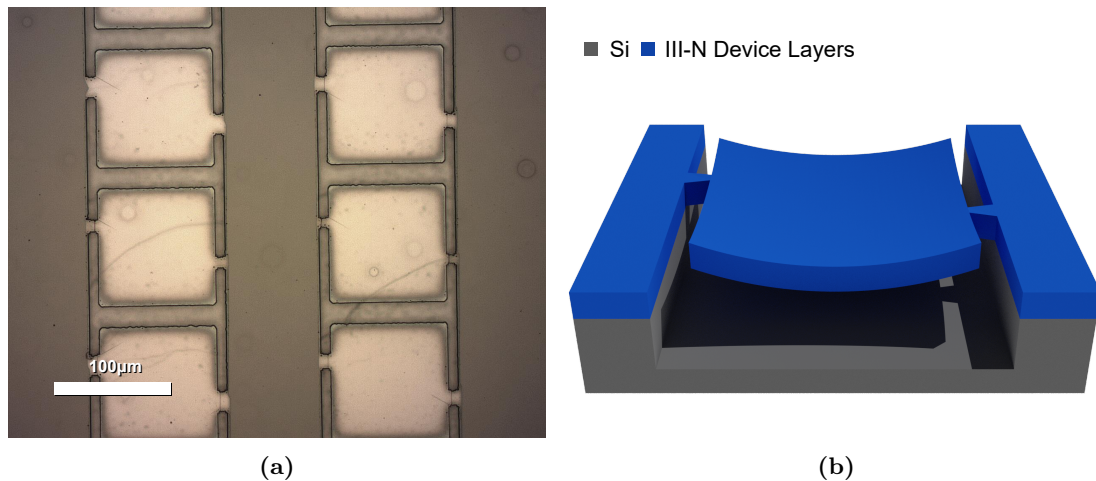


Figure 2.22: (a) Microscope image of a GaN LED sample of suspended membranes after removal of silica. (b) A computer generated 3D view of an individual membrane at this stage. The membrane is curved due to the under-etch releasing the counter-acting support structure causing the membrane to curl upwards under its own strain.

2.11 Metal Deposition - Electron Beam

For very thin layers of metal of thickness around tens of nanometres, the Edwards 306 electron beam evaporator deposition tool shown in Figure 2.23 is used. Such metal films are normally spreading layers for LED devices that need the current to be uniform across the p-side of the junction. The lateral conductivity of p-type GaN is low and



Figure 2.23: The E-beam evaporator used for thin metal film deposition.

so the thin metal layer allows the current to spread uniformly. For top-emitting LEDs with the primary light emission coming from the p-side, the spreading layer needs to be transparent to the produced light. Approximately 5 nm of nickel and 5 nm of gold should satisfactorily create a conductive sheet whilst remaining transparent to ~ 420 nm wavelength light that was typically worked with. The nickel provides better adhesion to the GaN, whilst the gold is the better conductor.

For bottom-emitting LEDs, palladium can be used as it is both highly conductive and reasonably reflective to the light. A thickness of 100 nm would have been used for this configuration and was used in my simulations of hybrid devices as described in Chapter 6.

2.11.1 Function of the E-Beam Deposition Tool

The tool itself consists of many crucibles of metal for deposition including: silver, nickel, palladium, gold, and titanium. Under a low pressure of at least 5×10^{-6} mbar an electron gun fires a beam of electrons at the crucible target which sublimates the material. The material is directed at the sample by removing a baffle and the deposition

begins. Only the surface of the sample is exposed to the evaporation so only that surface receives a coating, which is ideal for current spreading layers. Care is taken to time the duration of deposition as the calibration of the machine determines the rate at which material is added to the target. Excessive thickness of a spreading layer would prevent light to penetrate the layer and too thin a layer would not sufficiently spread the current.

2.12 RTA - Rapid Thermal Annealer



Figure 2.24: The rapid thermal annealing tool.

The rapid thermal annealing (RTA) tool used to anneal metal layers to the semiconductor devices is shown in Figure 2.24. The annealing process heats the device in a vacuum state to consolidate the two materials together, primarily to reduce the resistance between the layers. This fairly simple process can increase the electrical efficiency of devices greatly, and so is a standard step on most optoelectronic device fabrication. The conductivity is increased by lowering the contact resistance. For nitride LED devices with a Ni/Au spreading bilayer the process described in Table 2.1 is used.

Table 2.1: Process configuration for annealing Ni/Au bilayer on the RTA with 6 steps.

Step	Temperature (°C)	Duration (s)	Pure N ₂	Air
1	90	30	off	off
2	350	30	off	on
3	510	30	off	on
4	510	180	off	on
5	250	60	off	on
6	0	15	on	off

2.13 Metal Deposition - CVC Sputter

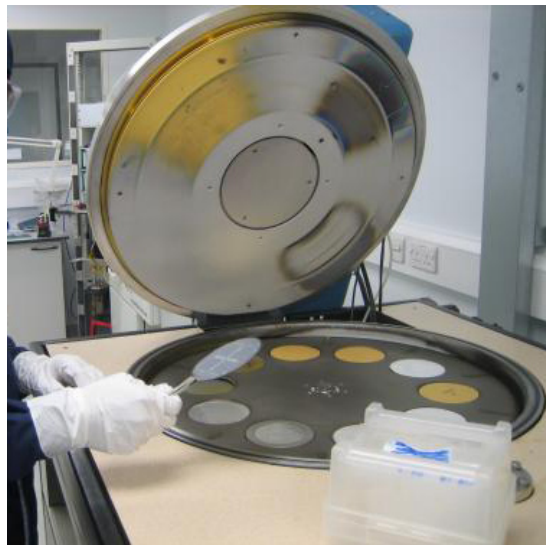


Figure 2.25: Wafers being loaded into the CVC sputter tool.

The CVC branded sputter tool is used for thicker layers of metal in the order of hundreds of nm, used for creating electrical contacts for the devices. After creating an appropriate mask on the surface of the devices using photoresist, the samples are stuck to a 150 mm carrier wafer using Kapton tape. The tape is used to prevent the samples falling as the wafers are loaded upside down into the machine as shown in Figure 2.25. For LED contacts a 100 nm layer of titanium is added for improved adhesion and then a 200 nm to 300 nm layer of gold for better conductivity.

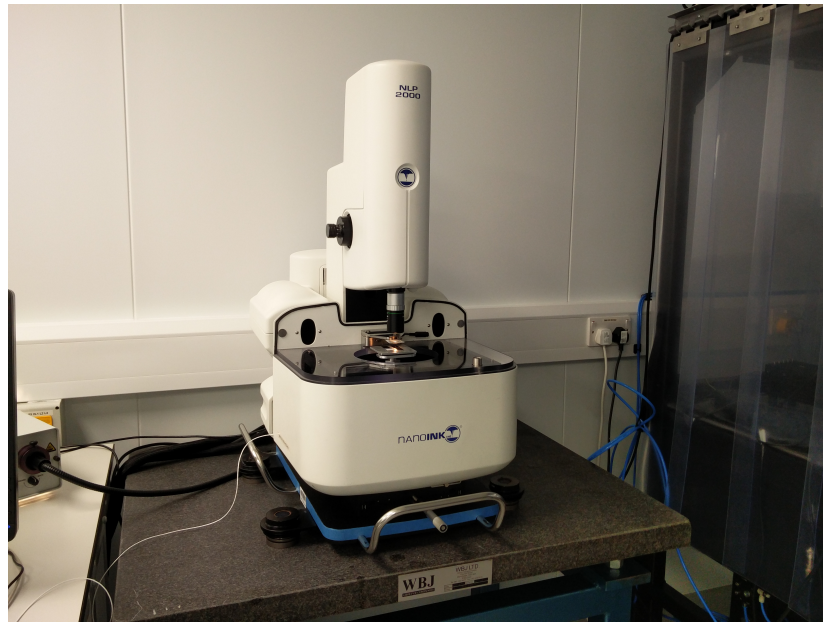


Figure 2.26: The converted Nanoink NLP2000 tool used for transfer printing.

2.14 Transfer Print Tool

The tool used for transfer printing is a Nanoink dip pen nanolithography system NLP2000 shown in Figure 2.26. The pen holder is modified to receive elastomeric stamps which can pick up suspended semiconductor coupons from one location and print them elsewhere. The stamp remains in a fixed position whilst the coupons and print location are moved using a multi-axis stage. The aluminium sample holding plate shown in Figure 2.31 can be moved using the provided software in xyz directions using piezo-driven linear stages and can tilt the plate about the x and y axes using encoded goniometric stages. A modification to allow the rotation of the plate in the z axis was added which is controlled by a separate control box next to the main computer. These controls have an accuracy of ± 25 nm and $\pm 0.00025^\circ$, respectively. Such precision would allow for transfer printing to be repeated consistently by saving the coordinate locations on the computer. In practice the positions were saved for the “donor” (where the individual coupons are picked up from) and the “receiver” (where the coupons are to be printed). In both cases these two positions are always such that the pyramids of the stamp are $50\ \mu\text{m}$ above each surface. This is so there is no accidental crashing

which will cause damage to the samples and misalign the setup.

The focus of the microscope is also controlled through the computer interface by either setting a value or using the buttons to jog a set amount, usually several microns. This means it is possible to switch between focusses quickly such as the surface of print locations as well as the face of the stamp.

The tool is mounted on a level anti-vibration table to prevent disruptions that would translate into large movements in the field of view of the transfer printing. The light source is used to illuminate the working area to be able to see the samples and stamp during the print process. Depending on the field of view and zoom used with the microscope, the brightness can be adjusted accordingly to display a clear image.

2.14.1 Elastomeric Transfer Print Stamps

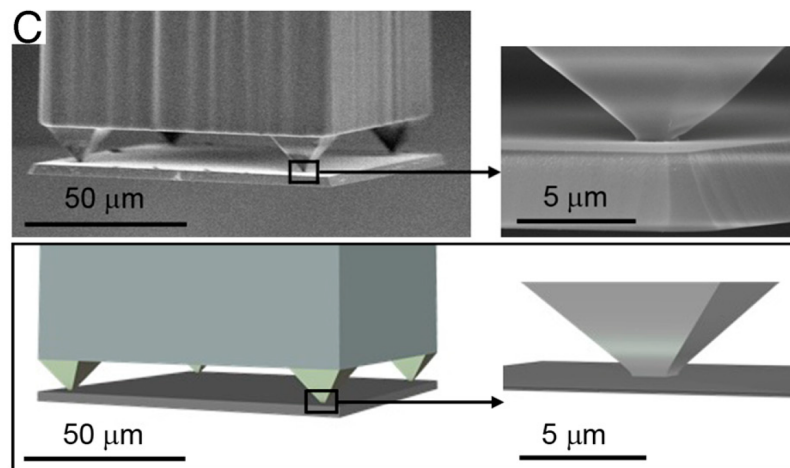


Figure 2.27: SEM image and graphic representation of a PDMS stamp holding a device. Adapted from [31].

The stamps used for printing are made from polydimethylsiloxane (PDMS) and follow a similar design to those of previous studies [2, 31] which use reversible adhesion to be able to move devices from one donor location to a receiver. The stamps have square profiles with protruding pyramids at each corner as shown in Figure 2.27. They are designed to match the size of the devices to be printed. In our case of the devices were $100\ \mu\text{m} \times 100\ \mu\text{m}$ squares and so the stamps matched those dimensions.

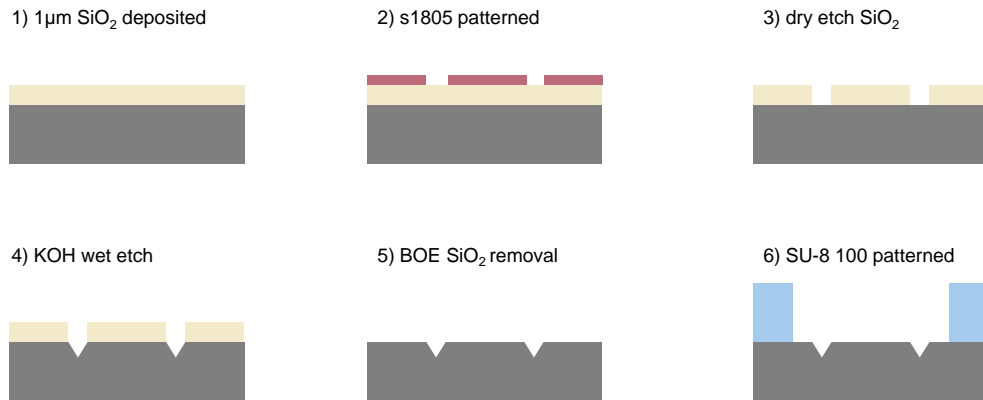


Figure 2.28: Cross sectional diagram showing the steps in fabricating a stamp mould to cast PDMS stamps.

The stamps degrade over time and regularly need to be remade. To make a stamp one must first make the mould for it to be cast in as is illustrated in Figure 2.28. A Si (100) wafer is used to form the base of the mould due to its specific characteristic when etched with KOH. A section of the wafer is first coated in 1 µm of SiO₂ using PECVD. S1805 is spun to create a 500 µm film and patterned using a mask to form small squares (~10 µm wide) in the locations for the pyramids. The sample is dry etched using RIE to reach the Si substrate. The sample is then submerged in a hot solution of KOH, as previously described in this chapter, to etch into the Si. The KOH etches the {111} planes much slower than the {110} meaning that due to the orientation of the wafer the etch terminates in an inverse pyramid shape [54–56]. A wet etch of BOE is then used to remove the SiO₂. SU-8 100 is then spun at 3000 rpm for 60 s to form a 100 µm thick layer: this method is adapted from the data sheet [57]. The resist is soft baked using a hotplate at 95 °C for 30 min. The pattern is then exposed using the mask aligner with an exposure duration of 20 s. The sample is then baked again for 15 min at 95° to selectively cross-link the exposed portions of the film. The pattern is then developed using propylene glycol methyl ether acetate (PGMEA) by submerging it for 5 min which removes the non-crosslinked areas of the film. Finally the resist is cured using a hard bake on a hotplate for 10 min at 150 °C. This finalises the stamp mould.

To create the stamp the Sylgard 184 Elastomer PDMS kit is used [58]. The stamp mould is mounted inside a Petri dish, SU-8 side face up, to contain the volume of silicone that starts out as a liquid. The usual ratio of base to curing agent is 10:1 to create a rigid yet moderately tacky stamp for transfer printing. Ratios can be varied up to around 14:1 and as low as 6:1. The base and curing agent are carefully syringed into a glass beaker, using a precise scale to measure the ratio. The beaker is vigorously stirred to combine the two parts which has the undesirable effect of including air bubbles into the mix. The beaker is then loosely covered with a glass lid and set inside a fume cupboard to de-gas for 2 h. Once the bubbles are no longer present, the beaker is then turned into the stamp mould. The mould should be filled such that there is at least 2 mm of PDMS above the SU8 which will later form the main body of the stamp. The Petri dish is covered and set in a very flat location such that both top and bottom surfaces of the stamp are co-planar. The auto-levelling base which the transfer print tool rests on is ideal for this. After 24 h the PDMS is fully cured. It is possible to speed up the process by raising the temperature but it was found that this made the PDMS more rigid and less tacky than the longer cooler method [59].

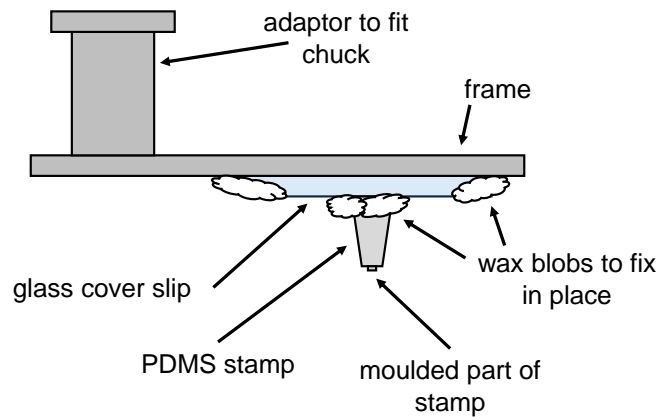


Figure 2.29: Diagram of a stamp adhered to its holder.

When fully cured, the PDMS is removed from the mould and set onto a cleanroom wipe stamp-face up. A surgical scalpel is then used to carefully cut a 3 mm by 3 mm square truncating outwards towards the bottom to around 5 mm by 5 mm to form a

truncated pyramid as shown in Figure 2.29. This is then cleaned in a beaker of IPA to remove any dirt. The large end of the truncated PDMS is put onto the centre of a microscope glass cover slip and then melted wax is pipetted around it to hold it in place. This is then placed upon a custom aluminium frame and fixed in place with a blob of melted wax in each corner as can be seen in Figures 2.29 and 2.30. This frame can then have a steel cylinder screwed into it which sits into the stamp holder of the transfer print tool.

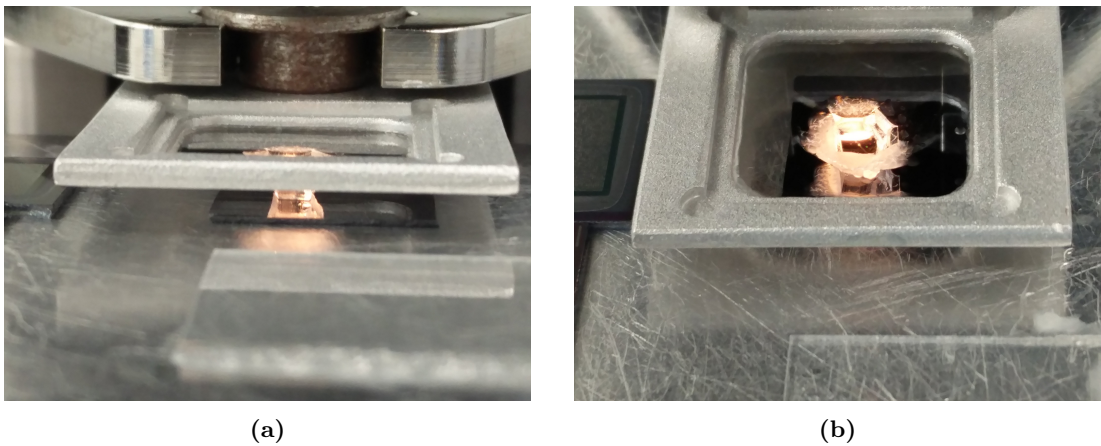


Figure 2.30: Two close up shots of the stamp and holder installed into the transfer print tool.

2.14.2 Sample Preparation

The aluminium plate shown in Figure 2.31 is removed from the holder and cleaned of any debris using a cleanroom wipe and some acetone. The plate is warmed slightly using a hotplate and then set down on a wipe until one is ready to add the samples. Thin wax is melted in a dish on the hotplate and then a small amount is placed in the intended locations for both the samples. The samples are then lowered on top of the melted wax and left to cool under the cover of a Petri dish; this process locks the samples in place. If there is too much wax the sample will not lay flat, which would interfere with the coordinate system of the transfer print tool.

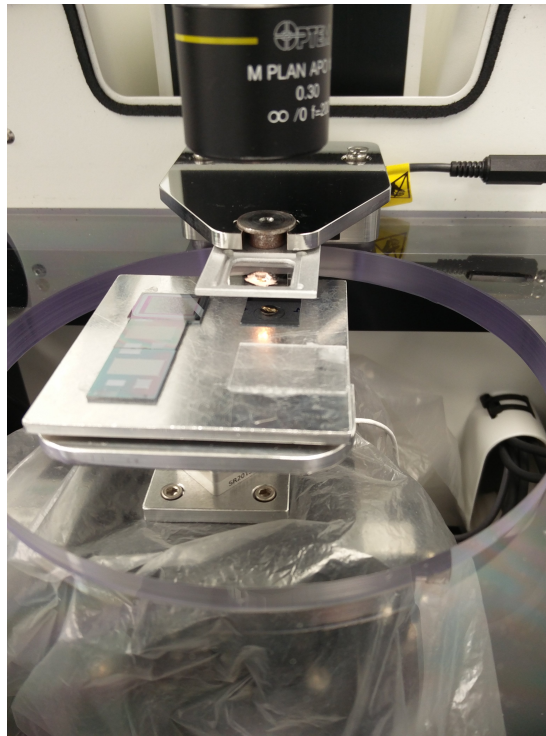


Figure 2.31: A closer view of the stage and working area of the transfer print tool.

2.14.3 Calibration of the Printing

As the machine is switched on, the stages are set to a calibration mode in which they will travel to each extreme in the xyz and tilting directions and then relocate to a “safe” position. This calibrates the stages. There is no calibration for the rotation of the plate due to this axis being added externally and being controlled by a control box on the side. One must ensure the plate is not rotated when calibrating or else it may collide causing it to fail. The z height is set to its lowest value “safe z ” when working around the stages to give the most room without knocking the stages which would de-calibrate them.

The locations of the donor and receiver are found by moving the stages using the software. A location $100\ \mu\text{m}$ above the surface is found by carefully bringing the pyramid tips of the stamp into contact with the surface using progressively smaller increments and then backing off $50\ \mu\text{m}$.

2.14.4 Making a Print

The method for using elastomeric stamps for printing devices used here is adapted from the literature [2, 31]. When making a print the donor location is set and the focus is set to the stamp face. The stamp is brought into contact with the suspended membrane with progressively smaller increments with the last increment being 500 nm, ideally with the stamp located as central to the device as possible. The stamp is then pressed into the membrane so that the pyramids flatten and the main area of the stamp comes in contact with the membrane as shown in Figure 2.27. The Van der Waals forces between the stamp and membrane are maximised when the complete surface area makes contact. The stamp is then quickly pulled away from the donor sample by lowering the stage 100 μm with the suspended membrane still attached to the stamp. Then the stages are moved so that the stamp is located above the receiver in the print location; the membrane should then de-collapse from the face of the stamp as the pyramids push out such that the membrane is only held by the tips of the pyramids. Now the surface area of contact is much lower with the stamp, the Van der Waals forces are also reduced allowing for easier separation. The membrane is gently brought into contact with the receiver surface making sure not to collapse the stamp into full-contact again. One can see that the membrane is making good contact by observing the Newton's rings forming which are visible through the stamp. The stage is then slowly lowered again leaving the membrane behind on the receiver, successfully completing the print.

2.15 Metrology Equipment

2.15.1 Optical Microscopy

In microfabrication it is very important to check between each processing step to verify whether the desired result has been achieved. An optical microscope provides a quick method to identify telling signs such as a failed exposure or development in the photolithography step. This error in geometry would then persist through further processing and render the end result invalid. When caught early the error may be undone which can save a lot of precious fabrication time.

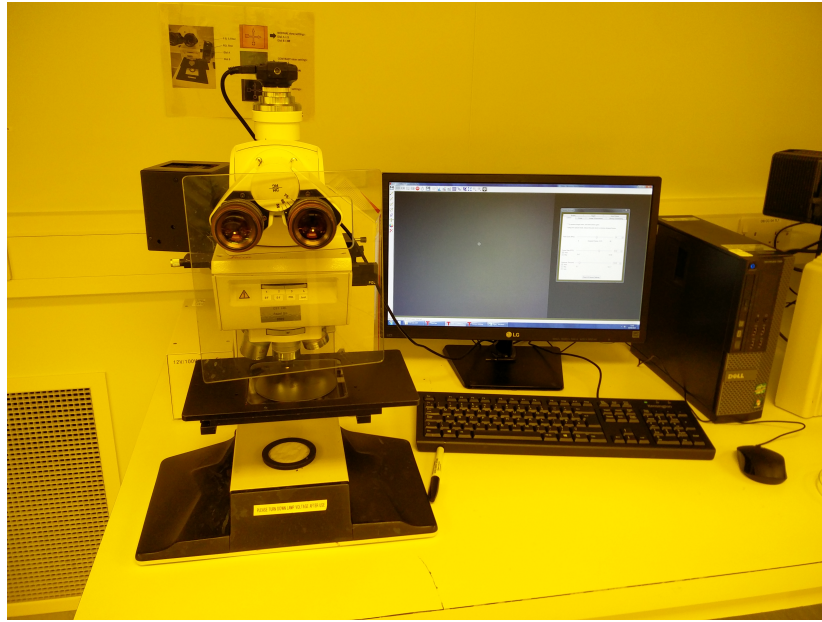


Figure 2.32: The Leica DMR microscope.

The primary microscope in use for our work is a “Leica DMR” shown in Figure 2.32, which has 5 \times , 10 \times , 15 \times , 20 \times , 50 \times , and 100 \times objectives for various levels of magnification. The wide field of view of the 5 \times objective lens allows the user to check for uniformity across a sample on the millimetre scale where hundreds of devices could be seen. Defects in the photoresist application step such as scrapes or detritus can easily be spotted and worked around. Poor quality of development would require re-processing. The 10 \times , 15 \times , and 20 \times objectives were used to quickly look with finer detail between processing steps and also capture a record of the sample using the attached digital camera and computer. The 20 \times objective allowed for four devices to be within the field of view whilst also offering a reasonable level of detail. The 50 \times objective gave a very good level of detail for individual 100 μm devices by taking up the entire field of view, and the 100 \times objective allowed one to get into the very fine details required such as assessing the edge quality of devices.

2.15.2 White Light Reflectometry

The Filmetrics F20 shown in Figure 2.33, is used to gauge the thickness of thin films using the reflectance spectra recorded from shining white light at the target surface. The



Figure 2.33: The Filmetrics F20 thin film measurement device.

spectra are then compared to a calibrated dataset to approximate the film thicknesses. A set of n and k values corresponding to the real and imaginary parts of the refractive index can be loaded into the supplied software for materials beyond the standard provided library. The complex layer structure of epitaxially grown semiconductor devices makes this tool unusable to measure their thicknesses.

2.15.3 Stylus Profilometry

The Veeco Dektak 3 shown in Figure 2.34, is used for measuring the height of features on devices such as steps or trenches, generally on the micron scale. The tool works by bringing an extremely fine diamond tipped stylus into contact with the surface of the object being measured. The stylus is cantilevered such that any deflection can be measured through a linear variable differential transformer as an electrical signal. These signals are then digitised and displayed onto the screen of the connected computer through the Dektak3 software.

A limiting factor when measuring particular features such as narrow trenches with this tool comes from the physical width of the stylus tip. The stylus tip has a radius of

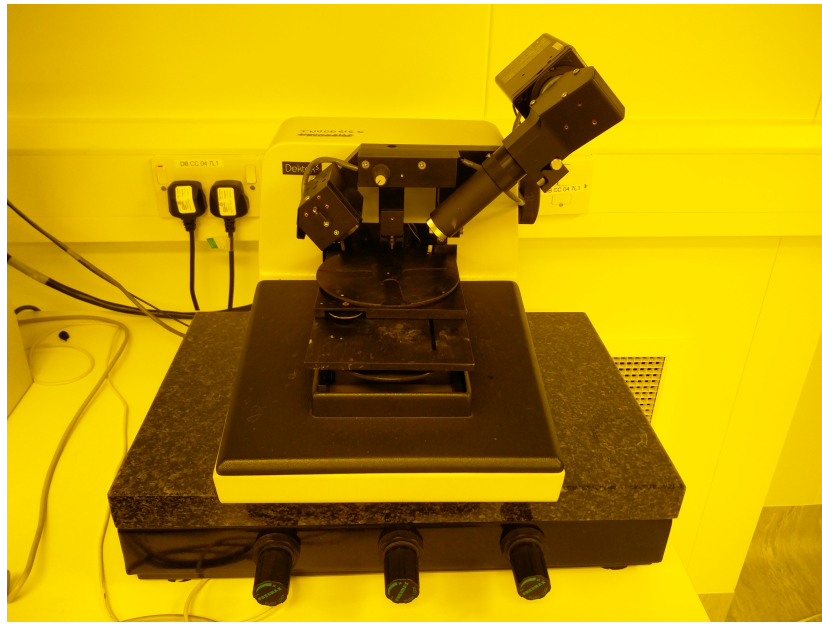


Figure 2.34: The Dektak 3 stylus profilometer.

12.5 μm , meaning that it cannot enter the features surrounding suspended membranes. If the size of the devices were to be reduced then one would have to accommodate areas to facilitate the access of the stylus tip to reach the bottom of an etched area. This could be done by designing the mask used in photolithography to include a large area that has a step in it. The physical contact of the stylus also prohibits measurements on delicate devices such as suspended membranes as it would cause damage.

2.15.4 Optical Profilometry of Suspended Membranes

The optical profilometer, a Veeco Wyko NT1100 shown in Figure 2.35, was used as a non-destructive means of measuring the surface of devices. These measurements provided good quality data for comparing different types of sample both qualitatively and quantitatively. Measurements were taken of the suspended membranes both suspended on their original substrate as fabricated, and on a new receiver substrate after being transfer printed.



Figure 2.35: The Wyko NT1100 optical profiling system.

2.15.5 Function of the Optical Profilometry Tool

This tool utilises a measurement system commonly known as vertical scanning interferometry (VSI) to record the heights of a sample by scanning discrete points in a raster format [60]. This involves a collimated white light source which is split using a beam splitter. One of the exit beams travels to a fixed optically flat mirror, returns back through the beam splitter and then is focussed onto a CCD as shown in Figure 2.36. The other beam is incident on the sample and also reflects back through the beam splitter and is focussed onto the CCD. The optical path length of the second beam directed at the sample is gradually varied using a piezo stage. The recombination of both beams will cause an interference pattern and the fringe contrast will be highest when the focus is on the surface of the sample which is calculated from the output of the CCD by the computer. So by iterating across a designated area that is measured piece by piece, the z value where the fringe contrast is highest can be determined to produce the best 3D map of the sample surface.

The dedicated software used to take measurements can be used to assess the results but more commonly it is used to output an *.opd* file containing all the 3D data. These

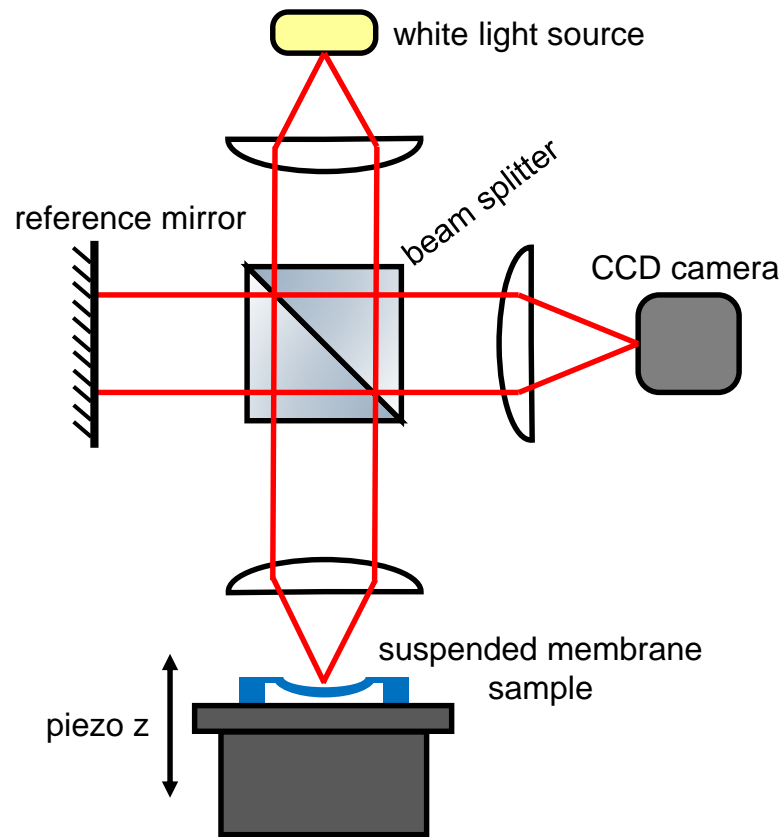


Figure 2.36: Simplified schematic diagram illustrating the workings of white light interferometry used for optically profiling suspended membranes.

files can then be further analysed and processed using the open source Gwyddion data analysis software [61] which is explained in greater detail in Chapter 3.

2.15.6 AFM - Atomic Force Microscopy

The atomic force microscope (AFM) tool made by Park Systems shown in Figure 2.37 was mainly used to investigate surface morphology on the nanometre scale compared to the microscale profilometry previously discussed. AFM is a useful technique to image and measure features on the nanometre scale such as very fine grating patterns for optical grating-couplers in photonic circuits and even being able to resolve individual atoms (in the z direction) [62]. The main features used for this study were the output

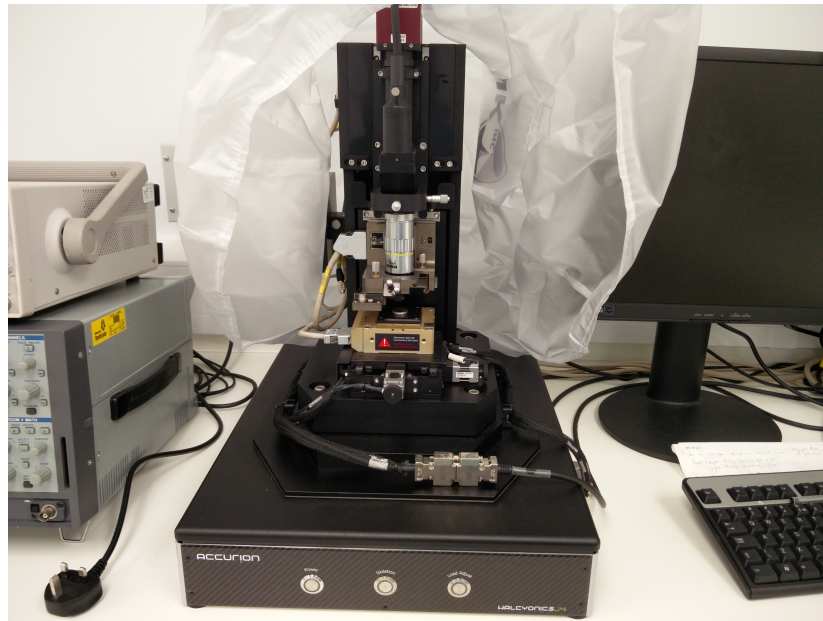


Figure 2.37: The Park Systems AFM.

of root mean square (RMS) roughness and a clear visual representation of the surface quality of fabricated devices. This can be a great indicator of how the devices will print as the smoother the surface, the stronger the Van der Waals forces between the devices and receiver which adhere them together.

2.15.7 Probe Station

The probe station, a Wentworth 280X shown in Figure 2.38, was used for measuring the current-voltage (IV) characteristics of LED devices. The probe tips are adjusted to touch the gold contact pads of the device, positive to the p-contact and negative to the n-contact. The machine is then set to run multiple sweeps over voltage and records the current. The data is output as a *.txt* file on a floppy disc which then is taken for further data analysis on a computer. This output unfortunately included mixed units as text alongside the data. A Python script was written to convert the inconsistent data output of the probe station into a new comma separated variable *.txt* file and plot the data as shown for example in Figure 2.39. The scripts to fix and plot the data may be found in appendix A.



Figure 2.38: The probe station tool.

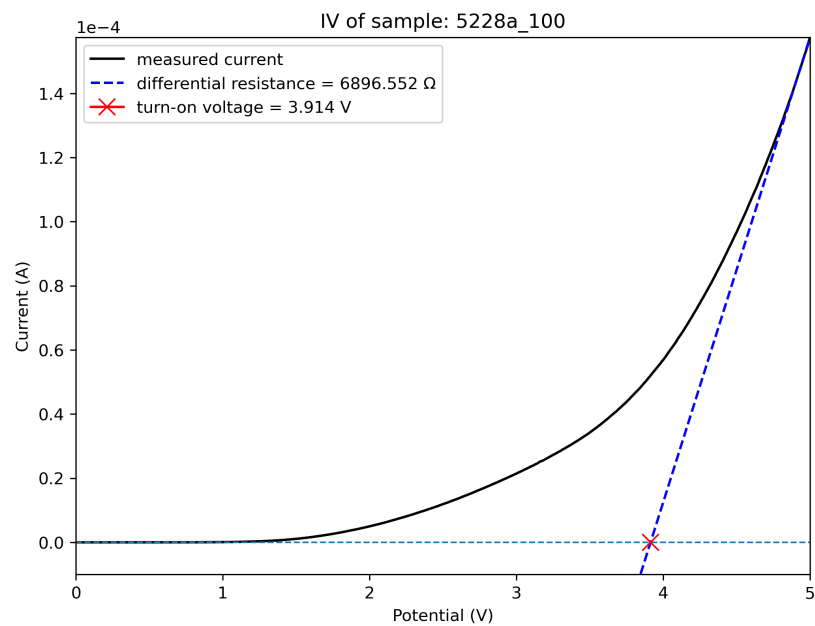


Figure 2.39: Figure produced from probe station IV data of a 100 μm diameter circular LED using Python script which plots the IV curve and extracts the turn-on voltage from the gradient. This figure is part of a larger set measuring the characteristics of custom-grown LED material.

Chapter 3

Effect of Ammonia Pre-Dose on Wafer-Level and Device-Level Flatness

The work in this chapter was published as

B. F. Spiridon and M. Toon, A. Hinz, S. Ghosh, S. M. Fairclough, B. J. E. Guilhabert, M. J. Strain, I. M. Watson, M. D. Dawson, D. J. Wallis, R. A. Oliver, “Method for inferring the mechanical strain of GaN-on-Si epitaxial layers using optical profilometry and finite element analysis,” *Optical Materials Express*, Vol. 11, no. 6, pp. 1643—1655, 2021. DOI: 10.1364/OME.418728.

3.1 Overview

This chapter focusses on the development of GaN-on-Si membranes for use in transfer printing and investigating the topographic flatness of the membranes achievable through epitaxial growth. In the growth of GaN-on-Si wafers, the various constituent materials are layered with a slight mismatch between their crystal lattices creating internal strain. Adding to this, the growth reactor reaches temperatures of over 1000 °C which expands each material different amounts depending on the material’s

thermal expansion coefficient, so as the epistructure cools the layers shrink to varying degrees and pull against each other. The suspended membranes then release part of this strain as a “relaxation” when they are under-etched causing the membranes to curve. This deformation is undesirable because it greatly hinders the printability of these membranes onto flat surfaces: only the centre section makes contact, lowering the contact force which is required to free a coupon from the stamp.

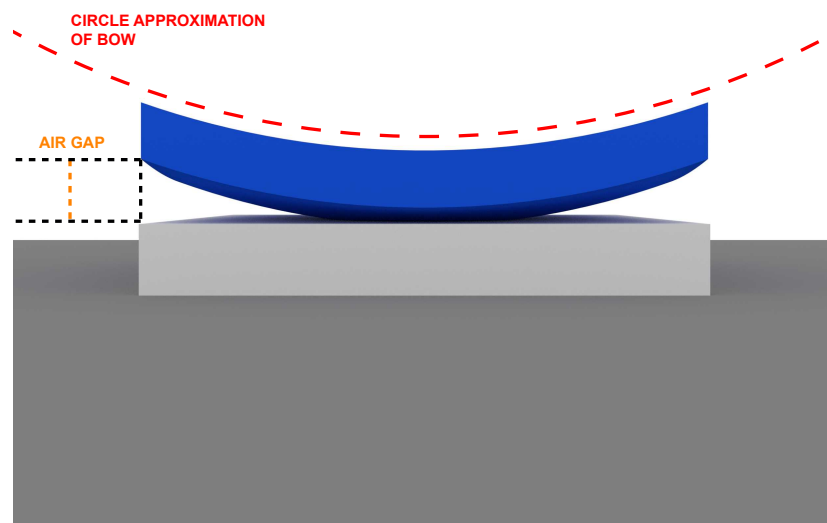


Figure 3.1: Graphic representation of a bowed membrane (blue) printed onto another flat device (grey) illustrating the air gaps introduced.

The photonic capabilities are also greatly affected. The primary device that was intended to be constructed was a resonant cavity light emitting diode (RCLED). If one of the layers creating the cavity were to be bowed then the intra-cavity length would alter and cause the device to fail. As well as this, small gaps between layers would form air pockets which create their own resonances within the semiconductor-air-semiconductor cavity as shown in Figure 3.1. This creates spurious resonances on the output spectra, as well as broadening the main output peak.

One method to counteract the bowing of the wafer is to include “buffer” structures. These are epitaxially grown layers of material which provide either a compressive or

tensile strain to the epistructure. The thicknesses of these layers determine the amount of compression or tension in the material to ideally create a balance resulting in a flat wafer. A downside to these buffer structures is that they add considerable thickness to the overall epistructure which uses more material and also compromises the ability to create transfer printable coupons as is explored in Chapter 4.

The development of flat transfer printable membranes required a coordinated programme of epitaxy, fabrication and metrology. The epitaxy work was carried out by collaborators at the University of Cambridge, led by Professor Rachel A. Oliver. The main parameter of investigation was the effect of the ammonia (NH_3) pre-dose in the growth of GaN devices on silicon substrates [63, 64]. The NH_3 was used to assist in the aluminium nitride (AlN) nucleation layer which is the first of the epitaxial growth layers on top of the Si substrate. It would be found that silicon nitride was created proportionally to the ammonia dosage and provided extra strain relief in the epistructure. The test material used initially was based on a series of six high electron mobility transistor (HEMT) epistructure wafers which had varying amounts of NH_3 pre-dose time to compare the flatness of the resultant individual suspended membranes using optical profilometry. As the buffer layer structures were also used in the proposed LED materials, the HEMT structure was a suitable analogue for the LED structures and had the advantage of being readily available at the time of this study.

This study consisted of two iterations of growth, with profile measurements from round one informing growth conditions for round two. In the second growth round there were two variants of an LED structure (instead of a HEMT) which were identical aside from the fact that one had a $10\ \mu\text{m}$ SiN_x dislocation blocking layer in the n-GaN region. The intention was that this layer might achieve higher uniformity and lower the internal stress of the structure. Suspended membranes were once again systematically fabricated with the addition of a sample from a commercial source to compare the flatness. Some of the suspended membranes were transfer printed to a SiO_2 receiver substrate and both types were measured using optical profilometry. We were able to produce

transfer-printable GaN-on-Si wafer devices that had flatter overall geometry than those fabricated from contemporary commercial material supplied by Plessey. The radii of curvature measured from a circular arc fit to the device profiles were approximately 0.9 mm and 3 mm for the commercial and bespoke materials, respectively, after having been printed. The measurements recorded in this study were a central element of a publication on the inference of strain in suspended GaN-on-Si epilayers [1].

3.2 HEMT Systematic Bowing Study

As covered in Chapter 2, transfer-printable coupons were created to measure the bow of the membranes. The high electron mobility transistor (HEMT) material was used as this was available and shared the same buffer structures with the LEDs which were the primary focus of this investigation. A similar section will follow outlining the different approach taken for the bespoke LED material obtained afterwards, each study being complimentary to understanding the processing of GaN epistructures. The active structures of the device had a negligible impact on this study as long as they are formed from GaN to a similar total thickness in each case. Inference was used to improve the growth of the LED structures using the HEMT data, which was performed by the collaborators in charge of the epitaxy. The buffer layers which mediate to the substrate are detailed in the full HEMT epistructure cross-sectional diagram in Figure 3.2.

This first epitaxial layer growth trial was primarily focussed on the effect of the ammonia dosage given to the silicon growth substrate when creating the AlN nucleation layer. The bow of the resulting grown epilayer wafers and the bow of the fully processed suspended coupons was compared to note any correlations. This relationship of wafer to coupon bow would potentially offer a method to tailor epitaxy processes to produce flat membranes for transfer printing.

It was conjectured that the ammonia pre-dose encouraged the growth of silicon nitride on the surface of the silicon before the deposition of the buffer layers [63]. This silicon nitride would provide strain relief to the following deposition of layers and hence increase the flatness of the wafers. The optimal dosage for wafer flatness was

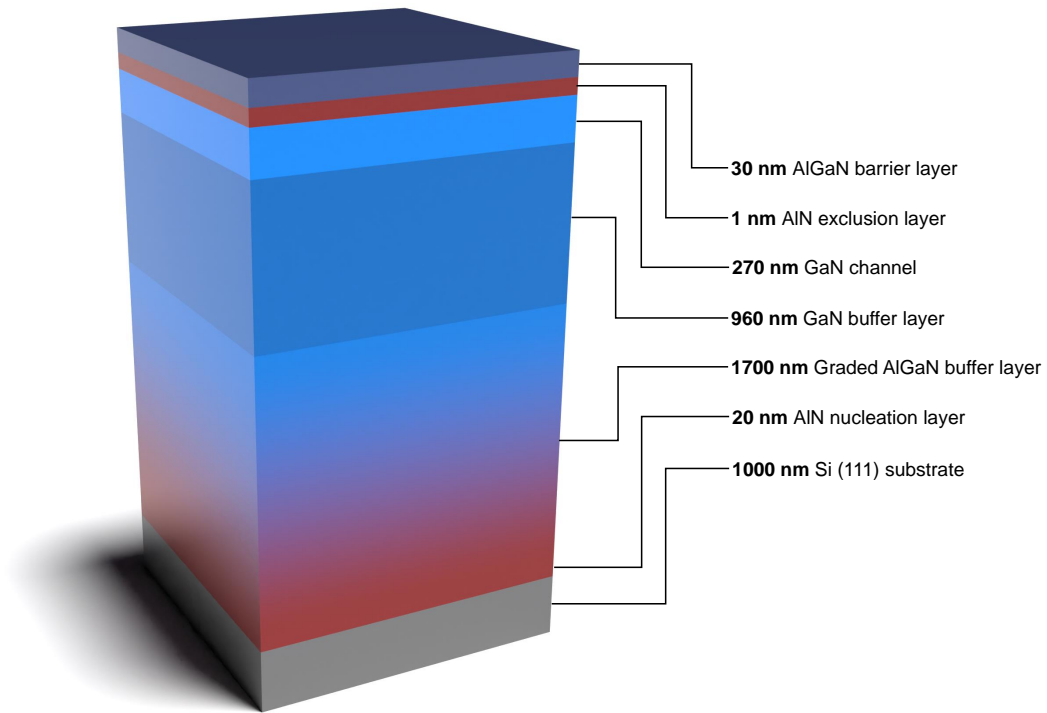


Figure 3.2: Epilayer HEMT structure grown on 1000 μm -thick Si (111) wafer used for the wafer bow experiments. The $\text{Al}_x\text{Ga}_{1-x}\text{N}$ was graded from mole fraction $x = 0.75 \rightarrow x = 0.25$. These values are an approximation from the intended growth and were not measured directly.

determined by running a series of growths with varying dosages of ammonia, whilst otherwise maintaining the same growth parameters. Figure 3.3 shows the series of epitaxy runs with ammonia predose duration as the variable parameter and measured wafer bow as the dependent variable. The wafer bow was measured from a central median surface to a three point reference plane from the perimeter of the 150 mm diameter wafers [65] which is a standard metric to compare wafers which share the standardised wafer diameter.

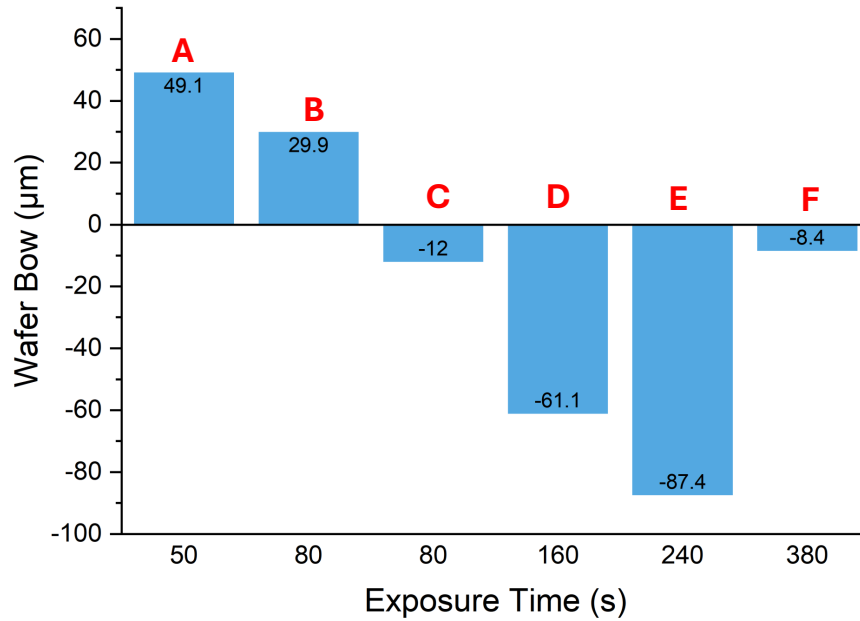


Figure 3.3: Graph of ammonia dosage given to the growth substrate for each sample labelled A to F in ascending order of duration and respective wafer bow measured by the University of Cambridge collaborators. The wafer bow measurement is defined as the displacements of the centre of the wafer from the plane created by three points on the edge of the wafer. A negative bow is denotes a concave dish-shape where as a positive bow denotes a convex shape.

3.2.1 Fabrication

The fabrication of the membranes followed the methodology presented in Chapter 2. Each of the wafers underwent the same fabrication processes in parallel to isolate the ammonia dosage as the independent variable. The exact parameters of this fabrication were as follows and applied to all five wafer types. The divergence from the standard fabrication was that a negative photoresist mask was used and so a negative resist ma-N 1410 [66] was also used. It was applied with spinner set at a speed of 3000 rpm for a duration of 60 s to achieve a film thickness of approximately 500 µm. The photoresist was soft baked on a hotplate at 100 °C for 90 s. The structures were defined with a mask aligner set to expose for 18 s, developed in ma-D5335 developer solution for 40 s and then rinsed in pure DI water. The hard mask was then formed using the RIE tool

in preparation for the ICP etch.

The mask used has a mix of different tether geometries and was chosen to see the effects on the resultant flatness of the membranes. This is illustrated in Figure 3.4 which shows a magnified section containing the repeated pattern that made up the entire array. The membranes were $100\ \mu\text{m} \times 100\ \mu\text{m}$ squares. The tethers were primarily a “straight” geometry with widths $5\ \mu\text{m}$, $7\ \mu\text{m}$, $10\ \mu\text{m}$ and $15\ \mu\text{m}$, respectively, with a third of the membranes having a tapered shape to give insight into the effect of the tether geometry. The wider tethers were expected to constrain the suspended membranes more, holding them flatter. The downside of the wider membranes is that they would require more force to be released when transfer printing.

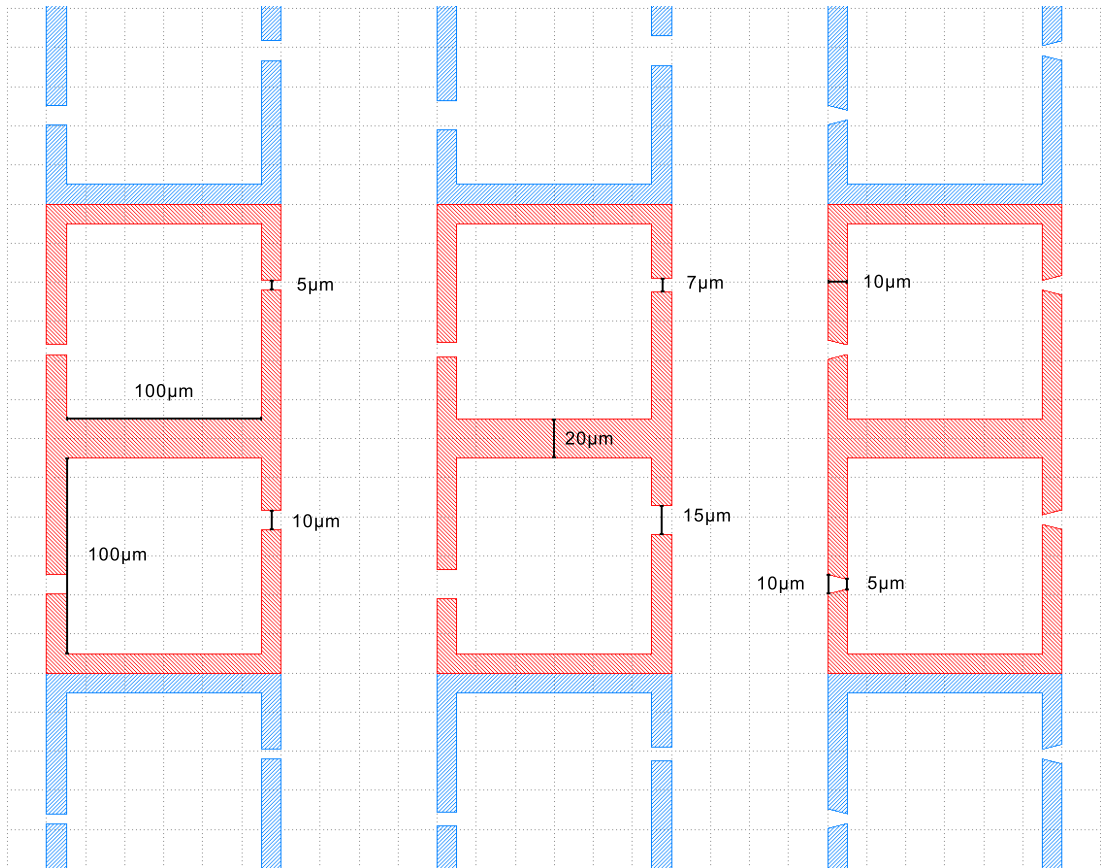


Figure 3.4: Section of the photolithography mask design in GDSII format which was used to create coupons with multiple tether geometries using the HEMT material. The repeated structure is highlighted in red with the rest of the array in blue.

For the following study, please refer to samples A-F in Figure 3.3.

In the ICP etch stage the samples were etched for 12 min to reach the silicon substrate. This duration was calculated using the last recorded etch rate of the recipe used that was 300 nm/min. After checking the etch quality using an optical microscope, as shown in Figure 3.5, it was decided to etch for a further 2 min as the bottom of the etched area should be a white colour of silicon and instead there was a dark granular pattern. The blackening observed increased with the ammonia dosage and was a layer of silicon nitride (SiN_x) created when the substrate was treated with ammonia in the growth of the wafers. This was confirmed by transmission electron microscopy (TEM) measurements [63] performed after this study was completed. The thin layer of silicon nitride would prevent the etch from completing because it was resistant to the etch chemistry used for III-nitrides. The darkened areas were originally believed to be contamination from the ICP chamber and so the issue was further investigated at the time of fabrication.

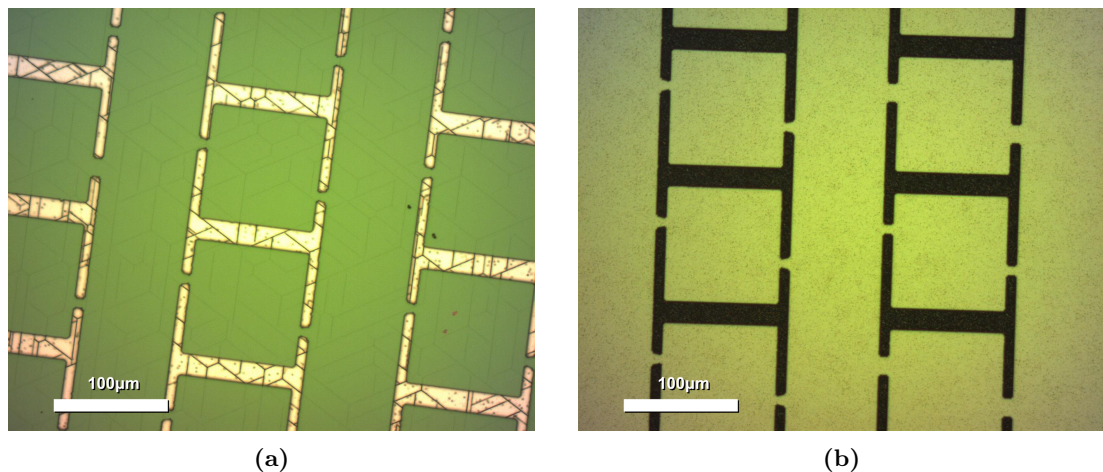


Figure 3.5: Microscope images of sample “A” (a) with the least ammonia dose and sample “F” (b) with the highest ammonia dosage after a 12 min ICP etch. The first image exhibits cracking in a hexagonal pattern from the GaN layers from insufficient strain compensation. The second image shows a darkened area of silicon nitride formed from the higher dose of ammonia which prevented the etch completion.

There was concern that the KOH solution might not be able to access the silicon substrate, due to the presence of SiN_x , when attempting to wet under-etch the membranes. A rough measurement of the depth of etch was carried out using the the

optical profiler. The samples with the lowest and highest ammonia dosages, 4889 and 4905, were measured to have etch depths of $5.8\ \mu\text{m}$ and $5.4\ \mu\text{m}$ respectively. Referring back to the epistructure illustrated in Figure 3.2 then it will be clear that the depth was more than adequate to reach the silicon substrate. The trenches were further deepened by an RIE dry etch process for silicon for 2 min to an extra depth of $4\ \mu\text{m}$ to ensure there was adequate access to the silicon substrate for the KOH wet etch.

The remaining processing steps were completed, revealing a series of under-etched membranes as shown in Figure 3.6 with quite a drastic visual variation. Most notably the low ammonia dosage sample “A” showed visible crack lines along the hexagonal GaN structure and the high dosage samples “E” and “F” showed dark speckles over the surface of the membrane increasing with ammonia dosage. The cracks in “A” demonstrate the fracture of the GaN layers on top the buffer structure due to insufficient strain compensation: with the thermal expansion mismatch of the layers during epitaxy the GaN layers were pulled apart and fractured along the weakest connection of the crystal which is between crystallographic structural planes.

3.2.2 Membrane Bow Measurements

To obtain the geometry of the membranes and measure the final bow a non-invasive method was used, based on the optical profilometer tool. This tool was chosen because AFM’s measurement range would not cover the $100\ \mu\text{m}$ width of the membranes and the Dektak stylus profilometer was too inaccurate to provide useful data.

With the hypothesis of there being a SiN_x layer formed at the bottom of the suspended membrane, there was also interest in looking at the roughness of the underside of the membrane using AFM. A smooth surface of the suspended membranes would indicate that these devices were suitable for transfer printing as they would bond extremely well: (SiO_2 deposited via PECVD is considered a smooth surface ideal for printing to as it has a root mean square roughness of $\sim 0.3\ \text{nm}$ [67]).

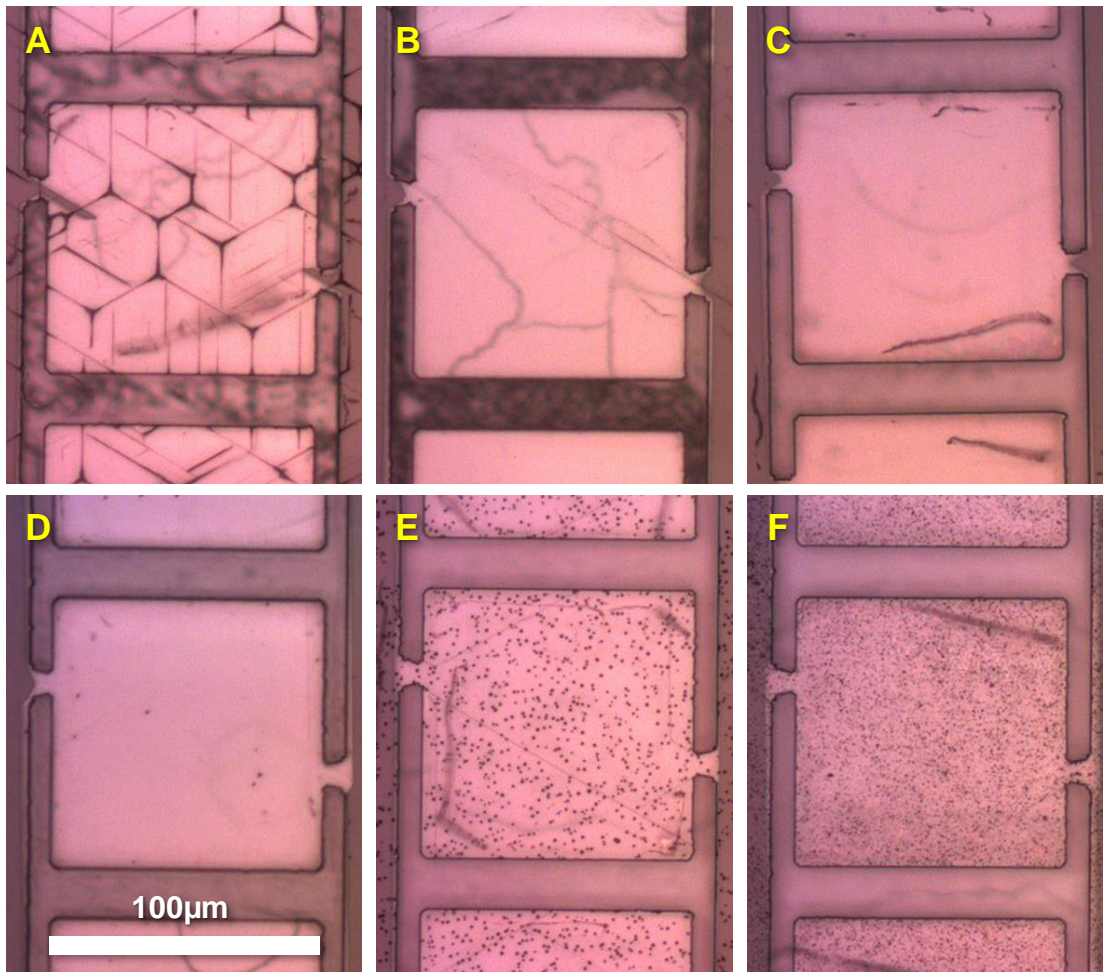


Figure 3.6: Side by side microscope image comparison of all HEMT suspended membrane samples, taken after the final silica removal process. Labels correspond to the ammonia pre-dose series in Figure 3.3.

3.2.3 Optical Profilometry

One measurement of each type of membrane and tether geometry was carried out due to time constraints, making a total of 30 measurements. The statistical significance as a result of the tether variation was unfortunately not sufficient to draw useful conclusions.

Each sample was placed in the Wyko optical profilometer making sure that it lay as flat as possible so that the height measurements were accurate. A slight tilt would be fine because the samples have areas of known flatness which the post-processing software can

correct for later. The tool was set such that only one individual suspended membrane was in the field of view for the final measurement to give a more detailed representation. For each sample type the sample was moved to focus onto a different type of tether and a measurement was taken. Each measurement consisted of an average of three scans to improve the accuracy. The data was saved in the form of an *.opd* file which contained a 3D height map in the form of a black and white image where each pixel's intensity related to the vertical height of the membrane. The 16-bit greyscale offers 65,536 levels which should be sufficient to resolve small features. A raw image is shown in Figure 3.7 which is displayed using the open source image analysis software Gwyddion [61] so it includes a scale bar, height map, and regions in which the data has been masked out in red for being out of the range of measurement (the etch trenches).

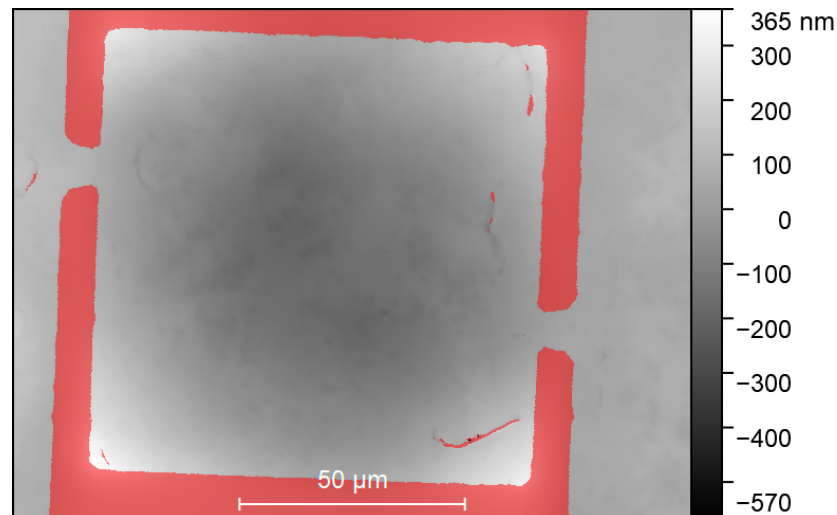


Figure 3.7: Raw image taken from the optical profiler of sample “E” viewed in the Gwyddion software. The red region is a mask automatically applied by the profiler’s software to discount any height data below a certain value; in this case it is the trench region of the suspended membrane.

3.2.4 Optical Profilometry Data Processing

The *.opd* files were each opened using the Gwyddion image analysis software and a consistent processing routine was carried out to generate comparable results for each sample type. The first process was to level the image plane such that the tilt introduced by manually setting each sample in place could be corrected. This was done by using

3. Effect of Ammonia Pre-Dose on Wafer-Level and Device-Level Flatness

the three point levelling function of the software which takes 3 manually selected 3D coordinates (x,y,z) from the image to create a plane which is the reference flat as shown in Figure 3.8. Each point is given a circular area of set 15 pixel radius to average the z -value to avoid picking a pixel with an image artefact unrepresentative of the height. This plane is then subtracted from every pixel coordinate to so that the original selected coordinates all read $(z=0)$.

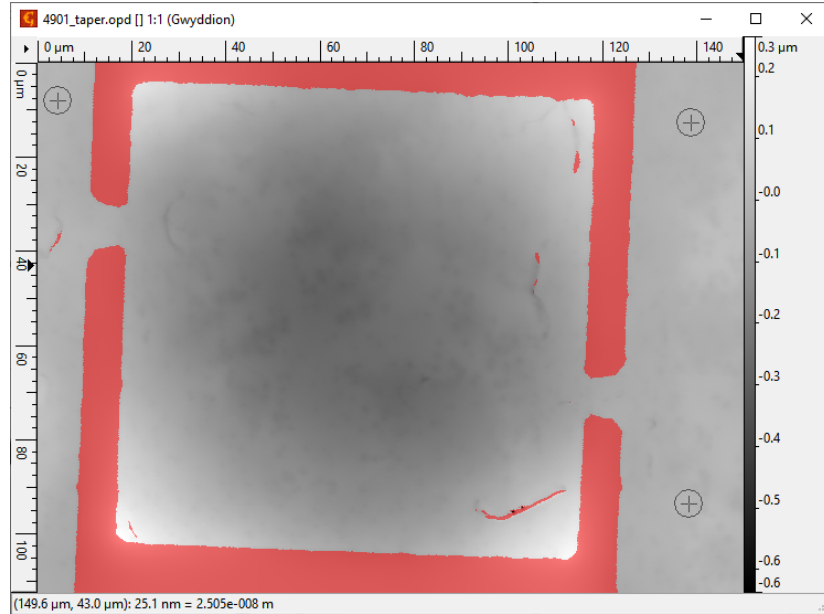


Figure 3.8: Selecting the points (black circles with crosses) on the known flats of the suspended membrane for the three point level function in Gwyddion.

The second step was to add a colourbar and set the scale to best represent the samples. A spectral colour style was added because it clearly showed different features and gradient transitions with high contrast, which is most suitable for a human qualitative assessment. This was done using another tool in the software in which a histogram of z -values is displayed with the option to select the range of values to start and end the colourbar. The stops were chosen to include each tail of the histogram and to be consistent for every sample processed so that one could easily compare one to the other. For the HEMT samples the range was set from $-0.4\ \mu\text{m}$ to $0.8\ \mu\text{m}$ and was determined by the sample with the largest height variation. The regions where the profile data should not be taken from, such as the etch trenches, were masked off so that they did

3. Effect of Ammonia Pre-Dose on Wafer-Level and Device-Level Flatness

not interfere with the profile measurements as they would contribute a large dip in height. For the HEMT samples the optical profilometer automatically detected where the height suddenly dropped and excluded the region using a mask stored in the *.opd* file. For other samples the mask would have to be manually set using the threshold tool to exclude regions below a certain height, as well as a manual paintbrush tool to draw specific locations to mask. Small defect areas were masked which included visual imperfections on the surface of the membrane as these would be interpreted as an undesirable and unrepresentative tall spike in a linear profile of the membrane. These processes are shown below in Figure 3.9.

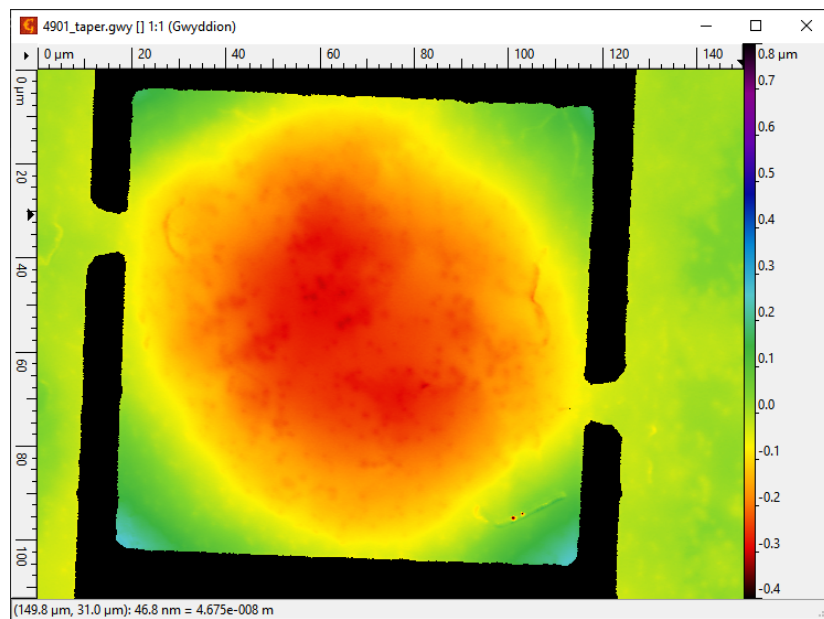


Figure 3.9: The spectral colourbar with z-range set to a suspended membrane. A threshold mask shown in black is applied to values below a certain height which was determined by the optical profilometer software.

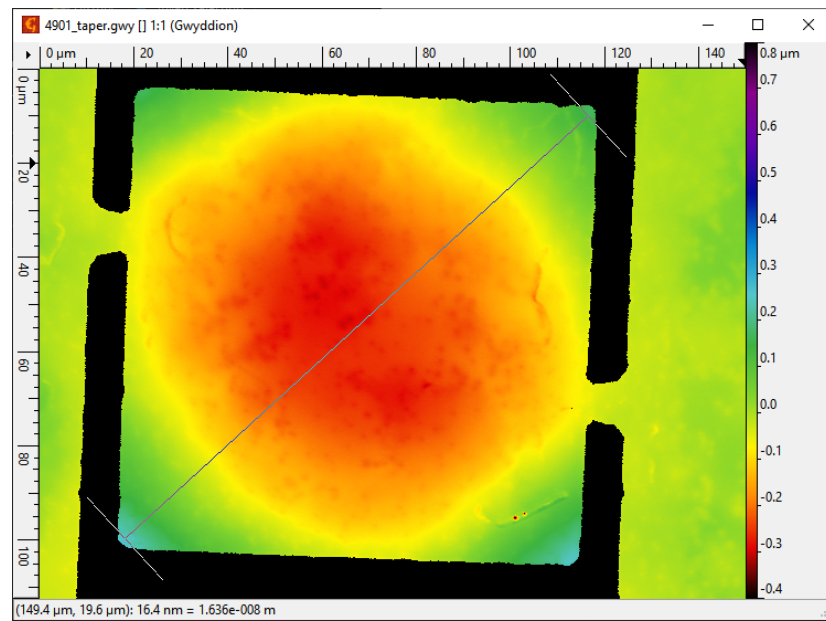
The linear profile tool was used to define a path to extract the height data from by drawing across the membrane surface as shown in Figure 3.10a. The line's width was set to average over 100 pixels to smooth the curve and avoid artefacts introducing unrepresentative spikes into the profile. The width profiled is illustrated by the perpendicular lines at either end of the profile. Areas that were masked off were ignored from the profile. From the profile window the raw data is saved as a *.txt* file which included the location along the profile as a distance and the height (both

in metres). Previously, multiple profiles had been extracted across the membrane including: vertical, horizontal, both diagonals, and tether-to-tether directions. None of these profiles were similar due to the asymmetry introduced by the tethers but it was found that the main profile selected shown in Figure 3.10a had the largest curvature due to its distance from the tethers. Conversely the tether-to-tether profiles were flatter.

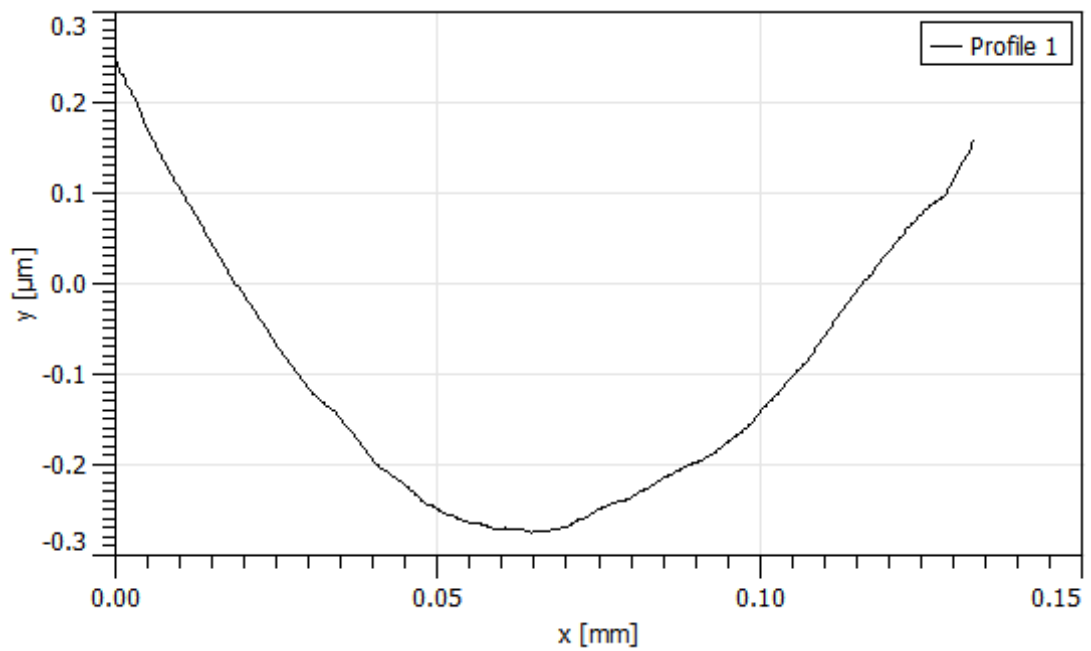
To quantify the curvature of these profiles the height change from the centre of the membrane to the highest point on the diagonal profile was measured. An extra step was done to characterise the radius of curvature (ROC) of the membrane which would give a value independent of the size of the membrane. This could be done because the membrane profiles closely approximated an arc of a circle. A Python script was written to take the batches of the extracted profile *.txt* files, extract the data points, re-plot the points, and use the data to approximate a circle using a least squares method [68, 69]. The code produced both a plot with all of the information presented on it as shown in Figure 3.11 as well as a *.txt* file containing the radius of curvature, the error, and the maximum displacement in a columnar format for the entire batch of samples. This process was done for all sample types “A” to “F” with just the tapered geometry tether types included in this work to avoid overcomplicating the study. The code may be found in appendix A.

The results from this process can be found below in Table 3.1. Sample “A” would appear to be the flattest membrane with the ROC of 17.44 mm which was 2.5 times the flatness of the next flattest sample and so was considered an outlier. This result corroborated with the visual evidence of the cracking present in the sample and so this value was rejected as a failed membrane. The samples “C” and “D” had the highest ROC and so their ammonia dosages would be optimal for further growth iterations. If there was a correlation between the wafer bow and the resultant membrane ROC then it would be expected to be nonlinear. The wafer bow decreased and then increased with the exception of sample “F” which drastically decreases. The membrane ROC increases (flatter) and then decreases respectively over the series.

3. Effect of Ammonia Pre-Dose on Wafer-Level and Device-Level Flatness



(a)



(b)

Figure 3.10: (a) The line drawn to extract the height profile of a membrane from sample “E”. (b) The resultant plot given from the profile. Here y is the vertical displacement and x is the distance along the line in 3.10a above.

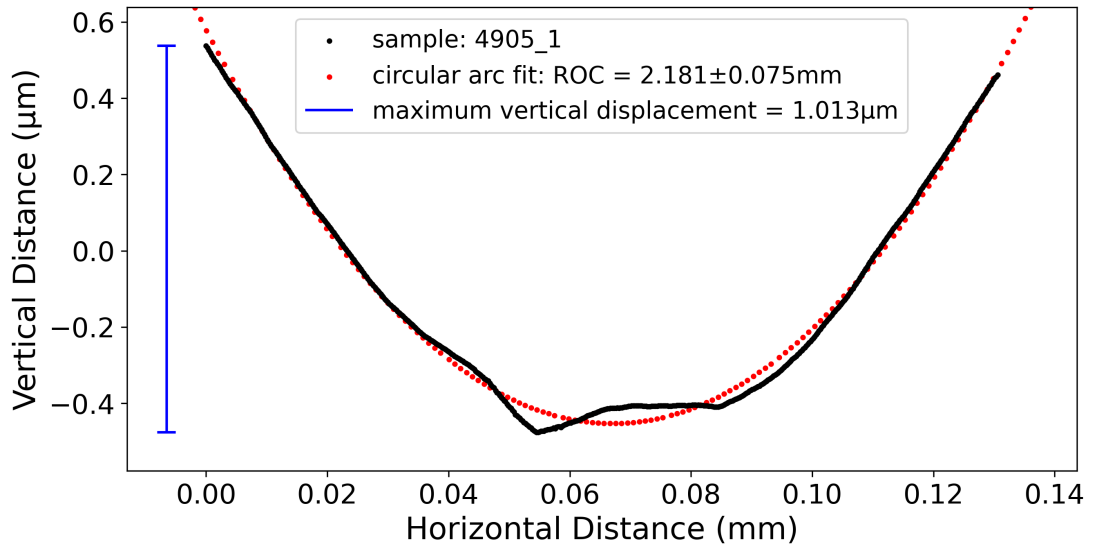


Figure 3.11: The output plot from the circle approximation Python code showing the radius of curvature of a circle fit to the profile of a membrane from sample “E”.

Table 3.1: Original wafer bow with data extracted from the diagonal linear profiles of the six HEMT suspended membranes. Note that sample “A” is an outlier due to cracking.

Sample	Wafer Bow (μm)	Max Vertical Displacement (μm)	ROC (mm)
A	49.1	0.512	17.44
B	29.9	0.820	3.22
C	-12.0	0.367	6.33
D	-61.1	0.343	6.85
E	-87.4	0.523	4.64
F	-8.4	1.013	2.18

3.2.5 AFM of Membrane Backsides

To measure the backside of the membranes they first had to be removed from their substrate and flipped over. A piece of Kapton tape was carefully lowered onto a section of the array of membranes on the sample, making sure not to apply any pressure to avoid damaging the individual membranes. The tape was then slowly peeled off from one edge to exfoliate the membranes. The tape was then flipped so that the adhesive side containing the membranes faced upwards and was mounted to a glass microscope slide using more tape to give the samples a flat rigid surface. This process was done for all six types of HEMT suspended membranes.

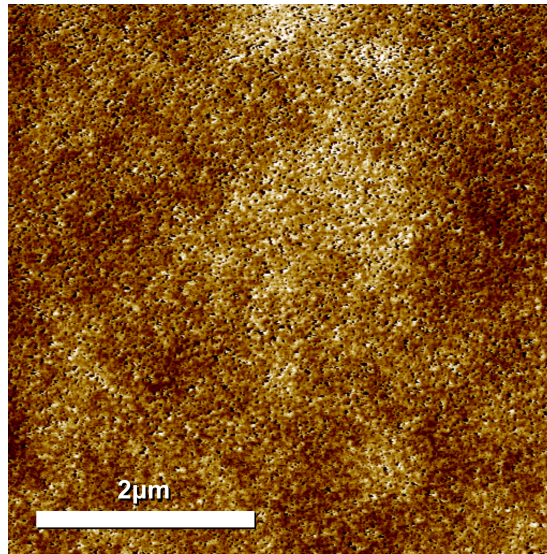


Figure 3.12: AFM image from a 5 μm by 5 μm scan of the backside of a membrane from sample “B”.

The samples were placed into the stage of the AFM and were measured over a 5 μm by 5 μm area on the centre of a membrane for each sample. The AFM exported the data as 8-bit **.tiff** images, storing the height data in the intensity of each pixel as can be seen in Figure 3.12. The now discontinued XEI software provided by Park systems [70] was used to level each image to remove any tilt and then extract the regional statistics. The root mean square roughness commonly referred to “RMS” or R_q was chosen as the best representation of the entire membrane. The RMS is the standard deviation of all the heights in the selected region, so a larger value means a rougher surface. The values measured here are shown in Table 3.2.

Table 3.2: Root mean square roughness of the backside of the HEMT material membranes.

Sample	R_q (nm)
A	1.449
B	1.617
C	2.416
D	1.502
E	1.388
F	1.528

All of the RMS roughness values were respectively low in comparison to the top-side of thin GaN films grown via MOCVD which can have their top surface R_q generally in the range 3 nm to 60 nm [71]. Personal experience of successfully printing similar GaN membranes to a silica substrate with R_q of ~ 0.3 nm [67] would indicate that these membranes would also be successful for printing.

3.3 LED Systematic Bowing Study

With the results taken from the HEMT study, our collaborators at the Cambridge Centre for Gallium Nitride were able to design and produce a typical LED epistructure using the buffer structure developed from the optimal HEMTs. These would better represent the bows expected for devices for integration into the target hybrid devices. A series of dummy wafers was produced initially to have the reactors conditioned for LED growth. When restarting a a different type of device growth the reactor chambers are relatively unstable due to containments from the previous growth recipe. When a clean and stable growth atmosphere is developed in the chamber from repeated growth cycles, high quality thin films can be produced with the high accuracy for structures such as the quantum wells inside an LED. For the purposes of the morphological study intended, the optoelectronic performance of the devices did not matter. Later iterations with a bespoke design would be used for any performance studies. Two LED wafer epistructures were provided and are illustrated in Figure 3.13. These are referred to as wafer sample 1 and 2, respectively, to be consistent with the publication that was a result of these findings [1].

The sole difference between these wafers is that sample 2 includes a SiN_x dislocation blocking interlayer in the centre of the n-GaN epilayer. The purpose of a dislocation blocking layer is to reduce dislocation density in the device's active layers by preventing dislocations progressing upwards though the epistructure. The uniform structure allows for a more efficient device.

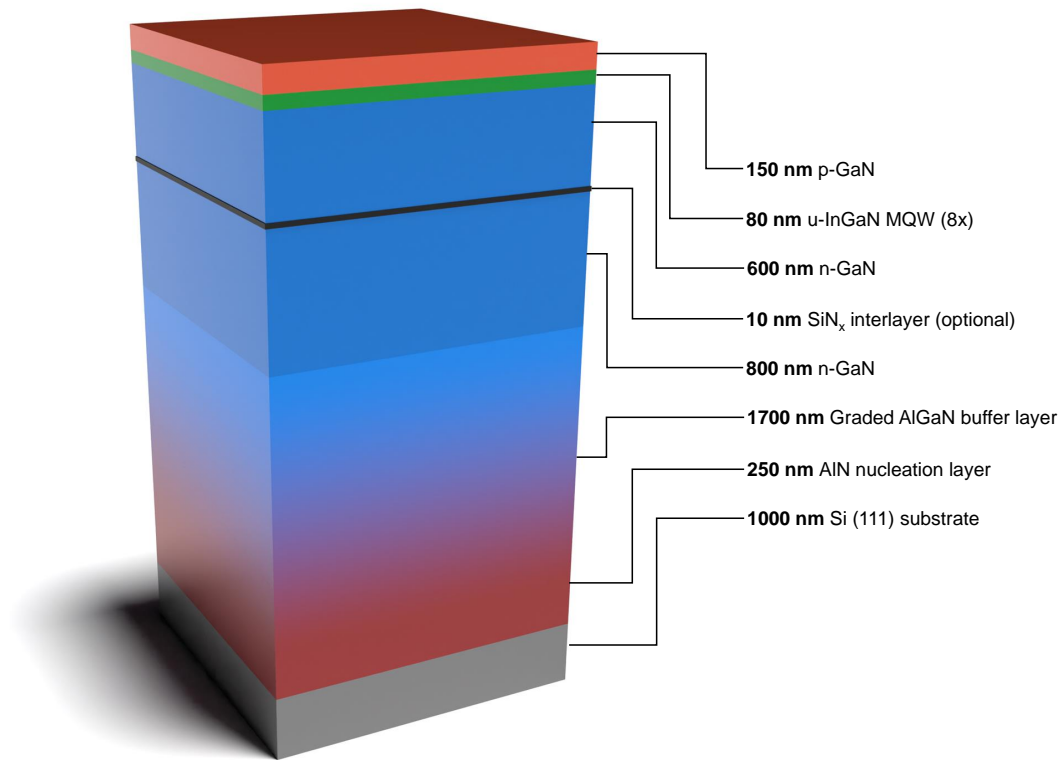


Figure 3.13: Epilayer LED structure grown on 1000 μm thick Si (111) wafer. Sample 1 and 2 follow the same structure as in this image but 2 has the inclusion of a 10 nm SiN_x dislocation blocking layer. These values are an approximation from the intended growth recipe and were not measured directly.

3.3.1 Fabrication

Both samples were processed in accordance with the the method outlined in Chapter 2, exactly the same as for the HEMT samples in the previous section and using the same mask. The only variation is that the ICP etch time had to be increased to account for the thicker epilayer structure. The resulting suspended membranes are shown in Figure 3.14.

As can be seen from the above figure, the material formed clear suspended membranes with minimal fabrication defects such as cracks or malformed photolithography. Both samples appeared to have a darker section around the edge of the membrane. This

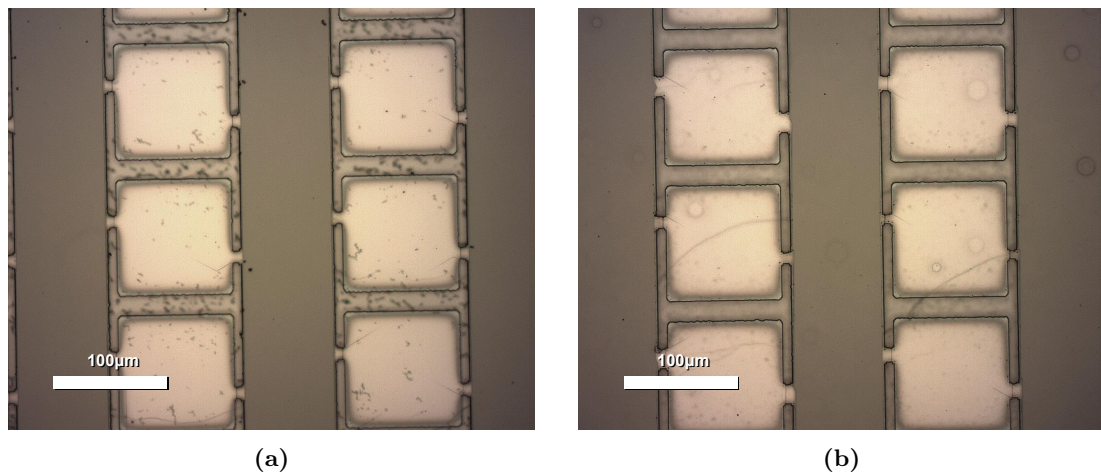


Figure 3.14: Microscope images of the LED suspended membranes after the last fabrication step, (a) sample 1, and (b) sample 2.

band was only present when looking at the suspended membranes, as when they were later transfer printed the dark region disappeared. The origin of this feature has not been resolved.

To add a comparison, a third GaN-on-Si LED wafer (sample 3) material provided by the commercial manufacturer Plessey Semiconductors Ltd was processed along with the other two wafers in parallel. The epistructure of sample 3 is unavailable due to the proprietary nature of the commercial material but it is an approximately 2.5 µm thick GaN epistructure on top of a Si (111) substrate. As the Plessey capability was created by acquisition of a University of Cambridge spin-out company formed by the group with which was collaborated with, it can be assumed that there are many similarities between the structures. The patterning photolithography was identical but the ICP etch step was shorter due to the thinner structure. Most notably a lot of the strain-countering buffer structures are not present in this sample and what follows will demonstrate why they will be necessary for transfer printing applications.

In the fabrication of the LED membranes another mask was used, in parallel with the original, which had a larger tether taper geometry. When it came to the KOH under-etch the new geometry prevented the etch progressing as it formed an etch stop. As the angle of the taper was close to the 120° angle between the {111} planes it caused

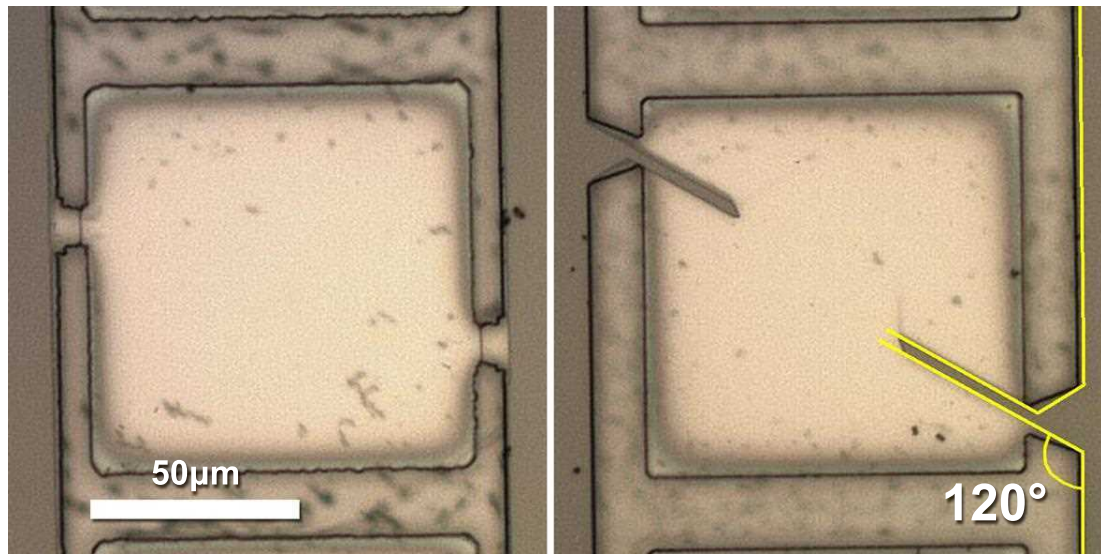


Figure 3.15: Microscope image side by side comparison of two suspended membranes from sample 1 using a different tether geometry. The larger taper tethers on the right show how each creates an etch stop for the KOH wet etch as they are close to the 120° angle between $\{111\}$ planes. This leaves the un-etched stick protrusions in the middle of the membrane shown in the right hand image.

the etch to stop and follow this direction instead which left the stick-like protrusions of un-etched silicon beneath the membrane as shown on the right hand side of Figure 3.15. With a straight geometry (not tapered) tether the KOH etch proceeds much quicker as it does not have to counteract newly formed etch stops which the tapered geometry would otherwise create. Reducing the time in the KOH etch is ideal as it mitigates damage to the membrane.

3.3.2 Transfer Printing of the LED Devices

To test if the membranes behaved as viable printable coupons, both samples were transfer printed to a SiO_2 -on-Si substrate receiver. It became apparent that the membranes could not be released from the tethers shown in Figure 3.16a. A grid was produced on a piece of silicon wafer using photoresist to create three distinct areas to print the samples to. There was a section for samples 1, samples 2, and for the commercial wafer. This was done as a quick method for easily and reliably identifying samples from different platforms on the common host substrate.

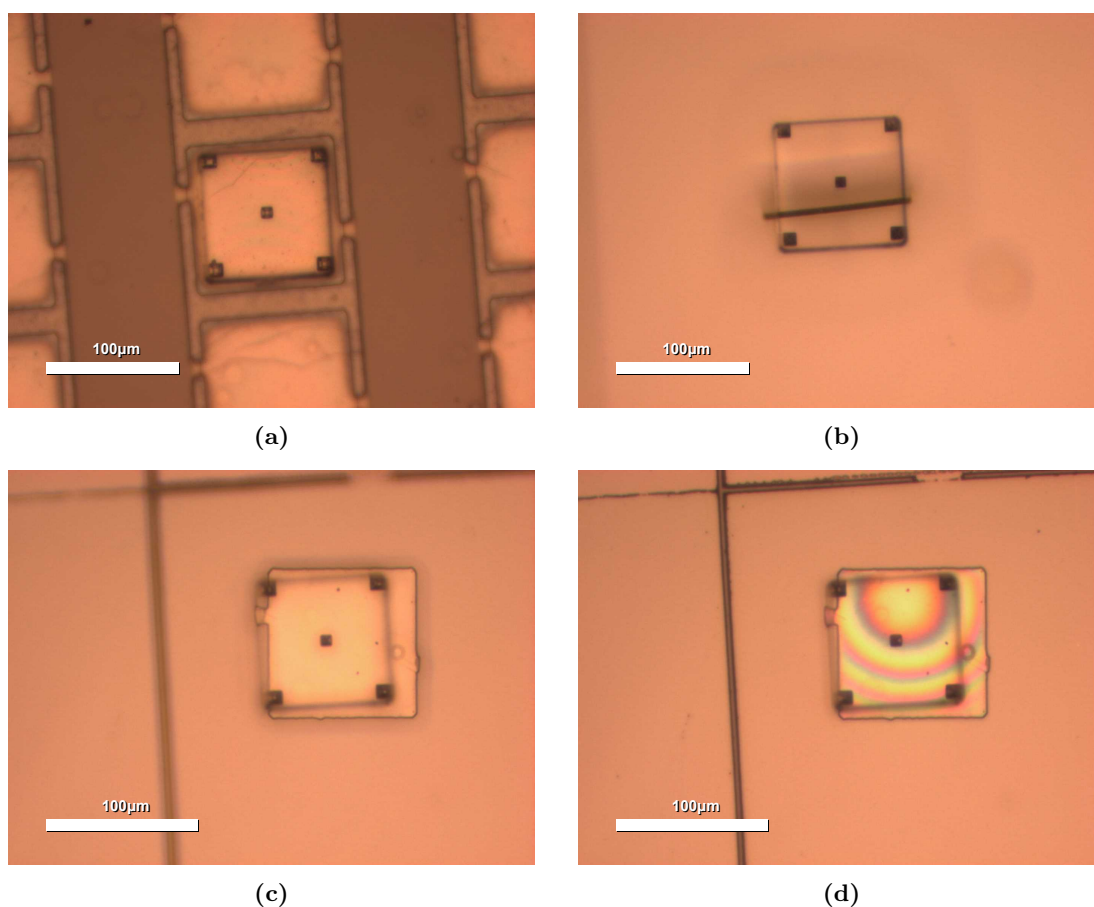


Figure 3.16: Images taken through the optical column of the transfer print tool showing (a) the pick-up in contact, (b) a vertically dangling membrane from an erroneous pick up, (c) a membrane on the stamp ready to print, and (d) a membrane in full contact with the receiver ready to release from the stamp.

Multiple unsuccessful attempts were made to make satisfactory prints from all of the samples. Samples 1 and 2 were both difficult to pick up due to the excessive thickness of their tethers ($3.59\ \mu\text{m}$). Sample 3 on the other hand was relatively easy to release because of the $2.5\ \mu\text{m}$ thick tethers that the transfer print method was designed for. In both cases the extreme difficulty came from the samples sticking to the stamp too well and not printing to the receiver surface. The samples should easily transfer once a contact was made but instead they were lifted back up once the stamp was retracted. At other times the membrane would make full contact with the full surface of the stamp and not de-collapse to just be held by the pyramid structures. This would be caused by the top surface of the membranes being too smooth. The high membrane underside

smoothness determined from the previous section's AFM measurements would not create a sufficient bond with the receiving substrate to compete with adhesion to the PDMS. Due to time constraints only a small number of membranes from each sample were successfully printed onto a single receiver as shown in Figure 3.17. This figure gives a clear demonstration of Newton's rings in which an interference pattern of concentric rings is created when a curved and planar surface meet [72, 73]. The distance of a light band from the centre is proportional to the square root of the radius of curvature of the curved surface meaning that the wider spaced bands of sample 1 and 2 imply flatter membranes.

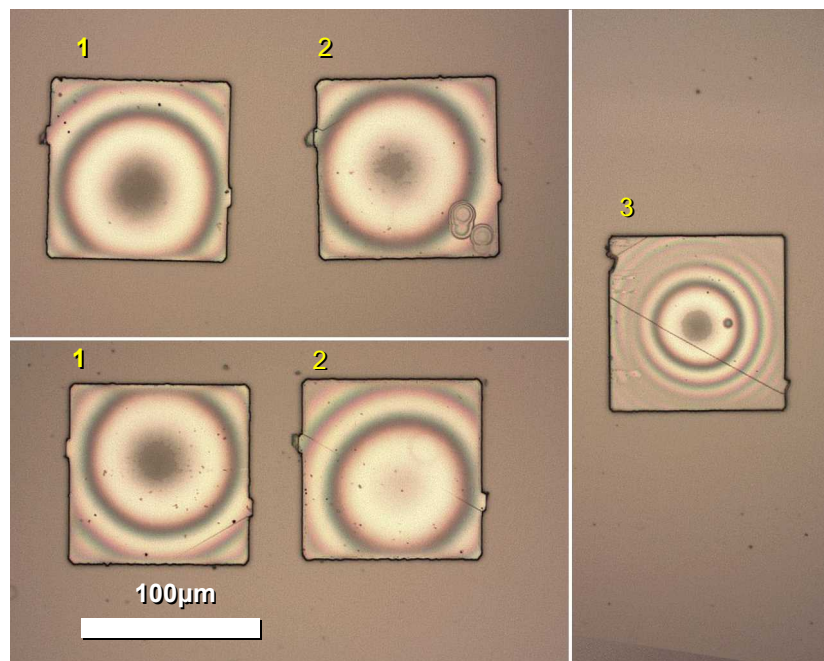


Figure 3.17: A composite image of all the membrane samples transfer printed onto a SiO_2 substrate. The examples shown here are respectively labelled with their wafer sample numbers.

3.3.3 Topography Measurements

Following the sample routine as with the HEMT samples, all three LED samples were measured using the same optical profilometry technique. 10 measurements of each sample were taken from different sections of the array of suspended membranes to best characterise the sample. The 5 printed membranes in Figure 3.17 were also

measured.

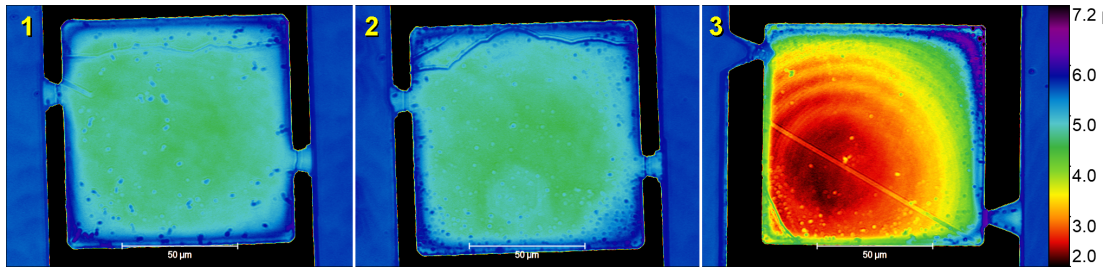


Figure 3.18: Side by side comparison of suspended membranes from all three sample types using optical profilometry with a false colour scale representing height in (μm).

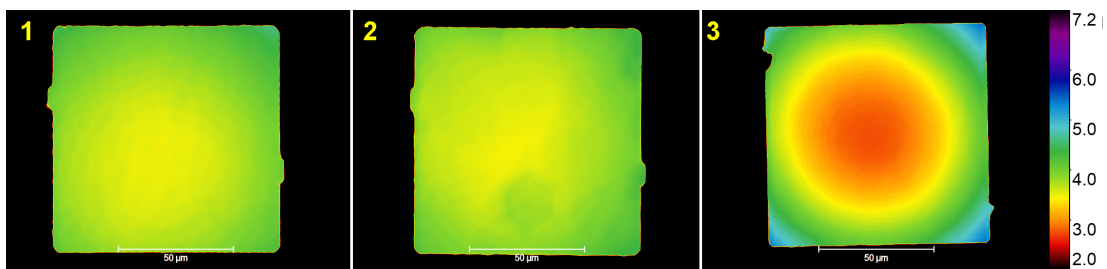


Figure 3.19: Side by side comparison of transfer printed membranes from all three sample types using optical profilometry with a false colour scale representing height in (μm).

Gwyddion was used once again to process the raw data to extract the linear profiles and then the Python script was used to find the radius of curvature from each measurement. The values were compiled and a mean and standard deviation was calculated for each sample. The data summarised in Table 3.3, clearly shows that sample 1 and 2 with the buffer structures were much flatter with their larger radii of curvature. When printed the radii increased by roughly 50% for both samples 1 and 2 which is likely to be caused by the release from the tethers as well as the attraction to the planar receiver surface when printed. Sample 3 from the commercial source did not change within experimental error when printed and so must be very resistant to flattening from external forces. This is made even more obvious when comparing the images from the optical profilometry with false colour scale bars in figures 3.18 and 3.19.

Between sample 1 and sample 2 there was little discernable improvement in the radius of curvature of both the suspended membranes, both being approximately 2 mm.

Table 3.3: The mean values of radius of curvature (ROC) for each sample type and the respective standard deviation (σ) for both suspended and transfer printed membranes calculated from a profile taken from the corner-to-corner diagonal direction.

Sample	Suspended		Printed	
	Mean ROC (mm)	σ (mm)	Mean ROC (mm)	σ (mm)
1	1.80	0.12	2.98	0.36
2	2.13	0.33	3.13	0.38
3	0.84	0.05	0.88	0.03

When transfer printed to a flat surface the radius of curvature improves, increasing by approximately 50 % to 3 mm each. The major comparison comes from comparing to the commercially available GaN LED epistructure on a Si (111) substrate. Sample 3 had a radius of curvature of 0.84mm, approximately half of the other two samples.

3.4 Summary and Discussion

From the series of six HEMT wafer types, sample ‘‘C’’ produced the flattest suspended membranes when all were processed in parallel. The measurements were taken using optical profilometry, extracting a linear profile from the diagonal corner-to-corner direction. The radius of curvature was extracted by approximating the profile to the arc of a circle using a least squares fit Python script to provide a quantitative metric for each sample. Sample ‘‘C’’ had a radius of curvature of 6.33mm and a backside RMS roughness of 2.416nm measured using AFM which were the best values out of the set and corresponded to an ammonia dosage time of 80s. This research was used to develop further growths relating to the work in this thesis as well as other publications which may be found in Appendix B [1, 63, 74].

The former publication [1] utilised the optical profilometry measurements of the two epilayer structures in this chapter with the finite element simulation software COMSOL to be able to predict the internal strain present in GaN-on-Si wafer structures. The experimental data was used to train the model and would discover strain estimates of roughly 4×10^{-10} . This would suggest that the material undergoes a plastic deformation

when transfer printing. The second publication [74] used this work in developing the flatter GaN-on-Si as a starting point for their material regime as it could provide devices which would be transfer printable.

The observation of the SiN_x layer formed from the ammonia dose provided insight into the fabrication. Too little SiN_x and the GaN structure would fracture, too much and the ICP would struggle to etch through to the substrate cleanly.

The second systematic study compared two almost identical LED epistuctures, with one having a SiN_x interlayer in the n-GaN region to block dislocations. Both samples were fabricated into suspended membranes in parallel alongside a third GaN-on-Si (111) LED sample from a commercial source for comparison. The membranes were processed and measured identically to the HEMT structures with the data processing also being the same. In addition, some of the membranes were also transfer printed to a flat surface to assess their curvature in this scenario. It was revealed that both bespoke grown samples had similar radii of curvature of 1.80 mm, and 2.13 mm for the sample with the interlayer. When transfer printed the samples flattened having radii of 2.98 mm and 3.13 mm respectively - an increase of approximately 50%. The third commercial sample was much more curved having a radius of curvature of 0.84 mm when suspended and 0.88 mm when printed. These results proved that the engineering of the buffer layers to counter the internal strain of the epistuctures is vital to produce flat coupons suitable for transfer printing. In addition, it was made clear that tapered geometries for membrane tethers were unsuitable for the KOH under-etch process on Si (111) as the geometric angle of the tapers approximate the slow etching {111} planes causing the etch to stop and leave stick-like protrusions of Si beneath the membranes. This last observation prompted a more detailed study of tether geometries presented in Chapter 4.

Chapter 4

Membrane Tether Design and PDMS Stamp Release Process

4.1 Overview

To achieve the ultimate goal of constructing a stacked hybrid device such as an RCLED, the transfer print method has to be reliable and repeatable with good accuracy. The electrical contacts must align, with each layer being seated flat against each other to form a functional device. The current methods relying on reversible adhesion of the suspended membranes are not consistent in the retrieval from the original substrate or deposition to the intended final destination as is evident from previous attempts in Chapter 3. This printing method is controlled by the adhesive forces between the polymer stamp and the contact surface of the membrane, and the underside of the membrane to the receiving substrate which are dominated by Van der Waals forces [2, 31]. These forces are determined by the adhesiveness of the PDMS polymer stamp, and the surface roughness of the membrane and printing surface. During the pickup phase, these adhesive forces are competing with the bond strength of the semiconductor tethers of the membrane to the surrounding mechanical structure.

In this part of the study a variety of tether geometries were tested to find the best design which created transfer printable membranes with a high yield. The number

of tethers suspending the membrane was also varied from one to four to test the distribution of support. Furthermore the widths of these tethers were varied to find the best compromise between membrane support and ease of release. The assessment was done by transfer printing 10 membranes per configuration and noting the success of both pick-up and release printing to a silica surface. In addition, the adhesiveness of the PDMS stamp was varied by altering the mixing ratio of base to crosslinker to find the optimal stamp formulation and performance.

The Heidelberg DWL66 laser lithography tool allowed for custom tether geometries to be prototyped and iterated on a time scale much shorter than traditional mask aligner based processing. Python scripts were written to facilitate the creation of the graphic design system (GDSII) files required for the operation of the DWL66. Using the custom grown LED material mentioned in Chapter 3, an array of suspended devices were created with varying tether geometries to find the optimal configuration.

With these results an optimal tether geometry for the GaN-on-Si epistructure material was generated using the aforementioned Python scripts which would allow for consistent suspended membrane fabrication as well as pick up from the donor substrate. A new tether shape which is predominantly straight with a central breakpoint ensures that the KOH under-etch does not terminate prematurely on an Si {111} plane. A section which narrows to 2 μm wide allows for the membrane to break free easily whilst not being so weak as to collapse during the fabrication. Future devices could now be fabricated using this particular material with confidence.

4.2 Custom GDS File Creation Using Python

The Heidelberg DWL66 tool offers fine alignment and control of feature size and geometry but requires a *.gds* file of GDSII format to create an exposure job and define a pattern. A Python module called GDS Helpers has been developed to generate photonic waveguide geometry using scripts [75]. The first tutorial shows how to create a waveguide as shown in Figure 4.1a which acts as an introduction to the syntax of creating the objects known as “Polygons” which make up the geometry of the final GDS

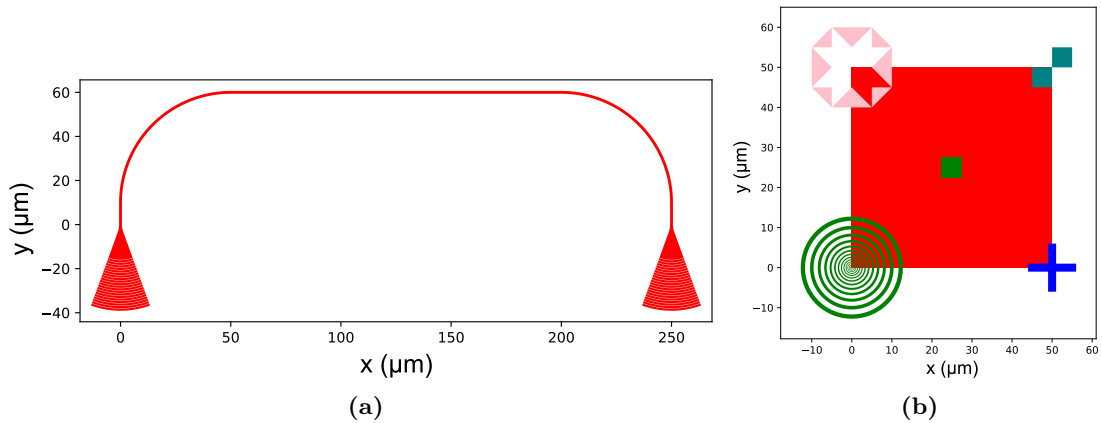


Figure 4.1: (a) Output of the GDS Helpers tutorial Python script showing a waveguide with two grating couplers. (b) Output of a Python script to experiment with available markers. These images are scalable vectors but the output GDSII stores the lengths (μm). The capabilities of the GDS Helpers was not satisfactory in itself to generate masks for transfer printable devices.

which is illustrated in Figure 4.2. These Polygons are added to a layer object which can be separated out in the DWL66 conversion software to make a single job. The layers are added to cells which may be saved as a *.gds* file at the end of the script. Multiple cells can be created per GDSII which themselves contain multiple layers. In the generation of an exposure job, cells can be included or omitted depending on the desired outcome giving flexibility to a single file. A script was created using the predefined markers in the GDS Helpers module to experiment with potential shapes for future use as alignment markers as shown in Figure 4.1b.

The GDS Helpers module was not designed for creating arrays of membranes because of the limiting nature of geometries and node system it used; instead it would generate components integral to photonic integrated circuits such as waveguides—sets of lines of varying widths terminating in grating couplers as in Figure 4.1a. GDS Helpers heavily utilises the Shapely module which offers a much more fundamental approach to creating shapes which could then be turned into the GDSII files using code from the former module [76, 77]. Using resources from both modules, many iterations of scripts and functions were compiled into a set suitable for membrane fabrication which allowed for the complete control of the geometry of a membrane, the array size and position as well as the tethers. A more developed version of the script used to create the various

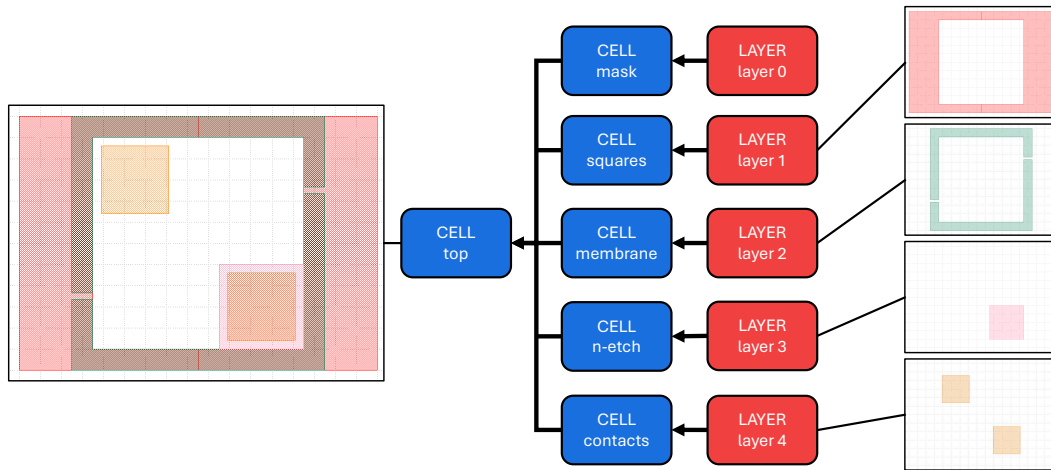


Figure 4.2: Schematic diagram showing the hierarchy of the GDSII format used to create the mask geometries for full LED fabrication. The Polygon objects are added to a specific LAYER (red) which can be enabled or disabled in the GDSII editing software such as KLayout. The layers are added to individual CELL objects (blue) which can be selected in the laser lithography tool software. The CELLS are grouped into one main CELL to be converted into the GDSII format as a single *.gds* file.

tether geometries may be found in Appendix A.

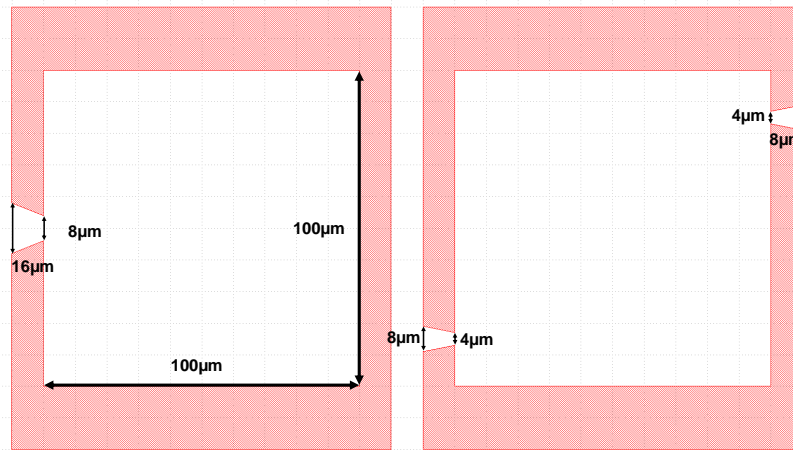


Figure 4.3: A close up of the GDSII output from a Python script to create membranes of varying tether widths and number. Both have a total contact length of 8 μm where the tethers meet the membrane.

The script was used to generate a GDSII that produced 13×57 grids of $100 \mu\text{m} \times 100 \mu\text{m}$ sized membranes with variable tether parameters. The number of tethers

was changed to 1, 2, and 4, and the total cumulative contact between the tether and membranes was changed to be 4 μm , 6 μm , 7 μm and 10 μm respectively. This is best illustrated in Figure 4.3 where one can see that the contact width to the membrane is divided amongst the number of tethers. Thus, for example, 16 μm for one tether and 8 μm each for two tethers. The idea of this was to investigate both the tether number and the total contact width. Having the contact strength distributed between four points may have given flatter membranes.

4.2.1 Membrane Fabrication Using the Heidelberg DWL66 Tool

Three samples of material were prepared from the already diced sample 1 LED wafer with the normal cleaning and silica deposition steps described previously. Positive S1805 photoresist was spun on to create a 500 μm thick layer. The DWL66 tool was then used to expose the geometries defined in the GDSII files, with each sample containing three 13×57 arrays of membrane styles with the same number of tethers but of varied widths. The samples were then processed into suspended membranes following standard processing defined in Chapter 2. The grouping of membrane styles caused many of the samples to fail because the KOH wet etch duration appeared to be dependent on the thickness of the tethers as is shown in Figure 4.4. The tethers should have been grouped so that each sample contains the same width of tethers instead of the same number. This would have allowed for all membranes to be under-etched without damaging the more delicate designs by altering the etch duration as required.

4.3 PDMS Stamp Ratio Adhesion Measurement

A study was also done to compare the PDMS mixing ratio in its ability to pick up and release the membranes. The recommended mixing ratio of PDMS to cross-linker is 10:1 [58] but based on prior experience with transfer printing it was found that this ratio may be too adhesive and prevent release. Ratios of 6:1, 8:1 and 10:1 were chosen as 8:1 had been a preference in past prints and so would make a good median value for the series of tests. The stamps were prepared using the same mould, mixed and allowed to

cure for the same duration so that the only difference was the mixing ratio.

An alternative method for curing the PDMS was investigated by using a vacuum oven to heat the mixture which reduced the time required for a full cure. At 150 °C and atmospheric pressure the curing took 10 min instead of the usual 48 h at 20 °C [58]. The increased temperature, however, also increases the Young's modulus of the resultant PDMS meaning that it is firmer and less sticky, independent of the mixing ratio [59]. This method for curing was therefore found unsuitable for the creation of transfer print stamps as 'stickiness' is required for the reversible adhesion transfer.

4.4 Transfer Print Measurement

As mentioned above, the premise of the experiment was to test each configuration of stamp ratio and tether type ten times each to gather enough data to be significant. Due to the unpredictable nature of transfer printing one had to set rules with printing so that each attempt was consistent. Time constraints limited the study to ten attempts per combination as there would already be 360 print attempts in total (3 tether variants \times 4 tether contact widths \times 3 PDMS stamp ratios \times 10 tries each). Each attempt consisted of locating a fully supported membrane with all tethers attached, slowly coming into full contact with the stamp head using 1 μm steps towards the end, and releasing by pulling the stamp away 100 μm in one fast step. If the membrane came away with the stamp then this was classed as a 'successful' pick up.

The second step was the print in which the stamp holding the membrane was moved over the receiver and brought down so the membrane was in full contact with the receiver similar to the first part of the pick up. The stamp was then slowly moved away. If the membrane remained on the surface of the receiver then the print was deemed a success. If there were no fully supported membranes then the attempt was deemed a failure.

The three samples were mounted to the aluminium sample plate of the transfer print tool, alongside a prepared section of silicon coated in a layer of silica to act as the receiver. The results obtained are summarised in Table 4.1.

4. Membrane Tether Design and PDMS Stamp Release Process

Table 4.1: Success rate of transfer printing suspended membranes with varying tether number, total tether width, and stamp PDMS mixing ratio with 10 attempts each. Tether width was measured cumulatively and is split evenly between the tether number, i.e. a tether number of two with a cumulative width of 4 μm will have two 2 μm tethers.

Tether Number	Total Tether Width (μm)	PDMS Ratio:	Pickup Success			Print Success		
			6:1	8:1	10:1	6:1	8:1	10:1
1	4		0.8	1	1	0	0	0
	6		1	1	1	0.1	0	0
	8		1	1	1	0.1	0	0
	10		1	1	1	0.1	0	0
2	4		1	1	1	0.3	0.3	0
	6		1	1	1	0	0	0.1
	8		0	0	0	0	0	0
	10		0	0	0	0	0	0
4	4		0	0	0	0	0	0
	6		0	0	0	0	0	0
	8		0	0	0	0	0	0
	10		1	1	1	0	0	0

From the experimental results it appears that the performance of the transfer print tool is low across all configurations which reflects the issues described in previous chapters. The *pick up success* can be seen to have been best with the single tether, followed by the two tether variant. The four tether membranes were almost entirely collapsed and missing from the substrate because the individual tethers were too small. The four tether, 10 μm total contact width, had 2.5 μm wide tethers which just survived the KOH etch and were able to be picked up. The *printing success rate* was very poor, however. Only one or two membranes out of the ten attempts would print in the best configuration which was the double tether with the lower 6:1 or 8:1 PDMS ratio. The 10:1 PDMS ratio was too sticky to allow the membranes to release. From this overall analysis the two tether and 4 μm total contact width using a 8:1 PDMS stamp would be the best option.

Observations over the entire sample revealed low yields of suspended membranes for certain configurations or lower quality membranes as shown in Figure 4.4. Every sample with 4 μm total contact width had the majority of the membranes missing or collapsed

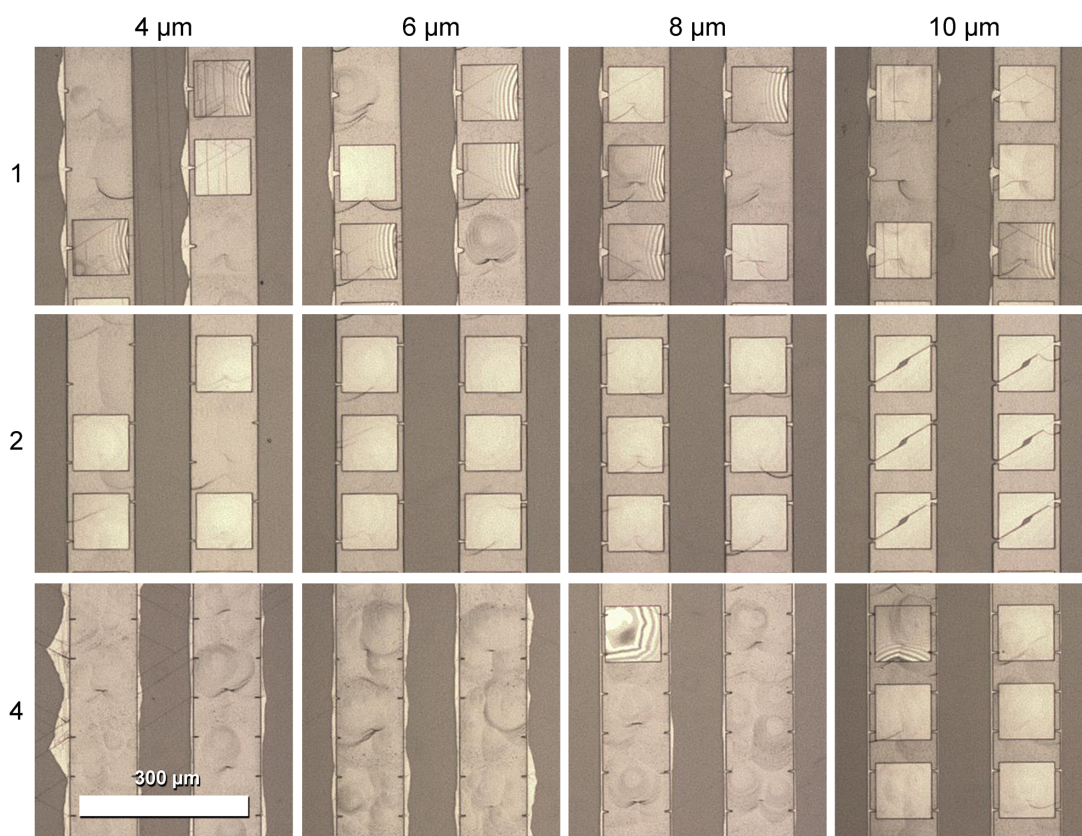


Figure 4.4: Microscope images of all the final suspended membranes with varied tether geometries giving a representation of the fabrication quality. The total contact width of tether to membrane increases along the horizontal and the total number of tethers increases down the rows.

meaning that it was difficult to find suitable devices to attempt to transfer print.

The single tether, 6 μm total contact width membranes also had a low yield, with many collapsing due to insufficient support. The two tether membranes had perfect yield and were also very easy to pick up with all stamp PDMS ratios and were the best of the variants. The four tether variants were completely lost with no membranes to pick up, the 1.5 μm wide tethers being too thin to support the membranes during the KOH etch and were washed away.

The single tether, 8 μm total contact width membranes had a relatively high yield and were removable but also picked up a lot of the tether and supporting material too. This would be unsuitable for hybrid devices that have restricted printing areas and so this

combination is not recommended. The two tether variants also had a high yield but were extremely difficult to pick up. The tethers were too strong for the conventional pick up method and only broke free when excessive force was applied downwards onto the membrane and so these were not suitable for device designs.

The single tether, $10\ \mu\text{m}$ total contact width had a high yield but the asymmetrical resistance to release caused a few membranes to flip such that they were only held by one edge making them impossible to print. The two tether variants did not fully under-etch and so were impossible to pick up. The four tether variants were very good with clean breaks at the end of each tether and a high yield. The four tether variant would be an option for further development as this had high yield and success in retrieval.

4.5 New ‘Bow Tie’ Tether Development and LED Fabrication Python Scripting

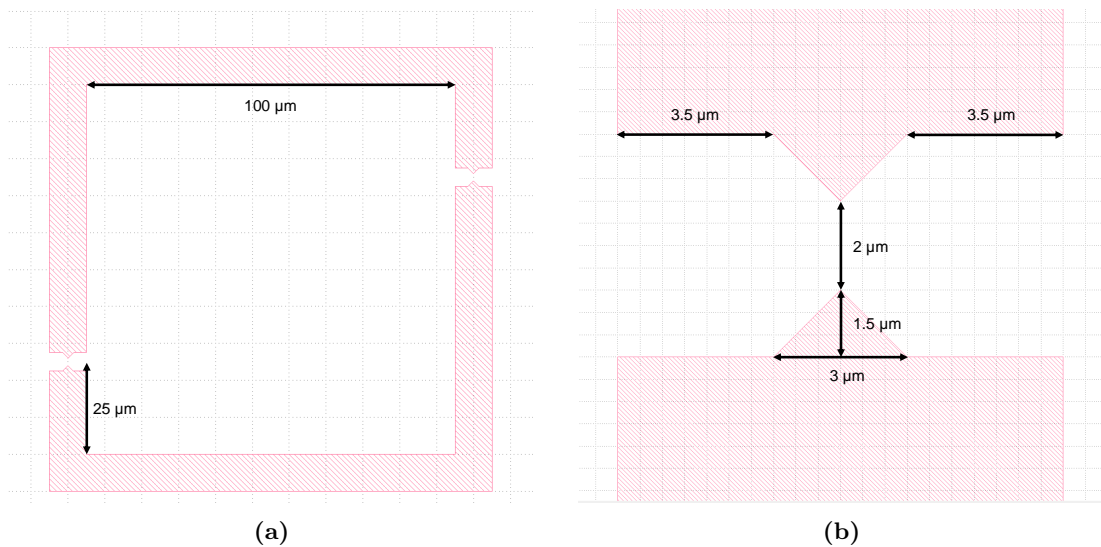


Figure 4.5: (a) A close up image of a single device using bow tie tethers. (b) The geometry, location, and the specific geometry of the tether itself.

The aforementioned Python script to produce suspended membranes was further adapted to generate customisable arrays of membrane geometry that included the optimal tether geometries that were discovered. Two styles of tethers were to be

produced in alternating columns of the array. One would have two tethers with the optimal straight tether geometry being $10\ \mu\text{m}$ long and $3\ \mu\text{m}$ wide. The other style, shown in Figure 4.5, built upon this by including a weak spot for the tether to break free in a consistent location. As shown, the $5\ \mu\text{m}$ wide tether narrows to $2\ \mu\text{m}$ in the centre with 45° tapers to avoid the 30° angle that causes the under-etch to fail (see Figure 3.15).

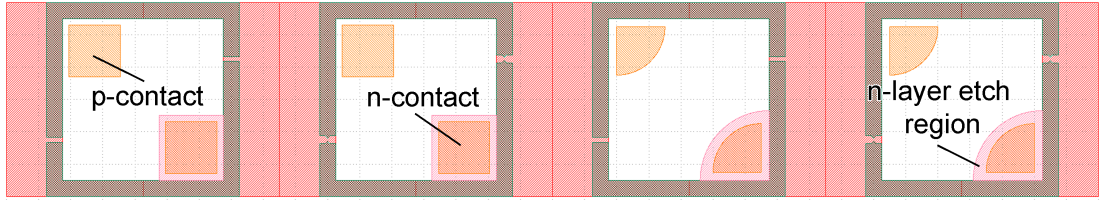


Figure 4.6: GDSII output of Python script containing all geometries required to create a suspended LED device.

The Python script was taken a step further to be adapted to include all mask geometries required to fabricate a suspended LED device. Etch regions for the negative contact were included as well as regions to apply the gold electrical contacts as shown in Figure 4.6. This functionality was added in preparation for the fabrication required for the full assembly of a hybrid device. This script can be found in Appendix A.

4.6 Summary and Discussion

The original design for the tethers supporting the suspended membranes had proven to be too difficult to break using transfer printing because the device layers were made thicker to approximately $3.5\ \mu\text{m}$ with the inclusion of the extra buffer layers to improve device flatness. A new, optimal geometry was therefore determined by systematically fabricating a series of suspended membranes with different tether numbers and sizes and attempting to print 10 of each. The ideal combination was found to be two tethers, each being $3\ \mu\text{m}$ wide, for this particular GaN LED material as it gave consistent device pick up as well as high yield in fabrication. The printing of the membranes was still unsuccessful, however, due to the stickiness of the PDMS dominating over the attractive forces between the membrane and the receiving substrate. Further research is therefore

needed to improve transfer printing yields. An improvement in stamp design with the ability to activate and deactivate the adhesion would vastly improve the process.

The Python script used to create the custom tether geometries was further adapted to produce arrays of suspended membranes as well as the full geometries required to fabricate an LED which would be needed to create the coupon for a hybrid device. A new bow tie tether geometry was generated in which a 5 μm wide tether tapers to 2 μm in the centre with a 45° angle. This should provide a weak point for the membranes to be released in a consistent location as well as avoid the issues arising from the tapered geometry approximating the angle between the silicon slow etch planes discussed in Chapter 3.

Chapter 5

DBR Membrane Fabrication for Transfer Printing

5.1 Overview

To construct a complex cavity-device such as an RCLED a transfer printable Distributed Bragg Reflector (DBR) coupon would need to be fabricated. This chapter summarises the work done to achieve this, including the characterisation of materials as well as the iterated fabrication methods required to create a transfer-printable coupon that meets the desired specifications. Different configurations of photolithography using both mask aligner and laser lithography exposure methods were used.

Two types of DBR material were supplied by collaborators at the University of Cambridge, with 5 and 10 repeated quarter-wave thick layer pairs designed to make 60% and 100% reflectivity mirrors respectively. The material utilised a porous GaN structure to lower the refractive index of the alternate layers [36]. This approach created multiple challenges in fabrication from it being both a relatively novel and delicate material. Two major issues were: the tether thickness being too large and the silica sidewall being insufficient to provide protection from the KOH under-etch step. The reflectivity was measured before and after the fabrication using a Filmetrics white light reflectometer to gauge the effect of the processing.

Two stage lithography was employed to selectively thin the areas of the DBR tethers so that they might break more easily. The laser lithography struggled with properly exposing the resist for the second lithography process due to the non-planar surface defocussing the beam. The mask aligner proved to be the best fabrication method as it more consistently exposed the photoresists. The resultant suspended DBR membranes were transfer printed to PDMS receiver substrates to prove their viability as printable coupons. The techniques developed here hold value for others intending to process epilayer nitride wafers on silicon substrates.

5.2 The Mesoporous GaN DBR Material

The DBR material provided by our collaborating group at Cambridge was used partly because it would be an appealing combination of new material and fabrication process. The material exhibited high reflectivities of $\sim 99\%$ and $\sim 60\%$ in reflectance measurements by the growth team at Cambridge, achieved with relatively low repeated layer counts because of the high refractive index contrast. Penetration depth into the DBR mirror is proportional to the layer count and refractive index contrast, so greater reflectivity at this lower layer count could enable smaller cavity length resonant devices [5]. The material was also provided with a Si (111) substrate so that it was possible to release it using the transfer printing method.

The material came as two half-wafers of 150 mm diameter, one grown with 5 repeated pairs of high refractive index GaN and low refractive index porous GaN, and one with 10 such pairs. These were tailored in thickness to reflect light in the 460 nm region but there was a lower confidence in their efficacy or structural integrity due to them being an early run for the Cambridge group's reactor. Upon visual inspection it was clear that the 10 layer structure was extremely fragile and had delaminated DBR layers in the outer regions of the wafer which can be seen in Figure 5.1b. The epistructure would be grown similarly to the previously mentioned LED structures and so there would have internal strain maintaining the flatness of the wafer. There were still many more iterations and modifications to growth parameters required to create a wafer



Figure 5.1: (a) The 5 layer DBR wafer material and (b) the 10 layer DBR wafer material as received from the Cambridge collaborators. The 10 layer structure showing clear delamination and flaking due to the stresses of growth shattering the GaN DBR layers. The wafers are each 150 mm in diameter.

that would be considered high quality. The material itself did not behave exactly as expected physically, or optically. The layered structure did not etch satisfactorily with damage to the repeated layer structure meaning that the process of under-etching devices repeatedly failed. Also, the optical measurements of reflection and transmission with the device did not coincide with a commercially available equivalent. Multiple attempts were made to produce a suspended DBR coupon, adjusting the standard suspended membrane fabrication process to work for this novel material.

5.2.1 Structure of the DBR Material

The layer structure diagram in Figure 5.2 shows the standard quarter wavelength stack distributed Bragg reflector structure provided, i.e. each layer thickness is one quarter of the target wavelength of light in that medium. The functional layers consist of non-intentionally doped (nid) GaN for the high refractive index layers and porosified n^+ -GaN for the low refractive index layers [36]. The indices were estimated from literature [36] to be 1.88 and 2.48 for the porosified and non-porosified GaN, respectively, for 450 nm light. Buffer layers identical to those used in the LED growth are used to keep the wafer from bowing and unfortunately would later prove to exhibit a challenge to fully etching the devices. The growth substrate once again is silicon

(111) which allows for the under-etch process to release the devices as suspended coupons.

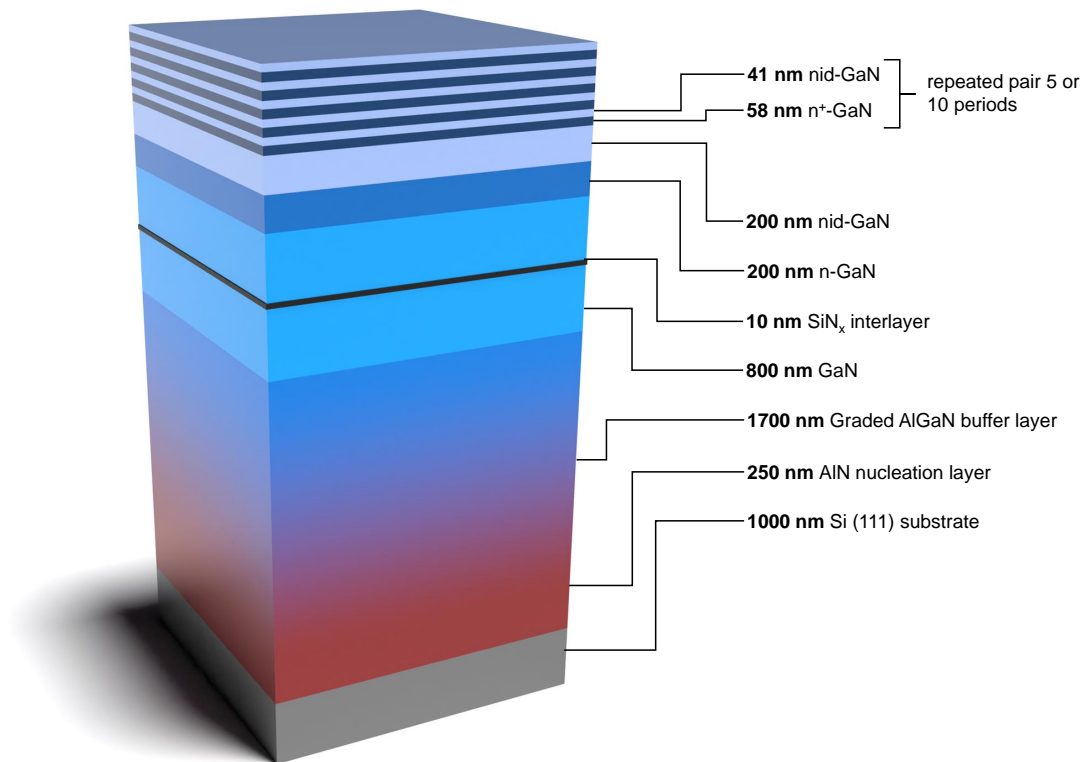


Figure 5.2: Layer structure design for the DBR material before the porosification of the n⁺ layers, with primary reflectance band centred on 460 nm. Material grown and provided by the University of Cambridge.

5.3 Optimising Microfabrication for Porous GaN DBR Material

The optimised process for defining structures on the GaN DBR material with photolithography was achieved mostly through an iterative process, starting from the standard fabrication for GaN LED material because of the structural similarities. Most of the epilayers were identical in these two structures and so it was thought that only the duration of the individual fabrication processes would need to be altered using an

iterative method. Variations in tooling and materials as well as minor human-induced error can all have a great effect on the outcome of microfabrication processes. This section outlines the various approaches made to create a transfer-printable coupon of the DBR device material.

5.3.1 Single Stage Photolithography Suspended Membrane Fabrication Using Mask Aligner

The initial approach for processing the DBR wafer material followed what was previously done for the LED membranes but with extra considerations for the ICP etch requiring different etch durations. The 5 layer and 10 layer structures were diced into $16\text{ mm} \times 12\text{ mm}$ samples. This size was chosen to increase the number of rectangular samples fitting the photolithography mask pattern intended to be used, as shown in Figure 5.3. These samples were large enough to comfortably accommodate an array of 80×80 (6400) devices of size $100\text{ }\mu\text{m} \times 100\text{ }\mu\text{m}$ with a 1 mm margin. Ideally the margin would be larger to prevent edge-effects from the photoresist spinning interfering with the mask design. Dicing was preferable to the cleaving method to minimise the risk of the DBR layers separating and flaking off as some of the 10 layer material had already done.

The following processing of the material followed the standard GaN-on-Si membrane process which was illustrated in the flowchart in Figure 2.1. The location of each piece in the original wafer was noted so that the devices could be compared and referenced to the initial measurements done by the growth team at Cambridge. A centrally located sample was taken from each wafer type and the back side silicon face was scribed with an arrow denoting the primary orientation flat direction to ensure proper lithography alignment, as well as a numeral denoting the number of layers: *X* for 10 and *V* for 5. The diamond tipped scribing tool leaves a superficial mark on the back without damaging the epilayer device structure or compromising the device strength whilst also being resistant to all of the subsequent processing operations.

The samples were then three-stage solvent cleaned, dried and oxygen plasma ashed

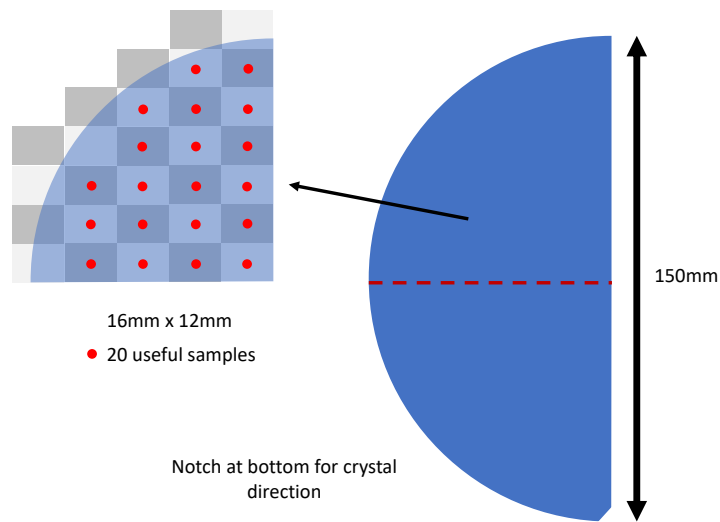


Figure 5.3: Schematic diagram showing the dicing of the DBR half-wafers.

at 250 °C for 5 min to remove any dirt or protective coatings from the surface of the material. This is the point at which the white light reflectometry measurements were taken to assess the pre-fabrication spectra, as the material would be at its cleanest state without of any foreign materials which would alter the spectra.

A 990 nm layer of SiO₂ was deposited onto both samples and two plain silicon ‘witnesses’ (for reference) using the PECVD tool. With HMDS used as a primer, a 500 μm thick layer of the positive photoresist Microposit™ S1805 was spun onto the surface of each sample. Once soft baked at 115 °C for 60s, each sample was exposed for 2.8s on the mask aligner with the aforementioned mask. The samples were then developed in a solution of equal parts Microposit™ developer concentrate and deionised water for 35 s.

The resulting lithography was observed to have adequate quality for further processing as shown in Figure 5.4 and this was confirmed to be true for the entire surface of both samples. The strong contrast between areas of photoresist and areas without, and the crisp straight edges of the pattern, suggested that the parameters chosen were viable. There was concern that the DBR material may have reflected extra light back

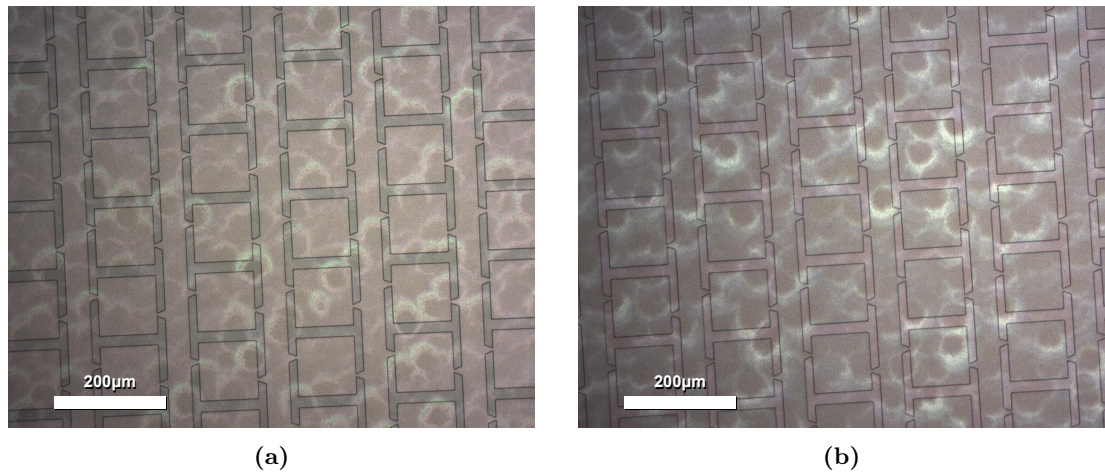


Figure 5.4: Microscope images using 10× objective lens to assess the quality of the photolithography on the (a) 5 layer and (b) 10 layer DBR samples.

through the photoresist causing a failed exposure but this proved to not be the case. The samples were then etched using the RIE tool to form the silica hard mask and the excess photoresist was removed.

The next step diverged from the normal fabrication process used for LED material because the total epistructure above the substrate was much thicker (3645 nm and 4140 nm for the 5 and 10 layer DBR, respectively) and used unusual porous material with unknown etch properties. Hence, a scrap piece of DBR material was patterned with silica covering half of the sample such that the ICP etch would form a measurable ridge. At the time of this work, the most recent recorded etch rate for the ICP GaN etch recipe was 450 nm/min which would make the required duration to fully etch each sample 8 min 6 s and 9 min 12 s, respectively. This etch rate was dependent on the condition of the ICP chamber, whether it had recently run a clean cycle or had maintenance performed, so it was advised to measure a test sample to confirm the current etch rate.

The test pieces, samples and witness were etched in the ICP for an initial duration of 8 minutes to stop just short of reaching the silicon on the 5 layer sample. A generous duration was used initially because this particular recipe had previously recorded etch rates as low as 300 nm/min for GaN based devices. The samples were removed and

5. DBR Membrane Fabrication for Transfer Printing

set aside whilst the test pieces were further processed. The test pieces had the silica masks removed using the RIE silica etch and the recently formed ridge was measured using the Dektak stylus profilometer. Three measurements were taken over a 600 μm scan distance for each 5 layer and 10 layer test sample to create an average and can be summarised in Table 5.1.

Table 5.1: Measured ridge height on DBR test pieces after being ICP etched for 8 min.

Sample	5 Layer	10 Layer
Ridge Height (nm)	1143.8	962.9
	1038.9	1006.7
	935.0	960.0
Average (nm)	1039.2	976.5

The 5 layer and 10 layer DBR sample results implied an etch rate of 129.9 nm/min and 122.1 nm/min, respectively, which was much lower than expected. The main samples were measured similarly including the silica hard mask which was kept for future etching if required, the results being shown in Table 5.2.

Table 5.2: Measured ridge height on DBR samples after being ICP etched for 8 min including the height of silica hard mask.

Sample	5 Layer	10 Layer
Ridge Height (nm)	3720	3378
	3933	3319
	3722	3228
Average (nm)	3791	3308

The silicon witness was measured on the Filmetrics white light interferometer which gave a reading of 360 nm, meaning that ~ 630 nm of material was removed. This value could then be assumed to have also been removed from the silica on the DBR samples too as they shared the same ICP run. So the height measured by the Dektak profiler would be the combination of the silica height 360 nm plus the depth of the etch into the GaN layers. A schematic diagram to aid in visualising this can be found in Figure 5.5. The actual etch depths were calculated to be 3431 nm and 2948 nm for the 5 and

10 layer samples, respectively. This puts the etch rate in the ICP to be 429 nm/min for the 5 layer sample and 369 nm/min for the 10 layer sample. However, due to the changing epilayer structure it was predicted that the true etch rate for the following layers would be closer to the 5 sample as these comprise AlGaIn. The 5 layer sample etched faster than the 10 layer one, and as the only difference was the top porous GaN structure it must be assumed that this is the cause. The porous GaN material may be resistant to the physical etching due to its sponge-like structure absorbing the kinetic energy of the etch ions.

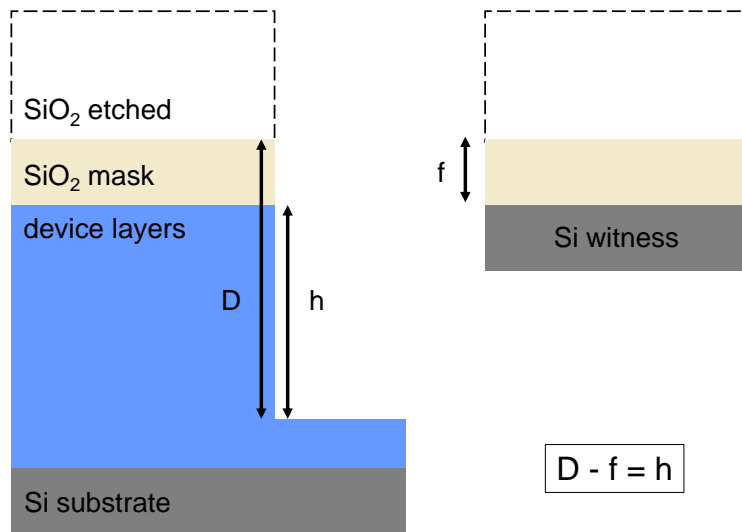


Figure 5.5: Schematic diagram illustrating the measurements taken of an ICP etched sample and Si witness to find etch depth h . The Filmetrics reflectometer measurement of SiO_2 thickness remaining on the witness f is subtracted from the total ridge height D measured on the sample using the Dektak stylus profiler.

The devices were returned to the ICP dry etching chamber for a further 1 min for the 5 layer device and 3 min 12 s for the 10 layer device. These times were calculated from the estimated remaining device thickness and the recently calculated etch rates. Both were then returned for an extra minute in the ICP after a quick visual inspection. The witness SiO_2 measured 285 nm, and the 5 layer structure was measured to have an etch depth of 3490 nm using the same method previously described. At this point the

10 layer structure was fully etched but the 5 layer one required an extra 2 minutes to complete, bringing the total etch times to be 11 min and 12 min 12 s for the 5 and 10 layer samples respectively.

RIE was used to etch further into the silicon to create an access point for the KOH etch. A sidewall protection layer of silica was deposited using the PECVD tool. A duration of 23 min produced a thickness of 1015 nm on a plain silicon witness sample and a cumulative thickness of 1148 nm on the witness used in the ICP etch processes.

The KOH wet etch was prepared in the standard configuration detailed in the processes section 2.10. The DI water was kept at 80 °C in a waterbath for the post-etch rinsing to minimise thermal shock which could potentially destroy the delicate suspended devices. The reaction was allowed to proceed for 50 min after which the samples were removed for visual inspection. The time was decided using the lower end of the usual duration for a GaN-on-Si under-etch using KOH with these set parameters. The visual inspection carried out with the microscope may be seen in Figure 5.6. As can be seen there was still silicon present underneath the devices after 50 min, more so on the 10 layer sample. Both samples were returned to the KOH solution for 5 min more, and then for 7 min 30 s for the 5 layer sample and 10 min for the 10 layer sample. From the observations in previous fabrication runs, this under-etch would have progressed much more effectively with straight tethers.

The remainder of the silica was estimated to be 113 nm thick by measuring the silicon witness with the Filmetrics tool. With the RIE silica etch recipe then etching at the rate of 25 nm/min both devices were etched for 5 min alongside the witness to remove all remaining silica. With the witness now measuring 0 nm it was assumed that the devices were also free of silica.

The final suspended devices shown in Figure 5.7 appear to be promising for the 5 layer devices with crisp clean edges at the upper surface focus and a mostly white silicon substrate visible in the trenches on the lower surface focus. The 10 layer sample looked poor in quality with extreme darkening in both the edges of the devices and the trenches. This darkening was noticed previously in Figure 5.6 as it progressed from the

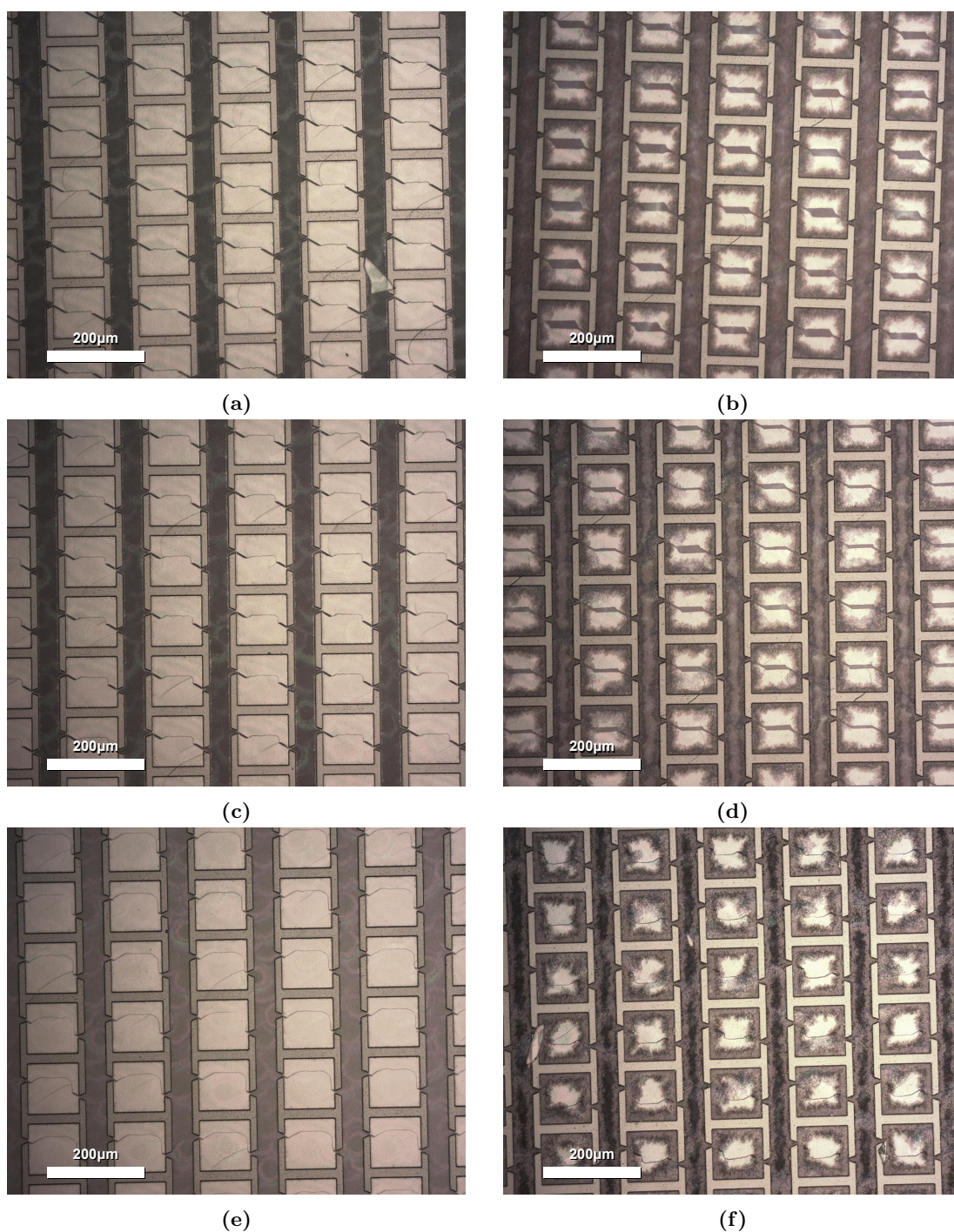


Figure 5.6: (a), (b) Visual inspection of the KOH under-etch progression at 50 min. (c), (d) Inspection at 55 min. Final inspections at (e) 62 min 30 s and (f) 65 min. The 5 layer sample on the left, and 10 layer sample on the right.

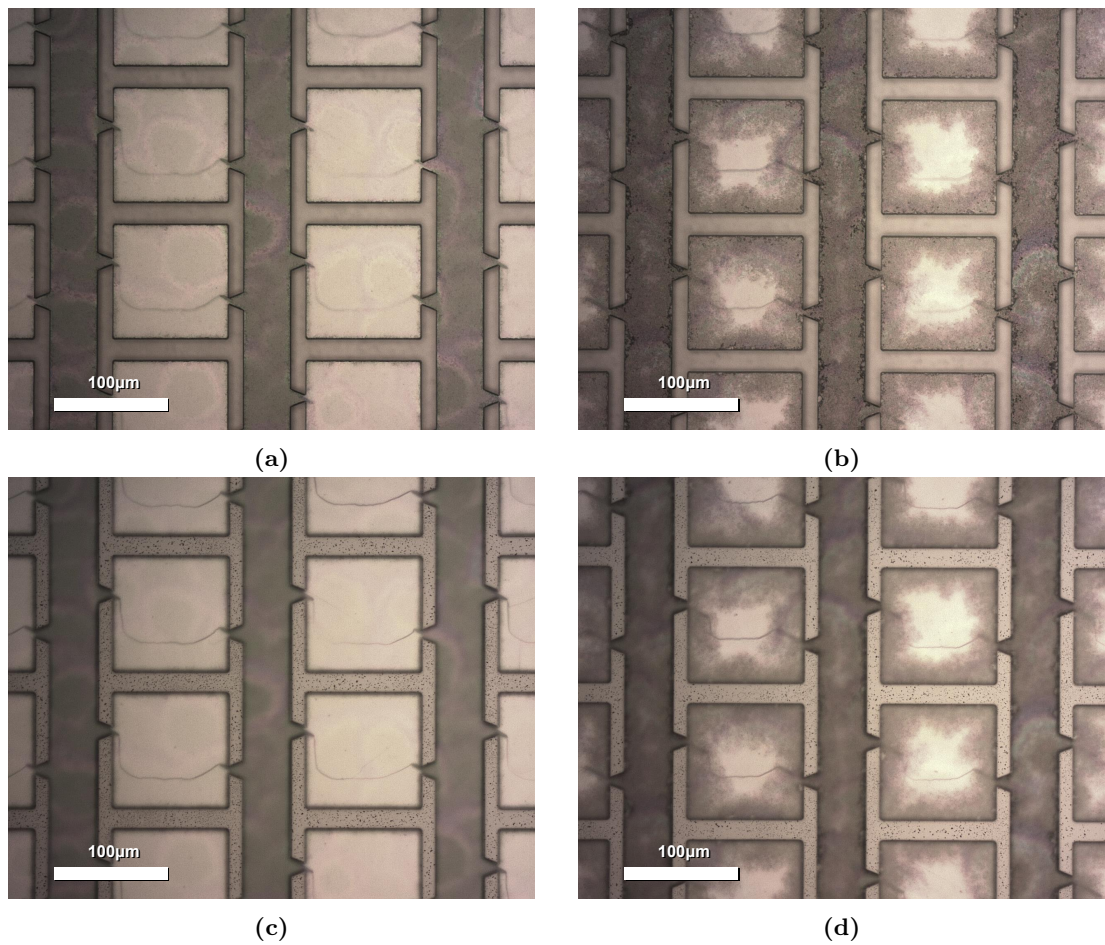


Figure 5.7: Final visual inspection of the DBR membranes after the removal of the silica sidewall protection. (a) 5 layer top surface focus, (b) 10 layer top surface focus, (c) 5 layer substrate surface (silicon) focus, (d) 10 layer substrate surface (silicon) focus.

edges towards the centre of the devices. It was theorised that the KOH had managed to penetrate the porous structure of the DBR from the sides in this case.

The 10 layer devices were imaged using scanning electron microscopy to give a better perspective on the morphology. The images produced such as in Figure 5.8 confirmed the suspicions that the DBR material had been attacked by the etch while leaving the other non-porous layers unaffected.

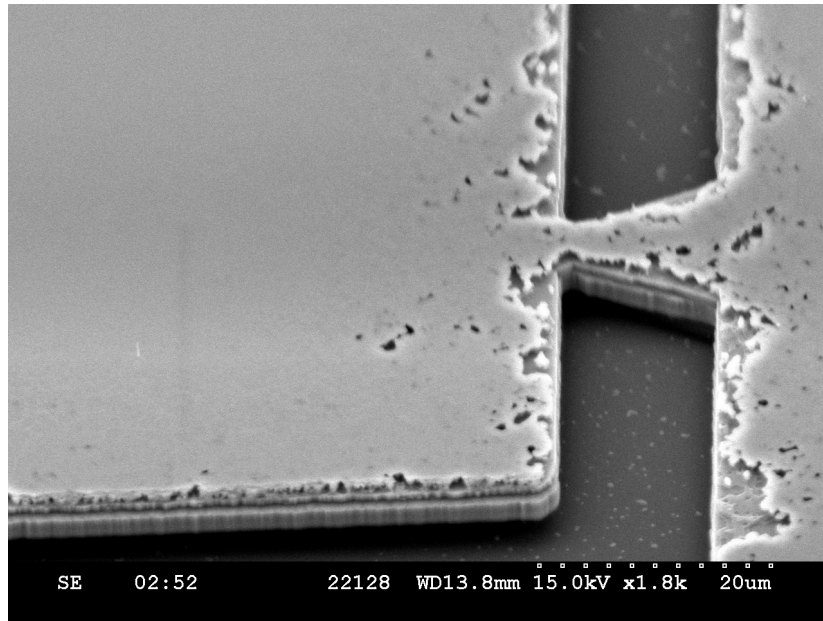


Figure 5.8: Close up image of the completed suspended 10 layer DBR captured using a scanning electron microscope, which clearly shows the separation of individual layers as well as the attached upper DBR structure.

5.3.2 White Light Reflectometry Measurements

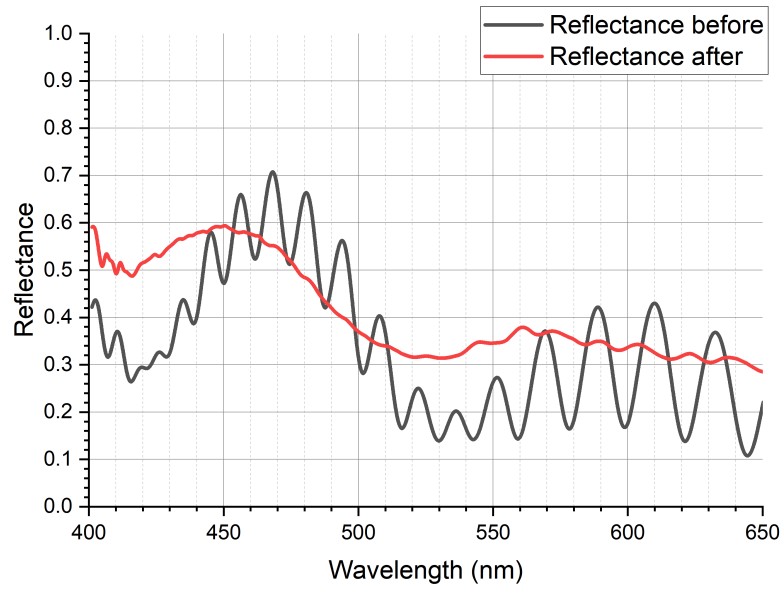
Investigating the effect of the under-etching fabrication processes on the optical functionality of the DBR material was clearly important. If the processing were to destroy the physical structures of the epilayers then the material would cease to operate as a distributed Bragg reflector, or at least reduce its functionality for use in any hybrid photonic devices.

The white light reflectometer described in Section 2.15.2 that is usually used for measuring the thickness of SiO_2 films was set to have a GaN-on-Si structure so that it would output spectra of the material. This model was $4\ \mu\text{m}$ of GaN-on-Si omitting any inclusion of porosification. As noted above the samples were measured before any fabrication steps (except cleaning) and after being fully prepared as suspended membranes to compare the change in reflectivity. The non-fabricated material had an AlN-Si interface whereas the suspended structure would be AlN-air. The white light illumination was targetted onto the centre of each sample in the array of suspended membranes. Ideally one would be able to specifically target the individual suspended

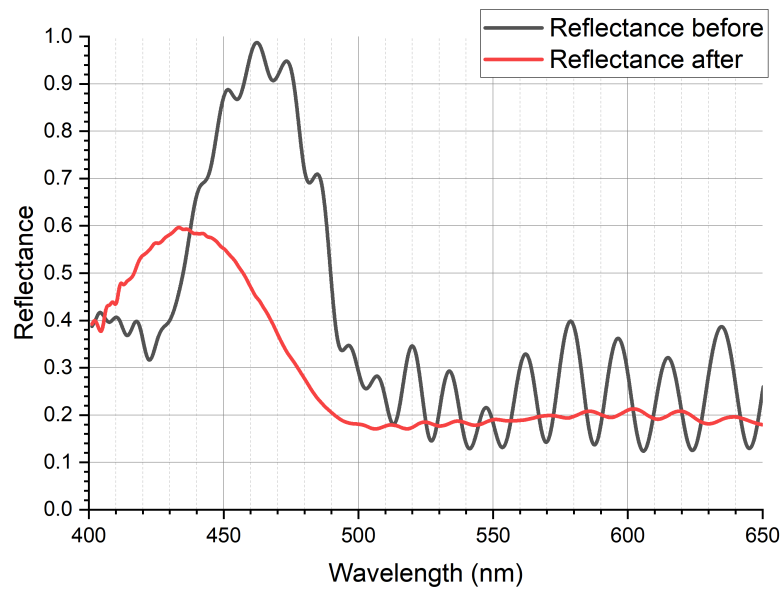
membrane to isolate it from the supportive structures which remain connected to the Si. Unfortunately this was impossible due to the illumination area of the Filmetrics tool.

Both the 5 and 10 layer DBR spectra before fabrication show a reflectivity peak near to 470 nm, when the growth was targeting 460 nm. This discrepancy was due to the material being an early growth iteration, as well as it being still attached to the Si substrate. The 5 layer sample shifts this peak reflectance to 450 nm and 10 layer to 435 nm when released which would need to be accounted for in future growths. This blueshift occurs because the material strain is reduced with the detachment from the substrate by under-etching. This in turn increases the bandgap of the material [78] and adjusts the refractive indices of each layer to shift the central reflectivity wavelength in the spectrum. Both samples exhibit a higher frequency spectral oscillation on the reflection envelope which can be attributed to a cavity formed inside the epistructure. This spectral modulation is removed with the suspension of the membranes, although a slight perturbation remains likely from the support structures. The narrow Gaussian shape of the spectra deviates from the conventional flat-topped stopband of a commercial DBR likely due to the relatively low refractive index contrast between the GaN and porous GaN.

The target reflectances were $\sim 60\%$ and $\sim 99.9\%$ for the 5 and 10 layer samples which proved to be approximately correct for the unprocessed material. The reflectance peaks as measured were $\sim 65\%$ for the 5 layer before, and $\sim 60\%$ after, the under-etch. This reduction in reflectivity may be attributed to the removal of the Si below the supporting structure as well as potential damage to the DBR structure. The reflectivity of the 10 layer sample changed much more, going from $\sim 95\%$ for the 5 layer before and $\sim 60\%$ after. The damage to the DBR from the KOH was responsible for this and so the processing had to be adapted to avoid it.



(a)



(b)

Figure 5.9: Spectral data from measuring both (a) 5 layer and (b) 10 layer DBR samples after the standard cleaning preparation step and after full suspended membrane fabrication. Taken using the Filmetrics white light reflectometer.

5.3.3 Transfer Printing Full Thickness DBR Membranes

An attempt was made to transfer print the full thickness DBRs to gauge the viability of the coupons created. A glass microscope slide was solvent-cleaned and Matrix ashed to be used as a transparent receiver. The goal was to be able to place the printed device in a micro-white light spectroscopy setup outside of the cleanroom to measure both transmission and reflectance [79].

The issue with the printing came from the tethers being the full thickness of the device layers. The work done to maintain the flatness and stresses of the devices through the engineering of the buffer structure had increased its thickness considerably. The thicknesses were 3645 nm and 4140 nm for the 5 and 10 layer devices, respectively, when the method developed for transfer printing used device thicknesses in the region of 2500 nm or lower. The mask used had a tapered geometry for the tethers that went from 10 μm to 5 μm , wide meaning that there was 10 μm of material connecting the membrane, much more than the 6 μm which was discovered to be optimal in the Chapter 4.

No matter what stamp type was used, from the firmest 6 : 1 PDMS ratio to the stickiest viable 12 : 1 ratio, the device could not be removed from the donor sample. A 6 : 1 ratio stamp was used to punch down into the suspended device in an attempt to overwhelm the strength of the tethers. Only after 30 attempts did this method manage to release a suspended membrane. This singular device was printed and is shown in Figure 5.10. The device should be able to be gently pressed into place and have the stamp slowly withdrawn to leave the device printed, otherwise one would not be able to print in a desired location to create a vertically stacked device. With these findings it was obvious that more work needed to be done to facilitate the ease of printing. This led to the work developing the tether thinning process that will follow in this chapter.

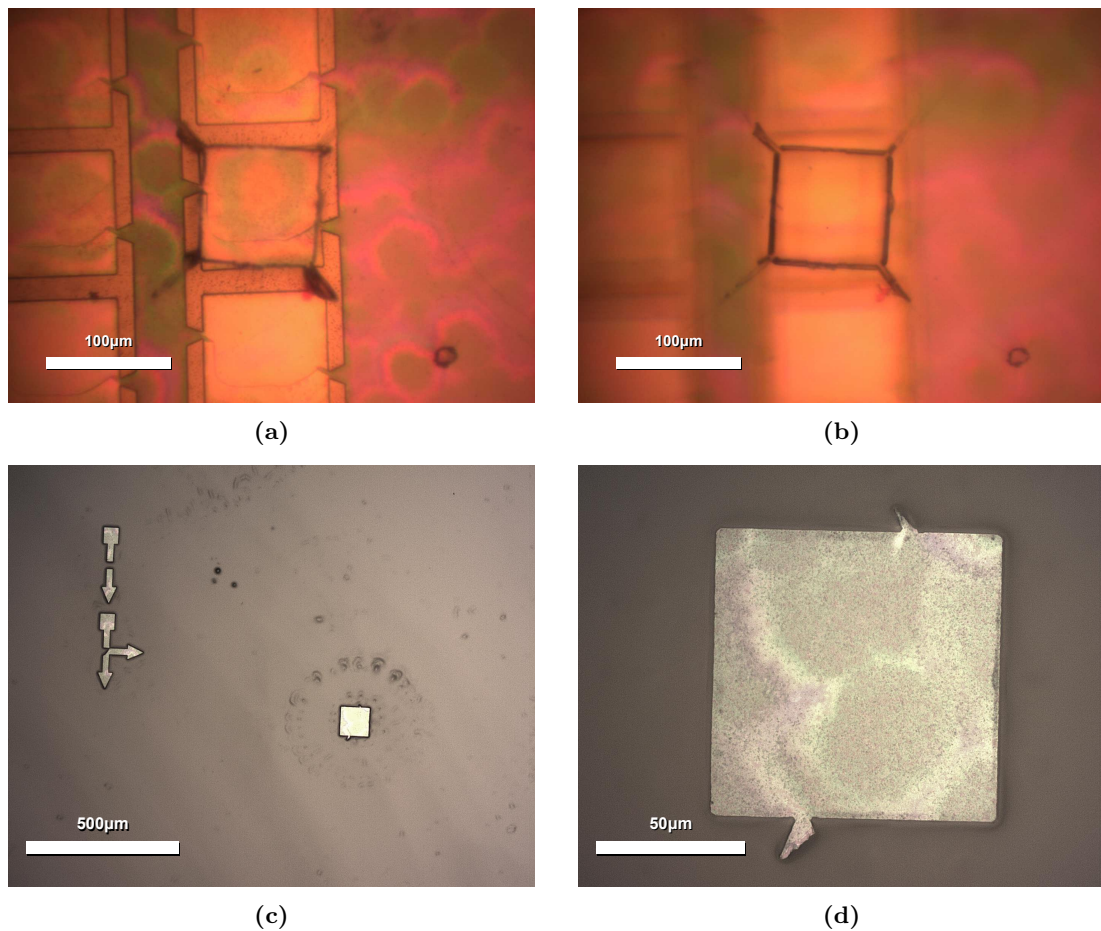


Figure 5.10: Images from the transfer printing of a full-thickness 5 layer DBR membrane. (a) The full-contact with the stamp. (b) The pick up. (c) The printed DBR showing extra alignment feature debris picked up. (d) A close up of a printed DBR.

5.4 Selectively Reducing the Thickness of the DBR Material

With the inability to pick up suspended devices in transfer printing attempts, it was decided to modify the tethers to account for their increased thickness coming from the enhanced buffer structures. Attempts were made to thin the tethers holding the device to the supportive rails, whilst protecting the device area as shown in the schematic in Figure 5.11. The trend of ever-thickening epilayer structures is notable in the commercial wafer supply too. Much of the fabrication processes investigated in this

section will be useful for other device structures when optimised appropriately.

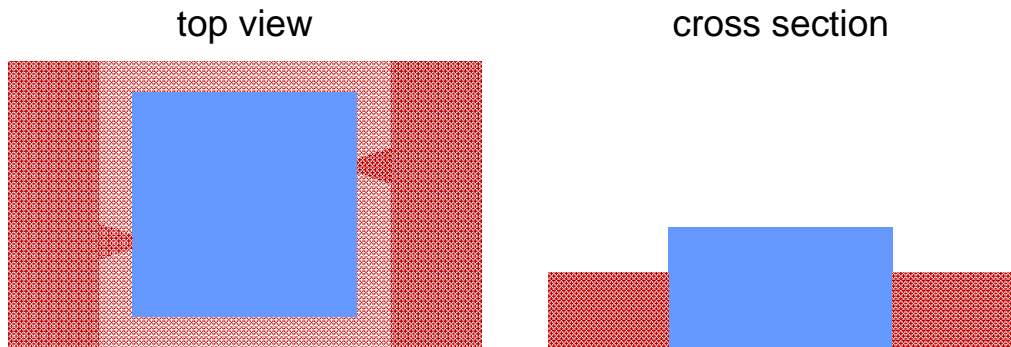


Figure 5.11: Schematic diagram illustrating the regions requiring etching in red to thin the material, along with a side profile of the resultant material removal. The blue region represents the un-etched DBR membrane.

5.4.1 Laser Lithography on Existing Membranes

Before starting another batch of devices, an attempt was made to selectively mask off regions of the previous suspended DBR membranes for a second ICP etch to thin the tethers. It was suggested that a thicker resist would be needed to span the gaps in the surface and so the Micro Resist TechnologyTM ma-N 1410 negative photoresist was chosen which satisfied the qualities required. Spinning at 3000 rpm for 60 s should produce a film thickness of 1 μm according to the data sheet [66]. The resist was soft baked at 100 $^{\circ}\text{C}$ for 90 s.

A GDSII file was created using the Python scripts previously developed, consisting of an array of squares the same size as the 100 μm membranes and all in the same positions such that they overlapped perfectly. As a negative resist was being used, the exposed area would remain and so the laser needed to follow a path covering each individual suspended device. Using the Heidelberg DWL66 laser lithography tool the GDS was loaded and converted to an exposure job with the values listed in Table 5.3.

These values were an estimate of the correct dosage from a predetermined parameter set when the initial calibration was done for the tool. After exposure the sample

5. DBR Membrane Fabrication for Transfer Printing

Table 5.3: Parameters used for the DWL66 laser lithography tool to expose ma-N 1410 photoresist on a GaN DBR substrate.

Parameter	Value
laser power (mW)	20
filter (%)	100
intensity (%)	60

was developed using Micro Resist Technology ma-D 533 developer via submersion for 40s. A visual check was made using a microscope which showed that the lithography had failed. As shown in the microscope image in Figure 5.12 the resist had retracted from the edges of the structure causing a non uniform coverage which is completely unusable for dry etch processing. The resist was removed after this failed attempt using a solvent clean and a Matrix ash so that the suspended devices could be used in other experiments. Spinning resist onto suspended membranes would not be viable to process them further.

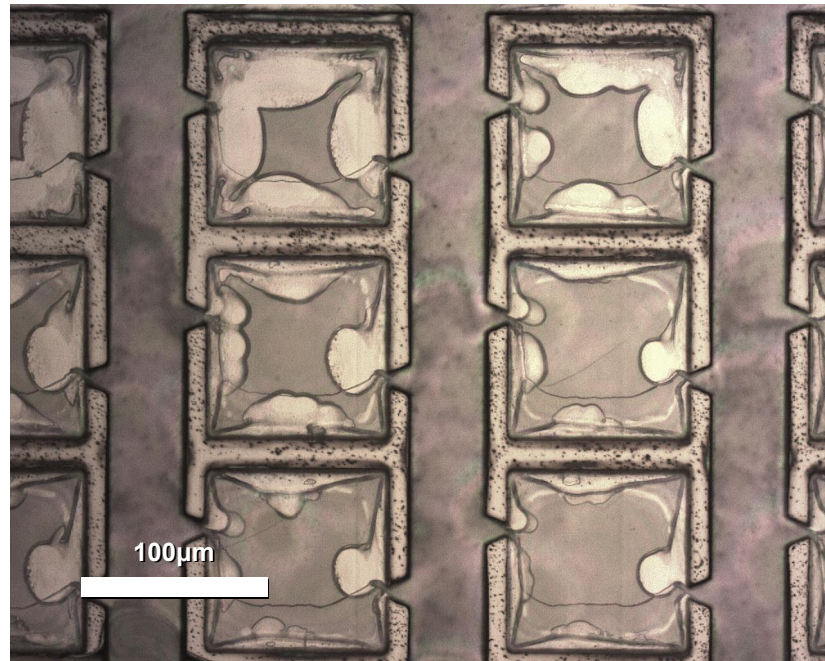


Figure 5.12: Microscope image of the 5 layer DBR sample after the development of the ma-N 1410 photoresist pattern used to isolate the suspended membranes.

5.4.2 Two Stage Laser Lithography to Thin Tethers

Instead of modifying the suspended membranes it was decided to start a new standard membrane fabrication process from the beginning, first thinning the regions which would become the tethers and leaving a raised mesa where the suspended membrane would be—as shown in Figure 5.11. The remaining silica would then be removed with a BOE etch to allow for a new photolithography step. Another deposition of silica and spinning of thick resist over the recently formed structures would then be processed into a second hard mask to define the tether structures through the standard fabrication method.

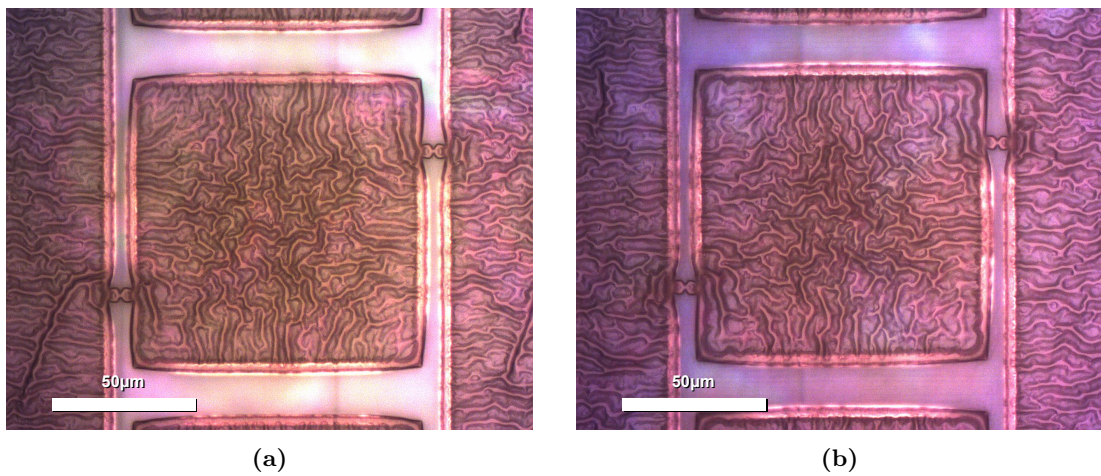


Figure 5.13: (a) An example of burnt thick S1818 resist after an RIE process to etch the silica hard mask with a 5 layer DBR sample and (b) a 10 layer DBR sample.

Parameter sweeps varying the laser power and the intensity were carried out on the laser lithography tool for the available thick resists including: ma-N 1410, S1818 and SPR220 to find the optimal setting for the DBR material. Each fabrication run raised an issue with the laser lithography tool being unable to properly expose the features on a non-planar surface—believed to be because the autofocus would detect the height changes. The developed resist mask would not transfer the pattern into the silica in the RIE etch, likely due to the photoresist not fully clearing out. The RIE step to etch the silica hard mask would also severely burn the thick resists causing the geometry of the mask to be warped or even prevent satisfactory etching as can be seen in Figure 5.13.

This issue was slightly mitigated by curing the samples in a vacuum oven for 24 h at 60°C and 10 mbar to evaporate the residual solvent in the resist in a low temperature, low pressure environment. A higher temperature would have re-flowed the resist causing it to lose its shape. None of the samples fabricated using laser lithography created successful suspended DBR membranes.

5.4.3 Two Stage Photolithography Suspended Membrane Fabrication Using the Mask Aligner

A suitable lithography mask was discovered with the geometries to mask off the required region for the global thinning etch as previously proposed. The mask contained an array of 90 μm \times 90 μm squares distributed identically to a complementary array of tethered 100 μm \times 100 μm membranes. The pitch of each feature, size of array, and alignment features were the same so that the photolithography could be overlaid precisely. The only downside was that the membrane tethers were tapered and would have the same under-etch problems previously experienced.

A sample of the 5 and 10 layer DBR were prepared in the standard photolithography process using the S1805 photoresist. The 90 μm squares were exposed, developed and etched into the silica layer with the RIE. The samples were then etched using the GaN recipe in the ICP for 3 min 40s to thin the material everywhere but these squares. BOE was used to remove the remaining silica so as to not to interfere with the next stage of photolithography as the extra height of the silica would make it harder to spin on the next application of photoresist. The Dektak tool was used to measure the depths, the 5 layer sample being found to be etched 2060 nm and the 10 layer sample 2066 nm. This left 2074 nm and 1585 nm of device material thickness for the tethers. Ideally there would have been more thickness remaining, \sim 2500 nm on each, to prevent the accidental loss of the suspended membranes but the estimated etch rates used for this were varying between each etch. The resultant mesas formed are shown in Figure 5.14.

A 605 nm deposition of silica was used to form the second hard mask, the thinner layer

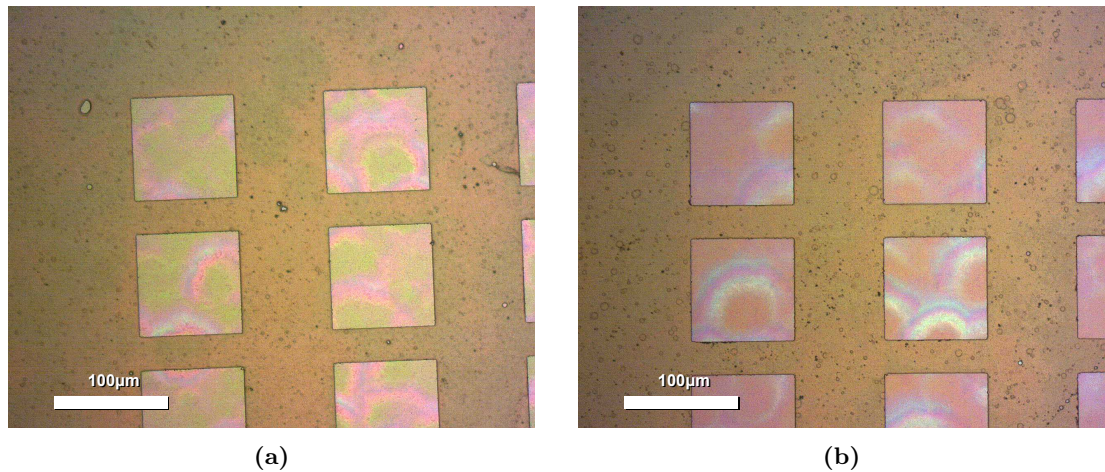


Figure 5.14: The raised 90 μm square mesas formed by globally etching the (a) 5 layer and (b) 10 layer DBR sample. The silica hard mask had just been removed.

requiring less time for the RIE to etch which would reduce the risk of burning. SPR 220 4.5 was chosen for the second lithography process as it produced a 3.8 μm thick film, a thickness in the middle of the available thick resists, when applied using a method adapted from the data sheet [80]. This would allow it to flow over the raised mesa structures and then also level out the surface whilst not being too thick as to burn in the RIE silica etch step. HMDS primer was applied in the standard process and then 0.1 mL of the resist was syringed to the centre of the samples through a 40 μm filter. The resist was spun by ramping up to 4000 rpm over 10 s and then holding that speed for 60 s. The samples were soft baked for 2 min at 105 $^{\circ}\text{C}$. The samples were then exposed on the mask aligner for 18 s, aligning the membrane structures over the mesas using the alignment features of the mask. The samples were left for 35 min loosely covered in a fume cupboard to rehydrate which is required to complete the photo-reaction. The samples were developed by submerging in a 1:1 mix of Microposit Developer concentrate and DI water for 50 s, rinsed in pure DI, and then dried with a dry stream of N_2 . To help prevent photoresist burning, the samples were baked in a vacuum oven for 24 h at 60 $^{\circ}\text{C}$ and 10 mbar.

The silica hard mask was formed using the RIE silica etch for 24 min 40 s which unfortunately still burnt the photoresist as shown in Figure 5.15. The resist had only slightly warped the hard mask which was revealed after a solvent clean but this was a

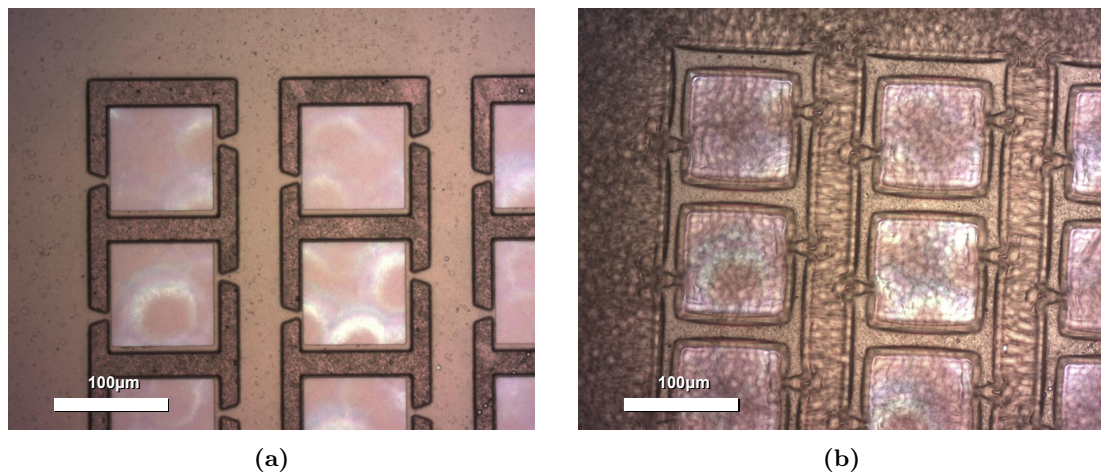


Figure 5.15: (a) The 5 layer DBR sample after vacuum baking the photoresist. (b) The same sample after etching the silica in the RIE showing the burnt resist.

insignificant defect and so processing continued. The GaN etch in the ICP was used to fully clear out the material to define the tether and membrane structures for 9 min. A 2 min RIE silicon etch was then used to deepen the trenches and then 1 μm of silica was deposited to protect the sidewalls. The KOH under-etch took 80 min which was also affected by the tapered tether geometry leaving the angled etch stop underneath the membrane mentioned in Chapter 3. This extended under-etch beyond the limit of the sidewall protection so the edge material was attacked as shown in Figure 5.16, where the silica had also been removed with BOE. This also caused some of the membranes to prematurely release and either collapse and be stuck to the bottom of the trench or float away in the KOH etch. A mask with straight tethers would have avoided the prolonged KOH etch. Extra sidewall protection in the form of 1.5 μm of silica would potentially help prevent the edges being eroded in future processes. A suitable mask with straight tethers was eventually found but due to time constraints the fabrication of suspended membranes was never completed.

5.4.4 Transfer Printing Thinned DBR Membranes

The DBR membranes were printed to two different surfaces to test their viability as coupons. Initially the membranes were transfer printed onto a scrap piece of 12:1 ratio PDMS which offered the highest likelihood of release. An 8:1 ratio stamp was initially

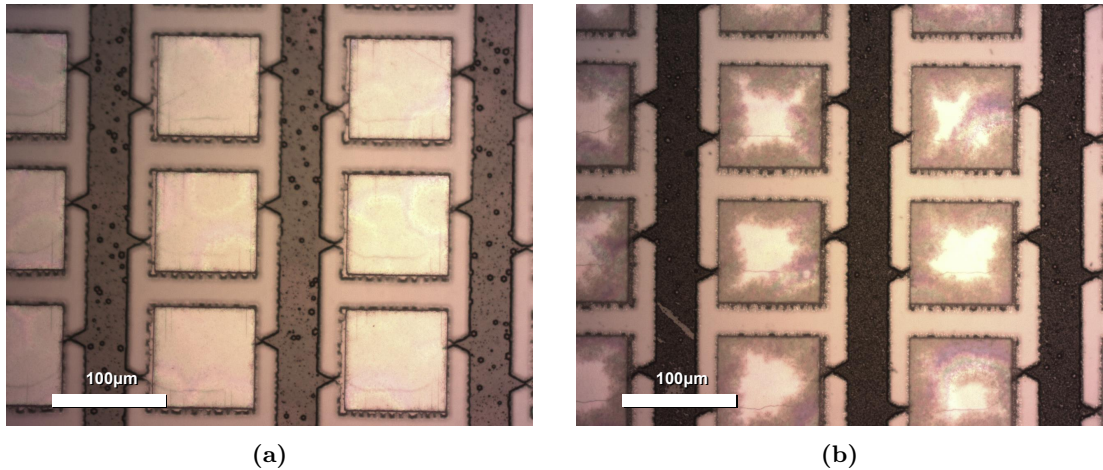


Figure 5.16: The finalised suspended DBR membranes after removing the silica protection with BOE. (a) 5 layer and (b) 10 layer DBR sample.

used but was unable to pick up any membranes however the stickier 10:1 stamp could. To release the 10 layer membranes the stamp had to overlap half of the membrane and apply downwards force to introduce a torsional force to break the tethers, as shown in Figure 5.17b. This method would not be ideal in future assembly as it leaves an excess of tether affixed to the released membrane as well as inconsistency in reproducibility and lack of scalability. A total of eight membranes were printed for each layer type, as can be seen in Figure 5.17.

The extra resistance to retrieval by the 10 layer DBR may be due to an incomplete under-etch as there were small protrusions of silicon still attached underneath the tethers. Another iteration of devices using the newly discovered thinner straight tether mask would improve the KOH etch process and also be easier to release.

5.5 Summary and Discussion

Within this chapter it was intended to create a transfer printable DBR coupon that could be used in conjunction with other photonic devices such as micro-LEDs to create novel 3D stacked hybrid devices. A set of full thickness DBR suspended membrane was created using novel mesoporous GaN material supplied by collaborators at the University of Cambridge. Two separate wafers had 5 and 10 repeated pair layers

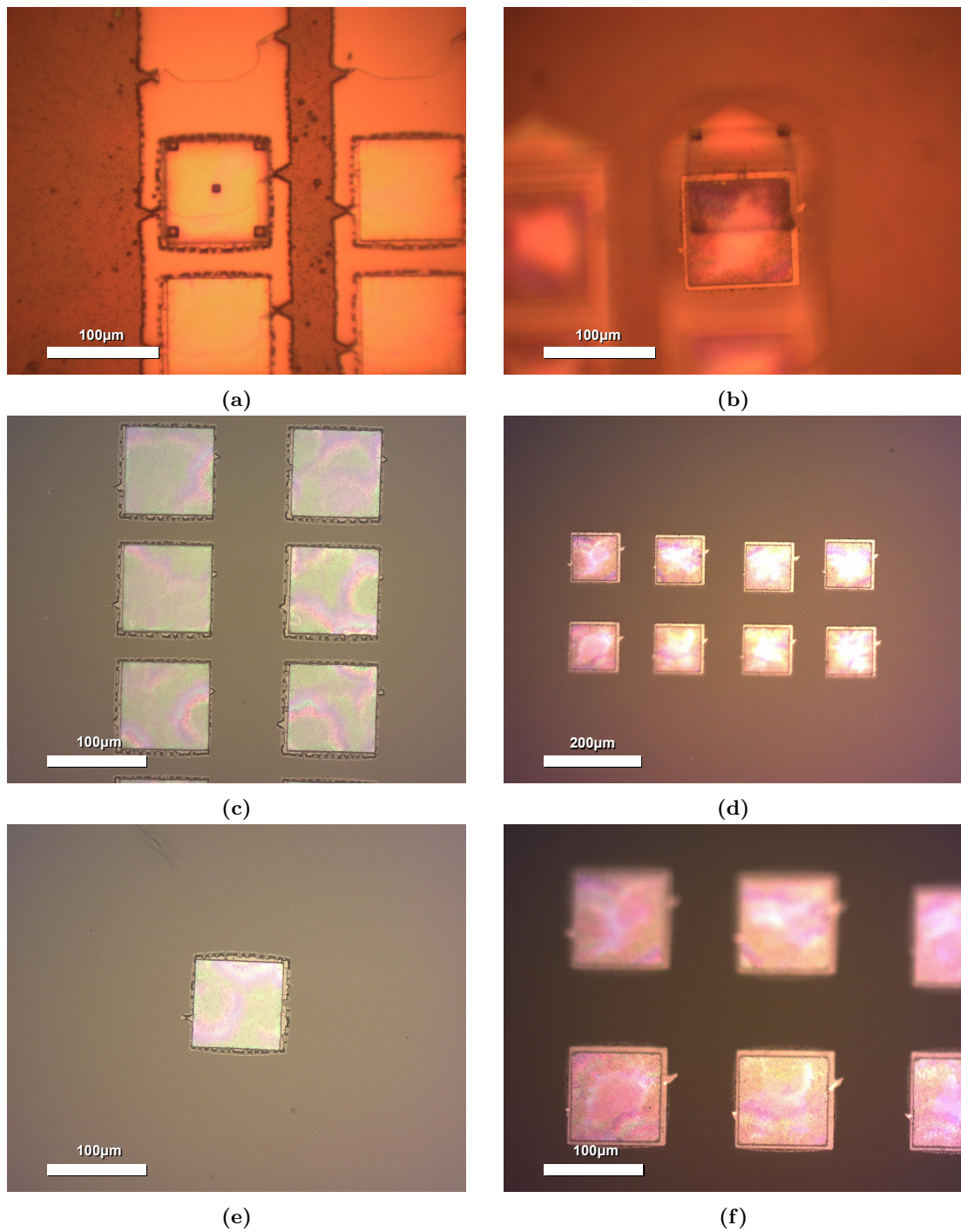


Figure 5.17: Microscope images of the transfer printing of DBR membranes with 5 layers on the left and 10 layers on the right. The pick up stage: (a) and (b). A broad area view of the printed membranes: (c) and (d). A closer view of the printed membranes: (e) and (f).

initially showing 65 % and 95 % reflectivity, respectively, but suffered significant reflectivity drops after fabrication into suspended membranes to both be roughly 60 %. The KOH etch damaged the porous layers which was identified visually and then verified through SEM.

The full thickness membranes were too thick to be transfer printed easily and so a process was developed to selectively thin the regions of the supporting tethers to weaken them. Laser lithography proved inadequate to define a mask on the non-planar surface after the selective regions had been thinned due to its reliance on focussing the beam. The mask aligner was able to develop the resist on the non-planar surface when a suitable mask was found to define the required features. The mask was a compromise as the design had the undesirable tapered tether geometry which produced thicker tethers and hindered the KOH under-etch. A result of this is that the membranes produced were corroded by the excessive time required in the KOH etch to clear out the Si under the membranes. Whilst easier to transfer print than the previous batch, they were still too resistant to pick up. A new custom glass-chrome mask with the bow tie tether design defined in Chapter 4 would alleviate the issues raised from the KOH etch.

It should be emphasised that the previous GaN DBR structures reported here were very novel and had not previously been considered optimised for transfer printing. The work described here investigated the requirements in detail and has produced essential information for the future optimisation of both the epistructures and processing for successful printing of suspended coupons made from these structures.

Chapter 6

Designing the GaN Resonant Cavity LED

6.1 Overview

The design of RCLEDs is challenging, especially for new materials and wavelengths. In this chapter the structure of the proposed GaN RCLED is designed using a mix of Python scripting to calculate DBR reflectivity from the quarter wave equation [81] and finite difference time domain (FDTD) simulation of the RCLED structure. Each element of the hybrid device was designed to work with the other, taking into consideration that the materials to be used would be adapted from the structures which were discussed in previous chapters. The real and imaginary components of the refractive indices (n and k) for some relevant materials were calculated using approximated formulae due to them not having measured data sets to borrow from [82].

The number of layers required to create the desired DBR reflectivity was calculated using the aforementioned script and found the optimal number of layers to be 4 and 10 for reflectivities of 68.1% and 98.4%, respectively. The structure of the LED from Chapter 3 was recreated in Lumerical FDTD simulation software and placed between the DBRs and then the thicknesses of the n-GaN and p-GaN regions were modified

to maximise the electric field antinode overlap with the quantum well region to boost the integrated enhancement, following the rules defined for optimal RCLED structures given by Schubert’s book “Light Emitting Diodes” [5]. An LED design was made for both a DBR and palladium metal (Pd) backside mirror configuration. The results from the simulation were shared with the collaborators at Cambridge with whom the LED structures were finalised and eventually grown. Initially the design was to target a central wavelength of 420 nm as it is the peak of the internal quantum efficiency for InGaN [83] but the target was changed to 450 nm to match existing growth processes. The fabrication of these new LED wafers into suspended LED coupons was not realised as they arrived towards the end of the laboratory time accorded to this PhD.

6.2 Creating Refractive Index Sets for Material Simulations

For an accurate representation of the intended device the refractive indices of each material must be input into the simulation for a range wavelengths about the central wavelength; in this case the range would approximately be 300 nm to 800 nm covering the visible spectrum. The materials present were: GaN, porous GaN, InGaN, AlN, AlGaIn, and palladium.

GaN, AlN, and palladium refractive indices were taken from online repositories of experimental data sets [84, 85]. The indices for the porous GaN were measured by the collaborators at Cambridge who produced the material from their publication [36] and are shown in Figure 6.1. The porosity of the GaN is non-uniform as the creation creates radial tunnels from the centre of the wafer and thus creates birefringence. The normal direction to the wafer surface, (the direction we are interested in using for the mirror), has a lower refractive index than that of the in-plane direction due to there being more air gaps.

6.2.1 III/V Nitride Alloy Ratios

The InGaIn indices had to be calculated because there were no reliable data sets available for the desired mole fraction. InGaIn is more formally expressed as,

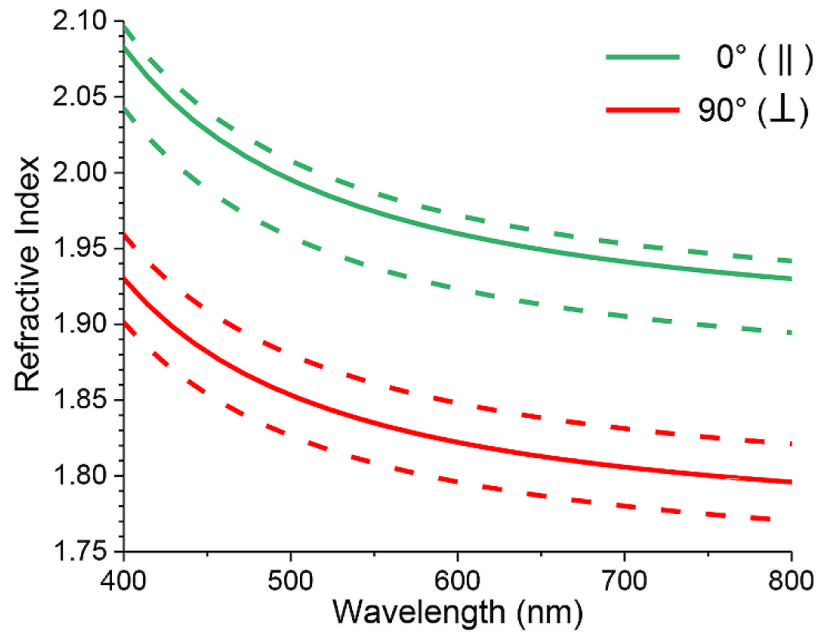


Figure 6.1: Plot of refractive indices against wavelength for mesoporous GaN taken from [36].

$\text{In}_x\text{Ga}_{1-x}\text{N}$, where the subscript x represents the ratio of indium to total number of cations in the compound. InGaN is the material that constitutes the quantum wells of the LED and this ratio is tuned to change the output wavelength. For the 450 nm target wavelength, this ratio was $x = 0.23$.

The method adopted follows the work detailed in Bergmann and Casey's process, based on the idea that refractive index would follow the shift in band-gap from the alloy ratio of ternary nitrides [82]. The shift is given by

$$n_{\text{InGaN}}(E) = n_{\text{GaN}}\{E - [E_g(\text{InGaN}) - E_g(\text{GaN})]\}, \quad (6.1)$$

where $n_{\text{InGaN}}(E)$ is the refractive index for InGaN at a given photon energy E and E_g is the band-gap energy. The value for $E_g(\text{GaN})$ was taken from literature [86] to be 3.44 eV. The value of $E_g(\text{InGaN})$ had to be calculated for the specific alloy ratio $x = 0.23$ using:

$$E_g(\text{InGaN}) = E_g(\text{InN})x + E_g(\text{GaN})(1 - x) - 1.4x(1 - x), \quad (6.2)$$

where $E_g(\text{InN})$ is given the value 0.64 eV [86]. The value 1.4 is the bowing parameter of the alloy and is a measure of how far the band gap deviates from the linear interpolation from the constituent materials. This bowing parameter is visualised in the $\text{Al}_x\text{In}_y\text{Ga}_{1-x-y}\text{N}$ regime Figure 1.1 in Section 1.1.1. Instead of using a formula dependent on the photon energy E , a wavelength dependent formula was used due to its simplicity. Bergmann and Casey *et al.* [82] opted to use the Sellmeier formulae [87] and data from Kawashima *et al.* [88] to calculate the refractive indices. This study utilised the simplified $n_{\text{GaN}}(\lambda)$ Sellmeier formula from Kawashima (Equation 6.3), as well as one from Barker *et al.* [89] (Equation 6.4) to give a comparison. The latter was chosen to match the origin of the refractive indices values of GaN used in the simulations. The first takes the form:

$$n_{\text{GaN}}^2(\lambda) = A + \frac{\lambda^2}{\lambda^2 - B}, \quad (6.3)$$

where $A = 4.37$ and $B = 0.088 \mu\text{m}^2$ are fitting parameters and λ is in μm . The second equation has the form:

$$n_{\text{GaN}}^2(\lambda) = 3.6 + \frac{1.75\lambda^2}{\lambda^2 - 0.256^2} + \frac{4.1\lambda^2}{\lambda^2 - 17.86^2}. \quad (6.4)$$

A Python script was written to calculate the refractive indices using these formulae for the range 300 nm to 600 nm centred about the wavelength of interest 450 nm and with a mole fraction $x = 0.23$, which can be found in Appendix A. The mole fraction was chosen as the value used by the collaborators at Cambridge to grow the InGaN quantum wells of the LED for this wavelength. The code generated an array of wavelengths in this range with increments of 20 nm to provide enough refractive index data for the simulation software. Each wavelength value was converted to eV using the formula:

$$E(\lambda) = \frac{hc}{\lambda} \approx \frac{1.23984}{\lambda}, \quad (6.5)$$

where h is Planck's constant and c is the speed of light in a vacuum. The energy is shifted using the shift factor from Equation 6.1—here energy is measured in eV and wavelength λ in μm . This new shifted energy was converted back into a wavelength using Equation 6.5 to be substituted into the $n_{\text{GaN}}^2(\lambda)$ formula of Equation 6.4. The script plots the $n_{\text{GaN}}(\lambda)$ and $n_{\text{InGaN}}(\lambda)$ against wavelength to see the shift which can be seen in Figure 6.2. The data is output as a columnated *.txt* file to be input into the simulation software.

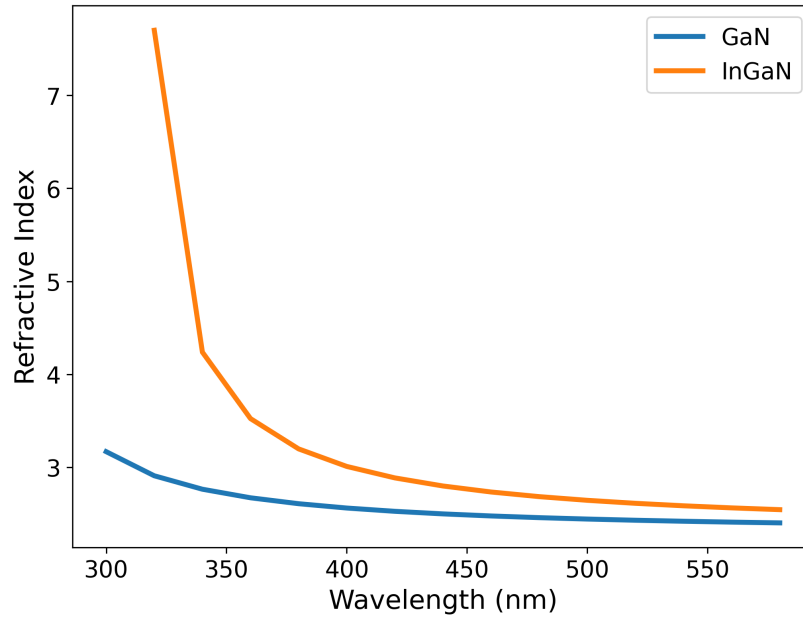


Figure 6.2: Plot of refractive indices of GaN and $\text{In}_x\text{Ga}_{1-x}\text{N}$ ($x = 0.23$) against wavelength calculated using a Python script utilising the Sellmeier equations [82, 86, 88].

The other material requiring refractive index calculation was the graded $\text{Al}_x\text{Ga}_{1-x}\text{N}$ present in the buffer structures as shown in Figures 3.2 and 3.13. The graded region would start at $x = 0.75$ at the substrate end and finish at $x = 0.25$ to make a transition from AlN-rich to GaN-rich. Methods utilising the Sellmeier equations state that the formulae would not work for alloy ratios of $x > 0.4$ [82] and so a number of alternate methods were reviewed [90–94]. It was decided that calculating and implementing a

graded index AlGa_N material into the simulation software was too ambitious and time consuming. Instead, many discrete layers would be calculated with 0.05 steps in x and stacked to form the gradient.

The most promising method came from the paper by Antoine-Vincent *et al.* [91] which utilises a Sellmeier equation in the form:

$$n_{AlGaN}^2(\lambda) = a + \frac{b \cdot \lambda^2}{\lambda^2 - c^2}, \quad (6.6)$$

with a , b , and c being fitting parameters and the wavelength λ in nm. These parameters were dependent on the mole fraction x and were given for six discrete values between $0 \leq x \leq 1$ and so were not limited to low alloy ratios. A Python script was written to calculate Equation 6.6 using a nested loop cycling through wavelengths λ between 360 nm to 600 nm in 20 nm steps and also through $0 \leq x \leq 1$ in steps of 0.05.

For each value of x a new set of fitting parameters were generated in the Python script by using linear interpolation with the data given [91], the results were a first order spline and can be seen in Figure 6.3. The Python script used to calculate these formulae can be found in Appendix A.

The Python script utilised these new fitting parameters with Equation 6.6 to produce a set of refractive indices for the required mixing ratios which are visualised in Figure 6.4. Once again, the numeric values were exported as a *.txt* file to be input into the simulation software as a new material.

6.3 Finding the Number of DBR Layers Required for ~ 0.6 and ~ 1 Reflectivities Using Porous GaN

The DBR structures detailed in Chapter 5 were used as a starting point for prospective future designs. As part of the design process the reflectivities of the DBRs were analytically approximated using the formula:

6. Designing the GaN Resonant Cavity LED

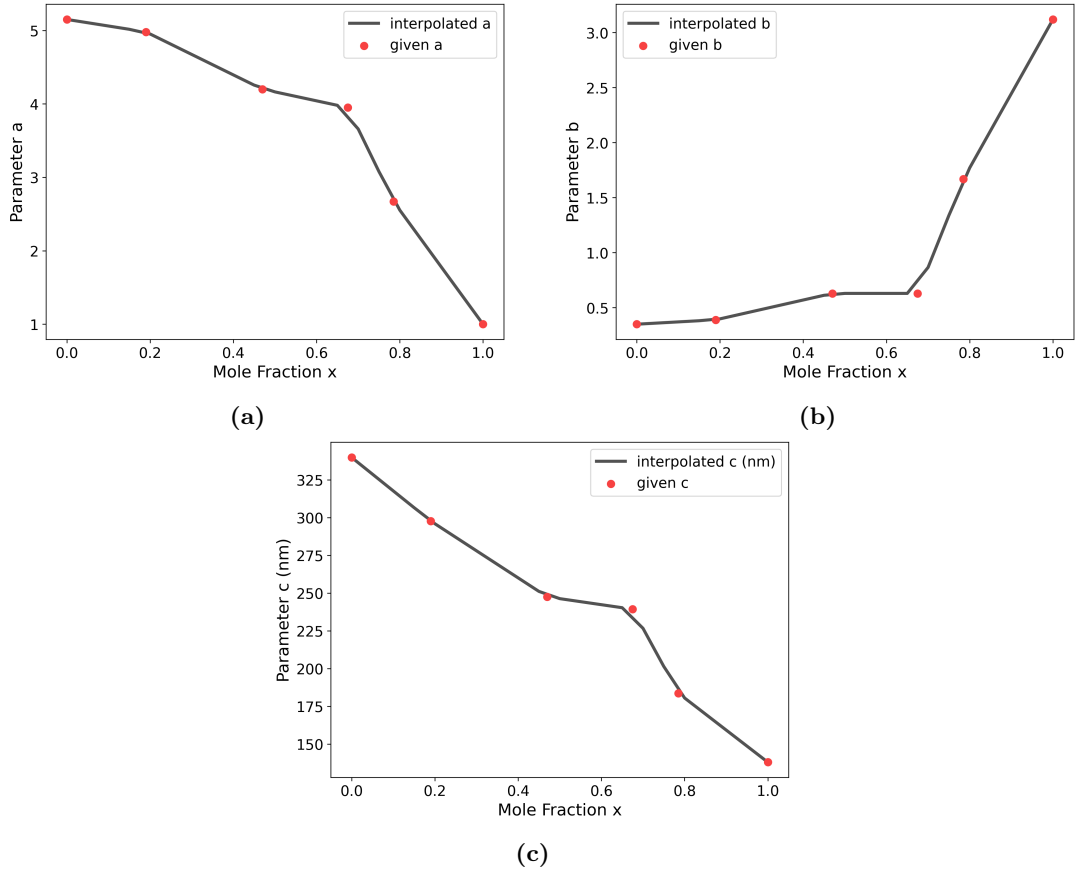


Figure 6.3: Interpolation of parameters a : (a), b : (b) and c : (c) for AlGaIn refractive index Sellmeier equation [91].

$$R = \left[\frac{n_o(n_2)^{2N} - n_s(n_1)^{2N}}{n_o(n_2)^{2N} + n_s(n_1)^{2N}} \right]^2, \quad (6.7)$$

where n_o , n_1 , n_2 , and n_s are respectively the refractive indices of the originating medium, the high index medium of the repeating pair, the low index of the repeating pair, and the terminating medium respectively, with N is the number of repeated pairs [81]. The formula assumes the thickness of the repeating pairs would be equivalent to a quarter of the wavelength of light in that medium, i.e. have $nd = \lambda/4$, where n is the refractive index of the medium and d is the thickness.

A Python script, available in Appendix A, was written to make these calculations and produce the graphs in Figure 6.5 for the wavelength 450 nm. Originally the target was 420 nm to target the peak external quantum efficiency of the InGaIn quantum wells [83],

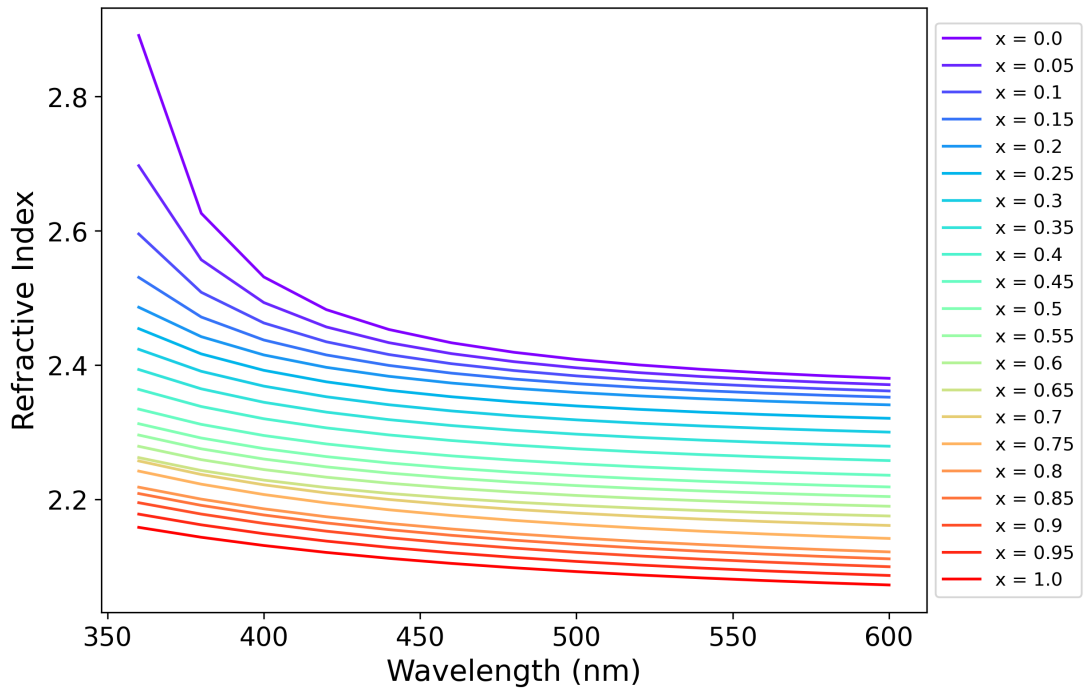


Figure 6.4: Plot of refractive indices of $\text{Al}_x\text{Ga}_{1-x}\text{N}$ against wavelength calculated using a Python script utilising the Sellmeier equation from [91] with $0 \leq x \leq 1$.

but this was later changed to 450 nm as a compromise with growth process constraints. For these calculations the exit mirror originating medium would be the AlN etch stop layer of the LED in the centre of the hybrid structure and the terminating medium would be the GaN in the buffer structure of the DBR coupon. For the bottom mirror the originating medium would be the p-GaN top layer of the LED and the terminating medium would also be the GaN in the buffer structure of the DBR.

For a device such as an RCLED the backside-reflector should be as reflective as possible, i.e. $R \rightarrow 1$ and the exit-reflector should have $R \sim 65$ [5]. In this configuration light would only pass from the exit mirror. These results indicate that the 5 layers DBR for the exit mirror would be too reflective with $R = 0.802$ which does not align with the reflectivities measured in Section 5.3.2 of Chapter 5. The discrepancy would come from the limitations of Equation 6.7 as none of the true layer thicknesses were taken into account. So whilst it provided a rough estimate of the reflectivity, a more in-depth simulation was needed.

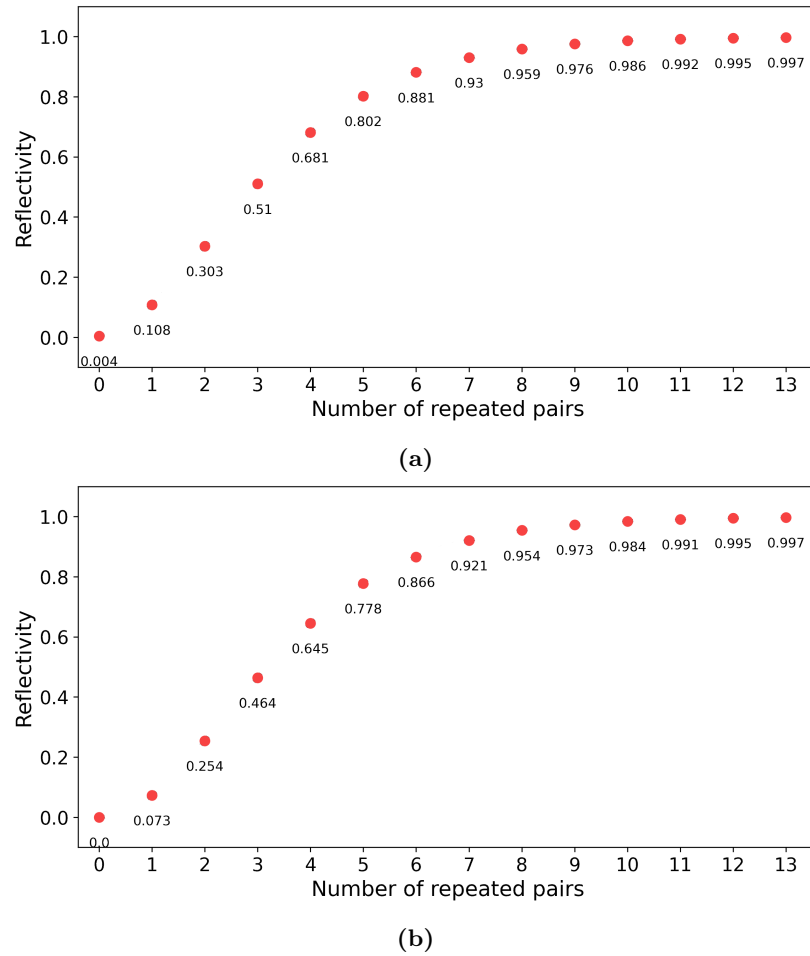


Figure 6.5: Calculated reflectivity dependent on number of repeated pairs in a DBR stack for 450 nm wavelength light for (a) exit mirror configuration and (b) bottom mirror. For both plots the DBR consisted of alternating layers of GaN and mesoporous GaN with GaN as the terminating medium.

6.4 DBR Design Using FDTD Simulations

The entirety of the simulation work was conducted using the Lumerical FDTD (finite difference time-domain) software [95]. This numerical analysis allows one to create photonic structures of many materials and record the progression of light in the medium. The structures are discretised into a grid called a “mesh” and the Maxwell’s equations governing the electric and magnetic fields are solved inside each. Using monitors one can extract key information from the simulation such as the strength of individual electrical or magnetic fields in a certain location or time.

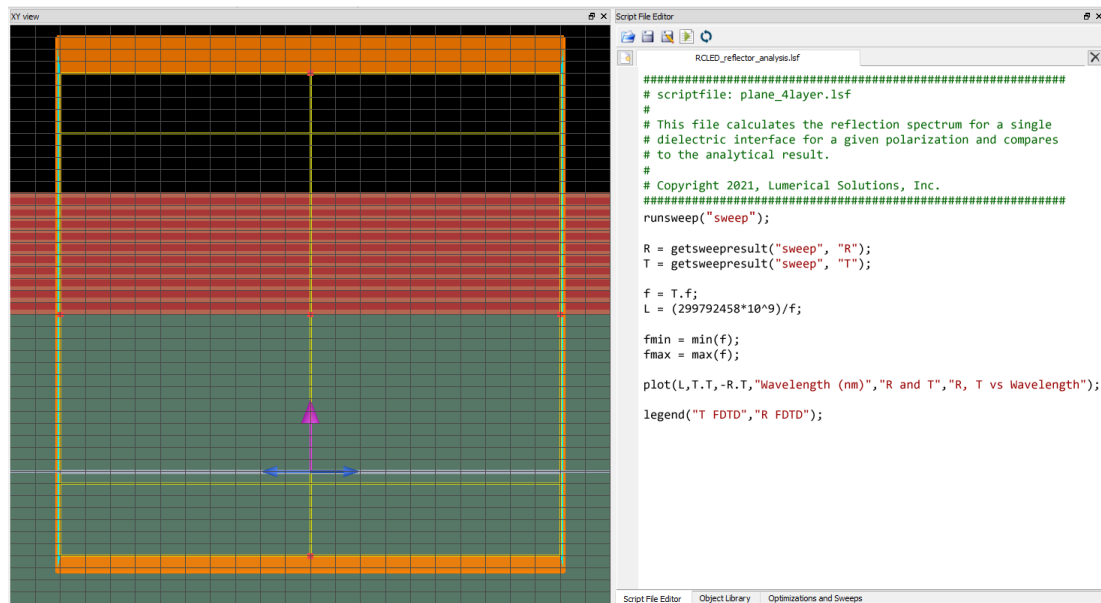


Figure 6.6: A window capture of a simulation set up in Lumerical software of a DBR structure simulation used to assess the response of a light source in the 420 nm range. The script used to capture the data and produce the following reflection and transmission plots is shown on the right and was written in Lumerical programming language.

A preliminary simulation prior to the wavelength change was set up with a 420 nm plane wave source directed at the DBR stack from below which is shown in Figure 6.6. The source originates from AlN material to simulate the light generation of an LED device next to the DBR. Behind the DBR layers is air as at least one side of a final device would be exposed as such. In hindsight, the buffer material of the DBR structure should have also been included as this would likely not be removed in processing. The air-DBR refractive index contrast would be much greater than the buffer-DBR refractive index contrast and so would not represent the true reflectivity of the DBR in the hybrid system.

There were two frequency domain power monitors added to measure the strength of the electric field in two locations: in the air behind the DBR stack to measure transmission, and within the AlN medium behind the light source origin to measure the reflection. It was important to place the monitor below the light source so that it would not measure the initial injected wave and only the reflected wave. A script file

6. Designing the GaN Resonant Cavity LED

plane4layer.lsf was copied from the Lumerical website [96] and modified to suit the DBR simulation. This script would automatically run the simulation multiple times to vary the source wavelength, gather the data from the monitors, convert the data from frequency domain to wavelength, and finally plot into a figure defined within the script which can be seen in Figure 6.7.

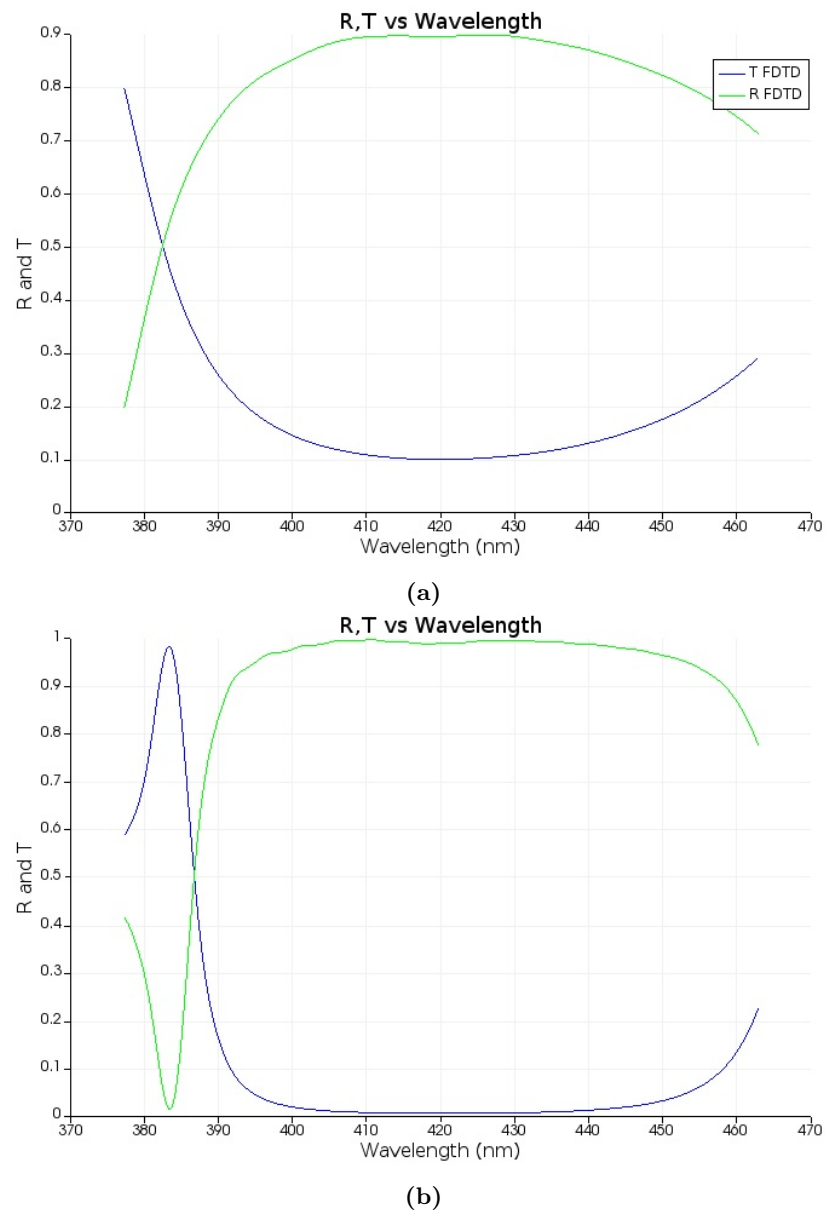


Figure 6.7: Reflection and transmission curves of a basic DBR produced in Lumerical software with (a) 5 layers and (b) 10 layers.

As can be seen from the resultant reflection and transmission plots returned from the FDTD simulation, they match what would be expected from the previous analytical approximations of reflectivity for a DBR, albeit with the wavelength centred at 420 nm. The DBRs were judged to be satisfactory in reflectivity to form the simulation of the full RCLED as the reflectivity about the target wavelength of 420 nm was $R \approx 0.9$ for the 5 layer and $R \approx 1$ for the 10. This combination would create an over-confined cavity resulting in low light output in a realised physical system, however the measurements of the DBR material in Chapter 5 indicate the actual reflectivities would be much lower.

The simulation was modified to replace the DBR mirror structure with a 100 μm thick layer of palladium to act as a first surface mirror in place of a 10 layer DBR bottom mirror. Pd was chosen given its reflective power in the visible spectrum [97] as well as previous examples of its employment in GaN based RCLEDs [98, 99]. The results of the reflectivity are given in Figure 6.8.

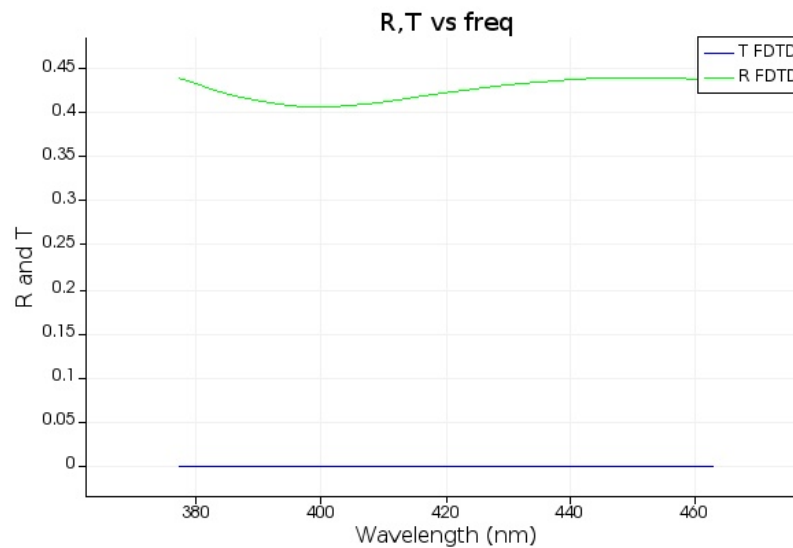


Figure 6.8: Reflection and transmission curves of a 100 μm Pd mirror produced in Lumerical software.

The reflectivity did not come close to the desired $R = 1$ for the bottom mirror as the metal itself had quite a high absorbance for this wavelength region. Figure 6.9 shows a plot of reflectivity for various common metals and their reflectivity spectra which would

indicate that silver or aluminium would have been a more appropriate mirror material with reflectivities $R \approx 0.93$ in the 450 nm wavelength. Both these alternative metals would tarnish causing an higher resistivity oxide layer which in turn would lower the efficiency of the resultant device through heat losses. The idea was saved for a possible iteration of devices later in development.

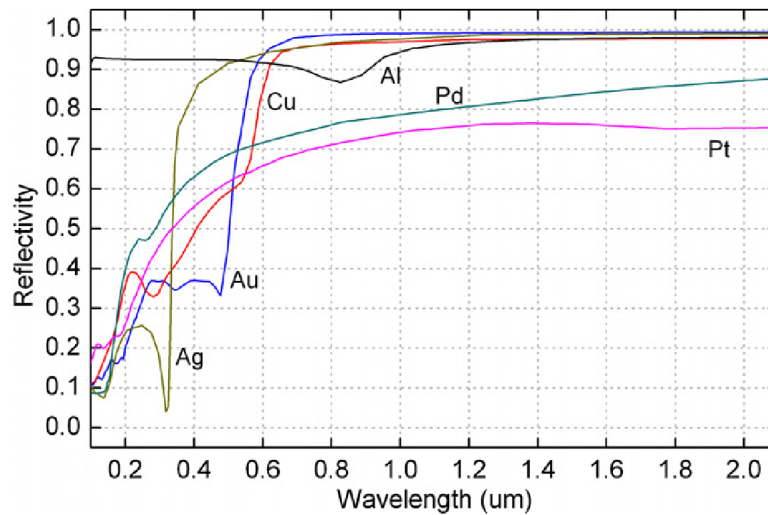


Figure 6.9: Reflectivity of common metals versus wavelength at normal incidence. Taken from [100].

6.5 RCLED Design Using FDTD Simulations

Two designs of RCLED were proposed and would require separate LED structures to create the optical cavity due to the optical properties of the different mirror choices. An initial design would have a palladium mirror as the bottom reflector as this would also be used as a positive contact onto the p-GaN, greatly reducing the complexity of fabrication but also reducing the efficiency because of absorption losses. With the LED flipped, a $R \sim 0.6$ DBR coupon would then be transfer printed atop the backside to create the cavity. The other design would instead utilise a $R \sim 1$ DBR as the bottom reflector which would increase the efficiency but create the technical boundary of electrically connecting the device. Both designs are illustrated in Figure 6.10

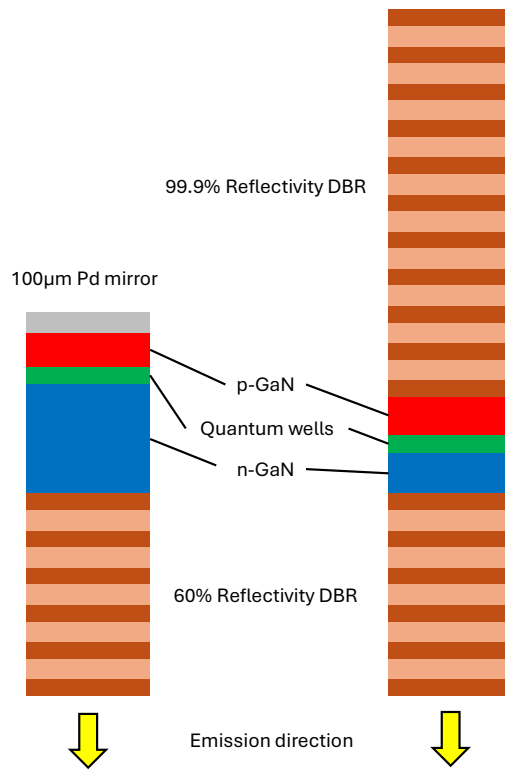


Figure 6.10: Illustration of the two designs for the RCLED, one with a Pd mirror and one with a double DBR.

6.5.1 RCLED Design Using Full Thickness LED Coupon

The structure of LED described in Chapter 3 was reconstructed in the Lumerical FDTD simulation software to serve as a foundation for the design as this would be similar to what would be grown by the team at Cambridge. The bottom layer was the LED p-GaN and the top layer was the AlN nucleation layer as if it were a released suspended membrane that had been flipped upside down. This was done because it was intended for the bottom side of the LED to be the emission end, it would be much more practical to metallise the p-GaN as an initial processing step which would act as the bottom mirror.

A profile monitor was used to measure the real part of the electric field and a refractive index monitor was used to indicate the profile of the structure. The magnitude of the electric field and the index were plotted against the vertical distance (arbitrarily y

6. Designing the GaN Resonant Cavity LED

for these simulations) to observe the locations of the nodes and antinodes of the field inside the cavity which is shown by Figure 6.11. In this figure it was clear that the LED structure was not optimised for creating the optical cavity required as there were too many antinodes—none of which overlapped the quantum region.

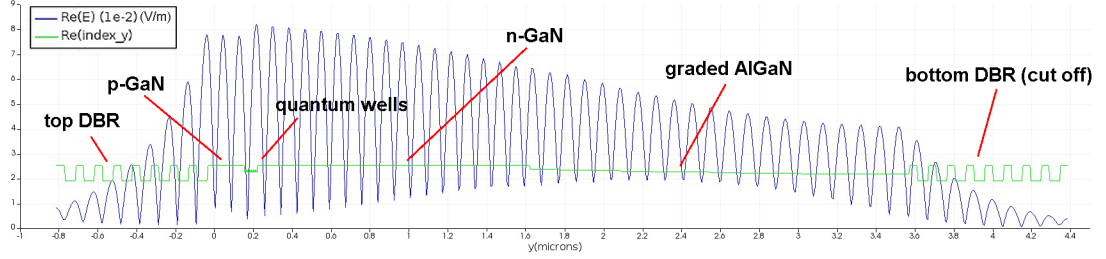


Figure 6.11: Labelled plot of electric field against length for full LED structure showing how the default structure would not overlap antinodes with the quantum well region for optimal performance.

To create the standing wave required for cavity enhancement, the length of the cavity L_c must be a half-integer multiples of the wavelength in the medium given by the relationship:

$$L_c = \frac{m\lambda_0}{2n_c}, \quad (6.8)$$

where m is the integer mode number, n_c is the refractive index of the cavity medium and λ_0 is the wavelength of light to be confined in the cavity in a vacuum. Equation 6.8 was used to estimate a rough length to target for the LED structure assuming the cavity was comprised of mostly GaN material. The DBR mirrors would also have a penetration depth to account for, meaning that the cavity would extend into these structures by an amount equal to the penetration depth. This depth L_{pen} is given by:

$$L_{pen} = \frac{L_1 + L_2}{4r} \tanh(2mr), \quad (6.9)$$

where L_1 and L_2 are the respective thicknesses of the repeated pairs, m is the number of repeated pairs, and r is the reflectivity of a single interface given by Fresnel's equation

for normal incidence:

$$r = \frac{n_h - n_l}{n_h + n_l}, \quad (6.10)$$

which uses the refractive indices of the high and low layers as n_h and n_l respectively [5]. The ideal cavity would be symmetrical with equal thicknesses of p-GaN and n-GaN either side of the quantum wells with a total cavity length equal to $\lambda_{cavity}/2$ such that the antinode of the fundamental mode peaks over the centre [5]. This was infeasible with the epitaxial growth methods for the LED.

6.5.2 RCLED Design Using Shortened LED Coupon

A compromise was decided on, to remove the buffer structures after fabrication via flipping the coupon using the transfer print tool and etching the backsides using ICP dry etch up to the n-GaN layer. The structure would be designed to minimise the cavity length by adjusting the p-GaN and n-GaN regions which would in turn reduce the mode number of the cavity according to Equation 6.8. This would increase the integrated enhancement of the cavity as is discussed in the literature, e.g. the book “Light Emitting Diodes” by Schubert [5]. The analytical calculation for cavity length would be used to estimate a starting point for the structure and then the simulations would be used to adjust it to be optimal.

In the Lumerical FDTD simulation setup the buffer structures were removed leaving just the p-GaN, quantum wells, and the n-GaN as shown in Figure 6.12. The DBR layers were adjusted to have thicknesses of 44.5 nm and 59.2 nm to change the target wavelength of the cavity to 450 nm as this was easier for the growth team at Cambridge to create.

The p-GaN and n-GaN were adjusted using a rough iterative method to achieve a good quality standing wave with the shortest possible cavity length. It was found that adjusting the p-GaN would shift the location of the quantum wells with respect to the electric field antinodes. An automated sweep was then used to finely adjust the

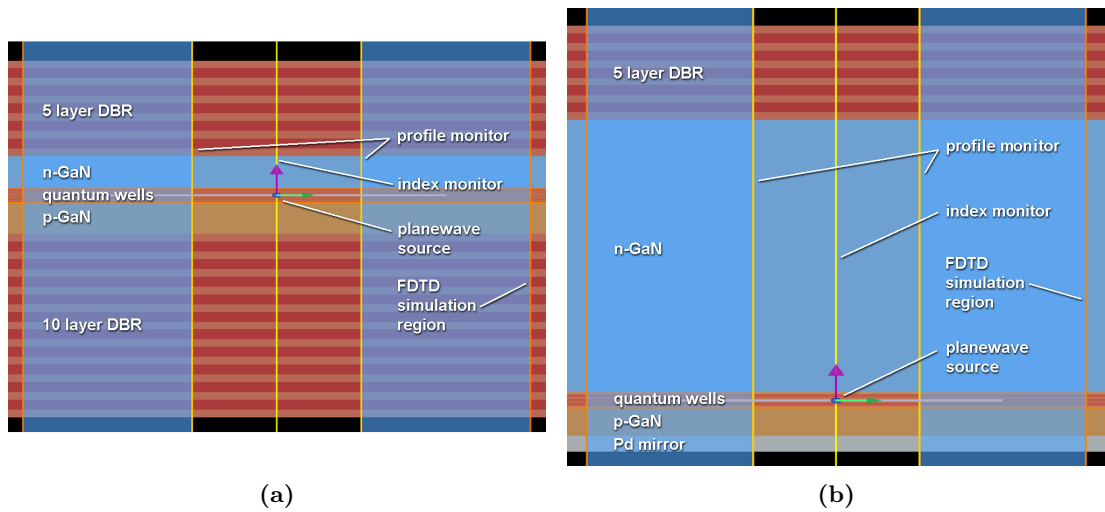


Figure 6.12: Labelled cropped capture of Lumerical FDTD simulation setup for (a) the double DBR configuration, and (b) the palladium mirror configuration. The FDTD simulation region is represented by the orange bounding box, the profile monitor is a narrower yellow bounding box, and the index monitor is a vertical yellow line.

thickness of the p-GaN in 1 nm steps between ± 20 nm of the rough estimate. Each sweep would run the simulation to produce different profiles for the electric field for comparison. Using the visualisation methods previously described for Figure 6.11, a zoomed-in view of the quantum wells region as shown in Figure 6.13 was used to visually identify which thickness of p-GaN centred the antinode over the span of the quantum wells. For the double DBR configuration the optimal p-GaN thickness was found to be 185 nm and for the metal mirror configuration it was 165 nm.

The optimised n-GaN thickness was similarly calculated with the addition of a Python script which is available in Appendix A which was used to calculate the integral of the electric field data over the quantum well region. The sweep would export *.txt* files which were then manually collated into a folder to be processed by the script. The peak amplitudes were found with n-GaN thicknesses of 188 nm and 1640 nm for the double DBR and metal mirror configurations respectively. The amplitude of the electric field in the metal mirror version was much lower than the double DBR likely due to the absorption losses in the metal. The n-GaN thickness for the metal mirror configuration was much larger as the iterations using thinner designs would diminish the electric field

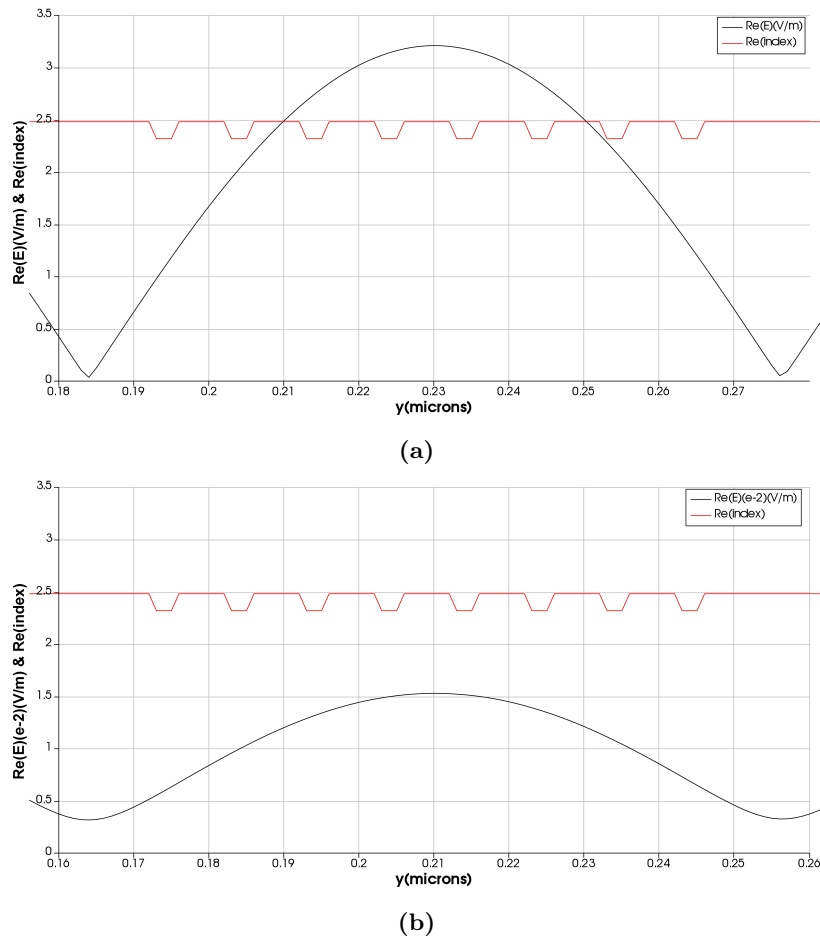


Figure 6.13: Visualisation of electric field magnitude and refractive index plotted against distance at optimal quantum well overlap for (a) double DBR configuration, and (b) the palladium mirror configuration.

significantly.

6.6 Post-Simulation Adjustments to Finalise the LED Designs

The simulated results and design were discussed with the growth team at Cambridge who were best suited to tailor the structure for the best results. The epistructures of the finalised designs may be found in Table 6.1. Added to the designs were non-intentionally doped GaN (nid-GaN) regions before the n-GaN to provide structural integrity, a 25 nm InGaN:Si capping layer to the n-GaN to transition better into the quantum wells, and

6. Designing the GaN Resonant Cavity LED

an optional 10 nm SiN_x dislocation blocking layer included in the n-GaN. It was decided to progress with an initial series with the metal mirror configuration in mind due to the ease of fabrication into RCLEDs.

Table 6.1: Finalised designs for LEDs to be grown by Cambridge University. The n-GaN may include a 10 nm SiN_x dislocation blocking layer inclusive in thickness.

Layer	Layer Thickness (nm)	
	Pd Mirror + DBR	Double DBR
Si (111) substrate	1000	1000
AlN nucleation layer	250	250
AlGaIn graded	1700	1700
nid-GaN	200	1000
AlN etch stop	20	20
n-GaN	1615	188
InGaIn:Si capping layer	25	0
InGaIn MQW (x8)	87	87
p-GaN	165	185

Six different wafers were produced with their details given in Table 6.2. Two samples were chosen for processing into devices from the later end of the series as their photoluminescence measurements of average peak wavelength value were on target at 450 nm.

Table 6.2: Details of LED growth data for the first series produced using the design from FDTD simulations. Samples* were chosen for processing into devices.

Sample	SiN_x interlayer included?	Cavity length (nm)	Deviation from target (1892 nm)	Avg. peak wavelength (nm) ± 4 nm	Wafer bow (μm) - convex + concave
1	no	1862	-30	460	-60
2	no	1844	-48	441	-18
3	no	1851	-41	468	-64
4*	no	1827	-65	450	-44
5	yes	1849	-43	443	-18
6*	yes	1901	+9	450	-31

Unfortunately due to time constraints the material was not processed into devices, but these custom designed structures will form part of future work in the group.

6.7 Summary and Discussion

In this chapter a framework was developed to design the structure of a GaN LED for use in a hybrid RCLED device which is a complex challenge. The refractive indices for the ternary nitride materials AlGa_N and InGa_N were approximated through adapted Sellmeier equations which were in turn converted into materials for the Lumerical FDTD simulations. The optimal number of DBR layers were both analytically and numerically estimated to be 5 and 10 repeated pairs for reflectivities $R \approx 0.6$ and $R \approx 1$ respectively. These estimates were deemed inconclusive and direct measurements with multiple growth iteration would be expected to achieve the target reflectivities without compromising the delicate structures.

A series of Lumerical FDTD simulations were made based on the original LED structure from Chapter 3 sandwiched between two DBRs to determine the optimal structure for an RCLED. Another design was simulated with one Pd mirror as the bottom mirror to give an option for simplified fabrication. The full structure including the graded AlGa_N buffer layers was deemed too thick to create an optical cavity for the target wavelength of 450 nm and so the design was changed to remove these areas. In the design this would be reflected by the addition of an AlN etch-stop layer to allow for the backsides of the LED coupons to be ICP dry etched accurately to a desired depth.

It was found that adjusting the thickness of the p-GaN would shift the location of the antinodes whilst adjusting the thickness of the n-GaN would alter the amplitude of the electric field intensity. The ideal p-GaN thicknesses were initially found to be 165 nm and 185 nm for the metal mirror and double-DBR configurations respectively. The ideal n-GaN thicknesses were initially found to be 1640 nm and 188 nm for the metal mirror and double-DBR configurations respectively. The simple metal mirror design was then produced with slight modifications by the growth team at Cambridge to optimise the LED as a series of six wafers. Two of the wafers were chosen for processing which will form the basis of future work.

Chapter 7

Conclusions and Future Work

This project was started with the goal to further the technical capabilities of the already established transfer printing method for assembling photonic components in a vertically stacked assembly. A target was to be able to eventually realise a stacked functional device such as a resonant cavity light emitting diode from individual printed coupons for each component function. To do this many aspects of the materials and fabrication methods required were improved and further understood, facilitating future iterations. This work predominantly centred on GaN based LED devices for their unique characteristics, challenges, and applications—but the investigative methods of this project could easily be translated to other platforms such as silicon-on-insulator, III-V semiconductors, or other nitrides.

7.1 Conclusions

In Chapter 3 the morphological properties of materials in both GaN epistructure wafers and under-etched membranes were assessed to optimise the epistructure design and growth parameters for a flatter printed end product. It was observed that the devices produced by under-etching the epistructures free from the silicon substrates tended to curl upwards to form a dish shape. This was induced by the lattice mismatch of the constituent epilayers of the device as well as the difference in thermal expansion

such that when the devices cooled from the growth reactors one layer would shrink more than another creating an internal strain. As the layers were released from the silicon they were free to minimise this strain by curling. For transfer printing flatter coupons are required to provide more surface adhesion between mating objects which is especially important when stacking vertically.

To address this, a thicker buffer structure was developed and a series of wafers were produced of conveniently available HEMT structures with identical parameters apart for an incremental dosage of ammonia which affected the bow of the wafer and in turn the bow of the suspended membranes. A systematic study was completed which processed all of the materials into suspended 100 μm by 100 μm square membranes in parallel and measured the resultant membrane bow using optical profilometry. The ideal ammonia dosage was relayed back to the growth team to guide a second generation series of LED wafers with the improved buffer structures. The same systematic study was done for the new material with the inclusion of commercially sourced GaN LED material to make a comparison. The bespoke grown suspended membranes were consistently flatter in both suspended state and when transfer printed to a flat surface, proving that the study had successfully improved the structural design of the wafer material for transfer printing. The results were published in papers showing the effect of internal strain of the membranes [1] and other strain managed devices [74].

Highlighted from this study was the formation of the SiN_x layer from the ammonia dosage. A higher dosage of ammonia resulted in a thicker SiN_x layer being formed which assisted in relieving the strain of the epistructure, resulting in the flatter printable devices. A benefit of this material layer is that it also provides an etch stop layer for the KOH under etch meaning that the undersides of the coupons would remain smooth and un-pitted.

A drawback of increasing the buffer structures was made evident when attempting to transfer print the under-etched devices as the tethers became too strong to break when releasing from the original substrate. This naturally directed the research to search for a way to facilitate the release the devices and so a study was devised to find the optimal

tether geometry as the previous designs were for much thinner epistructures.

Chapter 4 encompasses the study to find the optimal tether geometry. The width and number of connecting tethers was systematically studied to find the optimal combination for printing with this material platform. It was found that a two-tether configuration with 3 μm wide tethers gave the most consistent retrieval rate whilst maintaining a high fabrication yield. The PDMS mixing ratio of the stamps was also tested and showed that an 8:1 ratio is preferred for retrieval. However, the tests were all very poor for the printing of the membranes meaning that the employed reversible adhesion method is not always satisfactory for consistently printing photonic component coupons. The stamp adhesion problem had been worked on by collaborating members of the Hetero-Print grant (which this project was part of) which could see some improvement in the release of devices. This struggle to print highlighted the necessity to develop a switchable adhesion stamp to allow for the precise release of the devices in a controlled manner.

To compliment and this study, a Python module was created for generating the GDSII masks required for creating highly-customisable membrane arrays, with the ability to alter tether geometries, as well as another for generating customisable full LED fabrication layer masks. It was noted that the KOH under-etch step would stall on tapered tether geometries and so straight tethers were preferred—a new bow tie tether geometry was created which is predominantly straight with a small centrally located notched section to act as a weak spot. It would be good to repeat the tether study using this design to optimise its dimensions for future device fabrication. This discovery would greatly increase the reproducibility of the KOH under-etch to allow for shorter etch times. This would prevent excessive exposure of etchant to the device layers and yield higher quality devices as a result.

With the overarching goal to assemble a hybrid resonant cavity device via transfer printing, Chapter 5 addresses the necessity for reflector devices by detailing the fabrication process for making a suspended DBR membrane using a novel porous GaN-on-Si wafer. Due to the thickness of the buffer structure mentioned previously,

a two-stage photolithography process was used to first thin the material in the tether region and then the membrane structure was defined. There were still difficulties in consistently producing viable membranes due to ingress of KOH into the porous structures as well as the tethers still being too resistant to release. The project was limited by the resources available but using a glass mask with the appropriate straight tethers designed previously would help reduce the time required in the KOH under-etch. The combination of the new straight tethers and the selective thinning of the tether regions would prove to provide a much more consistent release from the original substrate without compromising on yield. With thicker device structures potentially becoming the norm for this transfer printing regime, this tether design and fabrication process could be implemented more generally.

Chapter 6 details the work done to simulate the materials and function of a potential hybrid GaN device using the results from the previous chapter's work being considered such as the optimal buffer structures. The epistructure of the custom LEDs was transferred into the Lumerical FDTD simulation software which included calculating the refractive indices of the various constituent ternary nitrides. By adding reflectors to either end, one with $R \approx 1$ and one with $R \approx 0.6$ an RCLED could be simulated. The thicknesses of each epilayer were adjusted such that the antinode of the electric field had the greatest overlap with the quantum well region whilst also minimising the total cavity length. The p-GaN thickness determined the location of the overlap whilst the n-GaN adjusted the electric field amplitude. The final designs were discussed with the growth team at Cambridge to produce a series of LED wafers for fabrication into RCLEDs—these designs utilised a palladium bottom reflector for ease of fabrication making the anode easier to connect.

With these simulations it was still evident that a low mode cavity was too difficult to produce with the facilities available. The buffer structures added too much thickness to the overall structure and so would likely need to be removed in a thinning process which would unfortunately remove the provided strain relief. Whilst it remains to be proven, it would be interesting to see if the contact forces holding a flipped transfer

printed LED device to a receiving substrate would maintain device-flatness after being thinned in situ.

7.2 Next Steps and Future Work

The next steps for this work would be to start processing the custom-designed LED material produced from the simulation work, initially to create a broad area LED device to measure the current-voltage characteristics using the probe station and also to measure the photoluminescence response to confirm the information provided by the collaborating group. As was shown in the blue shift in the reflectometry measurements of the fabricated suspended DBR, there may be an alteration to the output wavelength of the LED material after the internal stresses are released after under-etching. In parallel, a series of devices could be made to be transfer printed onto a DBR substrate and also a non reflective receiver could be used to measure the output enhancement from the DBR. This would be a novel approach to creating a DBR-enhanced microLED. The next steps would be to create the Pd-coated LEDs and transfer print flip to a substrate including gold tracks for powering the device—these would also be characterised and compared to the non-mirror variant. Eventually a tunnel junction would be used to connect the n-GaN beneath a top layer of transfer printed DBR to create an RCLED which would require further design considerations and an iterative approach to achieve a working device.

Consideration has been made on how to best improve the fabrication work for future projects. The ICP tool was equipped with an in situ reflectometer which is able to measure the reflectance spectra of the etched regions inside the ICP whilst running [101]. This tool was unfortunately not working at the time of the work included in this thesis but would have greatly improved the ability to precisely target specific layers of the epistructure such as the AlN etch stop layers included in the final designs of the LED material.

Producing a hard lithography mask for use with the mask aligner would speed up the fabrication process, avoiding the optimisation cycle required for working with the laser

lithography tool, as well as improve the consistency of final devices due to the uniform exposure. This would include all the required layers for creating an LED as well as the selective material thinning steps.

It is important to note, finally, that optimised approaches for GaN DBR-enhanced micro-LEDs and RCLEDs must be compatible with both high performance and mass manufacture. The work in this thesis has kept both of these major challenges in mind from the outset. This work has provided the basis of expected rapid developments in this area.

Bibliography

- [1] B. F. Spiridon *et al.*, “Method for inferring the mechanical strain of GaN-on-Si epitaxial layers using optical profilometry and finite element analysis,” *Optical Materials Express*, vol. 11, no. 6, pp. 1643–1655, Jun. 2021. DOI: 10.1364/OME.418728.
- [2] J. Yoon, S.-M. Lee, D. Kang, M. A. Meitl, C. A. Bower, and J. A. Rogers, “Heterogeneously integrated optoelectronic devices enabled by micro-transfer printing,” *Advanced Optical Materials*, vol. 3, no. 10, pp. 1313–1335, 2015. DOI: 10.1002/adom.201500365.
- [3] C. Klitis *et al.*, “Transfer printing of photonic nanostructures to silicon integrated circuits,” 2018. DOI: 10.1364/cleo_si.2018.sm2b.6.
- [4] Z. Wang, X. Shan, X. Cui, and P. Tian, “Characteristics and techniques of GaN-based micro-LEDs for application in next-generation display,” *Journal of Semiconductors*, vol. 41, no. 4, 2020, ISSN: 16744926. DOI: 10.1088/1674-4926/41/4/041606.
- [5] E. F. Schubert, *Light-Emitting Diodes*, 2nd ed. Cambridge University Press, 2006.
- [6] IEEE Electronics Packaging Society. “Heterogeneous Integration Roadmap.” (n.d.), [Online]. Available: <https://eps.ieee.org/technology/heterogeneous-integration-roadmap.html> (visited on 09/04/2024).
- [7] IEEE IRDS. “IRDS.” (n.d.), [Online]. Available: <https://irds.ieee.org/> (visited on 09/04/2024).

- [8] EPSRC. “Details of Grant.” (n.d.), [Online]. Available: <https://gow.epsrc.ukri.org/NGBOViewGrant.aspx?GrantRef=EP/R03480X/1> (visited on 08/07/2024).
- [9] Hetero-Print. “Hetero-Print.” (n.d.), [Online]. Available: <https://www.hetero-print.com/> (visited on 08/07/2024).
- [10] T. K. Ng *et al.*, “Group-III-nitride and halide-perovskite semiconductor gain media for amplified spontaneous emission and lasing applications,” *Journal of Physics D: Applied Physics*, vol. 54, p. 143001, Jan. 2021. DOI: 10.1088/1361-6463/abd65a.
- [11] N. Kaminski and O. Hilt, “SiC and GaN devices – wide bandgap is not all the same,” *IET Circuits, Devices & Systems*, vol. 8, no. 3, pp. 227–236, 2014. DOI: 10.1049/iet-cds.2013.0223.
- [12] T. Paskova, D. A. Hanser, and K. R. Evans, “GaN Substrates for III-Nitride Devices,” *Proceedings of the IEEE*, vol. 98, no. 7, pp. 1324–1338, 2010. DOI: 10.1109/JPROC.2009.2030699.
- [13] R. Zwierz, “Plasma enhanced growth of gan single crystalline layers from vapour phase,” Ph.D. dissertation, Jul. 2014.
- [14] “LED Lighting Market Size, Share & Trends Analysis Report By Product (Lamps, Luminaires), By Application, By Installation Type, By Sales Channel, By End-use, By Region, And Segment Forecasts, 2024 - 2030,” Grand View Research, Tech. Rep. GVR-2-68038-123-8, Jan. 2024.
- [15] M. M. Dumitrescu, M. J. Saarinen, M. D. Guina, and M. V. Pessa, “High-speed resonant cavity light-emitting diodes at 650 nm,” *IEEE Journal on Selected Topics in Quantum Electronics*, vol. 8, no. 2, pp. 219–230, 2002, ISSN: 1077260X. DOI: 10.1109/2944.999174.
- [16] A. J. Shaw, A. L. Bradley, J. F. Donegan, and J. G. Lunney, “GaN resonant cavity light-emitting diodes for plastic optical fiber applications,” *IEEE Photonics Technology Letters*, vol. 16, no. 9, pp. 2006–2008, 2004, ISSN: 10411135. DOI: 10.1109/LPT.2004.833116.

- [17] F.-M. Wu, C.-T. Lin, C.-C. Wei, C.-W. Chen, H.-T. Huang, and C.-H. Ho, "1.1-Gb/s White-LED-Based Visible Light Communication Employing Carrier-Less Amplitude and Phase Modulation," *IEEE Photonics Technology Letters*, vol. 24, pp. 1730–1732, Oct. 2012. DOI: 10.1109/LPT.2012.2210540.
- [18] PURELifi. "Our History." (n.d.), [Online]. Available: <https://www.purelifi.com/our-history/> (visited on 10/11/2024).
- [19] C.-H. Yeh, Y.-C. Yang, C.-W. Chow, Y.-W. Chen, and T.-A. Hsu, "VCSEL and LED based visible light communication system by applying decode-and-forward relay transmission," *Journal of Lightwave Technology*, vol. 38, no. 20, pp. 5728–5732, 2020. DOI: 10.1109/JLT.2020.3003352.
- [20] Fluke Networks. "LEDs vs. VCSELs." (n.d.), [Online]. Available: <https://www.flukenetworks.com/blog/cabling-chronicles/101-series-leds-vs-vcseles> (visited on 10/11/2024).
- [21] Firecomms. "Tech Briefs By Firecomms." (n.d.), [Online]. Available: <https://www.firecomms.com/news/tech-briefs-by-firecomms/> (visited on 09/09/2024).
- [22] R. Ji, S. Wang, Q. Liu, and W. Lu, "High-speed visible light communications: enabling technologies and state of the art," *Applied Sciences*, vol. 8, no. 4, 2018, ISSN: 2076-3417. DOI: 10.3390/app8040589.
- [23] R. X. G. Ferreira *et al.*, "High bandwidth GaN-based micro-LEDs for multi-Gb/s visible light communications," *IEEE Photonics Technology Letters*, vol. 28, no. 19, pp. 2023–2026, 2016. DOI: 10.1109/LPT.2016.2581318.
- [24] B. Corbett, R. Loi, W. Zhou, D. Liu, and Z. Ma, "Transfer print techniques for heterogeneous integration of photonic components," *Progress in Quantum Electronics*, vol. 52, no. February, pp. 1–17, 2017, ISSN: 0079-6727. DOI: 10.1016/j.pquantelec.2017.01.001.
- [25] J. Carreira *et al.*, "Integration of Micro-LED Array on CMOS by Transfer Printing," 2018, pp. 1–2. DOI: 10.1109/IPCon.2018.8527266.

- [26] B. Guilhabert *et al.*, “Transfer Printing of Semiconductor Nanowires with Lasing Emission for Controllable Nanophotonic Device Fabrication,” *ACS Nano*, vol. 10, no. 4, pp. 3951–3958, 2016, ISSN: 1936086X. DOI: 10.1021/acsnano.5b07752.
- [27] B. Guilhabert, J. McPhillimy, C. Kiltis, M. Dawson, M. Sorel, and M. Strain, “Nanoscale accurate heterogeneous integration of waveguide devices by transfer printing,” *2018 IEEE Photonics Conference (IPC)*, pp. 1–2, 2018. DOI: 10.1109/IPCon.2018.8527135.
- [28] J. McPhillimy, B. Guilhabert, C. Klitis, M. D. Dawson, M. Sorel, and M. J. Strain, “High accuracy transfer printing of single-mode membrane silicon photonic devices,” *Optics Express*, vol. 26, no. 13, pp. 297–300, 2018, ISSN: 10944087. DOI: 10.1364/OE.26.016679.
- [29] A. Hurtado *et al.*, “Transfer printing of semiconductor nanowire lasers,” *IET Optoelectronics*, vol. 12, no. 1, pp. 30–35, Feb. 2018, ISSN: 1751-8768. DOI: 10.1049/iet-opt.2017.0105.
- [30] C. Klitis *et al.*, “Transfer printing of photonic nanostructures to silicon integrated circuits,” *Optics InfoBase Conference Papers*, vol. Part F94-C, pp. 1–2, 2018. DOI: 10.1364/CLEO_SI.2018.SM2B.6.
- [31] S. Kim *et al.*, “Microstructured elastomeric surfaces with reversible adhesion and examples of their use in deterministic assembly by transfer printing,” *Proceedings of the National Academy of Sciences*, vol. 107, no. 40, pp. 17 095–17 100, 2010. DOI: 10.1073/pnas.1005828107.
- [32] C. Op de Beeck *et al.*, “Heterogeneous III-V on silicon nitride amplifiers and lasers via microtransfer printing,” *Optica*, vol. 7, no. 5, p. 386, 2020, ISSN: 2334-2536. DOI: 10.1364/optica.382989.
- [33] X-Celeprint. “X-Celeprint.” (n.d.), [Online]. Available: <https://x-celeprint.com> (visited on 09/16/2024).
- [34] XDisplay. “MTP Equipment.” (n.d.), [Online]. Available: <https://www.xdisplay.com/mtp-equipment> (visited on 09/16/2024).

- [35] EPSRC National Epitaxy Facility. "MTP Equipment." (n.d.), [Online]. Available: <https://www.nationalepitaxyfacility.co.uk/news-and-events/micro-transfer-print-tool-addition-at-the-national-epitaxy-facility> (visited on 09/16/2024).
- [36] P. Griffin and R. Oliver, "Porous nitride semiconductors reviewed," 2020. DOI: 10.17863/CAM.54111.
- [37] W. Cai *et al.*, "GaN-on-Si resonant-cavity light-emitting diode incorporating top and bottom dielectric distributed Bragg reflectors," *Applied Physics Express*, vol. 12, no. 3, p. 032004, 2019. DOI: 10.7567/1882-0786/ab023c.
- [38] T. Hamaguchi, H. Nakajima, and N. Fuutagawa, "GaN-based vertical-cavity surface-emitting lasers incorporating dielectric distributed Bragg reflectors," *Applied Sciences*, vol. 9, no. 4, 2019, ISSN: 2076-3417. DOI: 10.3390/app9040733.
- [39] W. Whyte, *Cleanroom technology: fundamentals of design, testing and operation*. John Wiley & Sons, 2010. DOI: 10.1002/0470858389.
- [40] S. Franssila, *Introduction to Microfabrication*, 2nd ed. Wiley-Blackwell, Sep. 2010. DOI: 10.1002/9781119990413.
- [41] D. Chinn, "Microfabrication techniques for biologists: a primer on building micromachines," in *Microengineering in Biotechnology*. Humana Press, 2010, pp. 1–53. DOI: 10.1007/978-1-60327-106-6_1.
- [42] Brigham Young University. "Automatic Dicing Saw." (n.d.), [Online]. Available: https://cleanroom.byu.edu/dicing_saw (visited on 06/24/2024).
- [43] Allwin21 Corp. "Plasma Ashing." (2017), [Online]. Available: <https://allwin21.com/plasma-ashing/> (visited on 04/10/2024).
- [44] Microchemicals. "Photoresists." (n.d.), [Online]. Available: <https://www.microchemicals.com/products/photoresists.html> (visited on 04/10/2024).
- [45] M. Iam. "Photoresists of Photolithography." (Mar. 2017), [Online]. Available: https://upload.wikimedia.org/wikipedia/commons/5/53/Photoresist_of_Photolithography.png (visited on 04/05/2024).

- [46] Microchemicals. “HMDS.” (n.d.), [Online]. Available: https://www.microchemicals.com/products/adhesion_promotion/hmgs.html (visited on 04/04/2024).
- [47] Shipley. “MICROPOSIT S1800 Series Photo Resists.” (n.d.), [Online]. Available: https://amolf.nl/wp-content/uploads/2016/09/datasheets_S1800.pdf (visited on 04/05/2024).
- [48] S. Wolf and R. Tauber, *Silicon Processing for the VLSI Era: Process technology* (Silicon Processing for the VLSI Era). Lattice Press, 2000, pp. 532–533, ISBN: 9780961672164.
- [49] J. F. C. Carreira, “Hybrid micro-LED devices enabled by elastomeric micro-transfer printing,” Ph.D. dissertation, University of Strathclyde, Nov. 2020.
- [50] Oxford Instruments. “Reactive Ion Etching (RIE).” (n.d.), [Online]. Available: <https://plasma.oxinst.com/technology/reactive-ion-etching> (visited on 04/09/2024).
- [51] Oxford Instruments. “Inductively Coupled Plasma Etching (ICP RIE).” (n.d.), [Online]. Available: <https://plasma.oxinst.com/technology/icp-etching> (visited on 04/09/2024).
- [52] S. Smith, C. Wolden, M. Bremser, A. Hanser, R. Davis, and W. Lampert, “Selective and non-selective etching of GaN, AlGaN, and AlN using an inductively coupled plasma,” in *Compound Semiconductors 1997. Proceedings of the IEEE Twenty-Fourth International Symposium on Compound Semiconductors*, IEEE, 1997, pp. 349–352. DOI: 10.1109/ISCS.1998.711652.
- [53] T. Kim and J. Lee, “Optimization of deep reactive ion etching for microscale silicon hole arrays with high aspect ratio,” *Micro Nano Syst. Lett.*, vol. 10, no. 1, Sep. 2022. DOI: 10.1186/s40486-022-00155-6.
- [54] K. Bean, “Anisotropic etching of silicon,” *IEEE Transactions on Electron Devices*, vol. 25, no. 10, pp. 1185–1193, 1978. DOI: 10.1109/T-ED.1978.19250.

- [55] S. Tan, R. Boudreau, and M. L. Reed, “Anisotropic etching of silicon on{111} and near{111} planes,” *Sensors and Materials (Japan)*, vol. 13, no. 5, pp. 303–313, 2001.
- [56] R. E. Oosterbroek *et al.*, “Etching methodologies in <111>-oriented silicon wafers,” *Journal of microelectromechanical systems*, vol. 9, no. 3, pp. 390–398, 2000. DOI: 10.1109/84.870065.
- [57] Microchem. “NANO SU-8 Negative Tone Photoresist formulations 50-100.” (n.d.), [Online]. Available: http://cleanroom.groups.et.byu.net/su8.parts/SU8_50-100.pdf (visited on 04/12/2024).
- [58] Dow. “Sylgard 184 Silicone Elastomer Kit Technical Content.” (n.d.), [Online]. Available: <https://www.dow.com/en-us/pdp.sylgard-184-silicone-elastomer-kit.01064291z.html#tech-content> (visited on 06/24/2024).
- [59] M. Kim, B.-U. Moon, and C. Hidrovo, “Enhancement of the thermo-mechanical properties of PDMS molds for the hot embossing of PMMA microfluidic devices,” *Journal of Micromechanics and Microengineering*, vol. 23, p. 095 024, Aug. 2013. DOI: 10.1088/0960-1317/23/9/095024.
- [60] J. Schmit, K. Creath, and J. C. Wyant, *Surface Profilers, Multiple Wavelength, and White Light Intereferometry*. John Wiley & Sons, Ltd, 2007, ch. 15, pp. 667–755, ISBN: 9780470135976. DOI: 10.1002/9780470135976.ch15.
- [61] D. Nečas and P. Klapetek. “Gwyddion.” (n.d.), [Online]. Available: <http://gwyddion.net/> (visited on 04/18/2024).
- [62] P. Eaton and P. West, *Atomic Force Microscopy*. OUP Oxford, 2010, ISBN: 9780199570454. DOI: 10.1093/acprof:oso/9780199570454.001.0001.
- [63] S. Fairclough, A. Hinz, S. Ghosh, B. Spiridon, D. Wallis, R. Oliver, *et al.*, “Direct evidence of an Al alloyed SiNx interlayer within an ammonia predosed AlN/Si interface via STEM-EELS,” in *Proceedings of Electron Beam Spectroscopy for Nanooptics 2021 (EBSN2021)*, 2021.

- [64] R. A. Oliver, M. J. Kappers, C. J. Humphreys, and G. A. D. Briggs, “Growth modes in heteroepitaxy of InGaN on GaN,” *Journal of Applied Physics*, vol. 97, no. 1, Dec. 2004, ISSN: 0021-8979. DOI: 10.1063/1.1823581.
- [65] Vitrek. “About Wafer Bow And Warp Measurement Systems.” (n.d.), [Online]. Available: <https://vitrek.com/applications/wafer-bow-and-warp/> (visited on 07/04/2024).
- [66] Micro resist technology. “ma-N 1400 series.” (n.d.), [Online]. Available: <https://www.microresist.de/en/produkt/ma-n-1400-series/> (visited on 05/30/2024).
- [67] M. R. Amirzada, A. Tatzel, V. Vierec, and H. Hillmer, “Surface roughness analysis of SiO₂ for PECVD, PVD and IBD on different substrates,” *Applied Nanoscience*, vol. 6, no. 2, Feb. 2016. DOI: 10.1007/s13204-015-0432-8.
- [68] M. Klear. “circle-fit 0.1.3.” (n.d.), [Online]. Available: <https://pypi.org/project/circle-fit/0.1.3/> (visited on 06/05/2024).
- [69] K. Kanatani and P. Rangarajan, “Hyper least squares fitting of circles and ellipses,” *Computational Statistics & Data Analysis*, vol. 55, no. 6, pp. 2197–2208, 2011, ISSN: 0167-9473. DOI: 10.1016/j.csda.2010.12.012.
- [70] Park Systems. “XEI Software Mmanual.” (n.d.), [Online]. Available: https://cores.research.asu.edu/sites/default/files/2020-08/XEIManual_1_8_0_0.pdf (visited on 06/06/2024).
- [71] N. Barradas *et al.*, “Roughness in GaN/InGaN films and multilayers determined with Rutherford backscattering,” *Nuclear Instruments and Methods in Physics Research Section B: Beam Interactions with Materials and Atoms*, vol. 217, no. 3, pp. 479–497, 2004, ISSN: 0168-583X. DOI: 10.1016/j.nimb.2003.11.009.
- [72] I. Newton, *Opticks: or, A treatise of the reflections, refractions, inflexions and colours of light*, 1st ed. Printed for Sam. Smith, and Benj. Walford, 1704. DOI: 10.5479/sil.302475.39088000644674.
- [73] H. D. Young and R. A. Freedman, *University Physics with Modern Physics Technology Update*, 13th ed. Pearson, 2013, ISBN: 978-0-321-69686-1.

- [74] N. K. Wessling *et al.*, “Fabrication and transfer printing based integration of free-standing GaN membrane micro-lenses onto semiconductor chips,” *Optical Materials Express*, vol. 12, no. 12, pp. 4606–4618, Dec. 2022. DOI: 10.1364/OME.472999.
- [75] QPIT Münster. “Welcome to the gdshelpers’ documentation!” (N.d.), [Online]. Available: <https://gdshelpers.readthedocs.io/en/latest/> (visited on 06/18/2024).
- [76] S. Gilles. “Shapely 2.0.4.” (n.d.), [Online]. Available: <https://pypi.org/project/shapely/> (visited on 06/18/2024).
- [77] S. Gilles. “Shapely 2.0.4 Documentation.” (n.d.), [Online]. Available: <https://shapely.readthedocs.io/en/stable/index.html> (visited on 06/18/2024).
- [78] M. Bikerouin and M. Balli, “Electric field and strain induced gap modifications in multilayered GaN,” *Applied Surface Science*, vol. 578, p. 151970, 2022, ISSN: 0169-4332. DOI: <https://doi.org/10.1016/j.apsusc.2021.151970>.
- [79] R. Frisenda *et al.*, “Micro-reflectance and transmittance spectroscopy: a versatile and powerful tool to characterize 2D materials,” *Journal of Physics D: Applied Physics*, vol. 50, no. 7, p. 074002, Jan. 2017. DOI: 10.1088/1361-6463/aa5256.
- [80] Dow. “MEGAPOSIT SPR 220 Series i-Line Photoresists.” (n.d.), [Online]. Available: <https://kayakuam.com/wp-content/uploads/2019/09/SPR-220-DATA-SHEET-RH-1.pdf> (visited on 07/21/2024).
- [81] C. J. R. Sheppard, “Approximate calculation of the reflection coefficient from a stratified medium,” *Pure and Applied Optics: Journal of the European Optical Society Part A*, vol. 4, no. 5, p. 665, Sep. 1995. DOI: 10.1088/0963-9659/4/5/018.
- [82] M. J. Bergmann and H. C. Casey, “Optical-field calculations for lossy multiple-layer $\text{Al}_x\text{Ga}_{1-x}\text{N}/\text{In}_x\text{Ga}_{1-x}\text{N}$ laser diodes,” *Journal of Applied Physics*, vol. 84, pp. 1196–1203, 1998. DOI: 10.1063/1.368185.

- [83] M. Auf der Maur, A. Pecchia, G. Penazzi, W. Rodrigues, and A. Di Carlo, “Unraveling the “Green Gap” problem: The role of random alloy fluctuations in InGaN/GaN light emitting diodes,” *Physical Review Letters*, vol. 116, Oct. 2015. DOI: 10.1103/PhysRevLett.116.027401.
- [84] S. Adachi, *Optical constants of crystalline and amorphous semiconductors*. Springer, Aug. 1999. DOI: 10.1007/978-1-4615-5247-5.
- [85] W. S. M. Werner, K. Glantschnig, and C. Ambrosch-Draxl, “Optical Constants and Inelastic Electron-Scattering Data for 17 Elemental Metals,” *Journal of Physical and Chemical Reference Data*, vol. 38, no. 4, pp. 1013–1092, Dec. 2009. DOI: 10.1063/1.3243762.
- [86] S. L. Chuang, *Physics of Photonic Devices*, en, 2nd ed. Wiley, Dec. 2008, ISBN: 978-0-470-29319-5.
- [87] R. Paschotta. “Sellmeier Formula.” (2005), [Online]. Available: https://www.rp-photonics.com/sellmeier_formula.html (visited on 05/28/2025).
- [88] T. Kawashima, H. Yoshikawa, S. Adachi, S. Fuke, and K. Ohtsuka, “Optical properties of hexagonal GaN,” *Journal of Applied Physics*, vol. 82, no. 7, pp. 3528–3535, Oct. 1997. DOI: 10.1063/1.365671.
- [89] A. S. Barker and M. Ilegems, “Infrared Lattice Vibrations and Free-Electron Dispersion in GaN,” *Phys. Rev. B*, vol. 7, pp. 743–750, 2 Jan. 1973. DOI: 10.1103/PhysRevB.7.743.
- [90] G. Laws, E. Larkins, I. Harrison, C. Molloy, and D. Somerford, “Improved refractive index formulas for the $\text{Al}_x\text{Ga}_{1-x}\text{N}$ and $\text{In}_y\text{Ga}_{1-y}\text{N}$ alloys,” *Journal of Applied Physics*, vol. 89, pp. 1108–1115, Feb. 2001. DOI: 10.1063/1.1320007.
- [91] N. Antoine-Vincent *et al.*, “Determination of the refractive indices of AlN, GaN, and $\text{Al}_x\text{Ga}_{1-x}\text{N}$ grown on (111) Si substrates,” *Journal of Applied Physics*, vol. 93, no. 9, pp. 5222–5226, May 2003, ISSN: 0021-8979. DOI: 10.1063/1.1563293.

- [92] C. Nayak, G. Palai, and P. Sarkar, "Investigation of mole fraction in nitride semiconductor using photonic bandgap analysis," *Optik*, vol. 127, no. 2, pp. 697–699, 2016, ISSN: 0030-4026. DOI: 10.1016/j.ijleo.2015.10.131.
- [93] S. I. Bahn *et al.*, "Determination of the Al Mole Fraction in Epitaxial $\text{Al}_x\text{Ga}_{1-x}\text{N}/\text{GaN}$ ($x < 0.25$) Heterostructures," *Journal of the Korean Physical Society*, vol. 43, no. 3, pp. 381–385, 2003, ISSN: 03744884.
- [94] J. A. Engelbrecht, B. Sephton, E. Minnaar, and M. C. Wagener, "An alternative method to determine the refractive index of $\text{Al}_x\text{Ga}_{1-x}\text{N}$," *Physica B: Condensed Matter*, vol. 480, pp. 181–185, 2016, ISSN: 09214526. DOI: 10.1016/j.physb.2015.08.047.
- [95] Ansys. "Ansys Lumerical FDTD." (n.d.), [Online]. Available: <https://www.ansys.com/en-gb/products/optics/fdtd> (visited on 08/07/2024).
- [96] Ansys. "Reflection and transmission calculations using a planewave." (n.d.), [Online]. Available: <https://optics.ansys.com/hc/en-us/articles/360042089573-Reflection-and-transmission-calculations-using-a-planewave> (visited on 08/07/2024).
- [97] W. W. Coblenz, "The reflecting power of various metals," *Journal of the Franklin Institute*, vol. 170, no. 3, pp. 169–193, 1910, ISSN: 00160032. DOI: 10.1016/S0016-0032(10)90867-3.
- [98] P. Maaskant, M. Akhter, B. Roycroft, E. O'Carroll, and B. Corbett, "Fabrication of GaN-based resonant cavity LEDs," *physica status solidi (a)*, vol. 192, no. 2, pp. 348–353, 2002. DOI: 10.1002/1521-396X(200208)192:2<348::AID-PSSA348>3.0.CO;2-6.
- [99] A. Shaw, A. Bradley, J. Donegan, and J. Lunney, "GaN resonant cavity light-emitting diodes for plastic optical fiber applications," *IEEE Photonics Technology Letters*, vol. 16, no. 9, pp. 2006–2008, 2004. DOI: 10.1109/LPT.2004.833116.

- [100] M. Fabian, E. Lewis, T. Neue, and S. Lochmann, “Optical fibre cavity for ring-down experiments with low coupling losses,” *Measurement Science and Technology*, vol. 21, p. 094034, Jul. 2010. DOI: 10.1088/0957-0233/21/9/094034.

- [101] W. Wang, Z. Lan, W. Wen, and Y. Gong, “Optical interferometry endpoint detection for plasma etching,” *2007 8th International Conference on Electronic Measurement and Instruments, ICEMI*, pp. 4252–4255, 2007. DOI: 10.1109/ICEMI.2007.4351131.

Appendix A

Python Code

```
1  # -*- coding: utf-8 -*-
2  """
3  Created on Fri Dec 18 13:37:27 2020
4  @author: MILES
5  fixes the mix of units and addition of letters to the output of probe station
6  when the option: "UNIT = YES" is selected
7  """
8  import numpy as np
9  import os.path
10 from tkinter import Tk
11 from tkinter import filedialog
12 #%%
13 root = Tk()
14 file = filedialog.askopenfile(initialdir="/", # select .txt file
15                               title="Open File",
16                               filetypes=(("Text Files", "*.txt"), ("All Files", "*.*")))
17 name = os.path.basename(file.name) # string for saving file later
18 root.destroy() # closing window after selection
19 my_file = open("temp_file.txt", "w+")
20 for line in file:
21     line = line.replace('-', '') # remove dashes
22     line = line.replace('V', '') # remove V unit
23     line = line.replace('  ', '') # remove triple spaces
24     line = line.replace(' ', '') # remove double spaces
25     line = line.replace(' ', '') # remove spaces
26     my_file.write(line)
27 file.seek(0)
28 my_file.seek(0)
29 d = np.loadtxt(my_file, delimiter=',', skiprows = 5, usecols=(1), dtype=(str))
30 for i in range(d.size): # finding and converting milli units
31     if "m" in d[i]:
32         d[i] = d[i][:-1]
33         d[i] = float(d[i]) * 0.001
34 V = d.astype(np.float)
35 my_file.seek(0)
36 #%% (cell separator)
37 e = np.loadtxt(my_file, delimiter=',', skiprows = 5, usecols=(2), dtype=(str))
38 for i in range(e.size): # replacing mixed units
39     if "pA" in e[i]:
40         this_i = e[i][:-2]
```

A. Python Code

```
41         this_i = (float(this_i))
42         e[i] = this_i * 0.000001
43     if "nA" in e[i]:
44         this_j = e[i][:-2]
45         this_j = (float(this_j))
46         e[i] = this_j * 0.001
47     if "uA" in e[i]:
48         this_k = e[i][:-2]
49         e[i] = (float(this_k))
50     if "mA" in e[i]:
51         this_k = e[i][:-2]
52         this_k = (float(this_k))
53         e[i] = this_k * 1000
54 I = e.astype(np.float) # converts all elements of array to float
55 I = I/1000000 # converting from uA to A
56 file.close() # closing files
57 my_file.close()
58 #%%
59 V2 = V[-501:] # selecting one trace out of five
60 I2 = I[-501:]
61 output = np.column_stack((V2, I2)) # making a single array
62 np.savetxt('new'+name, output, delimiter=',',header='V (V), I (A)')
```

Listing 1: A script to clean the *.txt* file produced from the Wentworth 280X probe station measuring I V data when the UNITS option is selected. Removes the units string from the numbers and converts everything to the same units as floats. Produces a double column *.txt* file.

A. Python Code

```
1 # -*- coding: utf-8 -*-
2 """
3 Created on Sat Dec 19 17:19:36 2020
4 @author: MILES
5 Opens IV data and plots, calculates switch on V and differential R
6 """
7 import numpy as np
8 import os.path
9 from tkinter import Tk
10 from tkinter import filedialog
11 import matplotlib.pyplot as plt
12 #%%
13 root = Tk()
14 file = filedialog.askopenfile(initialdir="/", # selecting .txt file with IV data
15                               title="Open File",
16                               filetypes=(("Text Files", "*.txt"), ("All Files", "*.*")))
17 name = os.path.basename(file.name) # string for saving file later
18 root.destroy() # closing window after selection
19 file.seek(0) # go to top line of file
20 iv = np.loadtxt(file, delimiter=',', skiprows = 1, usecols=(0,1), dtype=(float))
21 #%%
22 plt.plot(iv[:,0], iv[:,1], label='measured current', color='k') # IV curve
23 gradient = np.gradient(iv[:,1],iv[:,0]) # array of gradients along curve
24 m = gradient[-10] # value of gradient at end of line (where it is linear)
25 c = iv[:,1][-10] - m*iv[:,0][-10] # finding y intercept
26 y = m*iv[:,0] + c # creating straight line tangent to IV curve
27 Von = -1*c/m # switch on voltage (x axis intercept)
28 Vonr = round(Von,3) # rounding value
29 Rd = 1/m # differential resistance of LED
30 Rdr = round(Rd,3) # rounding value
31 plt.plot(iv[:,0],y, label='differential resistance = ' + str(Rdr)+ '  $\Omega$ ', color='b',
32          linestyle='dashed')
33 plt.hlines(0,0,5, linestyle='dashed', linewidth = 1) # zero line
34 plt.ylim((-0.00001,iv[:,1][-1])) # setting limits to plot
35 plt.xlim((0,iv[:,0][-1]))
36 plt.xlabel('Potential (V)')
37 plt.ylabel('Current (A)')
38 plt.ticklabel_format(style='sci', axis='y', scilimits=(0,0))
39 plt.plot(Von,0, marker='x', color='r', markersize=10, label='turn-on voltage = '+str(Vonr)
40          + ' V')
41 plt.title('IV of sample: ' + name[4:-4])
42 plt.legend()
```

Listing 2: A script to plot the IV data stored as a *.txt* file produced from the Wentworth 280X probe station. Calculates the turn-on voltage and the differential resistance then adds it to the plot.

A. Python Code

```
1 # -*- coding: utf-8 -*-
2 """
3 Created on Wed Apr 22 14:18:59 2020
4 @author: Miles Toon
5 Fitting a circular arc to profile data - central
6 """
7 import numpy as np
8 from circle_fit import hyper_fit as hf
9 import matplotlib.pyplot as plt
10 import os
11 from tkinter import Tk
12 from tkinter import filedialog
13 from pathlib import PureWindowsPath
14 import math
15 #%%
16 ''' methods '''
17 def makeCircle(xc,yc,R):
18     xarr=[]
19     yarr=[]
20     for i in range(14400):
21         y = yc + R*math.sin(i/40)
22         x = xc + R*math.cos(i/40)
23         xarr.append(x)
24         yarr.append(y)
25     return xarr, yarr
26
27 def valRange(A):
28     return (max(A)-min(A))
29
30 def Sag(R,l):
31     s = R - np.sqrt(R**2 - (l/2)**2)
32     return s
33 #%%
34 '''open folder and import files'''
35 root = Tk()
36 root.withdraw()
37 path = filedialog.askdirectory()+"/" # opens window to select folder
38 path_on_windows = str(PureWindowsPath(path))
39 fnames = os.listdir(path) # names of files
40 allData = [np.loadtxt(path + f) for f in fnames] # loads in data from files
41 #%%
42 '''loop through and plot'''
43 maxDisplacements = [("Sample", "Radius of Curvature (mm)", "Error (mm)",
44     "Vertical Displcement ( $\mu\text{m}$ )", "Sag ( $\mu\text{m}$ )")] # headers
45 i = 0
46 for data in allData:
47     plt.figure(figsize = (10,5))
48     x = data[:,0]
49     y = data[:,1]
50     xc, yc, R, err = hf(data) # hyperfit circle from data
51     Rmm =round((R*1000),3) # radius in mm
52     errmm = round((err*1000),3) # error on fit in mm
53     newx, newy = makeCircle(xc,yc, R)
54     S = Sag(R,100e-6)*1000000 # sag of circle over 70 microns in microns
55     newx2 = [i * 1000 for i in newx] # circle now in mm
56     newy2 = [i * 1000000 for i in newy] # circle now in microns
57     x2 = x * 1000 # original profile data now in mm
58     y2 = y * 1000000 # original profile data now in microns
59     xrange = valRange(x2) # location for max and min values
60     yrange = valRange(y2)
61     xbar = [(min(x2) - 0.06*xrange), (min(x2) - 0.04*xrange)]
62     ytop = [max(y2), max(y2)]
```

A. Python Code

```
63     ybot = [min(y2), min(y2)] # array for drawing max displacements on plot
64     fit = plt.scatter(newx2,newy2, 5, 'r') # draw circle fit
65     realdata = plt.scatter(x2,y2, 5, 'k') # draw original profile
66     maxDisp = plt.vlines(min(x2) - 0.05*xrange, min(y2), max(y2), 'b')
67     topBar = plt.plot(xbar,ytop,'b') # vertical displacement drawing
68     botBar = plt.plot(xbar,ybot,'b')
69     plt.xlim(min(x2) - 0.1*xrange, max(x2) + 0.1*xrange)
70     plt.xlabel("Horizontal Distance (mm)", fontsize = 18)
71     plt.xticks(fontsize = 16)
72     plt.ylim(min(y2) - 0.1*yrange, max(y2) + 0.1*yrange)
73     plt.ylabel("Vertical Distance ( $\mu\text{m}$ )", fontsize = 18)
74     plt.yticks(fontsize = 16)
75     plt.legend((realdata, fit, maxDisp),("sample: " + fnames[i][:-4],
76         "circular arc fit: ROC = " + str(Rmm) + "±" + str(errmm) + "mm",
77         "maximum vertical displacement = " + str(round(yrange,3)) + " $\mu\text{m}$ "),
78         loc = 9, fontsize = 14)
79     maxDisplacements.append((fnames[i][:-4], Rmm, errmm, round(yrange,3), round(S,3))
80     i+=1
81     ###
82     '''write text file'''
83     with open(fnames[0][:4] + "_data.txt", 'w') as output:
84         for row in maxDisplacements:
85             output.write(str(row)[1:-1] + '\n')
```

Listing 3: A script which approximate a circle using a hyper-fit algorithm using a .txt file profile. Used for analysing the optical profiler data of suspended membranes.

A. Python Code

```
1 # -*- coding: utf-8 -*-
2 '''
3 Created on Fri Sep 2 11:45:38 2022
4 @author: MILES
5 for creating suspended LEDs with various tether options
6 improved performance with single loop - origin at (0,0)
7 '''
8 import numpy as np
9 from gdshelpers.geometry.chip import Cell
10 from shapely.geometry import Polygon, Point
11 from shapely.ops import unary_union
12 from gdshelpers.parts.text import Text
13 from datetime import datetime
14 start = datetime.now() # to measure the run time of the script
15 #%%
16 ''' defining variables '''
17 maskx = 16000 # this is the width of your sample in microns
18 masky = 12000 # this is the height of your sample in microns
19 border = 2000 # this is the gap between the sample edge and your pixels
20 vspacing = 120 # the pitch of each pixel in y
21 hspacing = 170 # the pitch of each pixel in x
22 tether_length = 10 # how long each tether is
23 tether_width = 3 # thickness of the tethers in microns
24 tether_location = 0.25 # location along edge of pixel
25 pixel_size = 100 # how big each pixel is going to be in microns
26
27 # options for manual control of feature size, would need to modify code below
28 n_size = 43 # not actually used, scaled off the pixel size
29 contact_size = 30 # not actually used, scaled off the pixel size
30 contact_style = 1 # 0 for square (default), 1 for sector shape
31 rows = (masky-(border*2))/vspacing # sets the number of rows
32 columns = (maskx-(border*2))/hspacing # sets the number of columns
33 #%%
34 ''' methods '''
35 def box(x=0, y=0, width=100, height=100):
36     ''' creates a rectangle. Used for creating the membrane geometry '''
37     x1 = x-width*0.5
38     x2 = x+width*0.5
39     y1 = y-height*0.5
40     y2 = y+height*0.5
41     mybox = Polygon([(x1,y1), (x2,y1), (x2,y2), (x1,y2)])
42     return mybox
43
44 def bowtether(x=0, y=0, width=5, length=10, notch_width=3, notch_height=1.5):
45     ''' creates the bow tie tether geometry '''
46     x1 = x-length*0.5
47     x2 = x-notch_width*0.5
48     x3 = x+notch_width*0.5
49     x4 = x+length*0.5
50     y1 = y-width*0.5
51     y2 = y-(0.5*width)+notch_height
52     y3 = y+(0.5*width)-notch_height
53     y4 = y+width*0.5
54     tether= Polygon([(x1,y4), (x1,y1), (x2,y1), (x,y2), (x3,y1), (x4,y1), (x4,y4),
55 (x3,y4), (x,y3), (x2,y4)])
56     return tether
57
58 def crossmarker(x=0, y=0, size=100, thickness=2):
59     ''' creates a crosses for alignment '''
60     x1 = x - size*0.5
61     x2 = x - thickness*0.5
62     x3 = x + thickness*0.5
```

A. Python Code

```
63     x4 = x + size*0.5
64     y1 = y - size*0.5
65     y2 = y - thickness*0.5
66     y3 = y + thickness*0.5
67     y4 = y + size*0.5
68     cross = Polygon([(x2,y4), (x3,y4), (x3,y3), (x4,y3), (x4,y2), (x3,y2),
69                     (x3,y1), (x2,y1), (x2,y2), (x1,y2), (x1,y3), (x2,y3)])
70     return cross
71
72 def sector(center, start_angle, end_angle, radius, steps=200):
73     ''' an optional shape for the contacts '''
74
75     def polar_point(origin_point, angle, distance):
76         return [origin_point.x + np.sin(np.radians(angle)) * distance,
77                 origin_point.y + np.cos(np.radians(angle)) * distance]
78
79     if start_angle > end_angle:
80         start_angle = start_angle - 360
81     else:
82         pass
83     step_angle_width = (end_angle-start_angle) / steps
84     sector_width = (end_angle-start_angle)
85     sector_vertices = []
86     sector_vertices.append(polar_point(center, 0,0))
87     sector_vertices.append(polar_point(center, start_angle,radius))
88
89     for z in range(1, steps):
90         sector_vertices.append((polar_point(center, start_angle + z *
91                                             step_angle_width,radius)))
92     sector_vertices.append(polar_point(center, start_angle+sector_width,radius))
93     sector_vertices.append(polar_point(center, 0,0))
94     return Polygon(sector_vertices)
95
96 def hexagon(x, y, l):
97     '''
98     create a hexagon centered on (x, y)
99     :param l: length of the hexagon's edge
100    :param x: x-coordinate of the hexagon's center
101    :param y: y-coordinate of the hexagon's center
102    :return: The Polygon containing the hexagon's coordinates
103    '''
104    c = [[x + np.cos(np.radians(angle)) * l, y + np.sin(np.radians(angle)) * l]
105         for angle in range(30, 390, 60)]
106    return Polygon(c)
107
108 def arrow(x, y, l):
109     ''' creates a chevron to show direction '''
110     c = [[x + np.cos(np.radians(angle)) * l, y + np.sin(np.radians(angle)) * l]
111         for angle in range(30, 210, 60)]
112     new_list=[]
113     for i in c:
114         new_list.append([i[0],i[1]+100])
115     full_list = c + new_list[::-1]
116     arrow = Polygon(full_list)
117     return arrow
118
119 ###
120 ''' creating the arrays centred about origin '''
121 myrows_uncentred = np.empty([rows,1])
122 mycolumns_uncentred = np.empty([columns,1])
123 for i in range(rows):
124     myrows_uncentred[i] = (border+(i+0.5)*vspacing)
125 for j in range(columns):
126     mycolumns_uncentred[j] = (border+(j+0.5)*hspacing)
```

A. Python Code

```
127 # create functions to center data
128 center_function = lambda array: array - array.mean()
129 # apply functions to original NumPy array
130 mycolumns = center_function(mycolumns_uncentred)
131 myrows = center_function(myrows_uncentred)
132 ###
133 ''' creation of cell heirachy, each cell corresponds to a layer in the GDS '''
134 mycell = Cell('TOPCELL')
135 cell0 = Cell('MASK')
136 mycell.add_cell(cell0)
137 cell1 = Cell('SQUARES')
138 mycell.add_cell(cell1)
139 cell2 = Cell('MEMBRANES')
140 mycell.add_cell(cell2)
141 cell3 = Cell('N_ETCH')
142 mycell.add_cell(cell3)
143 cell4 = Cell('CONTACTS')
144 mycell.add_cell(cell4)
145 ###
146 ''' creation of markers '''
147 x1= -maskx*0.5+border-200 # location of markers
148 x2= maskx*0.5-border+200
149 y1= -masky*0.5+border-200
150 y2= masky*0.5-border+200
151 cross1 = crossmarker(x1,y1) # for alignment markers
152 cross2 = crossmarker(x1,y2)
153 cross3 = crossmarker(x2,y2)
154 cross4 = crossmarker(x2,y1)
155 cross5 = crossmarker(0,y1)
156 cross6 = crossmarker(0,y2)
157 box1 = box(x1,y1,120,120) # for alignment markers
158 box2 = box(x1,y2,120,120)
159 box3 = box(x2,y2,120,120)
160 box4 = box(x2,y1,120,120)
161 box5 = box(0,y1,120,120)
162 box6 = box(0,y2,120,120)
163 endpoint_box = hexagon(x1-350,0,500) # larger region to etch for endpoint detection
164 endpoint_arrow = arrow(x1-350,200,500) # denotes the first etch process
165 endpoint_box2 = hexagon(x2+350,0,500) # area for endpoint detection in second etch process
166 endpoint_arrow2 = arrow(x2+350,200,500) # two arrows for second etch process
167 endpoint_arrow3 = arrow(x2+350,400,500)
168 crosses = unary_union([cross1,cross2,cross3,cross4,cross5,cross6]) # grouping together
169 boxes = unary_union([box1,box2,box3,box4,box5,box6]) # grouping together
170 neg_markers = boxes.difference(crosses) # making a new set of negatives for alignment
171 # adding geometries to respective layers
172 cell1.add_to_layer(1,neg_markers,endpoint_box,endpoint_arrow) # selective etching to thin
    structure
173 cell2.add_to_layer(2,crosses,endpoint_box,endpoint_arrow)
174 cell3.add_to_layer(3,crosses,endpoint_box2,endpoint_arrow2, endpoint_arrow3)
175 cell4.add_to_layer(4,crosses)
176 ###
177 ''' CELLO - creation of mask size display (physical size of sample) '''
178 mymask = box(0,0,maskx,masky)
179 cell0.add_to_layer(0,mymask)
180 ###
181 ''' main loop to create the geometries '''
182 for i in range(rows):
183     for j in range(columns):
184         ''' CELL1 - creation of squares for selective etching tethers '''
185         outbox = box(mycolumns[j],myrows[i],hspacing,vspacing)
186         inbox = box(mycolumns[j],myrows[i],width=pixel_size,height=pixel_size)
187         mybox = outbox.difference(inbox)
188         cell1.add_to_layer(1, mybox)
189 ###
```

A. Python Code

```
190     ''' CELL2 - membrane geometry '''
191     x = mycolumns[j]
192     y = myrows[i]
193     outbox = box(x,y,(pixel_size+tether_length*2),vspacing)
194     pixel = box(x,y,width=pixel_size,height=pixel_size)
195     if (j%2)==0: # alternates between bowtethers and straight
196         tether1 = bowtether(x-(pixel_size+tether_length)*0.5,
197                             y-(tether_location*pixel_size))
198         tether2 = bowtether(x+(pixel_size+tether_length)*0.5,
199                             y+(tether_location*pixel_size))
200
201         inner= unary_union([pixel, tether1, tether2])
202         membrane = outbox.difference(inner)
203         cell2.add_to_layer(2,membrane)
204     else:
205         tether1 = box(x-(pixel_size+tether_length)*0.5,
206                     y-(tether_location*pixel_size),
207                     tether_length,
208                     tether_width)
209         tether2 = box(x+(pixel_size+tether_length)*0.5,
210                     y+(tether_location*pixel_size),
211                     tether_length,
212                     tether_width)
213         inner= unary_union([pixel, tether1, tether2])
214         membrane = outbox.difference(inner)
215         cell2.add_to_layer(2,membrane)
216     ###
217     ''' CELL3 - creation of n layer etch '''
218     if contact_style==1:
219         centre = Point(mycolumns[j]+pixel_size*0.5,myrows[i]-pixel_size*0.5)
220         sect = sector(centre,270,0,n_size)
221         cell3.add_to_layer(3,sect)
222     else:
223         nbox = box(mycolumns[j]+0.3*pixel_size,myrows[i]-0.3*pixel_size,
224                 width=pixel_size*0.4,height=pixel_size*0.4)
225         cell3.add_to_layer(3,nbox)
226     ###
227     ''' CELL4 - creation of contacts '''
228     if contact_style==1:
229         n_centre =
230             Point(mycolumns[j]+pixel_size*0.45,myrows[i]-pixel_size*0.45)
231         p_centre =
232             Point(mycolumns[j]-pixel_size*0.45,myrows[i]+pixel_size*0.45)
233         n_sect = sector(n_centre,270,0,contact_size)
234         p_sect = sector(p_centre,90,180,contact_size)
235         cell4.add_to_layer(4, n_sect, p_sect)
236     else:
237         n_contact = box(mycolumns[j]+0.3*pixel_size,myrows[i]-0.3*pixel_size,
238                       width=pixel_size*0.32,height=pixel_size*0.32)
239         p_contact = box(mycolumns[j]-0.3*pixel_size,myrows[i]+0.3*pixel_size,
240                       width=pixel_size*0.32,height=pixel_size*0.32)
241         cell4.add_to_layer(4, n_contact, p_contact)
242     ###
243     ''' cell text '''
244     celltext1= '{}x{} {}um pixels - Mesas'.format(columns,
245         rows,
246         pixel_size)
247     text1 = Text([x1+300,y1], 50, celltext1, alignment='left-center')
248     cell1.add_to_layer(1,text1)
249     celltext2= '{}x{} {}um pixels - {}um tether Membranes'.format(columns,
250         rows,
251         pixel_size,
252         tether_length)
253     text2 = Text([x2-300,y1], 50, celltext2, alignment='right-center')
```

A. Python Code

```
252 cell2.add_to_layer(2,text2)
253 #%%
254 ''' saving file '''
255 thetime = datetime.now().strftime("%I_%M_%S")
256 mycell.show()
257 mycell.save('LED_origin_'+ thetime +'.gds')
258 print('Execution Time (hh:mm:ss):', (datetime.now() - start))
```

Listing 4: A script which uses the GDS Helpers and Shapely module to create custom suspended membrane geometries, and full LED fabrication photolithography masks.

A. Python Code

```
1 # -*- coding: utf-8 -*-
2 """
3 Created on Mon Nov 16 15:39:11 2020
4 @author: MILES
5 """
6 import numpy as np
7 import matplotlib.pyplot as plt
8 #%%
9 ''' methods '''
10 def make_InGaN_gap(x):
11     '''
12     Creates the band gap for InGaN in eV adapted from
13     Shun Lien Chuang - "Physics of Photonic Devices"
14     '''
15     gap = 0.64*x + 3.44*(1-x)-1.4*x*(1-x)
16     return gap
17
18 def make_InGaN_gap_mod(x):
19     '''
20     Creates the band gap for InGaN in eV for a composition ratio x adapted from
21     Shun Lien Chuang - "Physics of Photonic Devices"
22     '''
23     Eg_InN = 0.64
24     Eg_GaN = 3.44
25     b = (1-x)*(11.4-19.4*x) # fitting constant dependent on composition x
26     Eg_InGaN = x*Eg_InN + (1-x)*Eg_GaN - b*x*(1-x)
27     return Eg_InGaN
28
29 def eV_converter(lam): # creates energy of photon in eV from wavelength in microns
30     return 1.23984/lam # derived from E = hc/lam
31
32 def new_lam(x, lam): # Bergmann and Casey
33     Eg_GaN = 3.44
34     new_E = eV_converter(lam) - (make_InGaN_gap(x) - Eg_GaN)
35     return eV_converter(new_E)
36
37 def make_index(lam): # GaN refractive index from A. S. Barker Jr. and M. Ilegems 1973
38     # https://doi.org/10.1103/PhysRevB.7.743
39     nn = 1 + 2.6 + (1.75*lam**2)/(lam**2 - 0.256**2) + (4.1*lam**2)/(lam**2 - 17.86**2)
40     return np.sqrt(nn)
41
42 def make_index2(lam): # GaN refractive index from Kawashima 1997
43     A = 4.37
44     B = 0.088
45     nn = A + (lam**2)/(lam**2 - B)
46     return np.sqrt(nn)
47 #%%
48 ''' set variables '''
49 x = 0.23 # mixing ratio of indium in the InGaN
50 Lam_vals = np.arange(0.300,0.600,0.020) # values for lambda (wavelength in microns)
51 store_vals = np.zeros([Lam_vals.size,3])
52 #%%
53 for j in range(Lam_vals.size):
54     lam = Lam_vals[j]
55     lam2 = new_lam(x, lam)
56     GaN_n = make_index(lam)
57     InGaN_n = make_index(lam2)
58     store_vals[j,0] = Lam_vals[j]*1000 #converting to nanometres for consistency
59     store_vals[j,1] = GaN_n
60     store_vals[j,2] = InGaN_n
61
62 plt.plot(store_vals[:,0],store_vals[:,1], linewidth=3, label = 'GaN')
```

A. Python Code

```
63 plt.plot(store_vals[:,0],store_vals[:,2], linewidth=3, label = 'InGaN')
64 np.savetxt('InGaN_'+str(x)+'.txt', store_vals,fmt='%1.1f %1.5f %1.5f')
65 plt.legend(bbox_to_anchor=(1, 1), loc='upper right',fontSize=14)
66 plt.yticks(fontsize=14)
67 plt.xticks(fontsize=14)
68 plt.xlabel('Wavelength (nm)',fontSize = 16)
69 plt.ylabel('Refractive Index',fontSize = 16)
```

Listing 5: Python script to calculate the refractive indices of InGaN material over a range of wavelengths with a certain mole fraction. This was used to generate indices sets for use in Lumerical FDTD simulations.

A. Python Code

```
1 # -*- coding: utf-8 -*-
2 """
3 Created on Mon Nov 9 15:39:16 2020
4 @author: MILES
5 Generation of AlGaN refractive indices for various mixing ratios 'x'. Based on
6 the publication:
7 N. Antoine-Vincent, et al. (2003)
8 Determination of the refractive indices of AlN, GaN, and Al(x)Ga(1-x)N grown
9 on (111)Si substrates
10 """
11 import numpy as np
12 import scipy as sp
13 import matplotlib.pyplot as plt
14 from matplotlib.pyplot import cm
15 %%
16 ''' methods '''
17 def make_index(a, b, c, L):
18     n = np.sqrt(a + (b*L**2)/((L**2)-(c**2)))
19     return n
20 %% Here the default coefficients from the paper are displayed.
21 ''' given data '''
22 x = np.array([0.0, 0.19, 0.47, 0.675, 0.785, 1.0])
23 a = np.array([5.15, 4.98, 4.20, 3.95, 2.67, 1.0])
24 b = np.array([0.35, 0.39, 0.63, 0.63, 1.67, 3.12])
25 c = np.array([339.8, 297.7, 247.5, 239.3, 183.7, 138.0])
26 %% The coefficients are made into arrays to be fed into the function, the
27 # coefficients change depending on the mixing ratio 'x'.
28 ''' set variables '''
29 x_vals = np.array([0, 0.05, 0.1, 0.15, 0.20, 0.25, 0.3, 0.35, 0.40, 0.45, 0.50,
30                   0.55, 0.60, 0.65, 0.70, 0.75, 0.80, 0.85, 0.90, 0.95, 1])
31 Lam_vals = np.arange(360,620,20)
32 store_vals = np.zeros([x_vals.size,Lam_vals.size,2])
33
34 %%
35 ''' interpolating original coefficients to give more points '''
36 new_x = x_vals # first order spline of parameters
37 new_a = sp.interpolate.interp1d(x, a, kind='slinear')(new_x)
38 new_b = sp.interpolate.interp1d(x, b, kind='slinear')(new_x)
39 new_c = sp.interpolate.interp1d(x, c, kind='slinear')(new_x)
40
41 plt.figure(0) # checking quality of interpolation
42 plt.plot(new_x,new_a, linewidth=3, c='#525252', zorder=0, label='interpolated a')
43 plt.scatter(x,a, s=50, c='#f74242', zorder=1, label='given a')
44 plt.legend(bbox_to_anchor=(1, 1), loc='upper right', fontsize=14)
45 plt.xticks(fontsize=14)
46 plt.yticks(fontsize=14)
47 plt.xlabel('Mole Fraction x', fontsize=16)
48 plt.ylabel('Parameter a', fontsize = 16)
49
50 plt.figure(1) # checking quality of interpolation
51 plt.plot(new_x,new_b, linewidth=3, c='#525252', zorder=0, label='interpolated b')
52 plt.scatter(x,b, s=50, c='#f74242', zorder=1, label='given b')
53 plt.legend(bbox_to_anchor=(0, 1), loc='upper left', fontsize=14)
54 plt.xticks(fontsize=14)
55 plt.yticks(fontsize=14)
56 plt.xlabel('Mole Fraction x', fontsize=16)
57 plt.ylabel('Parameter b', fontsize = 16)
58
59 plt.figure(2) # checking quality of interpolation
60 plt.plot(new_x,new_c, linewidth=3, c='#525252', zorder=0, label='interpolated c')
61 plt.scatter(x,c, s=50, c='#f74242', zorder=1, label='given c')
62 plt.legend(bbox_to_anchor=(1, 1), loc='upper right', fontsize=14)
```

A. Python Code

```
63 plt.xticks(fontsize=14)
64 plt.yticks(fontsize=14)
65 plt.xlabel('Mole Fraction x', fontsize=16)
66 plt.ylabel('Parameter c', fontsize = 16)
67 ###
68 plt.figure(3)
69 color=iter(cm.rainbow(np.linspace(0,1,new_x.size)))
70 for i in range(new_x.size): # loops to plot the results and save .txt file
71     for j in range(Lam_vals.size):
72         current_n = make_index(new_a[i], new_b[i], new_c[i], Lam_vals[j])
73         store_vals[i,j,0] = Lam_vals[j]
74         store_vals[i,j,1] = current_n
75     c=next(color)
76     plt.plot(Lam_vals,store_vals[i,:,1], c=c, label = 'x = '+str(new_x[i]))
77     np.savetxt('AlGaN_'+str(new_x[i])+'.txt', store_vals[i,:,:],fmt='%1.1f   %1.5f')
78
79 plt.legend(bbox_to_anchor=(1, 0.5), loc='center left', fontsize=10)
80 plt.xticks(fontsize=14)
81 plt.yticks(fontsize=14)
82 plt.xlabel('Wavelength (nm)', fontsize=16)
83 plt.ylabel('Refractive Index', fontsize = 16)
```

Listing 6: Python script to generate refractive indices for AlGaN over a range of wavelength and a ranges of mole fraction. This was to create the graded AlGaN layers in the LED and DBR epistructures in a Lumerical FDTD simulation. The given Sellmeier parameters a b and c are interpolated to generate indices over the full range.

A. Python Code

```
1 # -*- coding: utf-8 -*-
2 """
3 Created on Wed Oct 28 12:22:11 2020
4 @author: MILES
5 approximates the reflectivity of a distributed Bragg reflector
6 """
7 import matplotlib.pyplot as plt
8 import numpy as np
9 import scipy as sp
10 %% (cell separator)
11 """methods"""
12 def Reflectivity(no=1,n1=1,n2=1,ns=1,N=1): #defaults to R=0 with no index changes
13     return ((no*(n2**(2*N)) - ns*(n1**(2*N))) / (no*(n2**(2*N)) + ns*(n1**(2*N))))**2
14 '''
15 no = index of first material on reflection side of DBR
16 n1 = index of higher index material in repeated pair
17 n2 = index of lower index material in repeated pair
18 ns = index of material at transmission side of DBR
19 N = number of repeated pairs
20 '''
21 %%
22 """ define material refractive indices for 450nm light """
23 AlN = 2.18 # bottom of the sandwiched LED in an RCLED
24 GaN = 2.48 # high index in the porous GaN
25 porGaN = 1.88 # low index in the porous GaN
26 Air = 1 # for air gap cavity test
27 """ Data arrays """
28 Nmin = 0
29 Nmax = 14
30 N = list(range(Nmin,Nmax,1))
31 Rvals = []
32 %%
33 """ calculate for a range """
34 # bottom mirror order: GaN, GaN, porGaN, GaN, value
35 # exit mirror order: AlN, GaN, porGaN, GaN, value
36 for value in N:
37     R = Reflectivity(AlN, GaN, porGaN, Air, value)
38     R = round(R,3)
39     Rvals.append(R)
40     print(R)
41 %%
42 """ plot results """
43 x = np.array(N) # making a smooth line
44 y = np.array(Rvals)
45 new_length = 50
46 new_x = np.linspace(Nmin, Nmax-1, new_length)
47 new_y = sp.interpolate.interp1d(x, y, kind='cubic')(new_x)
48 plt.figure(figsize = (10,5))
49 plt.axis([-0.4,Nmax-0.4,-0.1,1.1])
50 plt.xticks(N)
51 plt.plot(new_x, new_y, linewidth=3, c='#525252', zorder=0) # plotting line
52 plt.scatter(N, Rvals, marker='o', color='#f74242', s=50, zorder=1)
53 for i, val in enumerate(Rvals):
54     plt.annotate(val, (N[i],Rvals[i]-0.1), ha='center')
55 plt.xticks(fontsize=14)
56 plt.yticks(fontsize=14)
57 plt.xlabel('Number of repeated pairs', size=16)
58 plt.ylabel('Reflectivity',size=16)
```

Listing 7: Python script to calculate the reflectivity of a DBR with a given number of repeated layers and a varied material structure. This was used to calculate the number of layers needed to achieve the desired reflectivity for the bottom and top mirrors of an RCLED.

A. Python Code

```
1 # -*- coding: utf-8 -*-
2 """
3 Created on Mon Mar 1 16:01:20 2021
4 To calculate the overlap of E field with quantum well region.
5 An integration of E field between the limits set by the QW region.
6 Select folder containt .txt files from Lmuerical plot over QW region.
7 @author: MILES
8 """
9 import os
10 import numpy as np
11 from tkinter import Tk
12 from tkinter import filedialog
13 from scipy import integrate
14 import matplotlib.pyplot as plt
15 #%%
16 ''' open folder and import files '''
17 root = Tk()
18 root.wm_attributes('-topmost', 1) # brings to front, only works with windows
19 root.withdraw()
20 path = filedialog.askdirectory(parent=root)+"/" # use window to select folder
21 root.destroy()
22 fnames = os.listdir(path)
23 #%%
24 ''' import into dictionaries '''
25 mydata = {}
26 position = {}
27 for myfile in fnames:
28     mydata[myfile] = np.loadtxt(path+myfile,delimiter=",",skiprows=3, max_rows=90)
29 #%%
30 ''' set variables '''
31 diff = mydata[fnames[0]][1,0] - mydata[fnames[0]][0,0]
32 dx = np.round(diff,6) # gets separation of data points for integration
33 #%%
34 ''' calculate integral '''
35 outarray = []
36 x = []
37 y = []
38 for name in fnames:
39     result = integrate.simps(mydata[name][:,1],dx=dx)
40     outarray.append([name,result])
41     x.append(float(name[:5]))
42     y.append(result*10**3)
43 outarray = np.array(outarray)
44 #%%
45 ''' create plots '''
46 xticks = x
47 ymin = min(y) - (max(y)-min(y))*0.1
48 ymax = max(y) + (max(y)-min(y))*0.1
49 plt.ylim([ymin,ymax])
50 plt.scatter(x,y, norm=True)
51 plt.grid(which='both',b=True)
52 plt.xticks(ticks=xticks)
53 plt.ylabel('Overlap ( $\times 10^{-9}$  V)')
54 plt.xlabel('n-GaN Thickness ( $\mu\text{m}$ )')
55 #%%
56 ''' write text file '''
57 outfile = 'wavelength_sweep.txt'
58 np.savetxt(outfile, outarray, fmt='%s', header='file\toverlap', delimiter='\t')
```

Listing 8: Python script which takes the Electric field intensity output from Lumerical FDTD RCLED simulation and integrates it to give a value of the overlap. The region in which it is integrated remains constant (where the quantum wells are) and the intensity of the E-field varies when adjusting the thickness of the n-GaN of an LED in an RCLED simulation. The filenames of the input text file must represent the thickness of the n-GaN in microns for the plotting to work.

Appendix B

Research Output

Publications

B. F. Spiridon, M. Toon, A. Hinz, S. Ghosh, S. M. Fairclough, B. J. E. Guilhabert, M. J. Strain, I. M. Watson, M. D. Dawson, D. J. Wallis, R. A. Oliver, “Method for inferring the mechanical strain of GaN-on-Si epitaxial layers using optical profilometry and finite element analysis,” *Optical Materials Express*, Vol. 11, no. 6, pp. 1643—1655, 2021. DOI: 10.1364/OME.418728.

N. Kolja Wessling, S. Ghosh, B. J. E. Guilhabert, M. Kappers, A. M. Hinz, M. Toon, R. A. Oliver, M. D. Dawson, M. J. Strain, “Fabrication and transfer printing based integration of free-standing GaN membrane micro-lenses onto semiconductor chips,” *Optical Materials Express*, Vol. 12, no.12, pp. 4606—4618, 2022. DOI: 10.1364/OME.472999.

B. J. E. Guilhabert, M. Toon, S. Ghosh, J. F. Carreira, R. A. Oliver, M. D. Dawson, M. J. Strain, “Heterogeneous Integration of GaN-Based Devices by Transfer Printing,” Manuscript in preparation.

Posters

M. Toon, B. J. E. Guilhabert, A. Hinz, B. F. Spiridon, S. M. Fairclough, I. M. Watson, R. A. Oliver, M. D. Dawson, M. J. Strain, “Strain Managed GaN LED Structures for 3D Transfer Printing,” Poster, Institute of Physics, Photon 2020. 2020.

Method for inferring the mechanical strain of GaN-on-Si epitaxial layers using optical profilometry and finite element analysis

B. F. SPIRIDON,^{1,*} M. TOON,² A. HINZ,¹ S. GHOSH,¹  S. M. FAIRCLOUGH,¹ B. J. E. GUILHABERT,²  M. J. STRAIN,²  I. M. WATSON,² M. D. DAWSON,²  D. J. WALLIS,^{1,3} AND R. A. OLIVER¹

¹Department of Materials Science and Metallurgy, University of Cambridge, Cambridge CB3 0FS, UK

²Institute of Photonics, Department of Physics, University of Strathclyde, Glasgow G1 1RD, UK

³Centre for High Frequency Engineering, University of Cardiff, Cardiff CF24 3AA, UK

*bfs25@cam.ac.uk

Abstract: GaN-on-Si has become a useful fabrication route for many GaN devices and applications, but the mechanical stress incorporated throughout the material stack can impact the viability of this approach. The transfer printing of GaN membrane devices, a promising emerging technology, is most effective with flat membranes, but in practice many GaN structures released from their Si substrate are highly bowed due to the strain in the epitaxial nitride stack. Our approach uses the optical profiles of epitaxial wafers and membranes as inputs for inferring the mechanical strain state of the material by multi-variable numerical model fitting using COMSOL Multiphysics. This versatile, adaptable and scalable method was tested on samples from two GaN-on-Si wafers, revealing the relationship between built-in strain and material bow in principal-component fashion, returning $3\text{--}4 \times 10^{-4}$ strain estimates for the AlGa_N (compressive) and GaN (tensile) layers, and suggesting the occurrence of plastic deformation during transfer printing.

Published by The Optical Society under the terms of the [Creative Commons Attribution 4.0 License](https://creativecommons.org/licenses/by/4.0/). Further distribution of this work must maintain attribution to the author(s) and the published article's title, journal citation, and DOI.

1. Introduction

3D integration of optoelectronic devices is an important future technology for applications in areas such as quantum dot in cavity, multi-layer photonic integrated circuits, flexible and advanced displays, and biosensors [1–3]. Transfer printing [1,4] is a particularly attractive method to achieve 3D integration, its key benefits including: the transfer of fully fabricated devices, the integration of multiple materials on a single target substrate, the opportunity to stack devices, and the lack of need for post-transfer material processing (when substrate removal is best avoided, especially in the case of multi-layer and multi-material assemblies).

GaN devices have shown superior and unique performance in optoelectronic and high-power devices compared with alternative semiconductor technologies, but GaN bulk substrates are still prohibitively expensive for the majority of applications and hetero-epitaxial growth of GaN on dissimilar substrates is therefore commonly employed [5–7].

The choice of Si as a substrate for GaN epitaxy is advantageous compared with alternatives, such as sapphire or SiC, as Si wafers benefit from wide availability, low cost, compatibility with existing processing lines [8] and relatively high thermal conductivity [9]. Furthermore, GaN-on-Si technology permits the use of Si micro-machining techniques for selectively removing substrate regions to create suspended nitride structures, including cantilevers [10], anchored chiplets [11], and membranes [12]. Such suspended GaN structures show interesting mechanical and thermal characteristics while inheriting many strengths of free-standing GaN, e.g. high

break-down voltage [13]. A particular advantage of creating anchored GaN structures is the possibility of detaching and transfer-printing [14] them onto alternative hard [15] or flexible [16] substrates, simultaneously enabling their integration with other semiconductor modules [11].

The manufacturing and processing of GaN-on-Si wafers are, however, limited by several mechanical aspects. These are predominantly related to the significant mismatch between the crystal lattice parameters and thermal expansion coefficients of GaN and Si, resulting in large levels of tensile stress in the epitaxial material. Device-specific design features, such as thick buffer regions or highly-doped layers, can further magnify the mechanical stress developed within the epitaxial GaN-on-Si stack. The effects of the built-in mechanical stress are detrimental both at the material level (promoting the development and propagation of crystal defects) and from a processing perspective (bowed wafers cannot be accurately processed using standard optical lithography processes).

Stress-mitigation architectures have been designed to reduce the epitaxial wafer bow, by introducing compressive strain to compensate the significant tensile stresses arising on cooling aiming to achieve a net-zero stress in the epitaxial stack [17–19]. However, this approach is not necessarily suitable for GaN-on-Si material intended for transfer printing, where GaN membrane devices are defined by deep trenches covering the majority of their perimeter (except for designated anchor regions) and the underlying region of the Si substrate is removed by chemical etching, resulting in suspended GaN membrane devices as shown in Fig. 1.

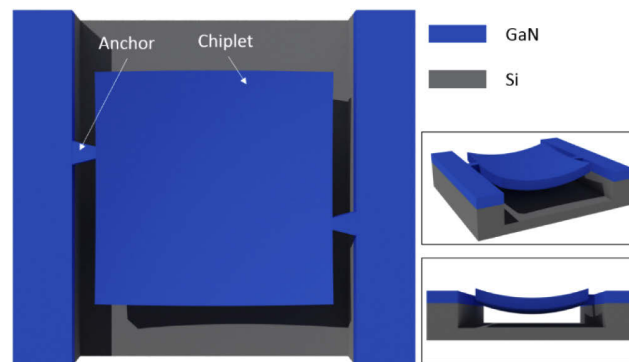


Fig. 1. Schematic structure of a GaN membrane device attached to its original Si substrate via anchors. Insets show additional 3D views of the same device, bowed by the complex mechanical stress built into its material

It was often observed [20–21] that such anchored GaN structures show a significant bow that persists or increases after the devices are released, posing a challenge for transfer printing and 3D integration, and supporting the case for robust design processes. While earlier transfer printing experiments circumvented this problem by using flexible receiver substrates [16] and intermediary adhesive layers [22–23], membrane devices can be transfer printed relying only on close-contact van der Waals-type adhesion forces [15,24–26]. This approach is advantageous e.g. for optical coupling [26] or heat dissipation [15], but is critically dependent on the device planarity, placing additional emphasis on the flatness of the GaN membranes.

Similar to wafer bow, membrane bow is a result of the built-in mechanical stress in the epitaxial material layers, but the type and magnitude of the bow at wafer and membrane level can be different. Understanding the relationship between wafer bow, membrane bow and the strain state of the epitaxy can provide insights which, for a particular epitaxial structure, may allow us to use wafer bow as an indicator of the expected behaviour of the membrane. To minimise the membrane bow, a balanced stress distribution must be ensured within the nitride epitaxy, ideally resulting in zero bending moment. This requirement is in addition to the low net-stress

specification for low wafer bow, which still applies to the membrane-device transfer printing technology.

Achieving balanced stress-compensated stacks is the key to manufacturing flat wafers and flat membranes, receiving considerable attention in the context of transfer printing. Such studies require objective and detailed feedback regarding the stress in different parts of the epitaxial stack, but conventional methods of measuring stress in nitrides can be impractical or not sufficiently accurate. For example, it is hard to differentiate layers of similar composition in complex structures using conventional X-ray diffraction. Micro-Raman spectroscopy can be performed on such small samples, but it is also unsuitable for analysing complex material stacks. Similarly, transmission electron microscopy can be used to observe mechanical strain at the atomic level, but it is a localised, laborious, destructive and expensive technique, and the necessary sample processing can affect the original mechanical state.

We propose an alternative method that uses simple measurements of the wafer and membrane bow for inferring the mechanical state of the samples, including the strain of individual layers within complex material stacks. Bow measurement is comparatively more accessible and is routinely performed by non-contact in-situ optical methods during and/or immediately after the epitaxial wafer growth. Similarly, optical profilometry is a standard technique for assessing the profiles of wafers, dies and devices within cleanroom laboratories. In parallel, finite-element analysis (FEA) simulators are becoming more powerful, accurate, and accessible. Our work demonstrates the possibility of extracting information about the mechanical state of the nitride epitaxy by observing the wafer and membrane profiles and fitting an FEA model twin to recreate the experimental dataset. For validation, the full process was run on a set of two GaN-on-Si wafers with comparable stack structures, which provided complementary information about the mechanical stress developed in several regions of the epitaxial material.

2. Methods

Two GaN-on-Si LED wafers, Sample 1 and Sample 2, with structures as shown in Fig. 2, were investigated in this work, their growth being detailed in the Supplemental Document in [Supplement 1](#). Their high epitaxial growth temperature, in the region of 1300 K, is an important source of mechanical stress upon cooldown due to thermal mismatch. The epitaxial structure of the LEDs is similar to the ones published in our previous works [27–28], being optimized to satisfy the electrical and stress-management requirements of GaN-on-Si LED technology to levels suitable for industrial production, hence having great relevance in the transfer printing context. Compared with Sample 1, Sample 2 contains an additional sub-monolayer SiN_x dislocation blocking interlayer in the n-GaN epilayer. Such interlayers have been shown in the literature [29–31] to be effective in reducing the dislocation density in the overlying epitaxy, but their impact on the strain state of the material is poorly understood.

The curvature of the two sample wafers was monitored during the high-temperature epitaxial growth using an in-situ EpiCurve (Laytec, DE) system. These observations were complemented with ex-situ bow measurements at room temperature using a custom-made system for recording the final position of a laser beam reflected off different points on the wafer surface. The detection limit of this experimental bow measurement method is estimated theoretically to be around 3 μm for a 150 mm wafer, with errors of a similar order to this limit.

Each of the LED wafers was diced into 19 × 15 mm² pieces for processing, with the subsequent fabrication steps illustrated in Fig. 3(a) and further detailed in the Supplemental Document in [Supplement 1](#). The mask used for the experiments defined square membranes with a side length of 100 μm, and a tapered anchor geometry with support and membrane contact widths of 10 and 5 μm respectively and a length of 10 μm. The anchors' design and their placement with a 30 μm relative offset along two opposite sides of the membrane device were previously observed to improve the transfer-printing yield and were used in this study to facilitate the integration

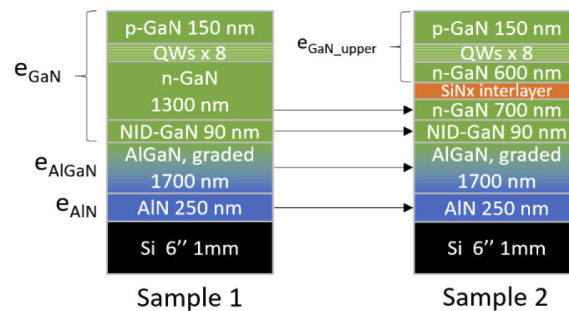


Fig. 2. Structure of the epitaxial GaN-on-Si material, with simplifying assumptions and parameter search strategy (discussed later): Sample 1 is segmented into three regions of distinct strains, constant along the growth direction; the best-fit values of these strains are transferred to Sample 2, which includes an additional strain level corresponding to the material region above the SiNx interlayer.

of our described method with the transfer-printing process. The mask pattern was aligned to give rows of membrane dies and intermediate support rails running parallel to Si $\langle 1-10 \rangle$, as shown in Fig. 3(b). This orientation exposed Si surfaces prone to fast etching under the sides of membranes running in the perpendicular direction [16,32], enabling suspension of dies each held by two thin anchors, themselves also fully underetched.

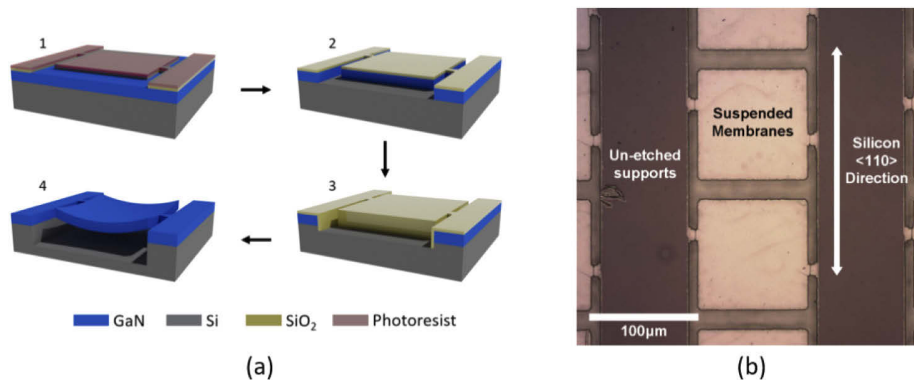


Fig. 3. The membrane device fabrication process (a): formation of the patterned silica hard-mask using RIE (1), ICP-RIE through the GaN device layers (2), second RIE for shallow Si etch, and PECVD deposition of silica sidewall protection (3), and final KOH

The membrane devices were individually transfer printed to a silicon receiver substrate using a reversible adhesion stamp comprised of elastomeric polydimethylsiloxane (PDMS) on a modified Nanoink dip-pen tool [11]. For each wafer, 3 membrane devices were printed onto a silicon substrate to allow for variations between devices to be assessed and an average membrane bow to be measured. Figure 4(a) shows a schematic of the printed devices. During printing, the membrane device is placed into contact with the substrate and pressure applied to ensure full contact between the surfaces. As the PDMS stamp is retracted, the device is released onto the substrate and the intrinsic membrane bow causes it to relax into a bowl-like shape. An optical microscope image, Fig. 4(b), of the released membrane device shows a circular interference pattern due to the air gap between the device bottom surface and the substrate. As the air gap

increases in dimension away from the device contact area, the interference fringe spacing gives an indication of the membrane bow [33].

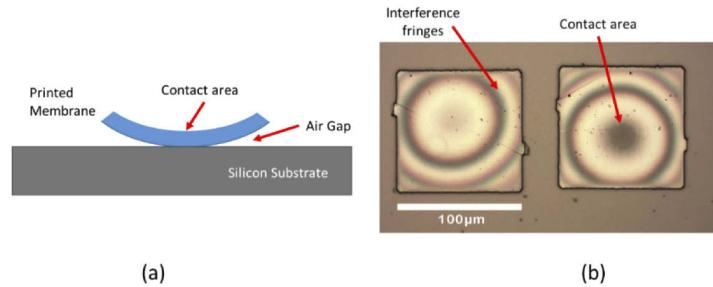


Fig. 4. (a) Schematic of the transfer printed membrane devices on Si illustrating the effect of membrane device bowing. (b) Optical microscope images of printed devices from different wafers (Left: Sample 1; Right: Sample 2)

To quantitatively assess the membrane bow, both as fabricated on their native wafer, and after transfer printing, the devices were measured using a Wyko NT1100 optical profiler instrument. To frame a single device, the 20x objective lens was combined with a 2x field of view lens. This allowed an accurate measurement of single devices with a depth resolution of a few nanometres.

The profiler image files were post-processed using Gwyddion [34] to extract the topology of the device top surface. Figure 5 shows extracted height maps of the membrane devices, both as fabricated (attached), and after transfer printing onto the recipient Si substrate. The steep profile changes over the peripheral $\sim 10 \mu\text{m}$ of the attached membrane devices were assigned to optical interference between the surface of the attached device and the etch-well surface, as confirmed by the lack of such effect in the transfer-printed devices.

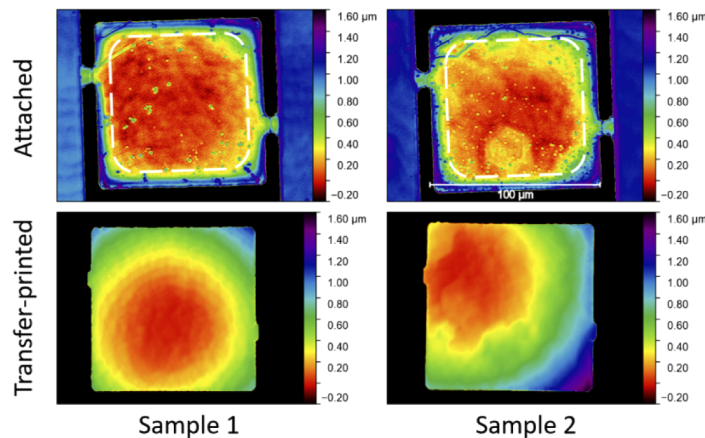


Fig. 5. Measured height maps of Samples 1 and 2 while attached and following transfer printing. The profiles of attached membrane devices are affected by an optical-interference measurement error in the peripheral regions marked by a dashed white line

COMSOL Multiphysics, a commercial FEA solver, was used to create a model of the GaN-on-Si material and to simulate the 3D profiles generated by built-in mechanical strain in different regions of the epitaxial stack. These strains, labelled as $e_{\langle \text{layer} \rangle}$ and referenced to the unstrained lattice parameters of the bulk materials, were the independent variables of the model and were provided as inputs in the simulation of bow values as detailed below.

A parameterised 3D geometry of the reduced wafer and membrane device was built, as shown in Fig. 6. The full 150 mm wafer diameter was reduced to 1 mm in the model to avoid unnecessary computational complexity, with the local radius of curvature (ROC) extracted from the reduced model and the equivalent bow then extrapolated to a 150 mm wafer equivalent.

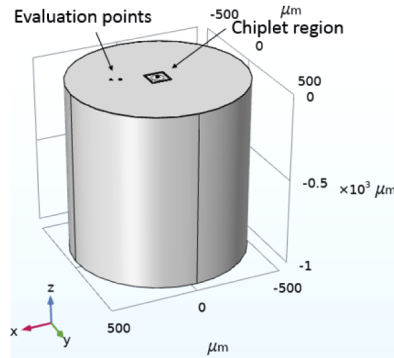


Fig. 6. 3D geometry of the reduced wafer and membrane device FEA model

The membrane device geometry and layer structure were reproduced in the model, as shown in Fig. 7, with the respective layer thicknesses defined as in Fig. 2, except for the SiN_x interlayer, not included due to its sub-monolayer thickness.

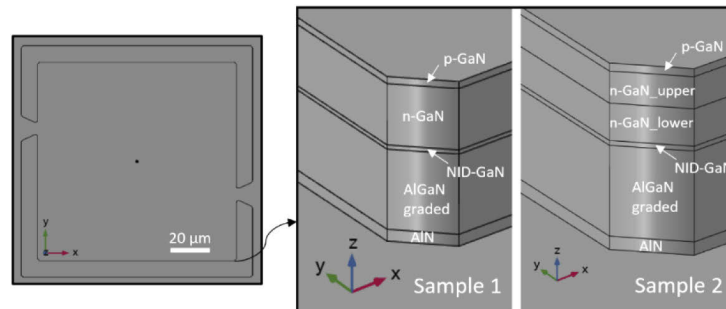


Fig. 7. Details of the membrane region of the model: (Left) plan view membrane device and anchors geometry and (Right) the structure of the epitaxial nitride layers of Samples 1 and 2

By solving for the mechanical deformation caused by the built-in strain, simulated profiles of the reduced wafer and membrane were obtained, as shown in Fig. 8. Three quantities of interest were extracted from these model solutions: the 150 mm-diameter full-wafer bow (B), the membrane bow along the anchors' direction (B_A), and the membrane bow along the diagonal away from the anchors (B_D). B is a commonly measured wafer property which was measured experimentally on full wafers and compared with the results of the reduced-size model by extrapolating the model bow to the equivalent bow of a 150 mm-diameter wafer. The direction along which B_A is measured is highly sensitive to the mechanical state of the substrate, while the direction along which B_D is measured yields the greatest membrane deformation, supporting greater experimental measurement accuracy. The membrane evaluation regions were limited to the central 70 μm to exclude any membrane edge effects. This choice of evaluation directions is supported by the direct effect of strain distribution within the layered stack on B_D and by the effect of the net mechanical state of the stack on B_A via the anchors. Together with the wafer

bow, B , they are viable model fitting directions in the search for the original mechanical strains generating them. The independent-variable strains were considered the fitting parameters, i.e. degrees of freedom (DOF) of the problem.

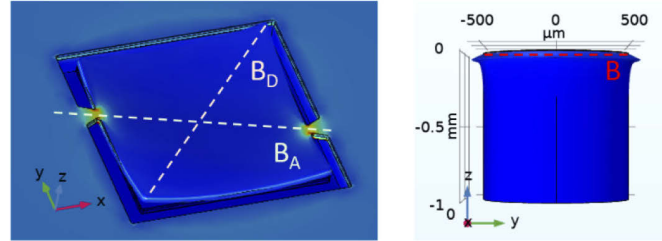


Fig. 8. Example of reduced wafer and membrane deformation (exaggerated) simulated using the FEA model

The FEA model results were compared against the experimentally recorded bow levels along the three directions of interest by calculating an equivalent 3D relative error, E_{rel} , as in Eq. (1) and using the result as the objective function for the model fitting process. In this process, the nominal values obtained experimentally were used, without including the experimental measurement errors. The fitting process relied on a multi-step exhaustive search method with progressively finer evaluation steps.

$$E_{rel} = \sqrt{\left(\frac{B_{FEA} - B_{exp}}{B_{exp}}\right)^2 + \left(\frac{B_{A,FEA} - B_{A,exp}}{B_{A,exp}}\right)^2 + \left(\frac{B_{D,FEA} - B_{D,exp}}{B_{D,exp}}\right)^2} \quad (1)$$

Given the three fitting dimensions, the search space dimensionality was reduced using simplifying assumptions, for a well-defined search problem. A multi-step approach was taken as shown in Fig. 2, where the system of built-in strain states in Sample 1 was reduced to three regions of constant strain and a further region was added when fitting Sample 2, taking into account the potential effect of the additional SiN_x layer on the strain state of the material grown subsequently. It is useful to note that, given the sub-monolayer thickness of the SiN_x region, its mechanical state does not significantly impact the overall mechanical state of the sample, hence the FEA model did not include this layer. This approach resulted in a 3-DOF problem for Sample 1 and an additional DOF for Sample 2. The direct transfer of best-fit strain levels from Sample 1 to Sample 2 is supported by the identical stack structures and epitaxial growth conditions between the two samples up to the SiN_x interlayer, while this additional DOF for Sample 2 is necessary as the SiN_x interlayer is expected to influence the mechanical state of the layer grown subsequently. Finally, the best-fit strain levels resulting from the two-step exhaustive searches were used to simulate the profile of free-standing GaN membrane devices and to compare them with the profiles of experimental transfer-printed devices, as observed using optical profilometry.

3. Results and discussion

Experimental optical profiles were recorded on sets of five attached and three transfer-printed membrane devices from each wafer (Sample 1 and Sample 2), extracting experimental values for the key parameters to be matched by the model, B_D and B_A , as summarised in Table 1 together with the associated standard errors and using the ‘positive-concave, negative-convex’ bow convention. The relative $B_D:B_A$ magnitude indicates the degree of non-spherical bow for attached membranes, more pronounced in Sample 1 than in Sample 2. The B values previously recorded by wafer bow measurements are also included. While the wafer bow readings are relatively low, they are still significant compared with the results obtained from fresh Si wafers

in the same batch for which the bow values were below the detection limit of the experimental method.

Table 1. Summary of optical bow measurements

Sample	SiN _x interlayer	B / μm	Step	B _D / μm	B _A / μm
1	No	-6 ± 2.7	Attached	0.15 ± 0.01	0.10 ± 0.01
			Transfer-printed	0.24 ± 0.03	0.24 ± 0.03
2	Yes	-8 ± 2.7	Attached	0.15 ± 0.03	0.16 ± 0.02
			Transfer-printed	0.22 ± 0.01	0.22 ± 0.01

The attached membrane devices of Sample 1 were simulated in a 3-DOF search space, with an initial coarse results series presented in Fig. 9. The labelled and colour-coded arrows in Fig. 9(a) indicate the principal directions of variation with changes in the strain states of the respective layers: e_{GaN} (red), e_{AlGaN} (blue), e_{AlN} (green). Each arrow's length is representative of the relative weight of each strained layer to the resulting bow state. While the large degree of correlation observed in Fig. 9(b) between B_A and B_D is undesirable for the parametric search as it reduces the accuracy of the results, the non-unity slope of the results locus in the B_A-B_D space indicates a non-spherical bow, as expected given the additional mechanical constraint introduced by the two support anchors.

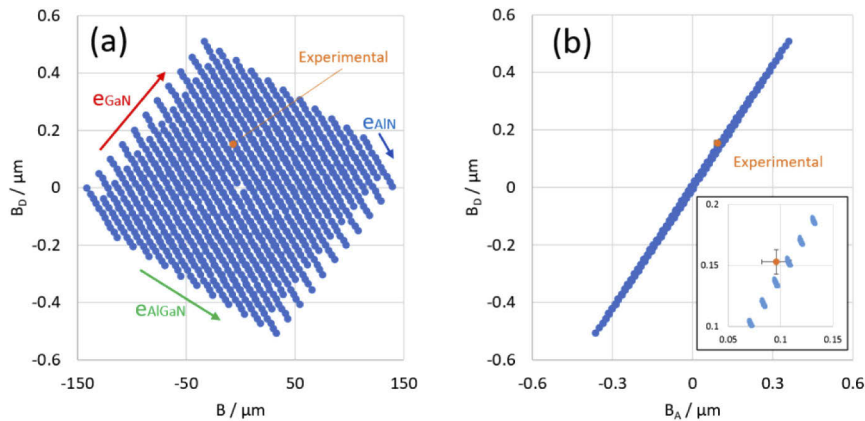


Fig. 9. 3D search space for attached membrane devices from Sample 1, generated by varying the three independent strain variables, e_{GaN} (red), e_{AlGaN} (green), and e_{AlN} (blue): variations and eigen-directions in the B-B_D space (a) and variations in the B_A-B_D space (b), with inset showing the region around the experimental results (standard-error bars)

These initial results showed that the membrane shape can be reproduced numerically by the FEA model, as judged by the proximity of experimental measurements to the numerical model results in Fig. 9. Further parametric searches with finer steps for the independent variables were performed until the best-fit results converged to approximately 8% relative error vs the experimental data. Since the B_A-B_D correlation results in a weaker problem definition, several good-fit combinations with relative errors in the range 8-10% were extracted for statistical analysis, shown in Fig. 10. These results indicate a tensile strain for the GaN region, compressive for the AlGaN layer, and slightly tensile for the AlN layer, albeit with a greater uncertainty.

It is important to note that the roughly equal-magnitude but opposite-sign strains of the lower AlGaN and upper GaN layers lead to both an essentially flat wafer, as their effects cancel at the wafer level, and bowed membranes, as a significant bending moment is developed at

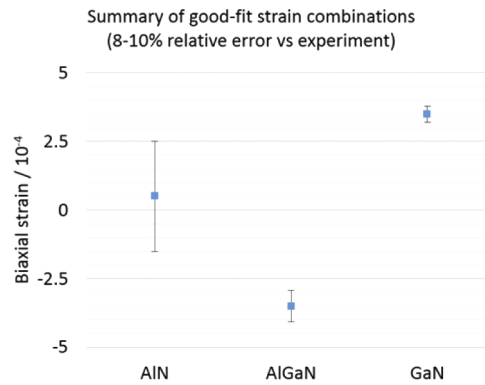


Fig. 10. Best-fit 3-DOF results for the attached membrane devices of Sample 1, with error bars indicating standard error

membrane-device scale. Consequently, flatter membranes can be achieved if the strain magnitude of both layers is reduced proportionally while maintaining a net-zero mechanical stress for flat wafers.

The best-fit strain values obtained from the attached membrane devices of Sample 1 were used in a second step, where the structures fabricated using Sample 2 were considered. An additional DOF was introduced as the equivalent strain in the GaN layers grown on top of the SiN_x interlayer and a 1-DOF exhaustive search was performed numerically, with the simulated results summarised in Fig. 11.

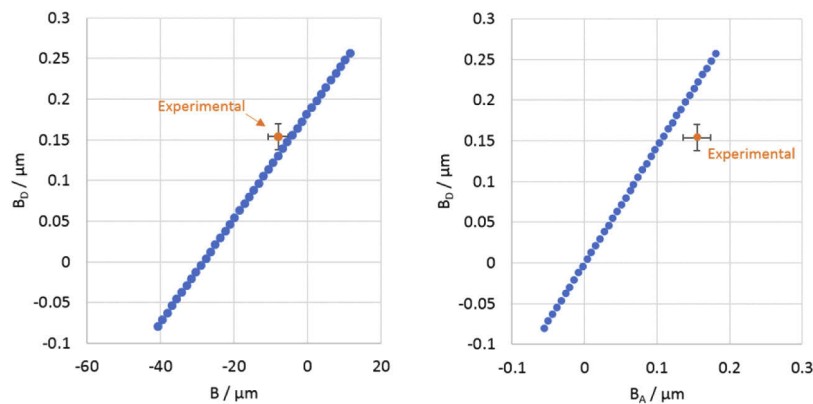


Fig. 11. Search space for attached membrane devices from Sample 2 (standard-error bars)

Regardless of the step size in the parametric step, the relative fit error was at least 40%, mainly attributed to the large deviation between simulated and experimental values in the B_D - B_A space, describing the membrane shape. A similar approach of considering several good-fit combinations with relative errors between 40% and 50% was taken, completing the statistical results presented in Fig. 12 with values for the GaN_upper strain independent variable.

The small reduction in mean strain estimate from GaN to GaN_upper suggests that the influence of the SiN_x interlayer on the strain state of the material is relatively small, supporting the use of such dislocation-reduction layers in GaN-on-Si epitaxy without substantially affecting their performance in a transfer printing context. Finally, the strain levels inferred from this method are

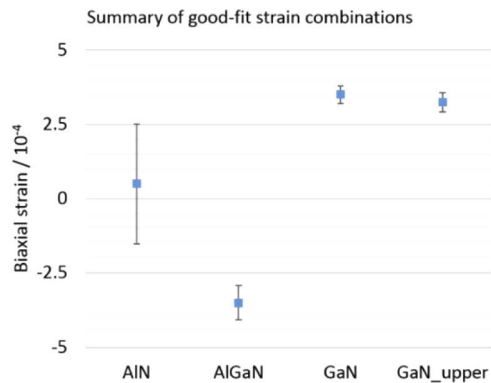


Fig. 12. Best-fit results for the attached membrane devices: AlN, AlGaIn, GaN results from Sample 1 with relative error 8-10% and GaN_upper result from Sample 2 with relative error 40-50%; the error bars indicate standard error

plausible in the context of lattice and thermal mismatch, layer relaxation through defects, and material-specific mechanical limits before cracks start occurring.

To verify the last aspect related to mechanical limits, the distribution of mechanical stress along the crystal growth direction developed in the best-fit scenario was extracted from the full 3D mechanical model results, as shown in Fig. 13. These results confirm that the stress levels are below 200 MPa, values typical for GaN-on-Si material grown by MOCVD [35] and within the fracture toughness of the GaN epitaxial material, known to be in the region of 350 MPa [36].

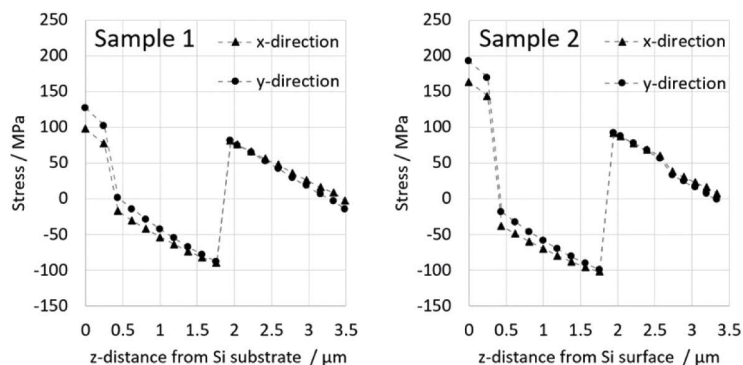


Fig. 13. Room-temperature mechanical in-plane stress levels at different levels along the wafer normal in the crystal growth direction, as extracted from the best-fit 3D FEA model results

It must be noted that, since significant levels of mechanical strain can be stored even in the initial Si substrates, several fresh Si wafers from the same batch were characterised ex-situ using the same laser bow measurement system and were found to be essentially flat, within the accuracy limits of the system. As a result, the model assumed initially relaxed Si substrates.

The best-fit mechanical strain levels inferred from the fitting of numerical simulation results to the experimental bow measurements were used to simulate the profile of free-standing GaN membrane devices detached from their original substrates. The numerical model results shown in Fig. 14 were compared with the experimental measurements, observing levels of bow between 22% (Sample 2) and 40% (Sample 1) lower than the experimental values.

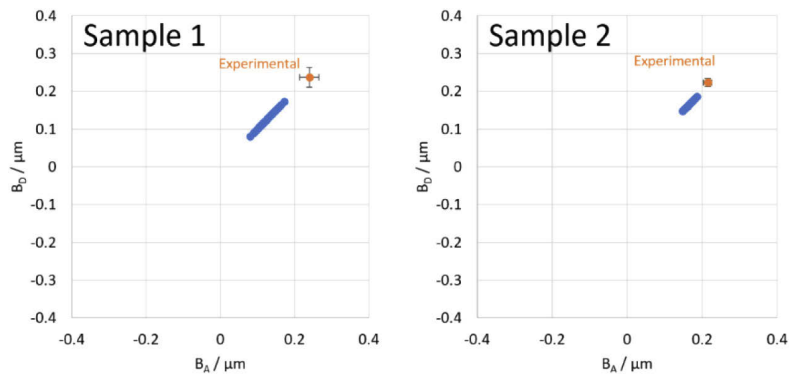


Fig. 14. Model strain estimates tested against experimental values for transfer-printed membrane devices, with error bars showing measurement standard error

The higher concave bow levels observed after transfer printing are unexpected, considering that the substrate was seen to apply a net compressive stress on the material. Similarly, the close-contact forces providing adhesion to the new substrate should only reduce the level of membrane bow. Instead, plastic deformation of the lower nitride layers, as a result of the downward forces applied by the printing head while breaking the anchors to release the membrane devices, is a plausible origin of the increased membrane bow. The results shown in Fig. 13 support the hypothesis of AlN cracking, as it experiences the greatest tensile stress. Additionally, the downward action of the print head applies more force to break the anchors and hence increases the tensile stress on the lower AlN layer, potentially inducing cracking and driving the system equilibrium towards a higher concave bow level. Given the unexpected result, the experimental verification of this hypothesis is an interesting topic for future research.

This FEA study of membrane devices provides additional insight over the mechanical state of nitride regions in two complex LED structures. Although several simplifying assumptions were necessary for a well-defined parametric fitting problem, this method expands the understanding of the GaN-on-Si epitaxial stacks beyond the level usually permitted by direct material characterisation. Its accuracy can be further increased with better problem definition. This can be achieved with simpler epitaxial structures and/or more independent experimental results. Nevertheless, this initial study demonstrated the viability of the technique using necessary simplifying assumptions on two complex LED structures, using a single test structure geometry. Further technique improvements also include simulating the formation and propagation of plastic defects and considering the weak close-contact adhesion forces in the case of transfer-printed membrane devices.

4. Conclusion

The use of GaN-on-Si material for transfer printing increases the importance of understanding and controlling the mechanical state of the material beyond the usual wafer-flatness criterion for optical lithography. The combined experimental and numerical technique described here infers the signs and levels of mechanical strain existing in such epitaxial structures by observing the wafer and membrane profiles and fitting these observations to a high-fidelity FEA model. This method is versatile and scalable to any levels of wafer and membrane bows, is adaptable to other materials and stack structures, and is easy to enhance with additional physics or geometry features.

The method was applied to two GaN-on-Si epitaxial wafers, returning valuable mechanical strain and stress estimates for the AlN, AlGaIn and GaN regions of the epitaxial stack, revealing

principal directions of wafer and membrane bow variation with the strain contained in each region, and highlighting the importance of mechanical stress balance in addition to net-zero mechanical stress. Specifically, the membrane bow was seen to depend on the imbalanced mechanical stress contrast developed in the nitride structure, which can be minimised through the general reduction of all built-in strain levels and by their more symmetrical placement along the growth direction.

The material analysis method described here can accelerate the research into GaN-on-Si stress management and the scale-up of the GaN-on-Si technology to larger wafer diameters, specifically 200 mm and beyond, by providing an accessible method of estimating the mechanical state of given epitaxial layers. Furthermore, this method can be directly integrated with complementary simulations (e.g. thermal or fluid dynamics) within the COMSOL Multiphysics FEA platform.

Funding. Engineering and Physical Sciences Research Council (EP/L015889/1, EP/N01202X/2, EP/R03480X/1); Cambridge Trust; Deutsche Forschungsgemeinschaft (HI 2141/1-1).

Acknowledgements. This work was part of the EPSRC Hetero-print project [EP/R03480X/1]. BFS is also a member of the EPSRC CDT Sensor Technologies and Applications [EP/L015889/1] and gratefully acknowledges the support from the Cambridge Commonwealth European and International Trust. AH would like to acknowledge funding for his position in the framework of a Research Fellowship by the Deutsche Forschungsgemeinschaft (DFG) under the grant number HI 2141/1-1. DJW acknowledges support from an EPSRC Manufacturing fellowship (EP/N01202X/2). The support offered by Mr. P. Hill in collecting the experimental optical profiler data is also gratefully acknowledged.

Disclosures. The authors declare no conflicts of interest.

Supplemental document. See [Supplement 1](#) for supporting content.

References

1. A. Carlson, A. M. Bowen, Y. Huang, R. G. Nuzzo, and J. A. Rogers, "Transfer printing techniques for materials assembly and micro/nanodevice fabrication," *Adv. Mater.* **24**(39), 5284–5318 (2012).
2. J. McPhillimy, C. Klitis, P. Hill, S. May, B. Guilhabert, M. D. Dawson, M. Sorel, and M. J. Strain, "Towards 3D optical integration by micro-transfer printing of ultra-thin membrane devices," in *Proceedings of 2018 IEEE British and Irish Conference on Optics and Photonics (BICOP)*, London, UK (2018), pp. 1–4.
3. M. Choi, B. Jang, W. Lee, S. Lee, T. W. Kim, H.-J. Lee, J.-H. Kim, and J.-H. Ahn, "Stretchable active matrix inorganic light-emitting diode display enabled by overlay-aligned roll-transfer printing," *Adv. Funct. Mater.* **27**(11), 1606005 (2017).
4. B. Corbett, R. Loi, W. Zhou, D. Liu, and Z. Ma, "Transfer print techniques for heterogeneous integration of photonic components," *Prog. Quantum Electron.* **52**, 1–17 (2017).
5. H. Amano, Y. Baines, E. Beam, M. Borga, T. Bouchet, P. R. Chalker, M. Charles, K. J. Chen, N. Chowdhury, R. Chu, C. De Santi, M. M. De Souza, S. Decoutere, L. Di Cioccio, B. Eckardt, T. Egawa, P. Fay, J. J. Freedman, L. Guido, O. Häberlen, G. Haynes, T. Heckel, D. Hemakumara, P. Houston, J. Hu, M. Hua, Q. Huang, A. Huang, S. Jiang, H. Kawai, D. Kinzer, M. Kuball, A. Kumar, K. B. Lee, X. Li, D. Marcon, M. März, R. McCarthy, G. Meneghesso, M. Meneghini, E. Morvan, A. Nakajima, E. M. S. Narayanan, S. Oliver, T. Palacios, D. Piedra, M. Plissonnier, R. Reddy, M. Sun, I. Thayne, N. Trivellin, V. Unni, M. J. Uren, M. Van Hove, D. J. Wallis, J. Wang, J. Xie, S. Yagi, S. Yang, C. Youtsey, R. Yu, E. Zanoni, S. Zeltner, and Y. Zhang, "The 2018 GaN power electronics roadmap," *J. Phys. D: Appl. Phys.* **51**(16), 163001 (2018).
6. B. Gill, *III-Nitride Semiconductors and their Modern Devices* (Oxford University Press, 2013).
7. D. Zhu, D. J. Wallis, and C. J. Humphreys, "Prospects of III-nitride optoelectronics grown on Si," *Rep. Prog. Phys.* **76**(10), 106501 (2013).
8. D. Marcon, B. De Jaeger, S. Halder, N. Vranckx, G. Mannaert, M. Van Hove, and S. Decoutere, "Manufacturing challenges of GaN-on-Si HEMTs in a 200 mm CMOS Fab," *IEEE Trans. Semicond. Manuf.* **26**(3), 361–367 (2013).
9. J. W. Johnson, E. L. Piner, A. Vescan, R. Therrien, P. Rajagopal, J. C. Roberts, J. D. Brown, S. Singhal, and K. J. Linthicum, "12 W/mm AlGaIn-GaN HFETs on silicon substrates," *IEEE Electron Device Lett.* **25**(7), 459–461 (2004).
10. S. Gorman, D. Gajula, S. Kim, and G. Koley, "Impact of volatile organic compound exposure on electrical breakdown in GaN dual channel microcantilevers," *Appl. Phys. Lett.* **114**(11), 114103 (2019).
11. J. F. C. Carreira, A. D. Griffiths, E. Xie, B. J. E. Guilhabert, J. Herrnsdorf, R. K. Henderson, E. Gu, M. J. Strain, and M. D. Dawson, "Direct integration of micro-LEDs and a SPAD detector on a silicon CMOS chip for data communications and time-of-flight ranging," *Opt. Express* **28**(5), 6909–6917 (2020).
12. A. S. Yalamarthy, H. So, M. Muñoz Rojo, A. J. Suria, X. Xu, E. Pop, and D. G. Senesky, "Tuning electrical and thermal transport in AlGaIn/GaN heterostructures via buffer layer engineering," *Adv. Funct. Mater.* **28**(22), 1705823 (2018).
13. P. Srivastava, J. Das, D. Visalli, M. Van Hove, P. E. Malinowski, D. Marcon, S. Lenci, K. Geens, K. Cheng, M. Leys, S. Decoutere, R. P. Mertens, and G. Borghs, "Record breakdown voltage (2200 V) of GaN DHFETs on Si with 2- μ m buffer thickness by local substrate removal," *IEEE Electron Device Lett.* **32**(1), 30–32 (2011).

14. S. Kim, J. Wu, A. Carlson, S. H. Jin, A. Kovalsky, P. Glass, Z. Liu, N. Ahmed, S. L. Elgan, W. Chen, P. M. Ferreira, M. Sitti, Y. Huang, and J. A. Rogers, "Microstructured elastomeric surfaces with reversible adhesion and examples of their use in deterministic assembly by transfer printing," *Proc. Natl. Acad. Sci.* **107**(40), 17095–17100 (2010).
15. A. J. Trindade, B. Guilhabert, E. Y. Xie, R. Ferreira, J. J. D. McKendry, D. Zhu, N. Laurand, E. Gu, D. J. Wallis, I. M. Watson, C. J. Humphreys, and M. D. Dawson, "Heterogeneous integration of gallium nitride light-emitting diodes on diamond and silica by transfer printing," *Opt. Express* **23**(7), 9329–9338 (2015).
16. H. Kim, E. Brueckner, J. Song, Y. Li, S. Kim, C. Lu, J. Sulkin, K. Choquette, Y. Huang, R. G. Nuzzo, and J. A. Rogers, "Unusual strategies for using indium gallium nitride grown on silicon (111) for solid-state lighting," *Proc. Natl. Acad. Sci.* **108**(25), 10072–10077 (2011).
17. H. Ishikawa, G.-Y. Zhao, N. Nakada, T. Egawa, T. Jimbo, and M. Umeno, "High-Quality GaN on Si substrate using AlGaIn/AlN Intermediate Layer," *Phys. Status Solidi A* **176**(1), 599–603 (1999).
18. A. Able, W. Wegscheider, K. Engl, and J. Zweck, "Growth of crack-free GaN on Si(111) with graded AlGaIn buffer layers," *J. Cryst. Growth* **276**(3–4), 415–418 (2005).
19. E. Feltn, B. Beaumont, M. Laugt, and P. de Mierry, "Stress control in GaN grown on silicon (111) by metalorganic vapor phase epitaxy," *Appl. Phys. Lett.* **79**(20), 3230–3232 (2001).
20. Y. Zhang, S.-W. Ryu, C. Yerino, B. Leung, Q. Sun, Q. Song, H. Cao, and J. Han, "A conductivity-based selective etching for next generation GaN devices," *Phys. Status Solidi B* **247**(7), 1713–1716 (2010).
21. M. Rais-Zadeh, V. J. Gokhale, A. Ansari, M. Faucher, D. Théron, Y. Cordier, and L. Buchailot, "Gallium Nitride as an Electrochemical Material," *J. Microelectromechanical Syst.* **23**(6), 1252–1271 (2014).
22. I. Christiaens, G. Roelkens, K. De Mesel, D. Van Thourhout, and R. Baets, "Thin-film devices fabricated with benzocyclobutene adhesive wafer bonding," *J. Lightwave Technol.* **23**(2), 517–523 (2005).
23. X. Sheng, C. Robert, S. Wang, G. Pakeltis, B. Corbett, and J. A. Rogers, "Transfer printing of fully formed thin-film microscale GaAs lasers on silicon with a thermally conductive interface material," *Laser Photonics Rev.* **9**(4), L17–L22 (2015).
24. E. Yablonovitch, D. M. Hwang, T. J. Gmitter, L. T. Florez, and J. P. Harbison, "Van der Waals bonding of GaAs epitaxial liftoff films onto arbitrary substrates," *Appl. Phys. Lett.* **56**(24), 2419–2421 (1990).
25. B. Guilhabert, J. McPhillimy, S. May, C. Klitis, M. D. Dawson, M. Sorel, and M. J. Strain, "Hybrid integration of an evanescently coupled AlGaAs microdisk resonator with a silicon waveguide by nanoscale-accuracy transfer printing," *Opt. Lett.* **43**(20), 4883–4886 (2018).
26. J. McPhillimy, B. Guilhabert, C. Klitis, M. D. Dawson, M. Sorel, and M. J. Strain, "High accuracy transfer printing of single-mode membrane silicon photonic devices," *Opt. Express* **26**(13), 16679–16688 (2018).
27. D. Zhu, C. McAleese, K. K. McLaughlin, M. Häberlen, C. O. Salcianu, E. J. Thrush, M. J. Kappers, W. A. Phillips, P. Lane, D. J. Wallis, T. Martin, M. Astles, S. Thomas, A. Pakes, M. Heuken, and C. J. Humphreys, "GaN-based LEDs grown on 6-inch diameter Si (111) substrates by MOVPE," *Proc. SPIE* **7231**, 723118 (2009).
28. D. Zhu, C. McAleese, M. Häberlen, C. Salcianu, T. Thrush, M. Kappers, A. Phillips, P. Lane, M. Kane, D. Wallis, T. Martin, M. Astles, N. Hylton, P. Dawson, and C. Humphreys, "Efficiency measurement of GaN-based quantum well and light-emitting diode structures grown on silicon substrates," *J. Appl. Phys.* **109**(1), 014502 (2011).
29. M. Häberlen, D. Zhu, C. McAleese, M. J. Kappers, and C. J. Humphreys, "Dislocation reduction in MOVPE grown GaN layers on (111)Si using SiNx and AlGaIn layers," *J. Phys. Conf. Ser.* **209**, 012017 (2010).
30. M. J. Kappers, M. A. Moram, Y. Zhang, M. E. Vickers, Z. H. Barber, and C. J. Humphreys, "Interlayer methods for reducing the dislocation density in gallium nitride," *Phys. B Condens. Matter* **401–402**, 296–301 (2007).
31. F. Yun, Y.-T. Moon, Y. Fu, K. Zhu, Ü. Özgür, and H. Morkoç, "Efficacy of single and double SiNx interlayers on defect reduction in GaN overlayers grown by organometallic vapor-phase epitaxy," *J. Appl. Phys.* **98**(12), 123502 (2005).
32. R. E. Oosterbroek, J. W. Berenschot, H. V. Jansen, A. J. Nijdam, G. Pandraud, A. van den Berg, and M. C. Elwenspoek, "Etching methodologies in <111>-oriented silicon wafers," *J. Microelectromechanical Syst.* **9**(3), 390–398 (2000).
33. P. Hill, E. Gu, M. D. Dawson, and M. J. Strain, "Thin film diamond membranes bonded on-demand with SOI ring resonators," *Diamond Relat. Mater.* **88**, 215–221 (2018).
34. D. Nečas and P. Klapetek, "Gwyddion: an open-source software for SPM data analysis," *Open Phys.* **10**(1), 181–188 (2012).
35. H. Marchand, L. Zhao, N. Zhang, B. Moran, R. Coffie, U. K. Mishra, J. S. Speck, S. P. DenBaars, and J. A. Freitas, "Metalorganic chemical vapor deposition of GaN on Si(111): Stress control and application to field-effect transistors," *J. Appl. Phys.* **89**(12), 7846–7851 (2001).
36. T. Zimmermann, M. Neuburger, P. Benkart, F. J. Hernandez-Guillen, C. Pietzka, M. Kunze, I. Daumiller, A. Dadgar, A. Krost, and E. Kohn, "Piezoelectric GaN sensor structures," *IEEE Electron Device Lett.* **27**(5), 309–312 (2006).

Fabrication and transfer printing based integration of free-standing GaN membrane micro-lenses onto semiconductor chips

NILS KOLJA WESSLING,¹  SAPTARSI GHOSH,²  BENOIT GUILHABERT,¹  MENNO KAPPERS,² ALEXANDER M. HINZ,^{2,3} MILES TOON,¹ RACHEL A. OLIVER,² MARTIN D. DAWSON,¹  AND MICHAEL J. STRAIN^{1,*} 

¹*Institute of Photonics, Department of Physics, University of Strathclyde, Glasgow, UK*

²*Cambridge Center for Gallium Nitride, University of Cambridge, Cambridge, UK*

³*Now at Fraunhofer FEP, Dresden, Germany*

**michael.strain@strath.ac.uk*

Abstract: We demonstrate the back-end integration of optically broadband, high-NA GaN micro-lenses by micro-assembly onto non-native semiconductor substrates. We developed a highly parallel process flow to fabricate and suspend micron scale plano-convex lens platelets from 6" Si growth wafers and show their subsequent transfer-printing integration. A growth process targeted at producing unbowed epitaxial wafers was combined with optimisation of the etching volume in order to produce flat devices for printing. Lens structures were fabricated with 6 – 11 μm diameter, 2 μm height and root-mean-squared surface roughness below 2 nm. The lenses were printed in a vertically coupled geometry on a single crystalline diamond substrate and with μm -precise placement on a horizontally coupled photonic integrated circuit waveguide facet. Optical performance analysis shows that these lenses could be used to couple to diamond nitrogen vacancy centres at micron scale depths and demonstrates their potential for visible to infrared light-coupling applications.

Published by Optica Publishing Group under the terms of the [Creative Commons Attribution 4.0 License](https://creativecommons.org/licenses/by/4.0/). Further distribution of this work must maintain attribution to the author(s) and the published article's title, journal citation, and DOI.

1. Introduction

Micron-sized optical elements are important components for the coupling of light between free-space and matter based systems. Dielectric micro-lens arrays (MLA) are commercially available and commonly used to focus light onto the photon-sensitive regions of CCD [1] and CMOS [2] photo-detector arrays, in order to increase quantum efficiency. Micro-optics are also used to improve the efficiency of light extraction from light emitting diodes (LEDs) [3] and μ -LEDs [4], for coupling to integrated photonic circuits (PICs) [5] as well as for improving pump and collection efficiency between microscope systems and semiconductor based solid state quantum emitters [6]. This latter application is particularly challenging due to the often random positioning of the quantum emitters and the large refractive index of the host material that leads to total internal reflection at the interface between the material and free-space.

There are two main routes to fabrication of micro-optics on semiconductor substrates, either additive materials patterning on the substrate, or direct fabrication of optical surfaces into the material itself. There are a number of techniques available for the fabrication of additive components, including imprint lithography [7,8], two-photon polymerization [9–11], thermal reflow [12–14], and inkjet printing [15,16]. Structures formed by these methods are commonly used as the final optical element themselves, but may also be used as a mask for a dry-etch shape transfer into the semiconductor. Two photon polymerization (TPP) is a particularly flexible

method and can be used to fabricate complex micro-optical systems such as multi-lens beam expanders on fibre tips [9] as well as vertical and end-fire couplers to PICs [10,11]. The relatively low refractive index n of TPP resins ($n = 1.5 - 1.6$ [17] compared with common semiconductor materials $n > 2.0$ [18–22]) limits the achievable numerical aperture (NA) of the polymer lenses. Furthermore, polymeric materials are susceptible to catastrophic optical damage at watt-level optical power [10].

Alternatively, solid immersion lenses (SIL) can be formed directly into semiconductor materials by focused ion-beam milling [23,24], laser-micromachining [25,26], photoresist reflow in combination with reactive ion etching [27,28], dual masking [29] and diamond turning [30,31]. These methods make use of the high refractive index of the material itself to avoid refractive index contrast at interface layers, produce high NA performance and are robust to optical damage. Individual lenses can be fabricated with high positional accuracy but require either serial, time consuming processing [23,24], or in the case of diamond substrates are limited in the form factors that can be achieved due to the mask-to-semiconductor etch selectivity [27,28].

In this work, we present an alternative and scalable fabrication scheme, whereby micro-lenses are directly fabricated in GaN material and subsequently transferred to a host chip as membrane devices. The use of a III-N material enables better etch selectivity than in e.g. diamond, while retaining a close refractive index match to semiconductor materials. The devices are fabricated using a combination of grayscale lithography and the photoresist reflow to create spherical photoresist micro-lenses, followed by inductively coupled reactive ion etching (ICP-RIE) to transfer the pattern into a GaN/AlGaN/AlN layer stack grown on 6" Si wafers [32]. The micro-lenses are suspended over the silicon substrate by wet chemical etching and transferred to

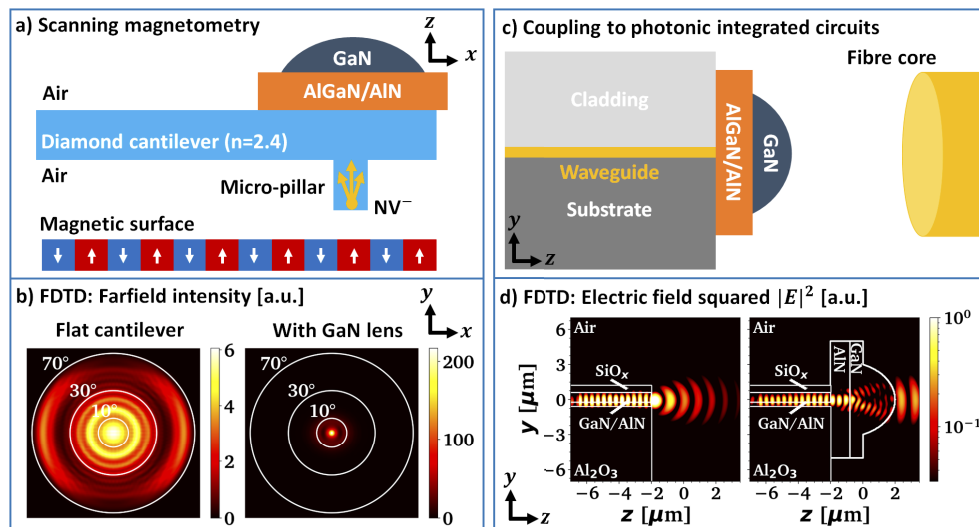


Fig. 1. a) Schematic application example for diamond NV scanning magnetometry, exploiting a GaN lens as a light coupler, b) Simulated far field of a dipole emitter placed in a 200 nm wide square micro-pillar (10 nm away from the pillar tip, assuming [111]-orientation) without and with a printed GaN micro-lens (ROC = 16 μm , 15 μm distance to the top of the pillar) at $\lambda = 650$ nm wavelength c) Schematic of a GaN micro-lens facilitating end-fire coupling between a photonic integrated circuit (left) and a fibre core (right), d) Simulated free-space divergence from the fundamental TE mode of an GaN/AlN waveguide (1.2 μm height, 2 μm width) without and with a GaN micro-lens (ROC = 3.3 μm) printed on the waveguide facet.

non-native substrates using a transfer printing process. We demonstrate transferred micro-lenses with micron scale radius of curvature (ROC) and focal length f on diamond substrates. We also show direct printing of a micro-lens onto the facet of a GaN waveguide chip. Two example applications are shown in Fig. 1. In a), light is coupled to and from a diamond nitrogen vacancy (NV^-) centre into free-space collection optics for scanning magnetometry [33,34]. By including a GaN micro-lens on the diamond substrate, the effective collection angle from the point emitter is significantly reduced, improving potential coupling efficiency with external, low NA optics and minimising total internal reflection losses. As the minimum detectable magnetic field scales with the square root of the collected fluorescence rate in NV^- based sensors, the cost of the instrument can be reduced while improving performance metrics such as the measurement acquisition time [35]. More generally, our transfer printing approach leaves the host crystal intact and allows for alignment to randomly positioned quantum emitters. Figure 1(b) shows a scenario where a micro-lens is integrated onto the facet of a GaN/AlN planar waveguide chip, improving modal coupling efficiency between the highly confined on-chip mode and low NA external optics such as a single mode fibre. In both applications, high-NA GaN micro-lenses could potentially substitute other high-NA optical components, while maintaining or improving the system's performance.

2. Fabrication and device transfer

Fig. 2 illustrates the process flow for GaN micro-lens fabrication and transfer.

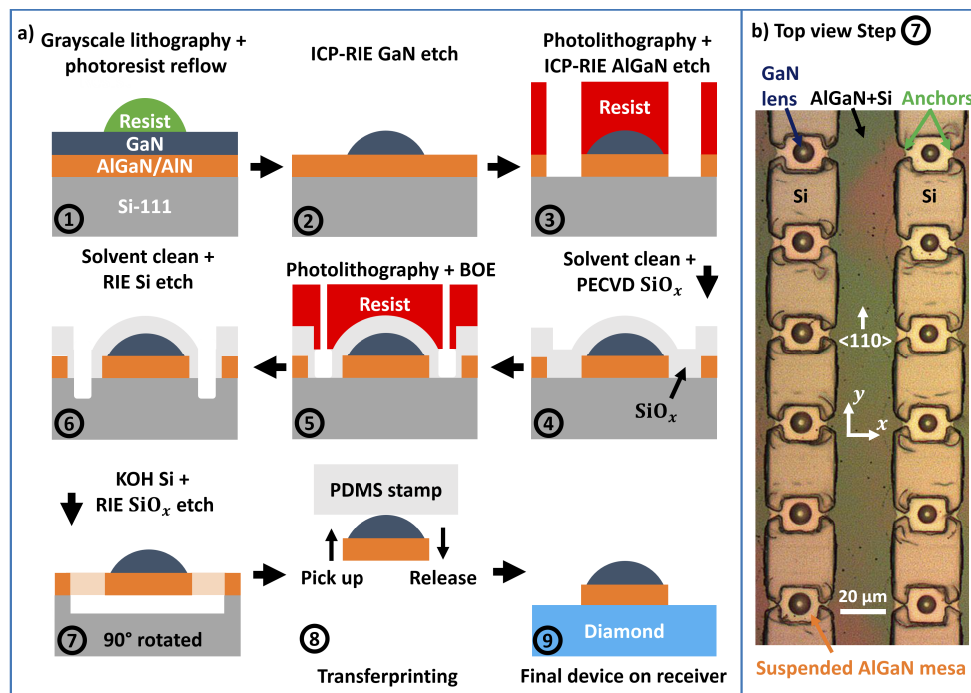


Fig. 2. a) Illustration of the process flow after growth, using CVD-grown, single crystalline diamond as receiver substrate, b) Microscope image of a GaN-on-Si donor chip corresponding to process step 6.

A wafer die is spin coated with "Shipley SPR220-4.5" photoresist and micro-lenses are defined in the resist using a combination of grayscale laser lithography (Heidelberg Instruments DWL66+) and thermal reflow on a hotplate at 130-150 °C ①. The grayscale preshaping allows control of

the lens diameter and rounds the resist edges. A step wise increase of the reflow temperature leads to a spherical resist lens with the targeted height and radius of curvature with a smooth surface finish. Alternatively, highly optimised grayscale lithography could be used to directly define the resist profile, with the cost of increased surface roughness. An Ar/Cl₂-based ICP-RIE (200 W coil power, 70 W platen power, 30 sccm Cl₂, 10 sccm Ar, 20 mTorr) is used to transfer the lens shape into the GaN ②. The ICP recipe yields etch rates of 200 nm/min for SPR220-4.5 and 150 nm/min for GaN/AlGaN, leading to a selectivity around 0.75. The etch rate drops to around 120 nm/min for AlGaN with Al content $x > 60\%$ and in the AlN layer. The reactive ion etching results in a lens profile transformation from a spherical resist lens to a parabolic shape of the etched lens, as previously observed in SiC [14], indicating a partly chemical etch and possibly ion channeling effects.

The defined GaN lenses are overlaid with a mesa pattern including suspension anchors using "Shipley SPR220-7.0" photoresist. The previously detailed ICP-RIE recipe is employed to remove the remaining AlGaN and AlN layers, leading to a slight overetch into Si ③. Fig. 2 b) shows a microscope image of already suspended devices, illustrating the etched anchor and mesa pattern defined in this etching step. The 7 μm thick photoresist is needed to successfully protect the GaN lens surface from the plasma, as about 3 μm resist is sacrificed during the etching and the spin coated resist is slightly thinner than the full 7 μm thickness over the protruding lens features.

After resist removal, a conformal layer of 1.8 μm thick SiO_x is deposited in step ④ by plasma enhanced chemical vapor deposition (PECVD, 70 W RF power, 170 sccm SiH₄, 710 sccm N₂O, 1 Torr, $T = 300\text{ }^\circ\text{C}$). This hard mask protects the GaN lens from the potassium hydroxide (KOH) wet etch in step ⑤, with thinner layers demonstrating susceptibility to local failure and subsequent chemical etching of the micro-lens features. SPR220-7.0 is used as a lithography mask to open windows at the bottom of the etched trenches and a buffered oxide etch (7:1) removes the SiO_x with a slight undercut, leaving a sidewall protection layer of SiO_x on the AlGaN/AlN mesa below the lens ⑥.

An anisotropic RIE etch (100 sccm SF₆, 8 sccm O₂, 25 mTorr, 50 W RF-power [36]) is applied after resist removal to etch the Si substrate using the SiO_x layer as a mask ⑥. The resultant trench allows access for a KOH wet etch solution (40% in weight, 85 $^\circ\text{C}$) to the (110) crystal plane, selectively removing the Si below the lens-mesa along the fast $\langle 110 \rangle$ etch direction ⑦. The schematic in Fig. 2 is rotated for this process step, indicating the anchors as semitransparent areas and showing the anisotropic nature of the KOH etch in Si(111). Fig. 2 b) shows a top view. As previously confirmed by scanning transmission electron microscopy [32,37], a nm-thin disordered AlSi_yN_x interlayer is formed between Si substrate and AlN nucleation layer, which provides an effective bottom protection against the KOH solution. The smoothness of the mesa bottom surface is confirmed by atomic force microscopy (AFM) measurements after flipping a flat membrane device with a PDMS stamp, yielding 0.4 nm root-mean-squared (r.m.s.) roughness.

The SiO_x layer is removed by RIE dry etching (5 sccm CHF₃, 15 sccm Ar, 30 mTorr, 120 W RF-power) to restore the GaN lens surface. AFM surface roughness analysis on a GaN micro-lens after SiO_x removal showed a surface roughness on the order of 1.4 nm r.m.s.

The suspended micro-lenses are transfer-printed to receiver substrates (single crystalline (SC) diamond or GaN/AlN waveguide facets) using a custom transfer printing system with sub-micron spatial precision [38]. The lenses are removed from their growth substrate using a soft polymer stamp fabricated using a 6:1 ratio Sylgard PDMS with a contact area of 30x30 μm^2 ⑧. The devices are finally aligned to the receiver chip position and released, making use of direct Van-der-Waals interaction between the lens bottom and receiver chip top surface ⑨.

Additional data on the process flow, surface roughness, lens-shape transformation and process yield is given in the supplemental document Fig. S1-5.

3. Material growth for membrane flatness

The success of the heterogeneous integration scheme detailed above relies on the flatness of the released membrane devices in addition to the back-side smoothness. If the membrane devices are too bowed, it becomes impossible to achieve a good contact with the receiver substrate, leaving an air cavity between the substrate and the device surface [39,40], which in the case of micro-lens devices can lead to interface reflections and distortion of the desired lens behaviour. Appropriately flat membranes are achieved via careful optimisation of the growth process for the GaN heteroepitaxial layers. The structures used for micro-lens fabrication in this work are grown by metal organic vapor phase epitaxy (MOVPE) on Si(111) substrates. As-grown, the multilayers consist of a $0.25\ \mu\text{m}$ AlN nucleation layer, a $1.7\ \mu\text{m}$ graded $\text{Al}_x\text{Ga}_{1-x}\text{N}$ buffer (with AlN mole fraction x decreasing from 75% to 25%), and a $2\ \mu\text{m}$ GaN layer (i.e. a total thickness of ca. $4\ \mu\text{m}$ nitride material). By successively growing layers with a decreasing Al content, each layer has a slightly larger relaxed lattice constant than that below it, so that the epitaxial growth induces compressive stress. This stress counteracts the post-growth cooldown related tensile stress originating from the thermal expansion mismatch between the silicon substrate and the nitride epitaxial layers. Post-growth, the wafer-bow is a function of the residual stresses and thickness of the individual epilayers. For a membrane released from the growth substrates, its deflection is also dependent on these in-built stresses in the remaining layers and related to the wafer bow [41].

The wafer bow can be controlled by exposing the substrate to ammonia at $1000\ ^\circ\text{C}$ prior to deposition of the AlN nucleation layer. By changing the duration of the ammonia pre-dose, the bow may be tuned from convex to concave. Initial trials of the membrane fabrication process with the pre-dose duration varying (without any lens fabrication) used a series of wafers in which a $1\ \mu\text{m}$ GaN epilayer was grown on top of similar underlying buffer layers to those employed for the micro-lens fabrication. These trials indicated that minimising the wafer bow also yielded the least bowed membrane (see supplemental document, Fig. S6). Based on this information, for the present studies with $2\ \mu\text{m}$ thick GaN layers, material from two nearly-flat wafers (having respective bow values of $+7\ \mu\text{m}$ and $-2\ \mu\text{m}$) are used for the experiments. It is observed that even for material from flat wafers, the material removal in the micro-lens fabrication needs to be further optimised to realise flat devices.

For example, Fig. 3 a) shows a test membrane with a planar surface (i.e. no lens topology) where material was removed by ICP-RIE until $1.2\ \mu\text{m}$ of the combined graded AlGaIn buffer and AlN nucleation layer remained. Though the source wafer had near-zero bow, when the resulting AlGaIn/AlN membrane is transferred to a diamond substrate, a clear interference fringe pattern appears. This indicates an air gap below the device. An AFM scan confirms convex bowing of the membrane, showing that the maximum width of the air gap is on the order of $250\ \text{nm}$.

Membranes with micro-lens topology are also bowed when etched to this same remaining thickness of $1.2\ \mu\text{m}$, as shown in Fig. 3 b). However, the effect is observed to be most pronounced for the smallest micro-lens whose colour fringes closely resemble the planar membrane device in Fig. 3 a). As the lens diameter increases, the coloured fringes decrease in spatial frequency, indicating a reduced membrane bow. This can be explained by the fact that in membranes where the original layer thicknesses are maintained, the summation of bending moments arising from each layer are balanced. Once the thicknesses and/or volumes are altered (e.g. by partial etching of the layers to create a lens geometry), this balance is disrupted, so that the membrane starts to bow, creating an additional bending stress restoring equilibrium. This effect is here further enhanced, since lens height and the diameter are for these particular devices positively correlated, with the height rising from $2\ \mu\text{m}$ to $3\ \mu\text{m}$, compare Fig. S7 for AFM data. As more material is removed, like in the case of small radius of curvature lens structures, the bow of the devices becomes larger. Hence, the optimised micro-lenses are designed to leave more of the epitaxial stack intact by limiting the lens etch depth to $2\ \mu\text{m}$, matching the thickness of the GaN epilayer.

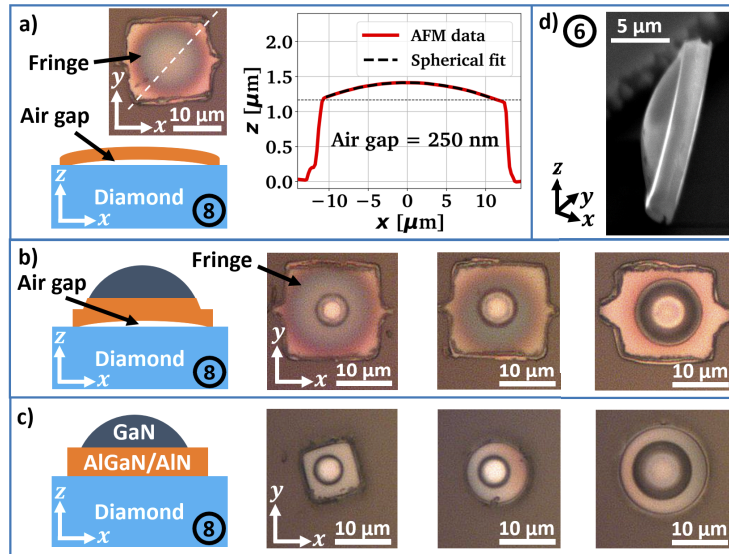


Fig. 3. a) Schematic, microscope image and AFM analysis of a $1.2\ \mu\text{m}$ thin AlGaIn/AlN membrane transfer printed onto SC diamond, b)/c) Schematic and microscope images of $2 - 3\ \mu\text{m}$ high micro-lenses in b) on bowed, $1.2\ \mu\text{m}$ thick mesas with anchors and in c) on flat, $2\ \mu\text{m}$ thick mesas without anchors printed on SC diamond, d) 40° tilted SEM image of a $2\ \mu\text{m}$ high GaN lens with a flat, $2\ \mu\text{m}$ thick mesa standing on the donor substrate.

As shown in Fig. 3 c), this balanced height of GaN micro-lens and AlGaIn/AlN mesa did not result in air cavity induced colour fringes after the transfer step. The flatness of these membranes can be further confirmed by the tilted SEM image in Fig. 3 d) which shows a micro-lens membrane from a side-view.

Fig. 4 a) shows SEM images of devices without anchoring tethers collapsed to the Si surface after KOH etch and SiO_x mask removal. For optical testing, we selected three similar micro-lenses with varying diameter (①,②,③) printed on a electronic grade single crystalline CVD diamond membrane from Element6 [$2 \times 2\ \text{mm}^2$, $N < 5\ \text{ppb}$], see Fig. 4 b) for microscope images. AFM profile scans of these devices are plotted in c) and fitted both with a spherical and parabolic function. Both fits match the data well, but the parabolic fit performs slightly better, showing r.m.s. deviation from the data of 30, 35 and 55 nm compared to 40, 60 and 105 nm for the spherical fit, ordered left to right according to device ①, ② and ③. The Maréchal criterion defines an optical focussing system as diffraction limited when the r.m.s. wavefront error is smaller than $\lambda/14$ across the full aperture [42]. For a wavelength of $\lambda = 650\ \text{nm}$, this corresponds to roughly 33 nm r.m.s. surface deviation (weighted by the index contrast $n - 1$). Devices ① and ② show surface variations from the spherical and parabolic fit close to this threshold, so we do not expect significant loss of optical performance. The smallest micro-lens, device ③, shows reasonable agreement with the parabolic shape, which should make it effective at collimating light from its focal position close to the diamond surface.

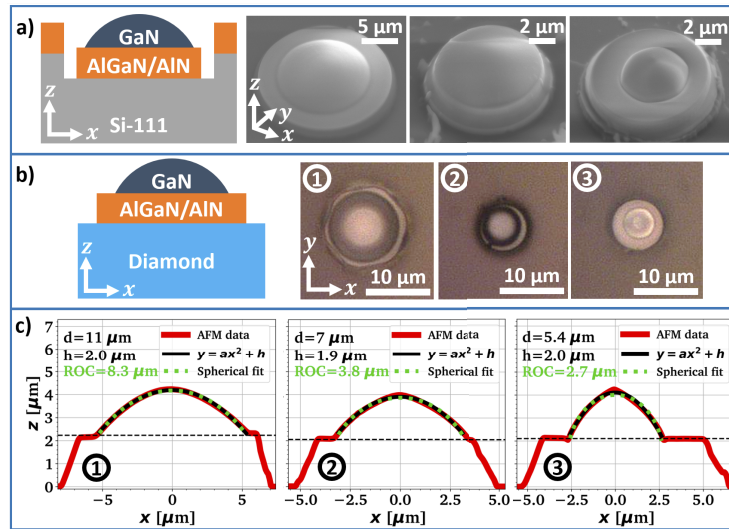


Fig. 4. a) Schematic and 40° tilted SEM images of collapsed micro-lenses on membranes without anchors on the donor substrate, b) Schematic and microscope image of the transfer-printed devices on SC diamond used for the optical analysis in Fig. 6, c) AFM topography and shape analysis of the devices shown in b), with lens diameter d , height h and ROC extracted from the correspondingly colored fit.

4. Optical analysis

The focal lengths of the three lenses printed onto a SC diamond substrate, shown in Fig. 4 b)/c), are measured using a custom built infinity-corrected microscope illustrated in Fig. 5, which is based on [43]. The light from a tungsten lamp (Ocean optics HL-2000-FHSA) is collimated with a convex lens (CL) and passed through a colour filter (CF) primarily transmitting green light. For additional spectral selection, only the green pixel channel of the CCD colour camera with a Bayer filter (Allied Vision Prosilica GC650-C) is used for the analysis, leading to a total of 10 dB rejection in the $\lambda = 525 \pm 50$ nm wavelength range. The measured transmission spectrum of the setup is shown in Fig. S8 in the supplementary document. The refractive index of GaN varies only by ca. 2% in this wavelength range [21]. The collimated beam is coupled through the back-side of the diamond substrate and then through the printed GaN micro-lenses on the opposite face. The wide field illumination allows imaging of the micro-lenses with an infinity-corrected 60x objective (Nikon Plan Fluor, NA = 0.85), using a 200 mm tube lens (TL, Thorlabs LA1708-A) to image onto a CCD array. A calibrated piezo controller (PI P-725.4CD with E-665CR) is used to manipulate the objective's z -position with sub-micron accuracy. Automated z -scans are constructed by taking images in synchronisation with the piezo position.

The focal length f_{air} of the micro-lens in air is extracted from the z -scan as a bright spot on the CCD camera, when the focal spot of the objective and micro-lens overlap. We then compare the z -travel distance between a sharp image of the micro-lens mesa and the image of the focal spot to extract f_{air} . The broadband source was used in these measurements to avoid the obscuring interference fringes generated by monochromatic sources.

The expected focal length of the three example micro-lenses is calculated using 3D FDTD simulations (Lumerical) in which the lenses are created to match the form factor of the measured devices, based on the AFM profiles, as shown in Fig. 4 c). The refractive index model for the micro-lens structure is based on [20–22,45], using $\text{Al}_x\text{Ga}_{1-x}\text{N}$ with $x = 38\%$.

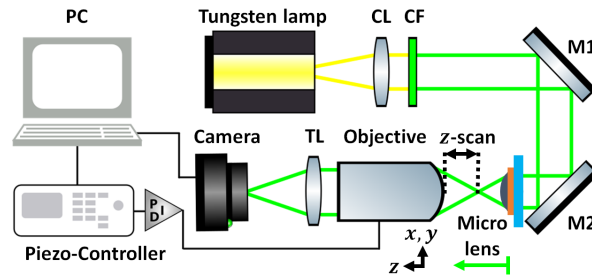


Fig. 5. Optical setup used to evaluate the focal length of GaN micro-lenses printed onto diamond, based on [43]. The convex lens CL, green colour filter CF, mirrors M1 and M2 and tube lens TL are annotated. Illustrations are taken from [44].

Fig. 6 a) shows the simulated electric field strength squared for a plane wave injected from the diamond substrate upwards through the micro-lens geometry at $\lambda = 525$ nm wavelength. We chose the apparent symmetry point of the focal spot to evaluate the focal length f_{air} measured from the GaN micro-lens tip. The results are displayed in Tab. 1 and compared to what would be expected from the geometric optics (GO) approximation for a spherical surface with index $n_{\text{GaN},\lambda=525\text{ nm}} = 2.43$ [21] (compared to $n_{\text{dia},\lambda=525\text{ nm}} = 2.43$ [20]). We evaluate the following equations [46] with the lens diameter d and height h found in the spherical fit in Fig. 4 c):

$$\text{ROC} = \frac{\left(\frac{d}{2}\right)^2 + h^2}{2h} \quad f_{air} = \text{ROC} \cdot \frac{1}{n_{\text{GaN},\lambda=525\text{ nm}} - 1}$$

The shortened focal lengths found in the FDTD simulations in comparison to the GO approximation shows the necessity to use a full Maxwell solver to accurately predict the micro-lens performance. The diffraction effect evident in the simulations is known as focal shift and is well documented for small scale micro-optics [47–49]. Diffraction is also reported to account for the visible "funneling" of light into a tube, rather than a distinct focal spot [47], and can be seen in Fig. 6 a).

Table 1. Results of the AFM and optical analysis of the lenses shown in Fig. 4 b)/c). Diameter d , height h , radius of curvature (ROC) and focal length f are given for the geometric optics (GO) approximation and FDTD simulations and compared to the experimental data (EXP). f_{air} is simulated at $\lambda = 525$ nm, while f_{dia} is simulated at $\lambda = 700$ nm wavelength.

	d	h	ROC	f_{air} GO	f_{air} FDTD	f_{air} EXP	f_{dia} FDTD	NA_{dia}
	[μm]							
①	11	2.0	8	6	4	4.5 ± 1.0	14	1.0
②	7	1.9	4	3	2	2.0 ± 1.0	7	1.4
③	5.5	2.0	3	2	1	1.5 ± 1.0	5	1.7

Fig. 6 b) shows the measured z -scan sections with $0.5 \mu\text{m}$ step size for each micro-lens. The lens geometries from the FDTD simulations are overlaid as a guide to the eye, with their locations defined by imaging the mesa structures. The measured position of the focal point is extracted as the highest intensity spot above the lens surface in air and is presented alongside the simulation values in Tab. 1. The measurement errors are dominated by the uncertainty regarding the lens surface position (found from the z -position of the mesa image) and the μm -large measured depth of focus in the measurement setup.

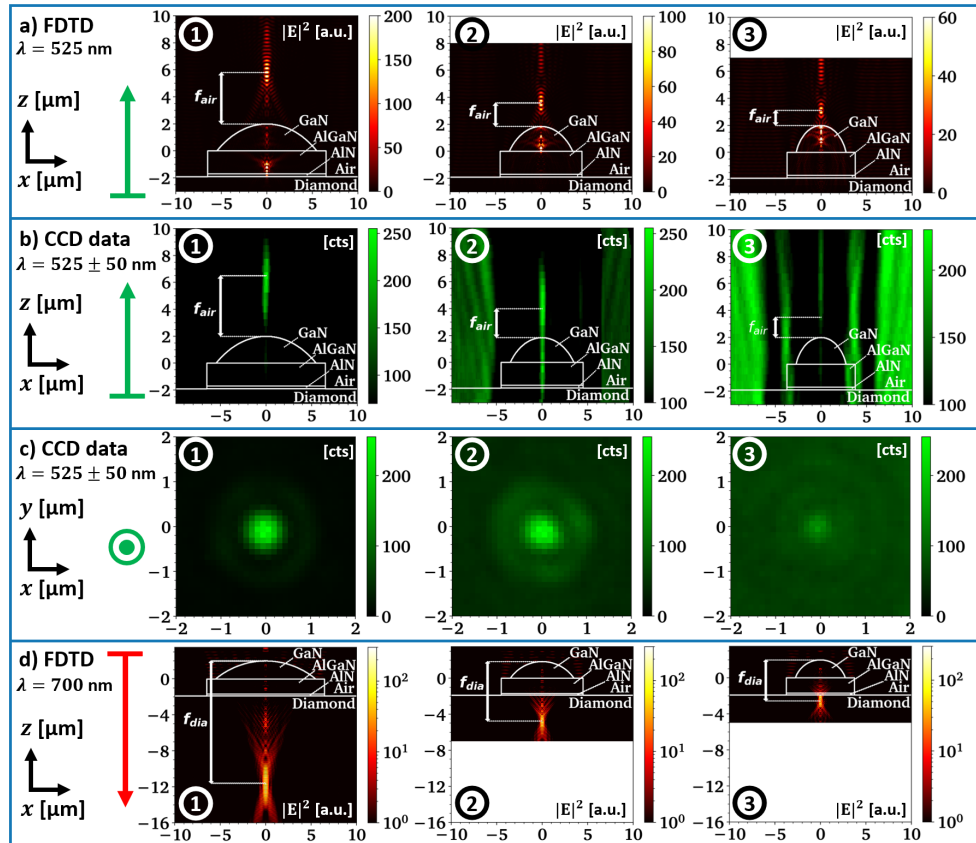


Fig. 6. Optical analysis of the GaN micro-lenses on diamond shown in Fig. 4 b)/c): a) FDTD simulations of the electric field squared with a linearly polarised plane wave injected at $\lambda = 525$ nm wavelength from diamond through spherical lens profiles, b) Measured z -scan of the x -profile through the xy -CCD data evaluated on the lenses with the setup shown in Fig. 5, overlaid with contours from the FDTD simulations in a), c) xy -CCD data at the objective's focal position matching f_{air} in b), d) FDTD simulations of the electric field squared with a linearly polarised plane wave injected at $\lambda = 700$ nm from air into the indicated spherical micro-lenses on diamond.

The xy -view of the selected focal spot is shown in Fig. 6 c). The full-width-half-maximum (FWHM) of the measured focal spot size is on the order of 700 – 800 nm, showing reasonable circular symmetry. We do not expect to reach the diffraction limited spot size (FWHM \approx 500 – 750 nm for $\lambda = 525$ nm and simulated NA in air of \approx 0.5, 0.4 and 0.35 for devices ①, ② and ③, respectively [43]) as we use a broadband beam with low coherence.

Expected and measured focal lengths agree well for lenses ① and ②, but the results for the highest-aspect ratio micro-lens ③ are more challenging to extract due to the lack of a clear signature of the focal spot. This may be partially due to the reduction of contrast due to the decreasing lens aperture, which is additionally masked by increasing total internal reflections when transitioning to a higher aspect ratio lens. This loss of contrast is visible in Fig. 6 c). Spherical aberration and astigmatism might also lead to a wider spread of the focus along the z -axis.

Due to the substrate thickness and high index contrast, it is experimentally challenging to measure the focal length f_{dia} of the micro-lenses in diamond. But as there is overall reasonable agreement between measured results and FDTD simulations, f_{dia} can be estimated by inverting the FDTD simulations, see Fig. 6 d). In this case, a linearly polarised plane wave is injected from the top of the sample through the lens and into the substrate. Here we use $\lambda = 700$ nm wavelength corresponding to the central wavelength of NV^- emission at room temperature [50], with $n_{GaN,\lambda=700\text{ nm}} = 2.37$ [21] and $n_{dia,\lambda=700\text{ nm}} = 2.41$ [20]. The focal length f_{dia} in diamond in reference to the GaN lens tip is assessed by identifying the symmetry point of the apparent focal spot, which leads to the results presented in Tab. 1. These values imply that the fabricated micro-lenses could be used to couple to NV^- centres both in nm-proximity to the diamond surface and in up to 10 μm depth. To illustrate the light collection potential of our demonstrated micro-lenses, we calculate the numerical aperture for collection from diamond using the following expression:

$$NA_{dia} = n_{dia} \cdot \sin \left(\arctan \left(\frac{d}{2(f_{dia} - h)} \right) \right)$$

which indicates potentially comparable performance to high-end oil immersion objectives.

5. Printed GaN micro-lens on a waveguide facet

To show the compatibility of the free-standing micro-lens transfer with challenging device geometries, we integrated a high-aspect ratio micro-lens onto the polished facet of a straight waveguide on a GaN-on-sapphire PIC with a 600 nm thin SiO_2 upper-cladding layer. The GaN/AlN waveguides have a total thickness of 1.2 μm , with 850 nm GaN on top of a 350 nm AlN nucleation layer. The waveguide width is 2 μm at the facet, but is tapered down to 1 μm on the chip. See Fig. 1 d) for the corresponding FDTD simulation.

A tilted SEM image of the micro-lens is shown in Fig. 7 a), while microscope images of the facet before and after printing are shown in b), including an overlay of images before and after printing in the center. The chip did not contain any local alignment markers to guide a print on the facet, which restricted the alignment accuracy to around ± 1 μm . The cladding layer is very thin, which causes roughly a third of the micro-lens to remain suspended in air, demonstrating the versatility of the approach and the flatness of the printed device. As previous work has shown nm-scale accuracy with transfer printing [38], alignment to a chip with dedicated markers and a thicker cladding layer should allow printing accuracy with sub-micron precision.

We imaged the light output from the waveguide facet through the micro-lens using a 60x objective with a 500 mm tube lens to reach 150x magnification. The output mode at $\lambda = 1630$ nm wavelength is shown in Fig. 7 c), indicating the transparency of the lens in this wavelength region. The top view image in Fig. 7 d) shows the lens after optical characterisation, validating the mechanical stability of the bond between lens and the polished facet even with the limited bond area.

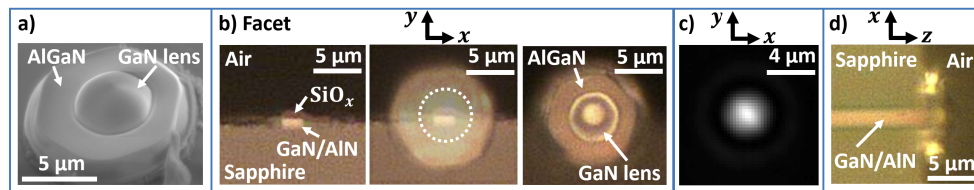


Fig. 7. High-aspect ratio GaN micro-lens printed on GaN-on-sapphire waveguide facet. a) 40° tilted SEM image of the micro-lens on the donor sample, b) Microscope images of the waveguide facet ($1.2 \times 2 \mu\text{m}^2$) before (left) and after (right) transfer printing, the centre image shows an overlay, c) Imaged output mode from the waveguide with printed micro-lens at $\lambda = 1630 \text{ nm}$ wavelength at 150x magnification, d) Top view of the printed lens after mode imaging.

6. Conclusion and Outlook

Gallium nitride is an attractive material for micro-lens fabrication due to its broad optical transparency, high refractive index and ready availability in epistructure format. Here, we have demonstrated the dry transfer of such GaN micro-lenses fabricated from GaN-on-Si, permitting back-end integration in an additive process for a range of applications. Importantly, this approach offers deterministic positioning of the micro-lenses and avoids the risk of fabrication induced damage to solid state quantum emitters in monolithic fabrication approaches. Additionally, the dry etch based fabrication and wafer-scale availability of GaN-on-Si potentially enables scaling the process flow.

Careful optimisation of the growth and fabrication steps enables direct contact printing of flat membrane devices onto semiconductor substrates, here demonstrated using CVD-grown single crystalline diamond as a receiver. The etch depth of the micro-lenses strongly affects the released device flatness, highlighting the interplay between material stress profile and etch geometry. The lens imaging measurements on the diamond substrate show good agreement with FDTD simulations, which are compatible with schemes for efficient coupling to diamond NV^- centres at a range of 0.1 to $10 \mu\text{m}$ depth from the material surface.

Additionally, we printed a GaN lens on a GaN/AlN waveguide facet, showing compatibility of additive micro-optics with μm -precision transfer, even when partially suspended in air. The print demonstrates both the flatness of our devices and the flexibility of the transfer-printing approach for end-fire coupling.

Future work aims to demonstrate light collection from colour centres in diamond and other high index materials such as GaN [51] or SiC [52] and efficient coupling to photonic integrated circuits in the VIS and NIR wavelength regime. Using highly optimised grayscale lithography, the benefits of free-form optics can be added to the developed additive GaN micro-optics platform.

Funding. Royal Academy of Engineering (Research Chairs, Senior Research Fellowships); Engineering and Physical Sciences Research Council (EP/N017927/1, EP/P00945X/1, EP/R03480X/1); Innovate UK (50414); Fraunhofer Lighthouse Project Qmag; NKW acknowledges funding of his PhD studentship by Fraunhofer UK.

Acknowledgments. The authors thank Jack Smith for providing the GaN-on-sapphire photonic integrated circuit chip, which was partially fabricated in the James Watt Nanofabrication center at the University of Glasgow.

Disclosures. The authors declare no conflicts of interest.

Data availability. Data underlying the results presented in this paper are available in Ref. [53].

Supplemental document. See Supplement 1 for supporting content.

References

1. R. Stevens and T. Miyashita, "Review of standards for microlenses and microlens arrays," *The Imaging Sci. J.* **58**(4), 202–212 (2010).

2. J. E. G. Douglas A. Baillie, "Zero-space microlenses for CMOS image sensors: optical modeling and lithographic process development," *Proc. SPIE* **5377**, 953–959 (2004).
3. A. Braeuer, P. Dannberg, U. Zeitner, G. Mann, and W. Karthe, "Application oriented complex polymer microoptics," *Microsyst. Technol.* **9**(5), 304–307 (2003).
4. H. W. Choi, E. Gu, J. M. Girkin, and M. D. Dawson, "Nitride micro-display with integrated micro-lenses," *phys. stat. sol. (c)* **2**(7), 2903–2906 (2005).
5. R. Marchetti, C. Lacava, L. Carroll, K. Gradkowski, and P. Minzioni, "Coupling strategies for silicon photonics integrated chips [Invited]," *Photonics Res.* **7**(2), 201 (2019).
6. A. Bogucki, L. Zinkiewicz, M. Grzeszczyk, W. Pacuski, K. Nogajewski, T. Kazimierzczuk, A. Rodek, J. Suffczyński, K. Watanabe, T. Taniguchi, P. Wasylczyk, M. Potemski, and P. Kossacki, "Ultra-long-working-distance spectroscopy of single nanostructures with aspherical solid immersion microlenses," *Light: Sci. Appl.* **9**(1), 48 (2020).
7. R. Voelkel, "Wafer-scale micro-optics fabrication," *Adv. Opt. Technol.* **1**(3), 135–150 (2012).
8. A. R. Moharana, H. M. Außerhuber, T. Mitteramskogler, M. J. Haslinger, and M. M. Mühlberger, "Multilayer nanoimprinting to create hierarchical stamp masters for nanoimprinting of optical micro- and nanostructures," *Coatings* **10**(3), 301 (2020).
9. T. Gissibl, S. Thiele, A. Herkommer, and H. Giessen, "Two-photon direct laser writing of ultracompact multi-lens objectives," *Nat. Photonics* **10**(8), 554–560 (2016).
10. P. I. Dietrich, M. Blaicher, I. Reuter, M. Billah, T. Hoose, A. Hofmann, C. Caer, R. Dangel, B. Offrein, U. Troppenz, M. Moehrle, W. Freude, and C. Koos, "In situ 3D nanoprining of free-form coupling elements for hybrid photonic integration," *Nat. Photonics* **12**(4), 241–247 (2018).
11. H. Gehring, A. Eich, C. Schuck, and W. H. P. Pernice, "Broadband out-of-plane coupling at visible wavelengths," *Opt. Lett.* **44**(20), 5089 (2019).
12. T. N. Oder, J. Shakya, J. Y. Lin, and H. X. Jiang, "Nitride microlens arrays for blue and ultraviolet wavelength applications," *Appl. Phys. Lett.* **82**(21), 3692–3694 (2003).
13. H. W. Choi, E. Gu, C. Liu, C. Griffin, J. M. Girkin, I. M. Watson, and M. D. Dawson, "Fabrication of natural diamond microlenses by plasma etching," *J. Vac. Sci. Technol. B* **23**(1), 130–132 (2005).
14. F. Sardi, T. Kornher, M. Widmann, R. Kolesov, F. Schiller, T. Reindl, M. Hagel, and J. Wrachtrup, "Scalable production of solid-immersion lenses for quantum emitters in silicon carbide," *Appl. Phys. Lett.* **117**(2), 022105 (2020).
15. A. Zolfaghari, T. Chen, and A. Y. Yi, "Additive manufacturing of precision optics at micro and nanoscale," *Int. J. Extrem. Manuf.* **1**(1), 012005 (2019).
16. A. C. Fischer, M. Mäntysalo, and F. Niklaus, "Inkjet printing, laser-based micromachining, and micro-3D printing technologies for MEMS," in *Handbook of Silicon Based MEMS Materials and Technologies*, (2020), pp. 531–545.
17. NanoScribe GmbH & Co. KG, <https://www.nanoscribe.com/en/products/ip-resins>, (2022).
18. M. A. Green, "Self-consistent optical parameters of intrinsic silicon at 300 K including temperature coefficients," *Solar Energy Materials and Solar Cells* **92**(11), 1305–1310 (2008).
19. C. Xu, S. Wang, G. Wang, J. Liang, S. Wang, L. Bai, J. Yang, and X. Chen, "Temperature dependence of refractive indices for 4H- and 6H-SiC," *J. Appl. Phys.* **115**(11), 113501 (2014).
20. H. R. Phillip and E. A. Taft, "Kramers-Kronig analysis of reflectance data for diamond," *Phys. Rev.* **136**(5A), A1445–A1448 (1964).
21. A. S. Barker and M. Ilegems, "Infrared lattice vibrations and free-electron dispersion in GaN," *Phys. Rev. B* **7**(2), 743–750 (1973).
22. J. Pastrňák and L. Roskovcova, "Refraction index measurements on AlN single crystals," *phys. stat. sol. (b)* **14**(1), K5–K8 (1966).
23. L. Marseglia, J. P. Hadden, A. C. Stanley-Clarke, J. P. Harrison, B. Patton, Y. L. Ho, B. Naydenov, F. Jelezko, J. Meijer, P. R. Dolan, J. M. Smith, J. G. Rarity, and J. L. O'Brien, "Nanofabricated solid immersion lenses registered to single emitters in diamond," *Appl. Phys. Lett.* **98**(13), 133107 (2011).
24. M. Jamali, I. Gerhardt, M. Rezai, K. Frenner, H. Fedder, and J. Wrachtrup, "Microscopic diamond solid-immersion-lenses fabricated around single defect centers by focused ion beam milling," *Rev. Sci. Instrum.* **85**(12), 123703 (2014).
25. H. M. Presby, A. F. Benner, and C. A. Edwards, "Laser micromachining of efficient fiber microlenses," *Appl. Opt.* **29**(18), 2692 (1990).
26. B. Hao, H. Liu, F. Chen, Q. Yang, P. Qu, G. Du, J. Si, X. Wang, and X. Hou, "Versatile route to gapless microlens arrays using laser-tunable wet-etched curved surfaces," *Opt. Express* **20**(12), 12939 (2012).
27. E. Gu, H. W. Choi, C. Liu, C. Griffin, J. M. Girkin, I. M. Watson, M. D. Dawson, G. McConnell, and A. M. Gurney, "Reflection/transmission confocal microscopy characterization of single-crystal diamond microlens arrays," *Appl. Phys. Lett.* **84**(15), 2754–2756 (2004).
28. C. L. Lee, E. Gu, M. D. Dawson, I. Friel, and G. A. Scarsbrook, "Etching and micro-optics fabrication in diamond using chlorine-based inductively-coupled plasma," *Diamond Relat. Mater.* **17**(7-10), 1292–1296 (2008).
29. Y. Zhang, Y. Li, L. Liu, C. Yang, Y. Chen, and S. Yu, "Demonstration of diamond microlens structures by a three-dimensional (3D) dual-mask method," *Opt. Express* **25**(13), 15572 (2017).
30. S. To, Z. Zhu, and H. Wang, "Virtual spindle based tool servo diamond turning of discontinuously structured microoptics arrays," *CIRP Annals* **65**(1), 475–478 (2016).

31. M. Mukaida and J. Yan, "Fabrication of hexagonal microlens arrays on single-crystal silicon using the tool-servo driven segment turning method," *Micromachines* **8**(11), 323 (2017).
32. S. Ghosh, A. Hinz, S. M. Fairclough, B. F. Spiridon, A. Eblabla, M. A. Casbon, M. J. Kappers, K. Elgaid, S. Alam, R. A. Oliver, and D. J. Wallis, "Origin(s) of anomalous substrate conduction in MOVPE-grown GaN HEMTs on highly resistive silicon," *ACS Appl. Electron. Mater.* **3**(2), 813–824 (2021).
33. G. Balasubramanian, I. Y. Chan, R. Kolesov, M. Al-Hmoud, J. Tisler, C. Shin, C. Kim, A. Wojcik, P. R. Hemmer, A. Krueger, T. Hanke, A. Leitenstorfer, R. Bratschitsch, F. Jelezko, and J. Wrachtrup, "Nanoscale imaging magnetometry with diamond spins under ambient conditions," *Nature* **455**(7213), 648–651 (2008).
34. P. Maletinsky, S. Hong, M. S. Grinolds, B. Hausmann, M. D. Lukin, R. L. Walsworth, M. Loncar, and A. Yacoby, "A robust scanning diamond sensor for nanoscale imaging with single nitrogen-vacancy centres," *Nat. Nanotechnol.* **7**(5), 320–324 (2012).
35. J. M. Taylor, P. Cappellaro, L. Childress, L. Jiang, D. Budker, P. Hemmer, A. Yacoby, R. Walsworth, and M. Lukin, "High-sensitivity diamond magnetometer with nanoscale resolution," *Nat. Phys.* **4**(10), 810–816 (2008).
36. K. A. Shaw, Z. L. Zhang, and N. C. MacDonald, "SCREAM I: A single mask, single-crystal silicon, reactive ion etching process for microelectromechanical structures," *Sens. Actuators, A* **40**(1), 63–70 (1994).
37. S. Fairclough, A. Hinz, S. Ghosh, B. Spiridon, D. Wallis, and R. Oliver, "Direct evidence of an Al alloyed Si interlayer within an ammonia pre-dosed AlN/Si interface via STEM-EELS," in *Proceedings of Electron Beam Spectroscopy for Nanooptics 2021 (EBSN2021)*, (2021).
38. J. McPhillimy, D. Jevtics, B. J. E. Guilhabert, C. Klitis, A. Hurtado, M. Sorel, M. D. Dawson, and M. J. Strain, "Automated Nanoscale Absolute Accuracy Alignment System for Transfer Printing," *ACS Appl. Nano Mater.* **3**(10), 10326–10332 (2020).
39. Z. Shaban, Z. Li, B. Roycroft, M. Saei, T. Mondal, and B. Corbett, "Transfer printing of roughened GaN "based light" emitting diodes into reflective trenches for visible light communication," *Adv. Photonics Res.* **3**(8), 2100312 (2022).
40. A. J. Trindade, B. Guilhabert, E. Y. Xie, R. Ferreira, J. J. D. McKendry, D. Zhu, N. Laurand, E. Gu, D. J. Wallis, I. M. Watson, C. J. Humphreys, and M. D. Dawson, "Heterogeneous integration of gallium nitride light-emitting diodes on diamond and silica by transfer printing," *Opt. Express* **23**(7), 9329 (2015).
41. B. F. Spiridon, M. Toon, A. Hinz, S. Ghosh, S. M. Fairclough, B. J. E. Guilhabert, M. J. Strain, I. M. Watson, M. D. Dawson, D. J. Wallis, and R. A. Oliver, "Method for inferring the mechanical strain of GaN-on-Si epitaxial layers using optical profilometry and finite element analysis," *Opt. Mater. Express* **11**(6), 1643 (2021).
42. H. Otevaere, R. Cox, H.-P. Herzig, T. Miyashita, K. Naessens, M. Taghizadeh, R. Völkel, H. Woo, and H. Thienpont, "Comparing glass and plastic refractive microlenses fabricated with different technologies," *J. Opt. A: Pure Appl. Opt.* **8**(7), S407–S429 (2006).
43. M. Baranski, S. Perrin, N. Passilly, L. Froehly, J. Albergo, S. Bargiel, and C. Gorecki, "A simple method for quality evaluation of micro-optical components based on 3D IPSF measurement," *Opt. Express* **22**(11), 13202 (2014).
44. A. Franzen, <http://www.gwoptics.org/ComponentLibrary/>, (2022).
45. G. M. Laws, E. C. Larkins, I. Harrison, C. Molloy, and D. Somerford, "Improved refractive index formulas for the Al_xGa_{1-x}N and In_yGa_{1-y}N alloys," *J. Appl. Phys.* **89**(2), 1108–1115 (2001).
46. W. Demtröder, *Experimentalphysik 2 - Elektrizität und Optik*, vol. 5 (2009).
47. P. Nussbaum, R. Völkel, H. P. Herzig, M. Eisner, and S. Haselbeck, "Design, fabrication and testing of microlens arrays for sensors and microsystems," *Pure Appl. Opt.* **6**, 617–636 (1997).
48. M.-S. Kim, T. Scharf, and H. P. Herzig, "Small-size microlens characterization by multiwavelength high-resolution interference microscopy," *Opt. Express* **18**(14), 14319 (2010).
49. G. J. Lee, H. M. Kim, and Y. M. Song, "Design and fabrication of microscale, thin-film silicon solid immersion lenses for mid-infrared application," *Micromachines* **11**(3), 250 (2020).
50. A. Gruber, A. Dräbenstedt, C. Tietz, L. Fleury, J. Wrachtrup, and C. Von Borczyskowski, "Scanning confocal optical microscopy and magnetic resonance on single defect centers," *Science* **276**(5321), 2012–2014 (1997).
51. A. M. Berhane, K. Y. Jeong, Z. Bodrog, S. Fiedler, T. Schröder, N. V. Trivino, T. Palacios, A. Gali, M. Toth, D. Englund, and I. Aharonovich, "Bright room-temperature single-photon emission from defects in gallium nitride," *Adv. Mater.* **29**(12), 1605092 (2017).
52. C. P. Anderson, E. O. Glen, C. Zeledon, A. Bourassa, Y. Jin, Y. Zhu, C. Vorwerk, A. L. Crook, H. Abe, J. Ul-Hassan, T. Ohshima, N. T. Son, G. Galli, and D. D. Awschalom, "Five-second coherence of a single spin with single-shot readout in silicon carbide," *Sci. Adv.* **8**(5), 1 (2022).
53. N. K. Wessling, S. Ghosh, B. Guilhabert, M. Kappers, A. M. Hinz, M. Toon, R. A. Oliver, M. D. Dawson, and M. J. Strain, "Data for: "Fabrication and transfer printing based integration of free-standing GaN membrane micro-lenses onto semiconductor chips"," University of Strathclyde, 2022, <https://doi.org/10.15129/1352ed1d-5b90-4b7f-9541-a9dcffed1d275>.